EFFECTS OF WELDING ON STRUCTURAL PERFORMANCE OF HIGH

STRENGTH STEEL THICK WELDED SECTIONS

JIN Hao

PhD

The Hong Kong Polytechnic University

2024

The Hong Kong Polytechnic University

Department of Civil and Environmental Engineering

Effects of Welding on Structural Performance of High Strength Steel
Thick Welded Sections

JIN Hao

A thesis submitted in partial fulfilment of the requirements for the degree of
Doctor of Philosophy

August 2023

CERTIFICATE OF ORIGINALITY

I hereby declare that this thesis is my own work and that, to the best of my knowledge and belief, it reproduces no material previously published or written, nor material that has been accepted for the award of any other degree or diploma, except where due acknowledgement has been made in the text.

 _____(Signed)

 _____JIN HAO_____(Name of Student)

ABSTRACT

Motivation

Structural steel sections have been extensively employed in the construction of buildings, bridges, offshore structures and heavy industrial machines for many years. Nowadays, with the development of modern metallurgical technology, high strength steels (HSS), especially Grade 690 steel, and the corresponding welding consumables become available for engineering applications. Compared with normal grade steel, it is seen that the use of high-strength structural steel leads to a reduction in the plate thickness of components and the overall weight of the structure. Consequently, this reduction in weight results in a decrease in the quantity of steel required, as well as a decrease in the dimensions of the weld and the materials used for welding. A reduction of 50% in plate thickness brings along a savings of about 67 to 75% in welding manpower and electrodes, depending on joint details.

However, strength reductions in high strength steel welded sections have been reported by many researchers, and the heat input energy should be controlled into a small value during welding. Such a restriction will severely limit the application of high strength S690 steel in the construction industry. Hence, it is highly desirable to examine and quantify such effects in these Grade 690 steel thick sections for applications in construction. In general, there is a lack of scientific understandings and engineering data on the effects of welding onto the structural performance of the welded sections of these Grade 690 steel with plate thicknesses up to 70 mm.

Objectives and scope of work

In the present research, it is aimed to investigate the effects of welding onto the mechanical properties, and hence, the structural performance of the high strength steel welded sections with thicknesses up to 70 mm through systematic experimental and

numerical investigations. The scope of work includes:

a) To investigate both thermal and thermomechanical responses of typical welded sections of thick high strength steel plates during and after welding, and hence, to establish through thickness distributions of welding-induced residual stresses within these welded connections.

b) To assess any reduction in the mechanical properties of these welded sections of thick high strength steel plates which are prepared with a practical range of heat input energy during welding, to establish advanced finite element models for accurate prediction to the structural behaviour of these welded sections.

c) To perform physical measurements and structural tests on these welded sections of thick high strength steel plates to provide test data for calibration of various finite element models.

Key research findings

➢ **Task 1. Mechanical properties of high strength steel thick welded sections**

In order to determine the effects of welding onto the mechanical properties of these thick welded sections, a total of 22 standard coupons extracted from the S690-QT 50 and 70 mm thick welded sections, and 22 standard coupons extracted from the Q620-TM 28 and 44 mm thick welded sections were tested under monotonic loadings. The range of heat input energy in preparing these thick welded sections varied from 2.4 to 5.0 kJ/mm, and it was considered to cover the heat input energy commonly used in practice. Images of Scanning Electron Microscope (SEM) were captured to illustrate microstructural evolutions within the heat affected zones of the welded sections.

In general, the effects of welding are demonstrated to be significantly less severe than anticipated as there is little or even no reduction in the mechanical properties of these thick welded sections. In many cases, the engineering stress-strain curves of these thick

III

welded sections follow closely with those of the base plates along the entire deformation ranges with a discrepancy smaller than 3 to 5%.

➢ **Task 2. Through thickness residual stresses of thick welded sections**

The through thickness residual stresses of thick welded sections of these high strength steel plates were assessed as follows:

- Firstly, the hole-drilling method was applied to the top and the bottom surfaces of a S690-QT 50 mm thick welded section to establish a reference set of residual stress distribution.

- Secondly, as the residual stresses distributed through the thickness of the welded section could not be measured directly, a large amount of the steel was removed from the top and the bottom parts of the welded section with milling and the hole-drilling method was then applied onto these newly formed surfaces. Owing to significant stress release in the welded section during removal of the steel, correction to the second set of residual stress distribution was necessary.

- Thirdly, an advanced finite element model was developed using ABAQUS, and both the processes of welding and removal of the steel were simulated. The heat transfer analyses were first calibrated with the measured temperature history during welding. Then, sequentially coupled thermomechanical analyses were conducted to predict the residual stresses of these welded sections. After careful calibration against the two sets of measured residual stress distributions, the finite element model was able to simulate the through thickness residual stresses of the welded sections with a high degree of accuracy.

In general, the effects of welding are demonstrated to be significantly less severe than anticipated as the residual stresses in these 50 mm thick welded sections are found to be significantly smaller than those 16 mm thick welded sections.

➢ **Task 3. Advanced modelling approach with critical sub-zones**

In order to establish a rational finite element model to simulate the structural performance of a thick welded section, critical sub-zones were proposed to be adopted in the heat affected zones of the welded section. Based on the predicted transient temperature history, the elements having a cooling time of $t_{8/5}$, i.e. a time for the temperature to decrease from 800ºC to 500ºC, were identified as the critical sub-zones. Hence, both the locations and the dimensions of the critical sub-zones were readily determined. The mechanical properties of these elements in the critical sub-zones were then assigned conservatively to lower bound values according to their $t_{8/5}$. It should be noted that these lower bound values of mechanical properties were obtained from a series of tensile tests on heat-treated coupons after a physical welding simulation process.

Finite element models have been established to simulate structural behaviour of:

i) welded sections of the S690-QT and of the Q620-TM steel with 2 heat input energy under tension; and

ii) stocky columns of the Q620-TM steel under compression.

Good comparison between the predicted and the measured test data was achieved.

Hence, the proposed modelling approach with the use of critical sub-zones are demonstrated to be highly effective in simulating the structural behaviour of these thick welded sections of high strength steel plates. It should be noted that the proposed approach is able to simulate the structural behaviour of the welded sections under tension with a small level of strength reductions at 1%, and also of the stocky columns under compression with a small level of strength reductions at 2 to 3 %.

Research significance

This research is an in-depth investigation into the effects of welding onto both S690-

QT and Q620-TM high strength steel thick sections. Both scientific understanding and engineering data on the mechanical properties, and hence, the structural performance of these welded sections have been obtained. An advanced finite element modelling approach is also proposed with the use of critical sub-zones in the heat affected zones of these welded sections, and finite element models have been established to simulate the structural behaviour of these welded sections under both tension and compression. Consequently, these models are able to quantify the effects of welding onto the structural behaviour of these welded sections in a rational manner.

ACKNOWLEDGEMENTS

TABLE OF CONTENTS

LIST OF FIGURES

XIII

XIV

LIST OF TABLES

XVIII

Chapter 1.   Introduction

1.1 Research background

Structural steel sections have been extensively employed in construction of buildings, bridges, offshore structures and heavy industrial machines for many years. Nowadays, with advanced development of modern metallurgical technology, high strength steels (HSS), especially Grade 600MPa steel, become available for engineering applications. Compared with normal grade steel, it is expected that the use of high-strength structural steel will lead to a significant reduction in overall weight of structure owing to their increased strengths.

Figure 1.1 shows S690 50 mm thick welded box section examined by the author in a construction site. This box section is 2.5 m in length, and an experienced welder spent 5.5 hours to perform welding of one single groove with submerged arc welding. If Grade S460 steel is used instead, the plate thickness of S460 steel should be 75mm in order to achieve the same cross-sectional resistance as follow:

$$50\text{mm} \times 690 \text{ N/mm}^2 = 75\text{mm} \times 460 \text{ N/mm}^2$$

As shown in Table 1.1, as the thickness increases with a factor of 1.5, the cross sectional area of the weldment increases by 1.5^2 times, i.e. 2.25. Hence, it will 2.25 times of the welding time to perform the welding, i.e. from 5.5 hours to 12 hours. Replacing thick steel plates of normal strength steel with thinner high strength steel plates will lead to considerable saving in construction time and manpower. Such effect is considered to be more significant with an increasing plate thickness.
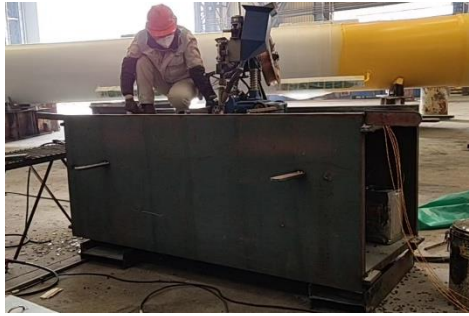
a) Overview of a box section
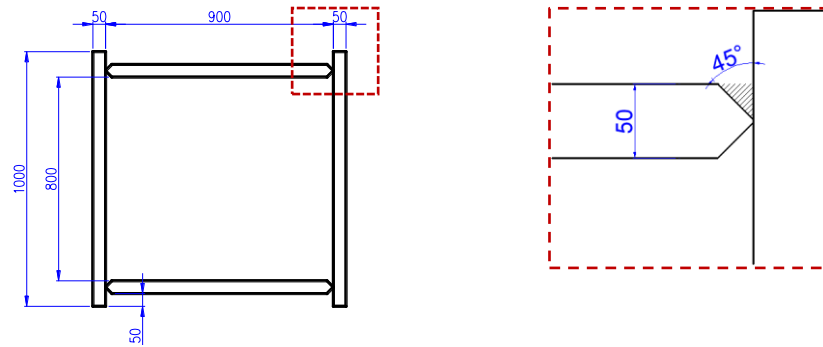
b) Typical weld joint for a 50mm thick steel plate
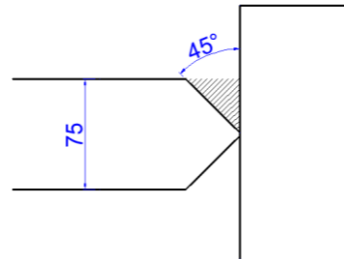
c) Typical weld joint for a 75mm thick steel plate

Figure 1.1 Design of a box section with S690 and S460 steel plates

Table 1.1 Advantage of using Grade S690 steel

Material	S690	S460
Plate thickness (mm)	50	75
Cross sectional area of weldment (mm²)	312	703
Time consumption (h)	5.5	12

It should be noted that this comparison is directly applicable if the heat input energy adopted in the welding process in both cases are the same. However, as reported by LIU (2018), the S690 QT 16 mm thick welded sections have reductions in mechanical

2

properties when compared with their base plate. The tensile strength of the S690 welded section with a heat input energy of 2.0 kJ/mm cannot even meet the strength requirement stipulated in EN ISO 15614-1 (ISO, 2017). The welding process may cause changes in microstructure of the S690 steel plates and, as a result, reduction may take place in mechanical properties in the heat affected zones of the welded sections. This occurs because of the specific chemical compositions and heat treatment process used to make these S690 steel. However, there is no such issue in most S460 steel plates.

Such a restriction on the heat input energy during welding will severely limit the application of high strength S690 steel in the construction industry. Thus, it is essential to look into the mechanical properties of the S690 thick sections after welding. High strength steels with two heat treatment procedures are examined, the quenching and tempering (QT) process and the thermo-mechanically (TM) controlled process.

Another issue caused by welding is the presence of residual stresses after welding, and they have substantial adverse impact on the stiffness of the welded sections, as well as on the stability of compression members. The patterns and magnitudes of residual stresses in typical welded sections may be found in many design standards for steel structures. However, these informations are developed for normal grade steel back in the 1980's and 1990's. It should be noted that there is little information on the residual stresses for the high strength steel. Additionally, the majority of the existing design standards take into account effect of residual stresses on steel sections up to Grade 460. Hence, it is important to conduct a thorough research into the residual stress distributions of high strength steel welded sections.

In addition, advanced numerical simulation on welding should be carried out because it provides technical data supplementary to experimental data. The transient temperature distribution history during welding, and the changes in the mechanical properties within the HAZ and the presence of residual stresses caused by welding are readily predicted using advanced finite element modelling technique.

3

1.2 Objective and scope of work

In the present research, it is aimed to investigate the effects of welding onto the mechanical properties, and hence, the structural performance of the high strength steel welded sections with thicknesses up to 70 mm through systematic experimental and numerical investigations. The scope of work includes:

d) To investigate both thermal and thermomechanical responses of typical welded sections of thick high strength steel plates during and after welding, and hence, to establish through thickness distributions of welding-induced residual stresses within these welded connections.

e) To assess any reduction in the mechanical properties of these welded sections of thick high strength steel plates which are prepared with a practical range of heat input energy during welding, to establish advanced finite element models for accurate prediction to the structural behaviour of these welded sections.

f) To perform physical measurements and structural tests on these welded sections of thick high strength steel plates to provide test data for calibration of various finite element models.

1.3 Key findings

➢ **Task 1. Mechanical properties of high strength steel thick welded sections**

In order to determine the effects of welding onto the mechanical properties of these thick welded sections, a total of 22 standard coupons extracted from the S690-QT 50 and 70 mm thick welded sections, and 22 standard coupons extracted from the Q620-TM 28 and 44 mm thick welded sections were tested under monotonic loadings. The range of heat input energy in preparing these thick welded sections varied from 2.4 to 5.0 kJ/mm, and it was considered to cover the heat input energy commonly used in

4

practice. Images of Scanning Electron Microscope (SEM) were captured to illustrate microstructural evolutions within the heat affected zones of the welded sections.

In general, the effects of welding are demonstrated to be significantly less severe than anticipated as there is little or even no reduction in the mechanical properties of these thick welded sections. In many cases, the engineering stress-strain curves of these thick welded sections follow closely with those of the base plates along the entire deformation ranges with a discrepancy smaller than 3 to 5%.

> **Task 2. Through thickness residual stresses of thick welded sections**

The through thickness residual stresses of thick welded sections of these high strength steel plates were assessed as follows:

- Firstly, the hole-drilling method was applied to the top and the bottom surfaces of a S690-QT 50 mm thick welded section to establish a reference set of residual stress distribution.

- Secondly, as the residual stresses distributed through the thickness of the welded section could not be measured directly, a large amount of the steel was removed from the top and the bottom parts of the welded section with milling and the hole-drilling method was then applied onto these newly formed surfaces. Owing to significant stress release in the welded section during removal of the steel, correction to the second set of residual stress distribution was necessary.

- Thirdly, an advanced finite element model was developed using ABAQUS, and both the processes of welding and removal of the steel were simulated. The heat transfer analyses were first calibrated with the measured temperature history during welding. Then, sequentially coupled thermomechanical analyses were conducted to predict the residual stresses of these welded sections. After careful calibration against the two sets of measured residual stress distributions, the finite element model was able to simulate the through thickness residual stresses of the welded

5

sections with a high degree of accuracy.

In general, the effects of welding are demonstrated to be significantly less severe than anticipated as the residual stresses in these 50 mm thick welded sections are found to be significantly smaller than those 16 mm thick welded sections.

➤ **Task 3. Advanced modelling approach with critical sub-zones**

In order to establish a rational finite element model to simulate the structural performance of a thick welded section, critical sub-zones were proposed to be adopted in the heat affected zones of the welded section. Based on the predicted transient temperature history, the elements having a cooling time of $t_{8/5}$, i.e. a time for the temperature to decrease from 800ºC to 500ºC, were identified as the critical sub-zones. Hence, both the locations and the dimensions of the critical sub-zones were readily determined. The mechanical properties of these elements in the critical sub-zones were then assigned conservatively to lower bound values according to their $t_{8/5}$. It should be noted that these lower bound values of mechanical properties were obtained from a series of tensile tests on heat-treated coupons after a physical welding simulation process.

Finite element models have been established to simulate structural behaviour of:

iii) welded sections of the S690-QT and of the Q620-TM steel with 2 heat input energy under tension; and

iv) stocky columns of the Q620-TM steel under compression.

Good comparison between the predicted and the measured test data was achieved.

Hence, the proposed modelling approach with the use of critical sub-zones are demonstrated to be highly effective in simulating the structural behaviour of these thick welded sections of high strength steel plates. It should be noted that the proposed approach is able to simulate the structural behaviour of the welded sections under

6

tension with a small level of strength reductions at 1%, and also of the stocky columns under compression with a small level of strength reductions at 2 to 3 %.

1.4 Significance of the research project

This research is an in-depth investigation into the effects of welding onto both S690-QT and Q620-TM high strength steel thick sections. Both scientific understanding and engineering data on the mechanical properties, and hence, the structural performance of these welded sections have been obtained. An advanced finite element modelling approach is also proposed with the use of critical sub-zones in the heat affected zones of these welded sections, and finite element models have been established to simulate the structural behaviour of these welded sections under both tension and compression. Consequently, these models are able to quantify the effects of welding onto the structural behaviour of these welded sections in a rational manner.

1.5 Outline of the thesis

- Chapter 1. Introduction

This chapter provides an overview of the research work. The research background, the scope of work, the methodology, the significance of this project, and the outline of this thesis are presented.

- Chapter 2. Literature Review

A comprehensive review on relevant research available in the literature on high strength steel is presented in this chapter, including the steel making techniques, typical welding methods, the effects of welding on mechanical properties and the presence of residual stresses, and various advanced numerical simulation of the welding process.

- Chapter 3. Mechanical properties of welded sections of high strength S690 and Q620 steels

The welding effects on the mechanical properties of the S690 QT and the Q620 TM welded sections are investigated systematically and reported in this chapter. The mechanical properties of these thick welded sections are compared with those of the 16 mm thick welded sections to identify the range of reductions in these sections. Scanning Electron Microscope (SEM) are employed to capture images of the microstructures within the heat affected zones.

- Chapter 4. Experimental and numerical investigation into residual stresses of S690 QT 50 mm thick welded sections

This chapter presents an experimental-numerical incorporated investigation into the welding-induced residual stresses of the S690 QT 50 mm thick sections, namely, Sections RS50-24 and RS50-50. A local material removal method is employed to determine the residual stress through the thicknesses of the welded sections. The results are compared with these 16 mm thick welded sections to illustrate the differences in the effects of welding on these residual stresses between thick and thin welded sections.

- Chapter 5. Modelling of standard tensile tests of S690 QT and Q620 TM welded sections

This chapter presents a proposed method for simulation of welded sections under tension. Only the most critical sub-zone within the HAZ is adopted in the proposed model so that the structural behaviour of the welded section can be obtained with limited computational resources. The proposed models for both high strength QT and TM welded sections are established and successfully validated against test data.

- Chapter 6. Structural performance of Q620 TM 28 mm thick welded H-sections with different heat input energy under compression

This chapter presents an experimental and numerical investigation into the structural performance of stocky columns of Q620 TM welded H-sections. A total of three reference H-sections together with three columns with welded splices are tested under

8

compression. Complementary finite element models with both the welding-induced residual stresses and modified mechanical properties in these welded sections are established. With the proposed method for simulation of these welded sections, the effects of welding onto these stocky columns are investigated. A comparison on the measured and the predicted structural performance of these stocky columns is also presented.

- Chapter 7. Conclusion

Conclusions of this project are summarized in this chapter. Recommendations for future work on welding simulation technology are also presented.

A flow chart of all the research work in this thesis is shown in Figure 1.2. The effects of welding on changes in mechanical properties within HAZ were investigated in Chapter 3 experimentally and in Chapter 5 numerically. The effects of welding on residual stresses were investigated with a combination of experiment and simulation approach in Chapter 4. The compression tests of welded H-sections were demonstrated in Chapter 6 and an advanced numerical model which considered both the changes of mechanical properties within HAZ and welding induced residual stresses was developed and calibrated against these test data.
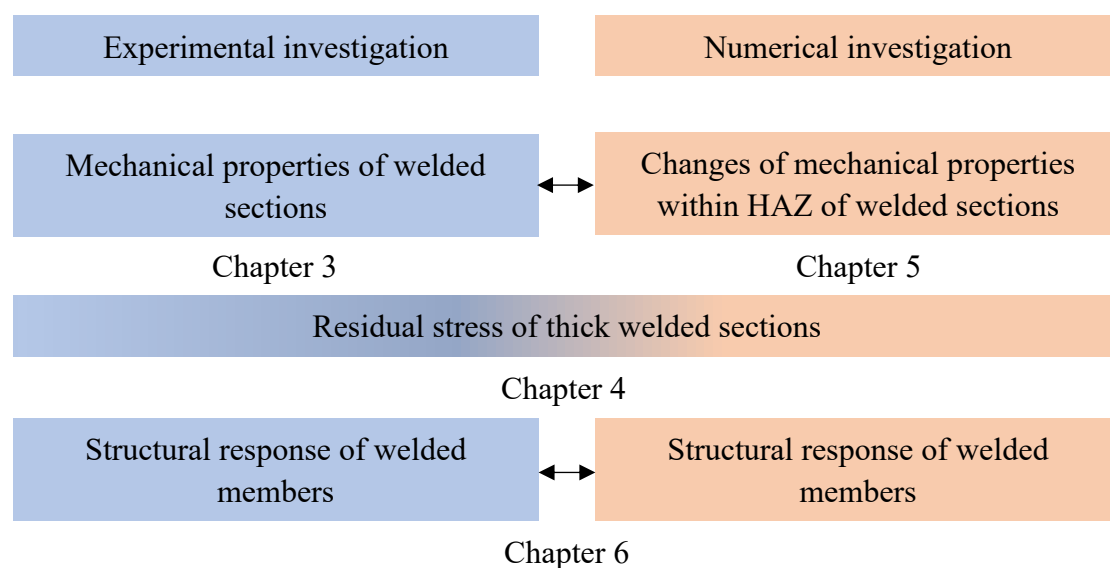
Figure 1.2 Flow chart of the research work

Chapter 2.   Literature review

2.1 Introduction

This chapter provides a literature review on high-strength steel (HSS) research studies. The following topics are thoroughly reviewed while the following key findings are presented:

I)   Material specifications and mechanical properties of high strength steel

II)   Welding processes and effects of welding onto microstructure changes, and

III) Experimental investigations into welding.

2.2 High strength steel

High strength steel (HSS) refers to structural steel with a yield strength of not less than 460 MPa (CEN, 2007). Recent advancement of modern steel making technology and development of welding consumables has brought HSS to be readily used in construction. Compared with common structural steel, HSS processes a larger strength, which helps reduce material usage and fabrication time. It also enhances aesthetic appearance of structures with members of reduced sizes.

2.2.1   Deliver conditions

In making of HSS, there are two commonly used heat treatment, namely, the Quenching and Tempering (QT) process, and the Thermal-Mechanically-Controlled-Processing (TMCP). These two processes are illustrated in Figure 2.1.
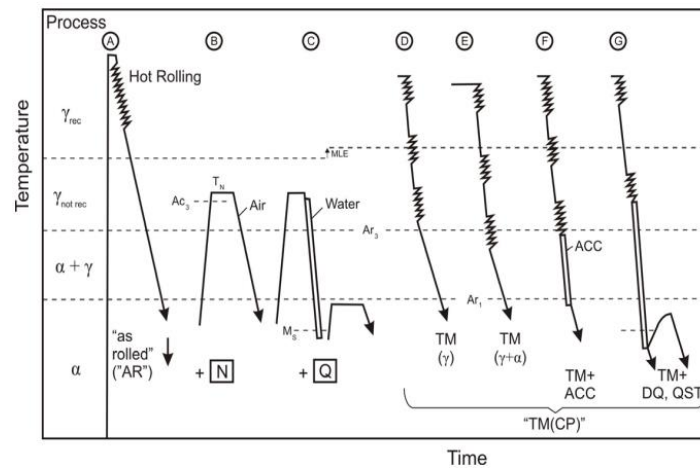
Figure 2.1 Heat treatment in QT and TMCP (Willms, 2009)

The Quenching and Tempering process is a two-stage heat treatment process:

In Stage 1, the steel is heated to a temperature above its recrystallization temperature, i.e. about 900°C and then, it is quickly cooled or quenched in water, oil, or forced air or inert gases such as nitrogen.

11

In Stage 2, the steel is tempered, i.e. to be heated under its critical point temperature, and then air cooled in order to obtain desired material properties. In general, the steel is tempered to attain improved toughness and ductility by decreasing its hardness. The amount of time for the quenched steel to be tempered depends largely on how much hardness is expected to be removed.

The TMCP involves a series of controlled heat treatment onto the steel. In general, the steel is heated to a temperature commonly used for hot working operations, i.e. about 1200°C. An initial hot working ('roughing') is then carried out in a normal fashion. However, the final hot work reduction or 'finishing pass' is carried out at a lower temperature, when compared with those in the normal processes. Plastic deformation at this lower temperature promotes fine grain sizes, and further cooling brings the steel to the transformation temperature range, so that austenite is transformed into ferrite with fine ferrite grains and fine dispersed precipitates. For some TMCP steel, this last stage of cooling, during which transformation is completed, is accelerated by water cooling, to give finer grain sizes. Accelerated cooling can sometimes result in bainite formation as well as, or instead of, ferrite formation.

2.2.2 Chemical composition

Both QT and TMCP are able to make steel with a wide range of strengths: EN 10025-6 (CEN 2019c) gives a number of technical delivery conditions for QT steel, and their yield strengths vary from 235 to 960 MPa. EN 10025-4 (CEN 2019b) gives a number of technical delivery conditions for TMCP steel, and their yield strengths vary from 235 to 500 MPa. GB/T 1591 (CNS, 2018) gives a number of technical delivery conditions for TMCP steel, and their yield strengths vary from 355 to 690 MPa.

Table 2.1 Chemical compositions of Grade 690 QT and TMCP steel in standards

	Grade	C	Si	Mn	P	S	N	Ni	Cr	Mo	Cu
EN 10025-6	-	0.22	0.86	1.80	0.030	0.017	0.016	4.10	1.60	0.74	0.55
GB/T 1591	Q620	0.18	0.60	2.60	0.030	0.030	0.015	0.80	1.00	0.30	0.80
	Q690	0.18	0.60	2.00	0.030	0.030	0.015	0.80	1.00	0.30	0.80

Table 2.2 Maximum CEV of Grades S620 and S690 QT steel in EN 10025-6

	Grade	≤50	> 50 ≤100	> 100 ≤125	> 125 ≤200
EN 10025-6	S620	0.65	0.77	0.83	0.83
	S690	0.65	0.77	0.83	0.83

Table 2.3 Maximum CEV of Grades Q620 and Q690 TMCP steel in GB/T 1591

	Grade	≤16	> 16 ≤40	> 40 ≤63	> 63 ≤150
GB/T 1591	Q620	0.48	0.48	0.48	0.49
	Q690	0.49	0.49	0.49	0.49

$$CEV = C + \frac{Mn}{6} + \frac{Cr+Mo+V}{5} + \frac{Ni+Cu}{15} \qquad (2.1)$$

It is obvious that the chemical compositions listed in Table 2.1 and the maximum CEV listed in Tables 2.2 and 2.3 are usually quite low in the TMCP steel, when compared with those of the QT steel of the same grade because they achieve higher strengths by means of accelerated cooling. In addition, the alloying composition usually increases with an increase of the plate thickness in order to ensure sufficient hardening of the steel in the core region of the plate, so the carbon equivalent value, i.e. CEV, calculated using Equation 2.1, also increases (Eleni, 2012).

2.2.3 Mechanical properties

Figure 2.2 presents typical stress-strain curves of four different steel grades. Obvious yield plateaus and strain hardening effects can be observed in the stress-strain curves

13

of both Grades 235 and 355 steel. Their yield plateau usually starts at a strain level of 0.2% and end at about 2.5%, and their tensile-to-yield (TS/YS) ratios vary from 1.25 to 1.67. With the increase in steel grade, the yield plateau becomes shorter, and it reduces to about 2.0% in Grade 460 steel, and there are no obvious yield plateaus in Grade 960 steel. What's more, the TS/YS ratio becomes close to 1.0 in high-strength steel compared with the normal grade ones. It is worth noting that in true stress-strain curves, the differences in ductility among all these steel of different grade are small, and necking happens in an early stage in these HSS (Langenberg, 2008).
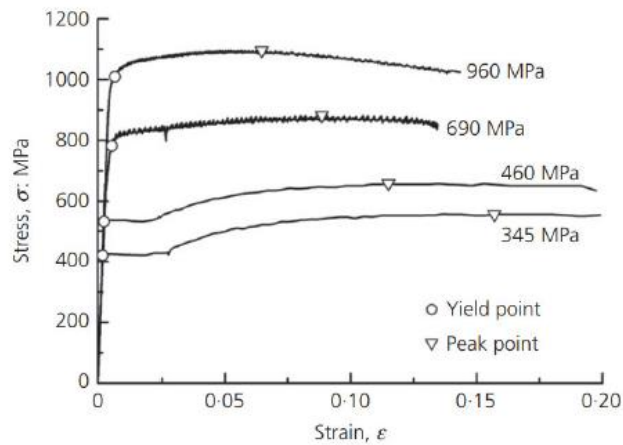
Figure 2.2 Typical stress-strain curves of different steel grades (Ban, 2012)

Tables 2.4 and 2.5 summarize minimum yield strengths, range of tensile strengths and minimum elongations at fracture of Grades 620 and 690 steel plates with different thicknesses.

Table 2.4 Mechanical properties of S620 and S690 QT steel at room temperature in EN 10025-6

Grade	Minimum yield strength (MPa)				Tensile strength (MPa)				Minimum Elongation (%)
	Plate thickness (mm)								
	≤50	>50 ≤100	>100 ≤125	>125 ≤200	≤50	>50 ≤100	>100 ≤125	>125 ≤200	
S620	620	580	560		700-890		650-830		15
S690	690	650	630		770-940	760-930	710-900		14

Table 2.5 Mechanical properties of Q620 and Q690 TMCP steel at room temperature

in GB/T 1591

Grade	Minimum yield strength (MPa)				Tensile strength (MPa)			Minimum Elongation (%)
	Plate thickness (mm)							
	≤16	> 16 ≤40	> 40 ≤63	> 63 ≤150	≤40	> 40 ≤63	> 63 ≤150	
Q620	620	610	600	580	710-880	690-880	670-860	15
Q690	690	680	670	650	770-940	750-920	730-900	14

With an increase in temperature, the mechanical properties of the steel decrease accordingly to different levels. EN 1993-1-2 (CEN, 2005) and ASM Material Handbook list out various formulae to calculate various properties, such as Young's modulus, yield strength and tensile strength under specific temperatures for normal grade steel. Owing to the differences in chemical compositions and microstructures, these formulae may not be applicable for high strength steel.

Many experimental investigations into the mechanical properties of both QT and TMCP high strength steel under elevated temperatures have been reported in the literature. (Chen, 2006; Qiang. X, 2012; Winful D.A, 2017; Wang W, 2018 and Xiong M.-X, 2020). Wang made a direct comparison between the measured mechanical properties of both Q690 and S690 steel with design values according to EN 1993-1-2, as shown in Figure 2.3. It is found that Eurocode 3 gives significantly higher yield strengths than the measured values of the high strength steel, while the design values of Young's modulus are acceptable.

Hence, the mechanical properties of both the QT and the TMCP high strength steel at elevated temperatures in these references are adopted in subsequent numerical simulation and finite element models.
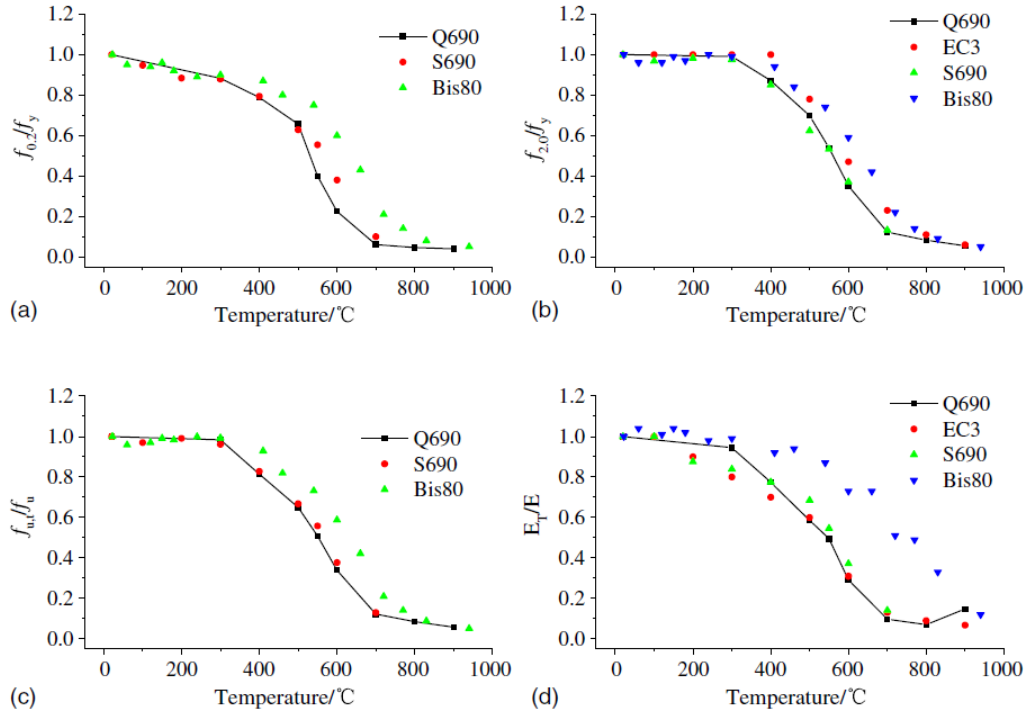
Figure 2.3 Comparison of mechanical properties of Q690 steel and S690, BISPLATE 80, and Eurocode 3: a) yield stress $f_{0.2}$; b) yield stress $f_{2.0}$; c) tensile strength f_u; d) Young's modulus (Wang, 2018)

2.3 Welding

Welding is a fabrication process whereby two or more parts are fused together by means of heat, pressure, or both forming a join as the parts cool (TWI, 2019). There are many types of welding, while Shielded Metal Arc Welding (SMAW), Gas Metal Arc Welding (GMAW) and Submerged Arc Welding (SAW) are the most frequently used processes in the construction industry. The mechanisms of these three types of welding are shown in Figure 2.4. The arc melts the filling metal and also adjacent base metal, and a shielding medium is usually needed to protect the molten pool from oxidation. In a SMAW process, the protecting gas comes from burning of the coating to the electrode. In a GMAW process, an external inert gas supply is needed. In a SAW process, a flux cover is needed to keep the air out during the welding process.
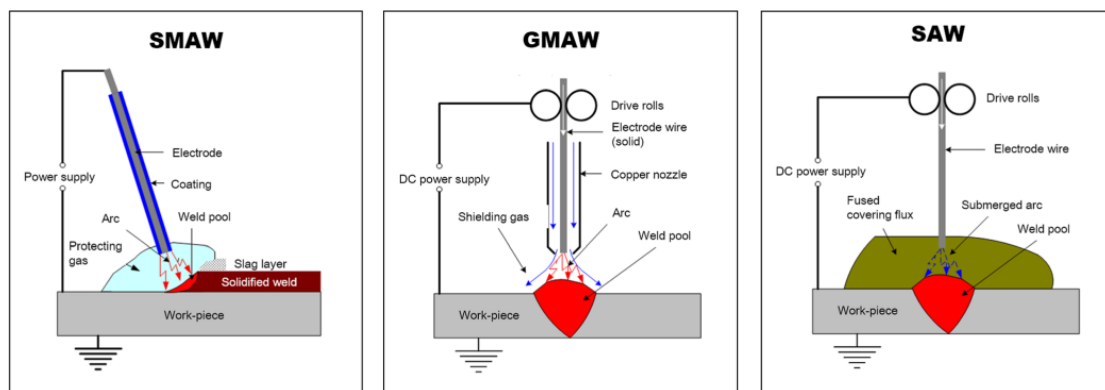
Figure 2.4 Mechanism of SMAW, GMAW and SAW (SubsTech, 2012)

2.3.1 Preheat, post heat and heat input energy

Welding is a process with heating and uncontrolled subsequent cooling, and a high cooling rate may lead to hard and brittle microstructures in heat affected zones (HAZ), especially for HSS, and an increase in the risk of cold cracking. In addition, a low cooling rate may lead to a reduction of strength and hardness. A lower cooling rate also gives time for hydrogen to diffuse out, and thus reduces the risk of hydrogen cracking (Funderburk, R., 1997). Hence, during welding of HSS, it is essential to adjust the

17

cooling rate within a specific range, together with a proper combination of preheat temperatures and heat input energy as demonstrated in Figure 2.5.

In AWS D1.1 (ANSI, 2004), two approaches are specified, namely, the HAZ hardness control method, and the hydrogen control method. In EN 1011-2 (CEN 2001), preheating temperatures are provided, and the values depend on hydrogen concentration, combined plate thicknesses, CEV, and heat input energy.
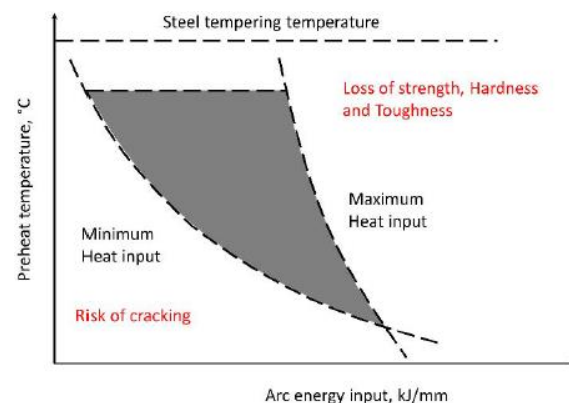
Figure 2.5 Combination of preheat and heat input energy (Håkansson, 2002)

Post-heating is used to minimize risks of hydrogen cracking. In general, post-heating should be used to eliminate hydrogen cracking as far as practically possible (Funderburk, R., 1998).

2.3.2   Changes of microstructures in the heat-affected zone

A critical temperature of the steel defines the temperature at which phase transition takes place between two phases of the steel. As the steel is heated above the critical temperature, it undergoes a phase change, and recrystallizes. There are two different critical temperatures:

➢ Lower critical temperature (Ac1). The temperature at which austenite starts to transform from ferrite.

➢ Upper critical temperature (Ac3). The temperature at which austenite is completely transformed from ferrite.

During the welding process, there is uncontrolled cooling in the base metal adjacent to the fusion zone, which leads to different microstructures in the heat affected zone, as demonstrated in Figure 2.6. There are two parameters that determine the transformation of microstructures: $t_{8/5}$, which means the time for cooling from 800°C to 500°C, and T_p, the peak temperature during welding.
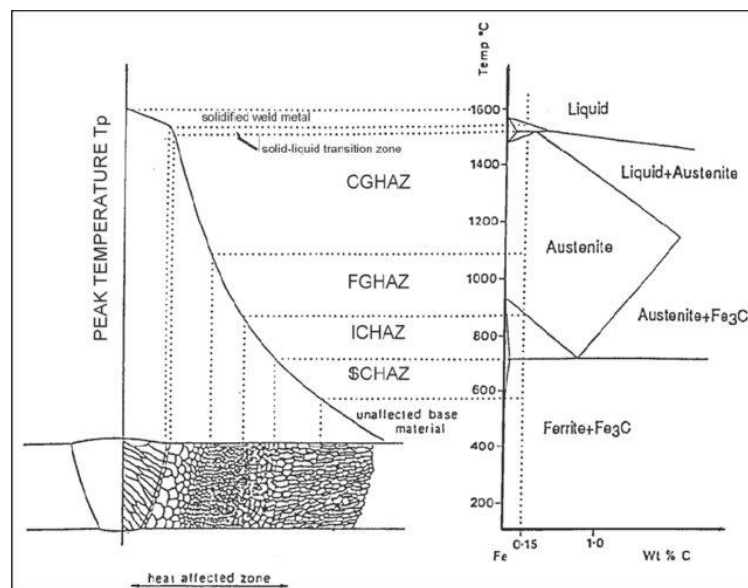
Figure 2.6 Schematic illustrations of the various single-pass HAZ regions with reference to the Iron-carbon equilibrium diagram (Ramirez, 2005)

To be more specific, the HAZ can be divided into four regions which are the coarse grain HAZ (CG HAZ), the fine grain HAZ (FG HAZ), the inter-critical HAZ (IC HAZ) and the sub-critical HAZ (SC HAZ). Each region experiences a specific heat treatment according to its distance from the fusion zone, and hence, the steel within each region have similar microstructure and properties.

The coarse grain HAZ (CG HAZ) is the region directly located next to the fusion zone. Therefore, it is subjected to the maximum temperature in HAZ during the welding process. As a result, the steel is exposed to a peak temperature far above the critical

19

phase-transformation temperature Ac3.

The fine grain HAZ (FG HAZ) is the region which is exposed to a maximum temperature slightly lower than that of the coarse grain HAZ but still above the critical phase-transformation temperature Ac3. The grain size in FGHAZ is also smaller than that of CGHAZ.

The inter-critical HAZ (IC HAZ) is subjected to a maximum temperature between the lower and the upper critical phase-transformation temperatures Ac1 and Ac3, which means the steel here is only partly transformed to austenite during the heating process. Therefore, this region is also called the partially transformed zone.

The sub-critical HAZ (SC HAZ) is also known as the annealed zone. It is the outermost region of the heat affected zone, next to the parent metal. In SC HAZ, the steel experience a heating and cooling cycle with a maximum temperature below Ac1. Theoretically, there is no change in microstructure or grain size in this region.

2.3.3   Changes of mechanical properties after welding

Due to changes of microstructures described in the previous section, the mechanical properties of these welded sections are usually reduced to various levels related to the heat input energy during welding and the plate thickness:

Tong (2021) conducted a number of tensile tests on Q550 20 mm welded sections and Q690 10 and 20 mm welded sections which were prepared with a heat input energy at 1.2 kJ/mm. The reduction factor of tensile strength, which is the ratio of tensile strength of the welded section over the base metal, is 0.96, 0.97 and 0.99, respectively.

Liu (2018) performed welding onto S690 16 mm steel plates with different heat input energy of 1.0, 1.5, 2.0 and 5.0 kJ/mm, and reduction factors of 0.98, 0.90, 0.86, and

0.70, respectively, for the yield strengths of these welded sections when compared with the base plate. For tensile strength, the reduction factors of the welded sections are 1.0, 0.97, 0.92 and 0.83. What's more, for welded sections with heat input energy of 2.0 and 5.0 kJ/mm, the tensile strengths were found to be smaller than the required value of 770 MPa as given in EN ISO 15614.

Chen (2020) investigated the mechanical properties of S690Q 16mm welded sections, and the heat input energy employed in preparing these welded sections were 1.14, 1.60 and 1.74 kJ/mm. The reduction factors of the yield strengths were found to be 0.86, 0.82 and 0.77, respectively, while the corresponding reduction factors of tensile strengths were found to be 0.92, 0.89 and 0.86.

Different levels of strength reduction were found in the welded sections of high strength steel by researchers, and some of them could not meet the minimum requirements in standards if the heat input energy were not properly controlled. While these research focused on 10 to 20 mm thick steel plates. Such a restriction of heat input energy during welding will definitely limit the application of high strength steel thick sections in construction industry. What's more, there is no systematic experimental investigations into the effect of welding in 30 to 70 mm thick steel plates of high strength steel.

2.4 Residual stress

Residual stresses are those stresses that remain in an object even in the absence of external loading or thermal gradients (TWI 2020). There are several causes of residual stresses: uniform thermal or mechanical loading, for example, hot rolling and rolling in the steel-making process, flame cutting and welding in the fabrication process, and structural mismatching in the construction process.

2.4.1   Initial residual stresses before welding

Before welding, there is usually flame cutting during fabrication of steel structures, and large residual stresses occur at cut edges with a stress level similar to or higher than the yield strengths of the base plate according to various researchers:

Wang (2012) studied the residual stress distribution of welded H-sections with flame-cut edges and tensile stresses at the cut edge were found to reach a level of 0.5 times the yield strength of the base plate. The plate thickness, in this case, was 21 mm.

For thick plates, Thiébaud, R. (2012) studied the residual stresses at the flame-cut edges with the sectioning method of 60 mm thick S355 steel plates. High tensile residual stresses at 300 MPa were found at the flame-cut edges. Jokiaho (2017) investigated the residual stresses at the edges caused by flame cutting onto a 40mm thick steel plate of ultra-high strength steel with a yield strength of 1200 MPa. The residual tensile stress around 1000 MPa was found in the region adjacent to the cut edge.

Alpsten (1970) studied the residual stresses caused by flame cutting in a 50 mm thick A36 thick plate. The minimum yield strength and the tensile strength of the steel were 250 and 400 MPa, respectively, and the maximum residual tensile stress was found to be 360 MPa at the cut edge (shown in Figure 2.7). Alpsten also compared the residual stress distribution of a welded H-section fabricated by milling with the same

dimensions but by flame cutting. Small compressive stresses were found at the edge of the flanges in the H-section by milling, while large tensile stresses were found at the edge of the flanges in the H-section by flame cutting (shown in Figure 2.8). In addition, the stress level at the middle of the flanges was also different, and this is readily explained with the force equilibrium principle.
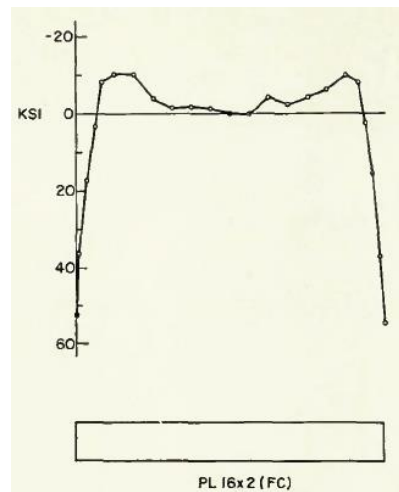
Figure 2.7 Measured residual stresses of 50mm A36 steel plate (Alpsten, 1970)

a) H-section with milled plates   b) H-section with flame-cut plates
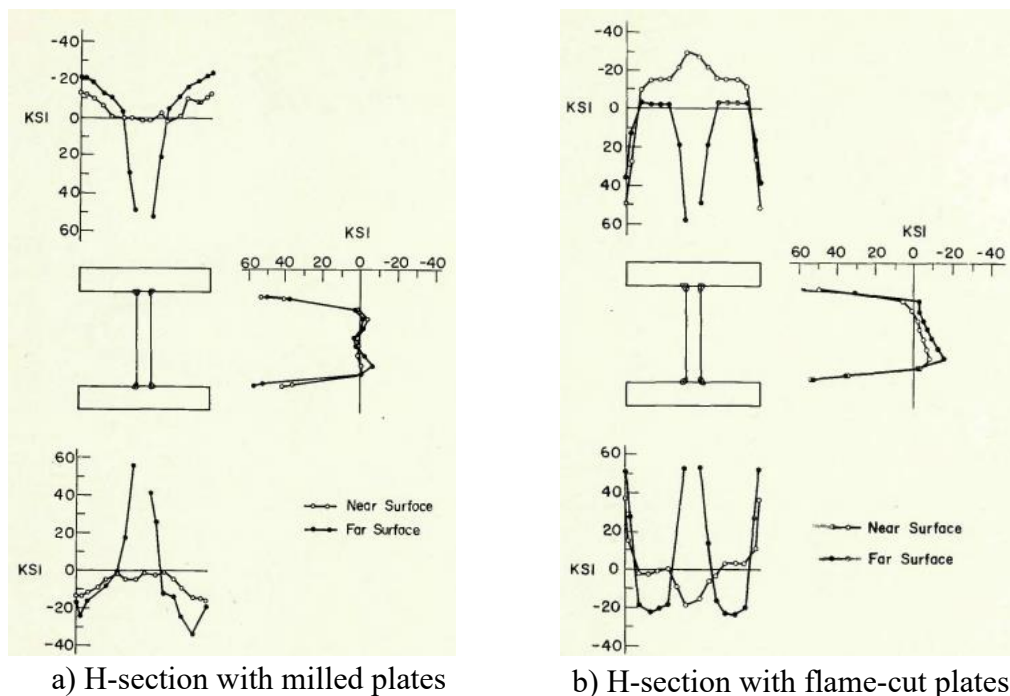
Figure 2.8 Comparison of residual stress distribution between H-section with milled plates and flame-cut plates (Alpsten, 1970)

ECCS (1976) also provides typical residual stress patterns caused by flame cutting, as

23

shown in Figure 2.9.
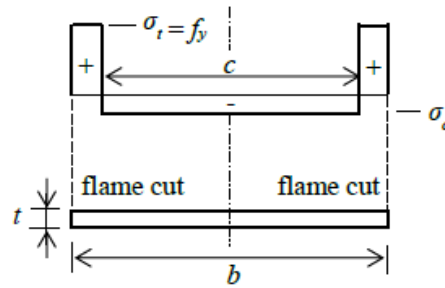
Figure 2.9 Residual stress pattern caused by flame cutting (ECCS, 1976)

Consequently, the residual stresses caused by flame cutting are considered to be the initial residual stress pattern before welding in all subsequent numerical modelling process.

2.4.2 Residual stresses by welding

Masubuchi explained the formation of residual stresses caused by welding (Figure 2.10):

A-A: Before welding, there is no change in temperature nor stresses.

B-B: The weld torch passes by, and the temperature reaches a maximum value, while metal here is in a liquid state, so it can not carry any stresses, so the stress level at this section is quite low. While in regions adjacent to the fusion zone, thermal expansion occurs, which leads to compressive stresses.

C-C: Temperature goes down, and contraction of the fusion zone develops. The surrounding base metal works as a constraint, which leads to tensile residual stresses in the fusion zone and also in adjacent areas.

D-D: Contraction of the fusion zone is fully developed, and tensile residual stresses in the fusion zone and the adjacent areas usually go beyond the yield strength of the base metal. Compressive stresses are readily detected in other parts due to the force

24

equilibrium principle.

Figure 2.10 Schematic representation of changes of temperature and thermal stresses during welding (Masubuchi, 1996)

2.4.3 Measurement of residual stresses

There are several well-developed methods for measurement of residual stresses, and they can be classified into destructive methods, semi-destructive methods and non-destructive methods (TWI, 2020):

Destructive methods:

➤ Contour method: an object is cut into two pieces, and the surface height map of the newly formed plane is measured so that the residual stresses normal to the new plane can be calculated. Wire electric discharge machining (wire EDM) is frequently used for cutting, while the size of the object is usually restricted by the dimension of the EDM machine.

25

- Sectioning method: an object is cut into longitudinal strips, and changes of the lengths of these strips are recorded. Residual stresses are calculated based on Hooke's Law. The sectioning method has been used for decades to measure residual stresses in steel members. It has proven itself adequate, accurate and economical if proper care is taken in preparation of the specimens and the procedure of measurement (Tebedge, 1973). In general, the object is fully destroyed after measurement.

Semi-destructive methods:
- Hole-drilling method: a strain gauge rosette is first to stick onto the surface of the object, and a small hole is drilled at the centre of the rosette. The released strains can be measured after the drilling process, and residual stresses at this point can be further calculated based on the released strains. This method is easy to handle, and the hole-drilling machine is small, so it can be used on most objects. Both ASTM (2013) and GB/T 31310 (CNS, 2014) give standard procedures for the hole-drilling method.

Non-destructive methods:
- X-ray diffraction: the strain in the crystal lattice of an object is measured, and the associated residual stresses are determined from the elastic constants assuming a linear elastic distortion along on appropriate crystal lattice plane. While this method is limited to measuring very thin surface layers.

- Neutron diffraction: neutrons penetrate much deeper than X-rays in most materials, so neutron diffraction is able to measure stresses from the interior of an object (Pintschovius, 1983). While the equipment in the diffraction method is highly expensive, and specimen sizes are limited.

2.5 Numerical simulation of the welding process

In early days, experimental measurement was the only way to investigate magnitudes and distributions of residual stresses in welded sections. However, most of the tests were time-consuming and labor-intensive. In recent years, with development of finite element methods and advanced modelling techniques, numerical simulation on welding induced residual stresses has become possible.

The basic theory of heat transfer in welding was established in the 1940s. American scholar Rosenthal (1947) first studied heat conduction of solid point heat sources. Later, the former Soviet scientist Rykalin used an analytical method to solve the heating cycle process of welding on the basis of a heat conduction problem of the point heat source, and established the basic theory of heat transfer of welding, thus forming the classic theory of heating cycle process for welding, i.e. the Rosenthal-Rykalin formula system (Rykalin, 1960).

Nowadays, there are different well-developed simulation platforms: ABAQUS, ANSYS, SYSWELD and MSC.Mar for effective welding simulation.

2.5.1   Heat source model

In a welding simulation process, the heat source works as an external loading to welded sections for calculation of the temperature field, and then, the calculated temperature field is input as load for calculation of the stress field. So a correct heat source model is essential for the welding simulation process. There are several well-developed heat source models:

➢   Gaussian surface flux distribution model

Developed by Pavelic (1969), the Gaussian model defines a heat flux over a surface as

shown in Figure 2.11, and the flux distribution is defined in Equation 2.2. It is obvious that the maximum flux is located at the centre of the heat source, and then it decreases when it goes further. Researchers have conducted satisfactory simulation results on welding of a thin plate, or a bead-on-plate welding (Teixeira, 2014; Balasubramanian, 2008; Deng, 2008). While it may not be suitable for welding simulation with deep penetration, like GMAW and SAW, as there is no flux defined in the thickness direction.
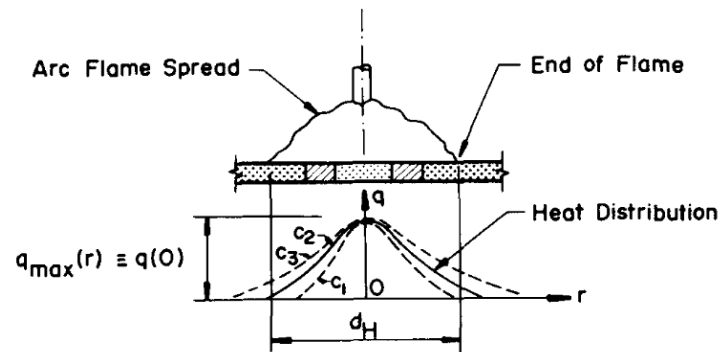
Figure 2.11 Flux distribution in the Gaussian model (Pavelic, 1969)

$$q(r) = q(0)e^{-Cr^2} \tag{2.2}$$

where $q(r)$ is the surface flux at a radius r [W/m^2];

$q(0)$ is the maximum flux at centre [W/m^2];

C is the concentration factor and $C_1 > C_2 > C_3$ [m^{-2}]; and

r is the radius from the centre and $d_H = 2r$.

➤   Double ellipsoidal heat source model

Goldak (1984) established this 3-D model with different distributions of flux in the front and the rear hemispheres, which simulated the dimensions of the weld pool, as shown in Figure 2.12. Both the front and the rear hemispheres share the same width (d) and depth (c), but they have different values in the length, a_1 and a_2, and this follows the shape of the weld pool in practical welding.

28
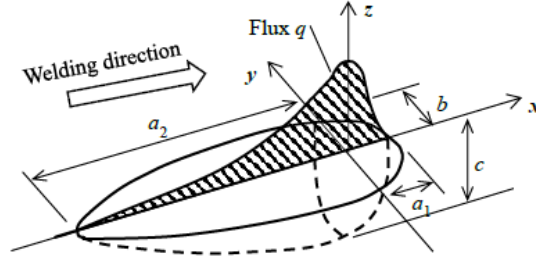
Figure 2.12 Double ellipsoidal heat source model (Goldak, 1984)

The heat flux distributed in both the front and the rear hemisphere are computed using Equation 2.3:

$$\begin{cases} q_1(x, y, z) = \dfrac{6\sqrt{3}f_f Q}{a_1 bc\pi\sqrt{\pi}} \exp\left(-\dfrac{3x^2}{a_1^2}\right)\exp\left(-\dfrac{3y^2}{b^2}\right)\exp\left(-\dfrac{3z^2}{c_1^2}\right) \\ q_2(x, y, z) = \dfrac{6\sqrt{3}f_r Q}{a_2 bc\pi\sqrt{\pi}} \exp\left(-\dfrac{3x^2}{a_2^2}\right)\exp\left(-\dfrac{3y^2}{b^2}\right)\exp\left(-\dfrac{3z^2}{c_1^2}\right) \end{cases} \tag{2.3}$$

where q_1 and q_2 are the volumetric heat flux in the front and the rear [W/m^3];

a_1, a_2, b, and c are semi-axes of the double ellipsoid [m];

Q is the total heat energy input of welding [J];

x, y, and z are the local coordinates, as shown in Figure 3.6; and

f_f and f_r are fractions illustrating energy distribution, then $f_f + f_r = 2$.

Due to the 3-D distribution of the heat flux, the double ellipsoidal heat source model performs well on simulating both the GMAW and the SAM processes, as demonstrated by researchers (Sonti & Amateau, 1989; Bonifaz, 2000; Chukkan et al., 2015; Liu, 2018). It is noticeable that the simulated temperature field is directly related to the magnitude of a$_1$, a$_2$, b, and c, so usually, the measured temperature history during welding is often required for calibration of these coefficients in the heat transfer analysis.

2.5.2   Simulation of changes of mechanical properties after welding

In general, prediction of the resistance of a welded section can be a complex task. As shown in Section 2.3.2, the temperature changes continuously in the HAZ and also the microstructures, hence, the mechanical properties within the HAZ are highly non-uniform. Both the mechanical properties and the dimensions of various sub-zones within the HAZ are the most intricate factors to be define in a finite element model.

M. Khurshid (2015) calculated both the yield strengths and the tensile strengths for the whole HAZ of the welded sections using the Vickers hardness of the HAZ area, while assuming that the hardening parameters were the same as those of the base metal. Material scientists (Pavlina, 2008; Barsoum, 2014) have correlated the relationship between hardness and yield strengths for various materials. However, it should be noted that the true stress-strain curves utilized in finite element modeling cannot be derived using only data of yield and tensile strengths.

S.P. Chiew (2014) and Chen C. (2019) tested some heat-treated coupons which were prepared with an oven. Thermocouples were attached on these coupons to measure the temperature history during heat treatment. However, there was a concern on whether these heat-treated coupons were accurately prepared to reflect the mechanical properties of sub-zones in the HAZ of the welded sections as the cooling rates in these coupons could not be controlled effectively.

As to the dimensions of these sub-zones, many numerical investigations were reported, and the HAZ regions were determined with etching and hardness tests (Khurshid, 2015; Mochizuki, 2004). Although it is believed that such a measurement can determine the widths of these sub-zones, it is unable to anticipate these dimensions. Chen (2019) used a calibrated heat transfer model to predict the temperature distribution history of a welded section, then, the locations and dimensions of these sub-zones within the HAZ were successfully defined. The proposed method provided an effective approach to anticipate the locations and dimensions of these sub-zones, if the temperature limits of each sub-zone were identified.

Chapter 3. Mechanical properties of welded sections of high strength S690 QT and Q620 TM steels

3.1 Introduction

Mechanical properties and microstructures of high strength S690 QT and Q620 TM base plates and their welded sections with various heat input energy were investigated and described in this chapter. Owing to the large thicknesses of the base plates, tensile tests were carried out on coupons with different dimensions and extraction locations. The digital Image Correlation (DIC) system was used during these tensile tests of both the base plates and the welded sections to investigate non-linear strain distributions of different regions under tension. Metallographic analysis on the cross sections of these welded sections were conducted, and their images were compared systematically to illustrate microstructural evolution within the heat-affected-zones of the welded sections.

The chemical compositions of both the S690 QT and the Q620 TM steel used in this thesis are shown in Tables 3.1 and 3.2 respectively. Submerged arc welding (SAW) was used for both QT and TM steel considering the plate thickness and the welding efficiency. The chemical composition of the welding consumable, namely SAW wire Y-80J, is listed in Table 3.3.

In general, TM a high level of control during heat treatment, and only a few modern steel mills are able to produce them. Their yield strengths range from 460 to 690 N/mm^2 and their thicknesses range from 6 to 44 mm. As a whole, the availability of Grade 690 TMCP steel is rather restrictive.

Table 3.1 Chemical composition (%) of S690 QT steel plates

Thickness (mm)	C	Si	Mn	P	S	Cr	Cu	Mo	Nb	Ni	Ti	V	Zr
50	0.17	0.33	1.25	0.012	0.001	0.83	0.02	0.361	0.032	0.31	0.015	0.004	0.003
70	0.17	0.33	1.25	0.012	0.001	0.83	0.02	0.361	0.032	0.31	0.015	0.004	0.003

Table 3.2 Chemical composition (%) of Q620 TM steel plates

Thickness (mm)	C	Si	Mn	P	S	Cr	Cu	Mo	Nb	Ni	Ti	V	Als
28	0.076	0.049	1.40	0.007	0.002	0.45	0.30	0.27	0.033	0.41	0.013	0.003	0.025
44	0.062	0.12	1.28	0.009	0.002	0.40	0.32	0.35	0.027	0.86	0.012	0.003	0.028

Table 3.3 Chemical composition (%) of welding consumable

Consumable	C	Si	Mn	P	S	Cr	Cu	Mo	Ni
NSSW Y-80J	0.10	0.01	1.72	0.011	0.007	0.60	0.08	0.57	2.5

3.2 Standard tensile tests of S690 QT 50 and 70 mm steel plates

3.2.1 Design of tensile tests

In a typical steel production of QT steel, there is a hot rolling process followed by a heat treatment process i.e. the quenching and tempering process. Restricted by significantly different cooling conditions at both the outer surfaces and the core, temperatures along the thickness direction during the heat treatment process may not be uniform, and this will lead to a difference in the microstructures, and hence the mechanical properties of the steel plates at different locations along their thickness direction. Hence, the specimens for the tensile tests of the 50 and the 70 mm base plates were designed as shown in Figure 3.1.

a) Extraction locations of coupons

b) Dimensions of coupon
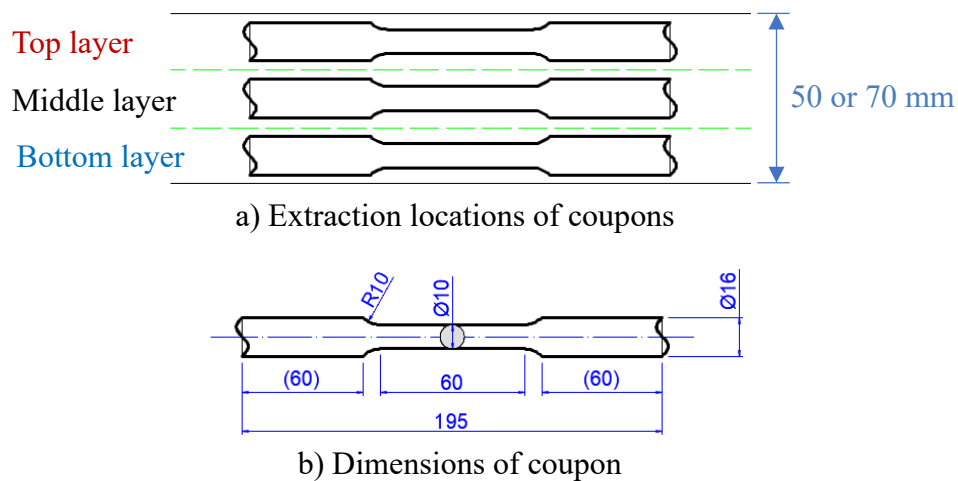
Figure 3.1 Design of coupons for tensile tests

The steel plates were divided into three equal layers, namely Top, Middle and Bottom layers, and standard coupons (shown in Figure 3.1 b)) were machined from these layers. A designation system is established as shown in Figure 3.2.

33

Thickness, i.e. 50 mm (50) or 70 mm (70).

Location, i.e. Top (T), Middle (M) or Bottom (B) layers.

50 – T 1

Sequential code of the coupon in the same series, i.e. 1, 2
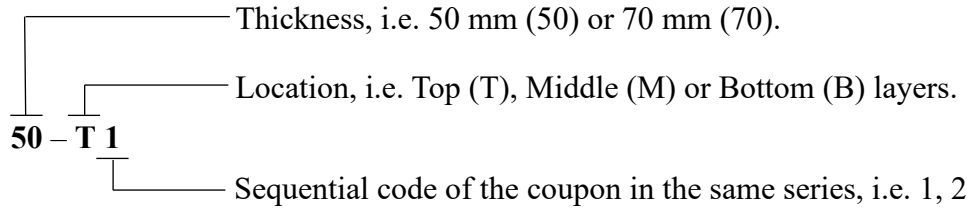
Figure 3.2 Designation system of tensile tests on coupons of S690 QT base plates

Two repeat coupons were tested for each layer, and there are 12 coupons in total. The test program is listed in Table 3.4.

Table 3.4 Test program of monotonic tensile tests of S690 QT base plates

Test series	Thickness (mm)	Layer	Diameter (mm)	Gauge length (mm)	Quantity
50-T		Top	10	50	2
50-M	50	Middle	10	50	2
50-B		Bottom	10	50	2
70-T		Top	10	50	2
70-M	70	Middle	10	50	2
70-B		Bottom	10	50	2

The gauge length (L) of the standard coupons is calculated using the following equation given in EN ISO 6892-1 (CEN, 2019):

$$L = 5.65 \times \sqrt{A_0}$$

where A_0 is the cross-sectional area of the parallel section of the standard coupon.

3.2.2 Test set-up and instrumentations

A high precision testing machine, i.e. a Instron 8803 Servo hydraulic Fatigue Testing system, was employed to conduct these tensile tests. Figure 3.3 illustrates the test set-up and the instrumentation of the tensile tests. An extensometer with a gauge length of 50mm was used to measure the elongation of the coupon. The travel limit of this

extensometer is -10mm to +25mm so the elongation of the coupon up to fracture can be readily measured. A Photographic Digital Analysis (PDA) method (LIU, 2018) was also adopted in this study just in case that necking of the coupon takes place outside the extensometer.
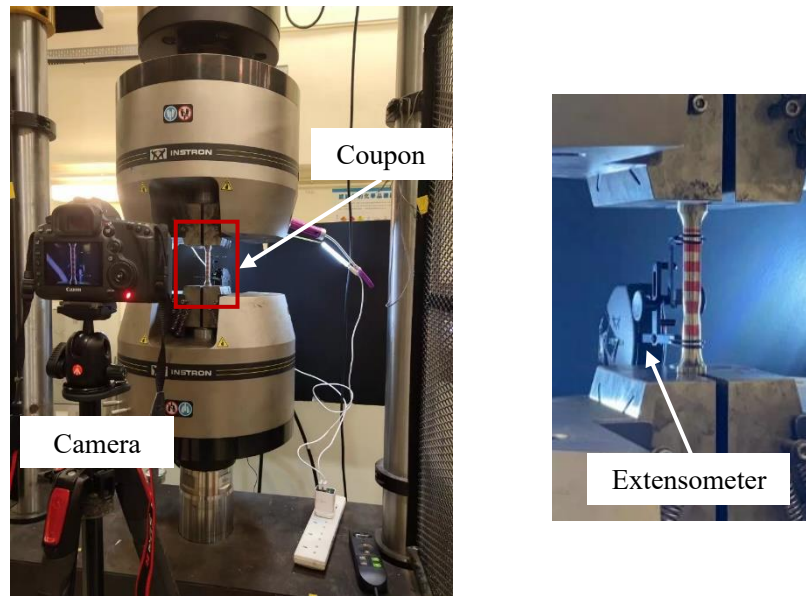
Figure 3.3 Test set-up and instrumentation for tensile tests

3.2.3 Tests results

A total of 12 coupons were tested, and all the fractured coupons are shown in Figure 3.4. Typical tensile fracture failure within the gauge length is observed in these coupons. The measured mechanical properties of these coupons are summarized in Table 3.5 while Figure 3.5 presents their full range engineering stress-strain curves.

a) Coupons extracted from 50 mm thick plate

b) Coupons extracted from 70 mm thick plate

c) Typical failure of coupon
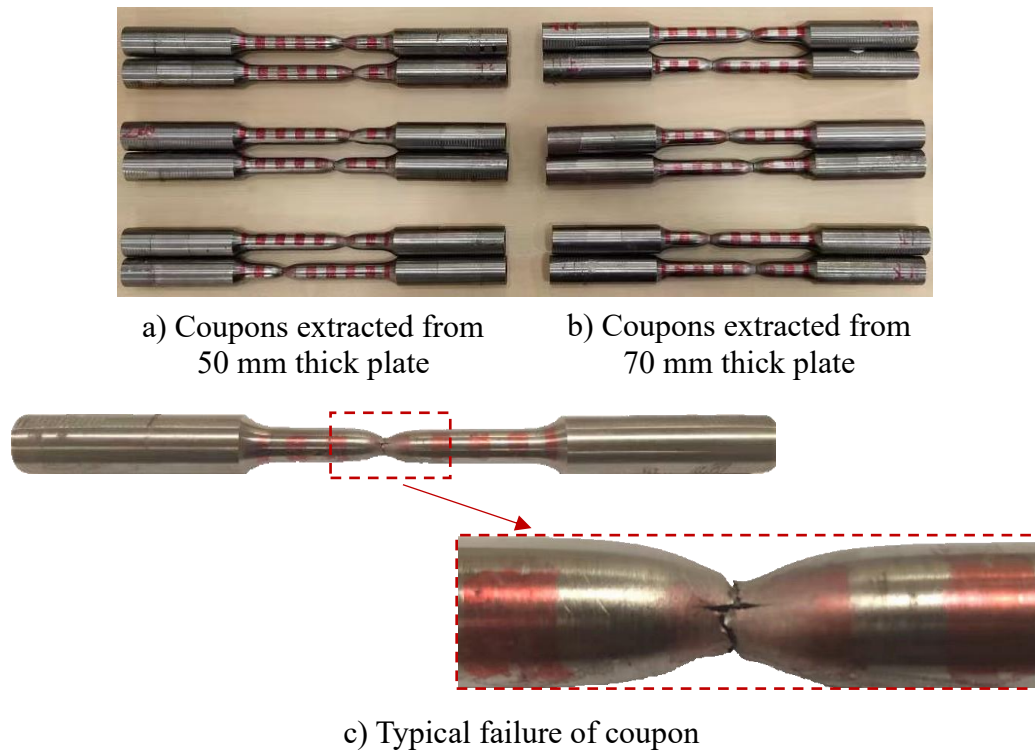
Figure 3.4 Fractured coupons of S690 QT 50 and 70 mm thick base plates

Table 3.5 Measured mechanical properties of S690 QT 50 and 70mm thick base plates

Specimen	Layer	Young's Modulus, E (kN/mm²)	Yield strength, f_y (N/mm²)	Tensile strength, f_u (N/mm²)	f_u/f_y	Elongation at fracture, ε_L (%)
50-T1	Top	205	796	856	1.07	20.7
50-T2		213	795	856	1.07	18.5
50-M1	Middle	206	792	857	1.08	19.9
50-M2		213	791	856	1.08	18.9
50-B1	Bottom	214	791	852	1.08	19.0
50-B2		213	791	850	1.07	20.7
70-T1	Top	212	760	832	1.09	20.1
70-T2		213	758	832	1.10	19.8
70-M1	Middle	206	707	778	1.10	20.9
70-M2		213	710	779	1.10	19.9
70-B1	Bottom	211	770	838	1.09	20.1
70-B2		214	765	834	1.09	19.4

36
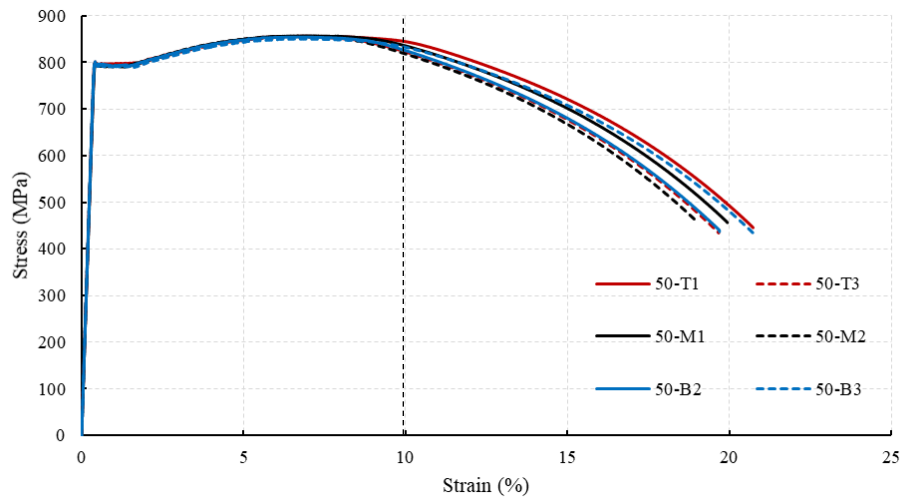
a) 50 mm thick base plates
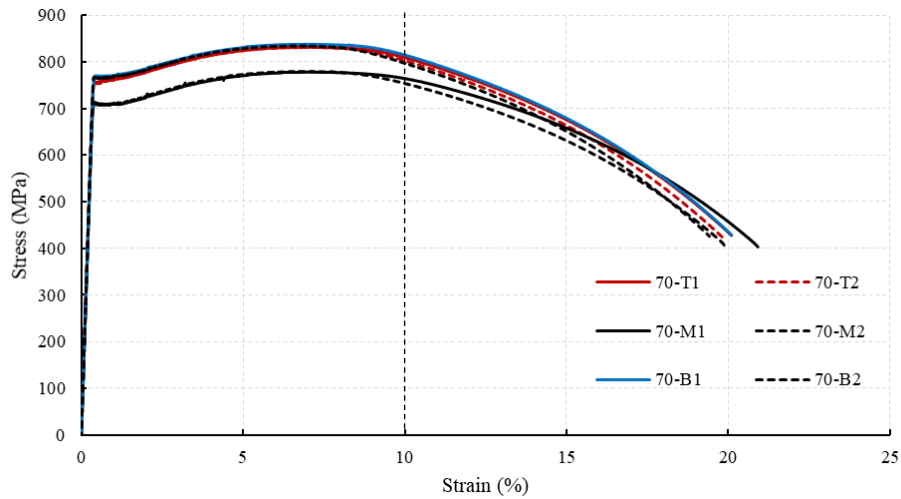
b) 70 mm thick base plates

Figure 3.5 Full range engineering stress-strain curves of S690 QT high strength steel plates

It is shown that:

1) The yield strengths of these steel plates are found to vary from 707 N/mm^2 to 796 N/mm^2. According to EN 10025, the elongation at fracture ε_L for steel having a yield strength up to 700N/mm^2 should be larger than 10%, and its f_u / f_y ratio should be at least 1.05. Hence, the thick steel plates in this project are demonstrated to

satisfy these requirements.

2) By comparing the yield strength f_y and the tensile strength f_u of these steel plates with different thicknesses, the strengths are shown to be decreased when the thickness is increased, even though both the 50 and 70 mm thick steel plates have exactly the same chemical compositions.

3) It is shown that for the 50 mm thick steel plates, the mechanical properties have a variation less than 1% at various location along their thickness. However, for the 70 mm thick steel plates, a reduction to both the yield and the tensile strengths of those coupons extracted from the middle layer is found when comparing with those from the top and the bottom layers, and the reduction factors are found to be to 0.93 and 0.94, respectively. Nevertheless, both the yield and the tensile strength of the coupons extracted from the middle later, i.e. 708 and 778 N/mm^2, do exceed the minimum values stipulated in EN 10025-6, i.e. 650 and 760 N/mm^2.

Consequently, these standard tensile tests are able to demonstrate that the S690 QT 50 mm thick steel plate possess highly consistent mechanical properties at various locations within their thicknesses. However, for S690 QT 70 mm thick steel plates, a reduction factor of 0.93 is applicable to the yield strength of the middle layer of the steel plate.

The strength variation along the thickness direction in the 70 mm thick steel plates is readily explained as during the quenching and tempering in the steel making process, the temperature history in steel plates is strictly controlled. However, the cooling condition of these surfaces of steel plate is different from that of the inner part, which leads to a difference of microstructures along the thickness direction of the steel plate.

3.3 Tensile tests of welded sections of S690 QT 50 and 70 mm thick plates

3.3.1 Welding and machining of test specimens

A total of six butt welded sections were fabricated with the S690 QT 50 mm and the S690 QT 70 mm thick base plates using three different heat input energy during welding, i.e. q= 2.4, 3.5, and 5.0 kJ/mm. The test program is shown in Table 3.6, and the joint design of both the 50 and the 70mm thick steel plates is illustrated in Figure 3.6. In order to achieve a high welding efficiency with a minimum amount of welding, an X-shape groove is adopted.

Table 3.6 Welding of S690 QT steel plates

Thickness (mm)	Length L (mm)	Width W (mm)	Heat energy input (kJ/mm)		
			2.4	3.5	5.0
50	920	800	1	1	1
70	960	800	1	1	1

a) Dimension of plates   b) Joint design
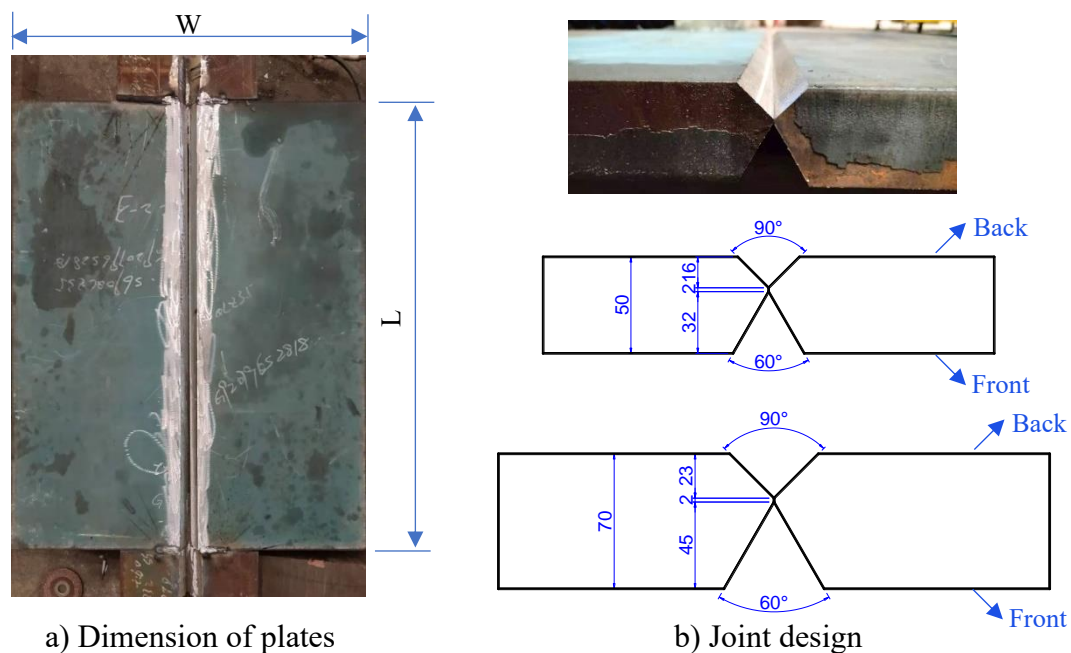
Figure 3.6 Butt-welded sections with an X-shaped groove

The dimensions of the test coupons and the extraction locations are shown in Figure 3.7. The coupon is 45 mm deep in the thickness direction of the welded sections, and both the butt welded connections of the 50 and the 70mm thick plates use the same design in order to allow for a direct comparison. Figure 3.8 illustrates the designation system of these coupons.

a) Extraction of coupons

b) Dimensions of coupon
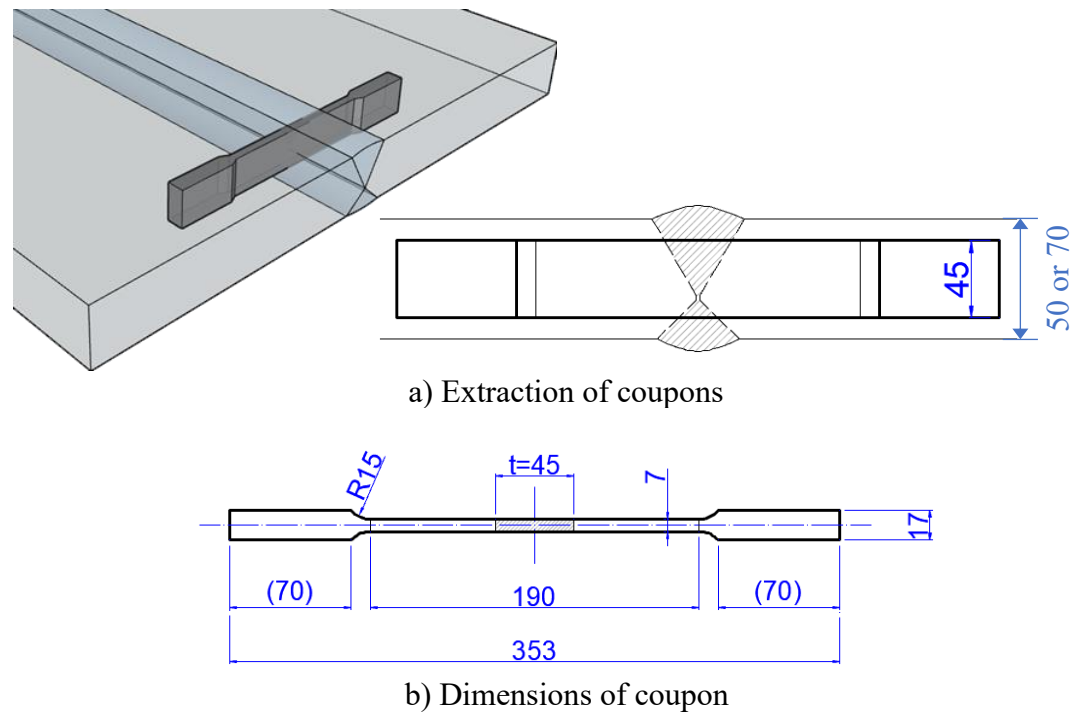
Figure 3.7 Extraction location and dimensions of S690 QT tensile test coupons

Thickness, i.e. 50 mm (50), or 70 mm (70).

50 –35 – 1

Sequential code of the coupon in the same series, i.e., 1, 2, 3
Heat input energy, i.e. Base plate (BP), 2.4 kJ/mm (24), 3.5 kJ/mm (35) or 5.0 kJ/mm (50).
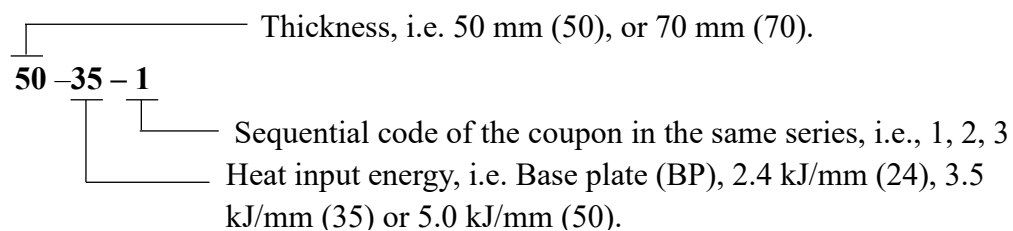
Figure 3.8 Designation system of tensile tests on coupons of S690 QT butt-welded sections

3.3.2 Test program

The test program of the tensile tests on the coupons of the butt-welded sections of the S690 QT 50 and 70 mm thick base plates together with corresponding control groups is listed in Table 3.7. An extensometer with a gauge length of 100 mm was used to measure the elongations of the coupons. The Photographic Digital Analysis (PDA) method (LIU, 2018) was also employed which was able to give accurate measurement even when necking took place outside the gauge length of the extensometer. It should be noted that for each series, one side of the coupon was measured with the DIC technique. In addition, as etching on the other side of the coupon was carried before test, the fracture location was readily detected. Typical coupons before test are illustrated in Figure 3.9.

Table 3.7 Test program of tensile tests on coupons of 50 and 70 mm butt-welded sections

Test series	Thickness (mm)	Cross sectional dimension (mm × mm)	Gauge length (mm)	Quantity	Remarks
50-BP		45 × 7	100	2	1 with DIC
50-24	50	45 × 7	100	3	1 with DIC
50-35		45 × 7	100	3	-
50-50		45 × 7	100	3	1 with DIC
			Total	11	
70-BP		45 × 7	100	2	1 with DIC
70-24	70	45 × 7	100	3	1 with DIC
70-35		45 × 7	100	3	-
70-50		45 × 7	100	3	1 with DIC
			Total	11	

Notes: Gauge length $L = 5.65 \times \sqrt{A_0}$, where $A_0 = 45 \times 7$

41

After etching

After spraying of pickles for DIC measurement
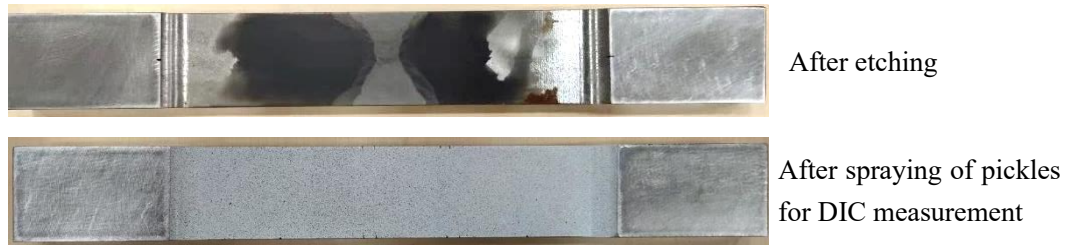
Figure 3.9 Typical coupons of S690 butt-welded connections before test

It should be noted that the extensometer with a gauge length of 100 mm was set in the middle of the coupon to cover the HAZs and the fusion zone.

3.3.3　Test set-up and instrumentation

An Instron 8803, with a maximum tension capacity of 500 kN, was employed to carry out the tensile tests. A digital image correlation system (DIC) using two high-definition cameras was employed to measure surface deformations of the coupons during loading. Through an optical digital programming and real-time operation, both the strain field and their changes were accurately measured. The test set-up is illustrated in Figure 3.10.
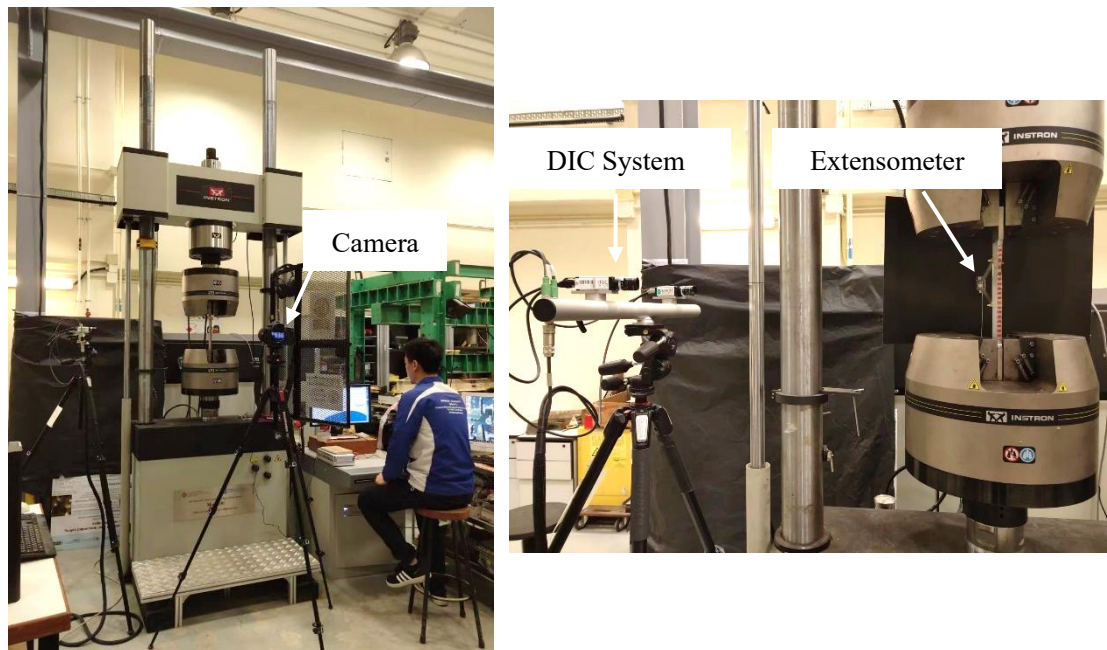
Figure 3.10 Test set-up and instrumentation

3.3.4 Test results

A total of 22 coupons of the 50 and the 70 mm butt-welded sections were tested. All the fractured coupons and typical failure modes are illustrated in Figure 3.11. The measured mechanical properties of the S690 QT 50 mm and the S690 70 mm thick base plates and their welded sections under three heat input energy are summarized in Table 3.8. Figures 3.12 and 3.13 plot the measured stress-strain curves of the 50 mm and the 70 mm thick steel plates respectively. It can be seen that the curves follow closely among all those with the same heat input energy, and hence, the results are shown to be consistent. There is no obvious yield plateau in the measured stress-strain curves of the welded sections, and thus, the 0.2% proof strength is adopted as the yield strengths of these coupons.

a) 50 mm thick welded sections   b) 70 mm thick welded sections
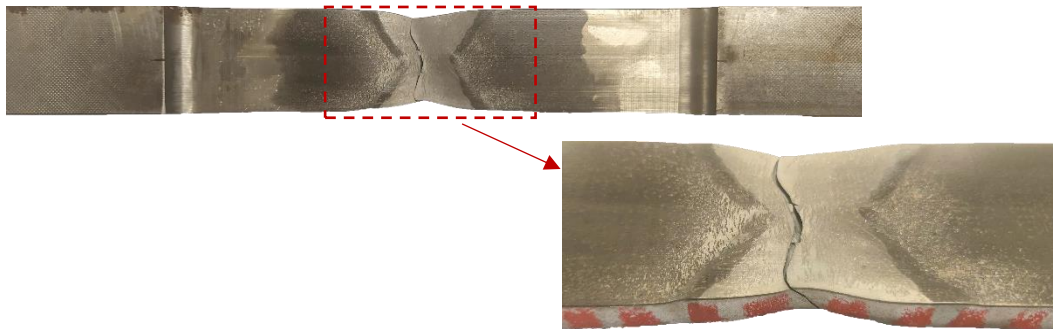
1) Fracture at weld metal
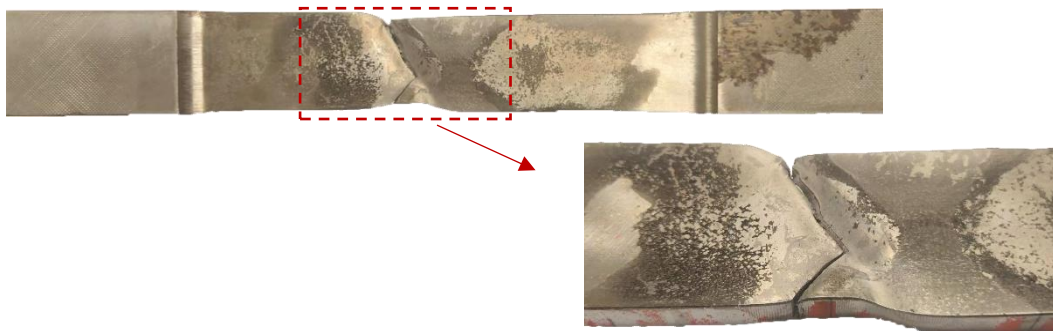
2) Fracture at HAZ
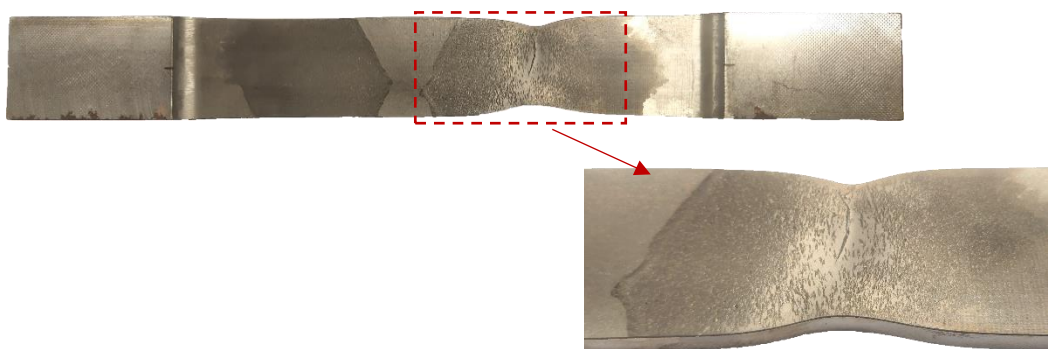
3) Fracture at base metal

c) Typical failure modes of welded sections

Figure 3.11 Fractured coupons of S690 QT 50 and 70 mm the butt-welded sections

Table 3.8 Measured mechanical properties of 50 and 70 mm thick base plate and their welded sections

Specimen	Young's Modulus, E (kN/mm²)	Yield strength, f_y (N/mm²)	Tensile strength, f_u (N/mm²)	f_u/f_y	Elongation at fracture ε_L (%)	Location of fracture
50-BP-1	218	817	863	1.06	14.8	-
50-BP-2	210	820	866	1.06	15.4	-
50-24-1	218	766	832	1.09	15.7	BM
50-24-2	209	767	833	1.09	14.4	HAZ
50-24-3	220	768	832	1.08	14.4	BM
50-35-1	216	752	826	1.10	13.6	WM
50-35-2	212	754	826	1.10	13.1	HAZ
50-35-3	221	748	822	1.10	13.5	WM
50-50-1	220	751	835	1.11	13.2	HAZ
50-50-2	209	759	836	1.10	14.2	BM
50-50-3	210	754	833	1.10	12.2	HAZ
70-BP-1	214	736	808	1.09	15.6	-
70-BP-2	216	738	806	1.08	16.0	-
70-24-1	219	730	799	1.09	15.8	BM
70-24-2	215	728	796	1.09	14.5	BM
70-24-3	218	727	796	1.09	13.9	BM
70-35-1	213	726	796	1.10	15.0	HAZ
70-35-2	214	722	792	1.10	14.7	HAZ
70-35-3	214	724	796	1.10	16.5	HAZ
70-50-1	218	720	799	1.11	15.2	BM
70-50-2	213	722	798	1.11	14.2	HAZ
70-50-3	220	722	796	1.11	14.9	HAZ
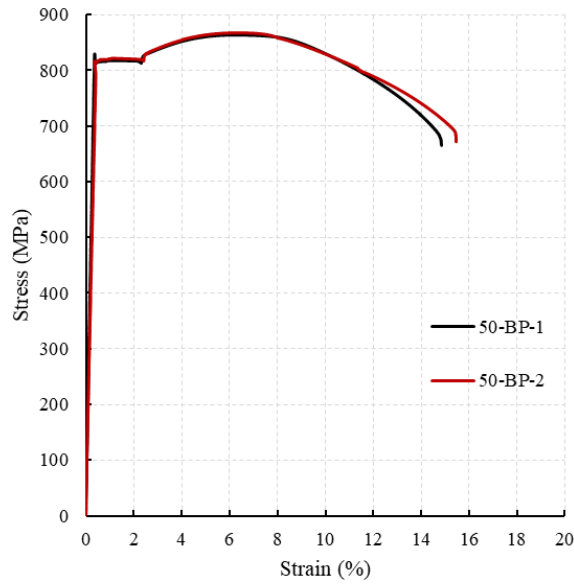
a) Base plate

b) q= 2.4 kJ/mm
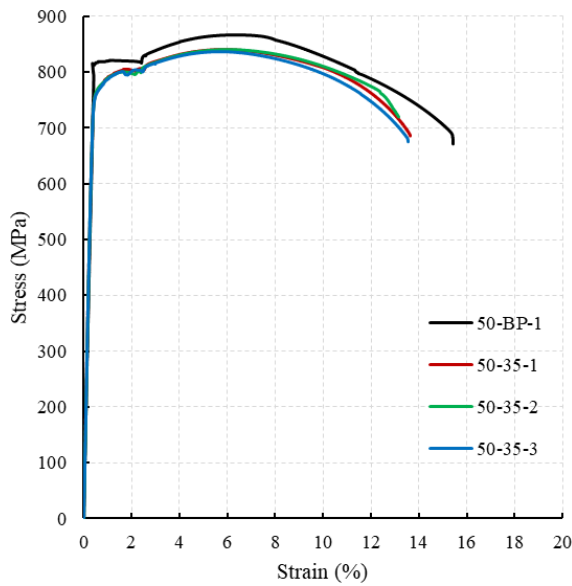
c) q=3.5 kJ/mm
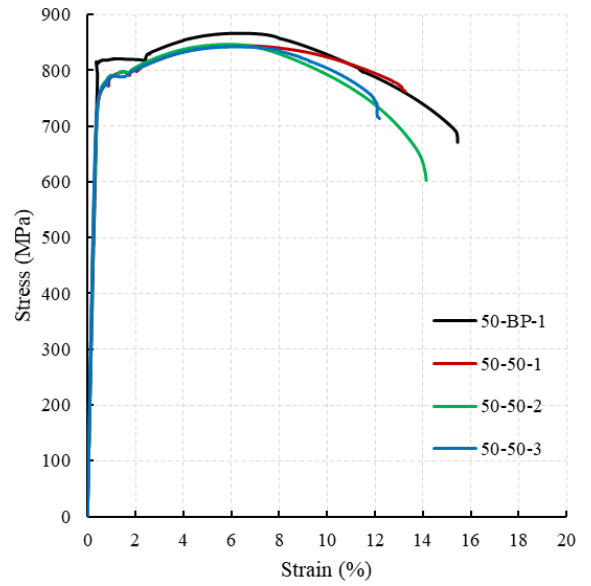
d) q=5.0 kJ/mm

Figure 3.12 Full-range stress-strain curves of the coupons of the 50 mm thick butt-welded sections

a) Base plate

b) q= 2.4 kJ/mm

c) q=3.5 kJ/mm

d) q=5.0 kJ/mm

Figure 3.13 Full-range stress-strain curves of the coupons of the 70 mm thick butt-welded sections

It is shown that:

a) Being different from those of the base plates, the stress-strain curves of the 50 mm and the 70 mm thick butt-welded sections have no obvious yield plateau after yielding.

b) As shown in Figures 3.12 and 3.13, only small reductions in the stress-strain curves of the welded sections are present, and the averaged mechanical properties of the base plates and the welded sections are summarized in Table 3.9. It is shown that the 70 mm thick welded sections have smaller reduction factors in their mechanical properties when compared with those of the 50 mm thick welded sections, as shown in Table 3.10.

c) As the heat input energy increased from 2.4 to 5.0 kJ/mm, it was found that the mechanical properties of the welded sections did not vary significantly as shown in Table 3.9. The average yield strengths of the 50 mm thick welded sections were shown to vary merely from 755 to 767 N/mm^2, i.e., 2% of that of the base plates. The tensile strengths of the welded sections were shown to vary merely from 825 to 835 N/mm^2, i.e., 1% of that of the base plates. The corresponding reduction factors range from 0.94 to 0.92 for the yield strengths and 0.95 to 0.97 for their tensile strengths, as shown in Table 3.10.

d) Similarly, the average yield strengths of the 70 mm thick welded sections were shown to vary merely from 721 to 725 N/mm^2, i.e., $\leq$ 1% of that of the base plates. The tensile strengths of the welded sections were shown to vary merely from 795 to 798 N/mm^2, i.e., $\leq$ 1% of that of the base plates. The corresponding reduction factors range from 0.99 to 0.98 for the yield strengths and 0.99 to 1.00 for their tensile strengths, as shown in Table 3.10.

e) According to EN ISO 15614-1, the tensile strength of any coupon of welded sections shall not be less than the corresponding specified minimum tensile strength of the base plate. In this case, it should be 770, 770 and 760 N/mm^2 according to EN 10025-6 for 16, 50 and 70 mm S690 QT steel plates, respectively. As shown in Table 3.9, for the 16 mm plates, the tensile strengths of the welded sections prepared with heat input energy of 2.0 and 5.0 kJ/mm are 745 and 678 N/mm^2, respectively, and hence they are obviously unqualified. However, situations are proved to be

quite different in the 50 mm and the 70 mm thick plates that all the welded sections with a wide range of heat input energy are shown to possess qualified mechanical properties. What's more, the mechanical properties of the S690 QT 16 mm welded sections welded sections reported by LIU (2018) change significantly with the heat input energy.

f) According to the results above, it is concluded that with an increase of the plate thickness, the effect of welding on the mechanical properties of the welded connections becomes less significant. Hence, these S690 thick steel plates do not necessarily suffer from any significant reduction in their mechanical properties after welding if the welding process is properly controlled.
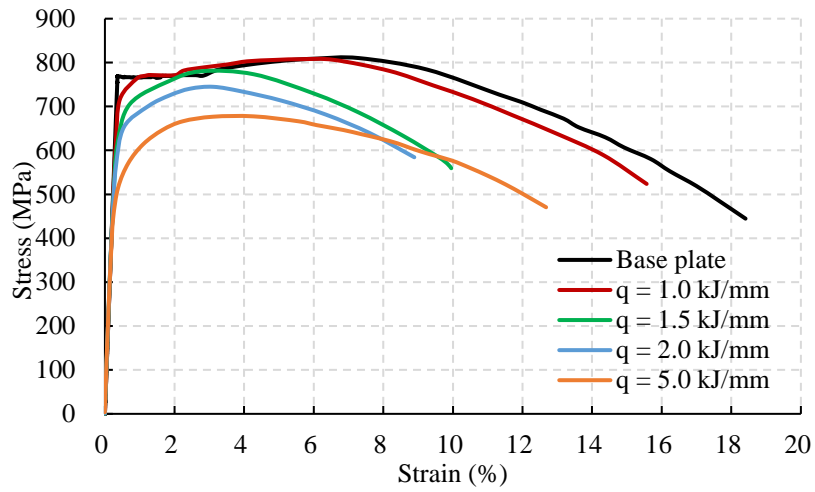
a) Test results of 16 mm thick plates (LIU, 2018)
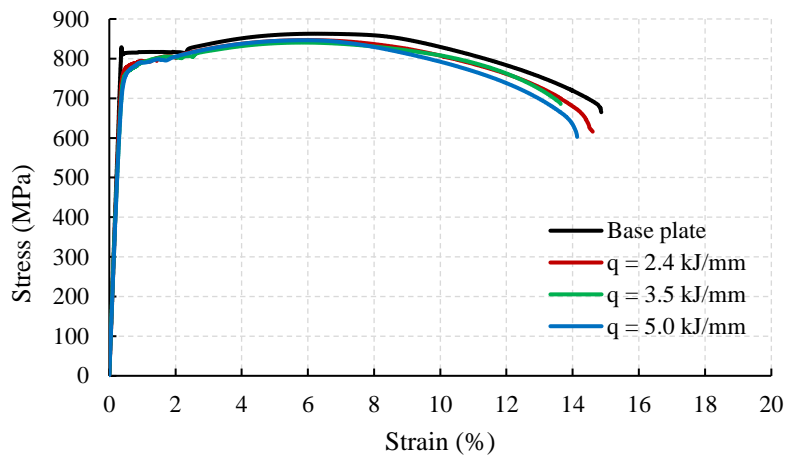
b) Test results of 50 mm thick plates
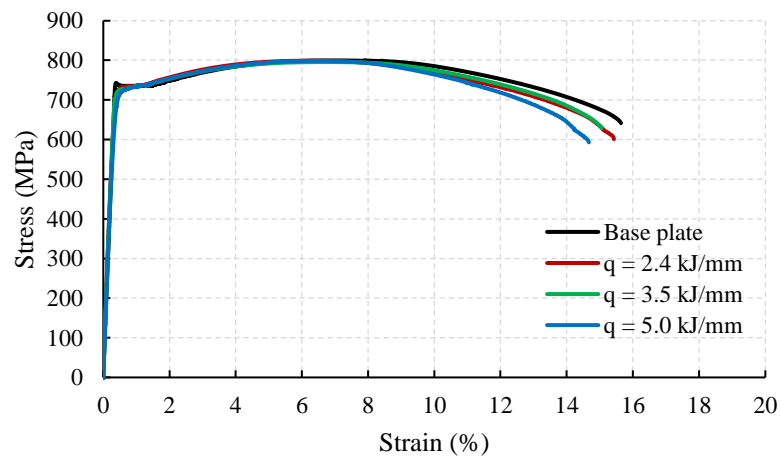
c) Test results of 70 mm thick plates

Figure 3.14 Comparison of test results of various steel plates

Table 3.9 Average mechanical properties of S690 QT base plates and welded sections

Thickness (mm)	Heat input energy (kJ/mm)	f_y (N/mm²)	f_u (N/mm²)	Elongation at fracture ε_L (%)
16 (LIU, 2018)	Base plate	761	810	18.3
	1.0	748	808	14.2
	1.5	656	785	10.3
	2.0	657	746	9.4
	5.0	533	670	12.5
50	Base plate	819	865	15.1
	2.4	767	832	14.8
	3.5	751	825	13.4
	5.0	755	835	13.2
70	Base plate	737	800	15.8
	2.4	728	797	14.7
	3.5	724	795	15.4
	5.0	721	798	14.8

Table 3.10 Reduction factors of mechanical properties of welded sections

Thickness (mm)	Heat input energy (kJ/mm)	$\dfrac{f_y}{f_{y-BP}}$	$\dfrac{f_u}{f_{u-BP}}$	$\dfrac{\varepsilon_L}{\varepsilon_{L-BP}}$
16 (LIU, 2018)	1.0	0.98	1.00	0.78
	1.5	0.90	0.97	0.56
	2.0	0.86	0.92	0.51
	5.0	0.70	0.83	0.68
50	2.4	0.94	0.96	0.98
	3.5	0.92	0.95	0.89
	5.0	0.92	0.97	0.87
70	2.4	0.99	1.00	0.93
	3.5	0.98	0.99	0.97
	5.0	0.98	1.00	0.93

Note:

f_{y-BP}, f_{u-BP} are the yield strength and the tensile strength of the base plate.

ε_{L-BP} is the elongation at fracture of the base plate.

3.4 Tensile tests of welded sections of Q620 TM 28 and 44 mm thick plates

According to the results obtained in Section 3.2, no significant variation in the mechanical properties of a steel plate thinner than 50 mm is expected. Hence, no investigation into the stress-strain curves of cylindrical coupons extracted from various locations within the plate thickness was performed.

3.4.1   Welding and machining of test specimens

A total of six butt welded sections were fabricated with the Q620 TM 28 mm and the Q620 TM 44 mm steel plates using three different heat input energy, i.e., q= 2.5, 3.5, and 4.5 kJ/mm. The test program is shown in Table 3.11, and the joint design of both the 28 and the 44 mm thick steel plates is illustrated in Figure 3.15. In order to achieve a high welding efficiency with a minimum amount of welding, an X-shape groove is adopted.

Table 3.11 Welding of Q620 TM steel plates

Thickness (mm)	Length L (mm)	Width W (mm)	Heat input energy (kJ/mm)		
			2.5	3.5	4.5
28	1400	600	1	1	1
44	2000	600	1	1	1
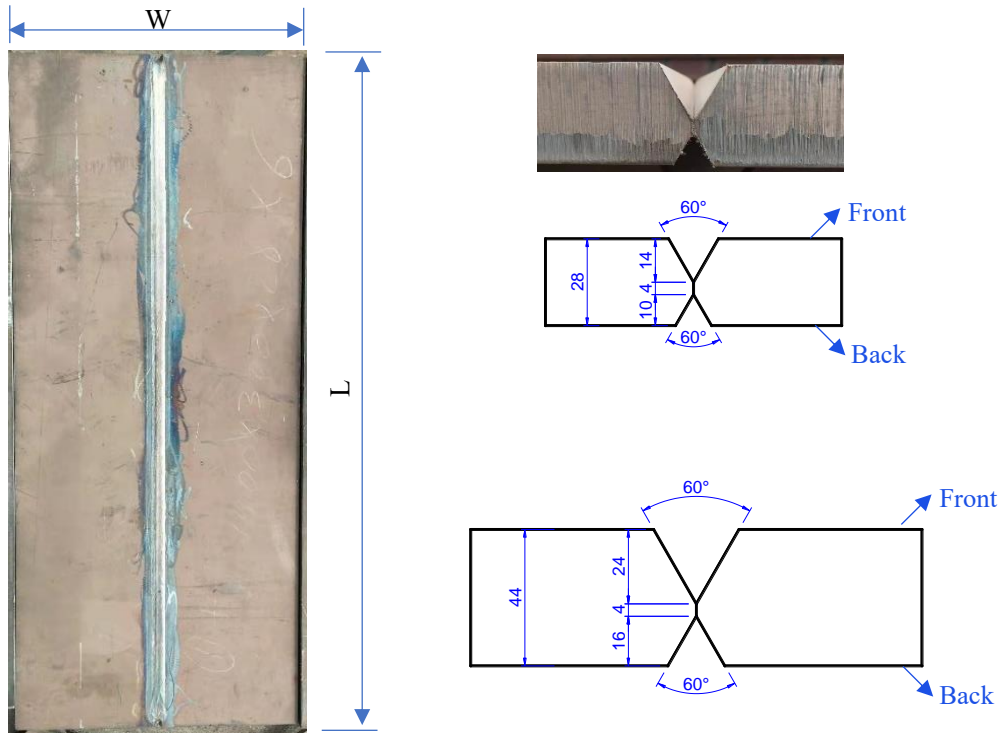
Figure 3.15 Butt-welded sections of Q620 TM steel with an X-shaped groove

The dimensions of the coupons and the extraction locations are shown in Figure 3.16. The coupon is 28 mm wide in the thickness direction of the welded sections, and the same design is adopted in the 44 mm thick welded sections in order to allow for a direct comparison. A designation system is shown in Figure 3.17.

a) Dimensions of coupon

a) Extraction of coupons
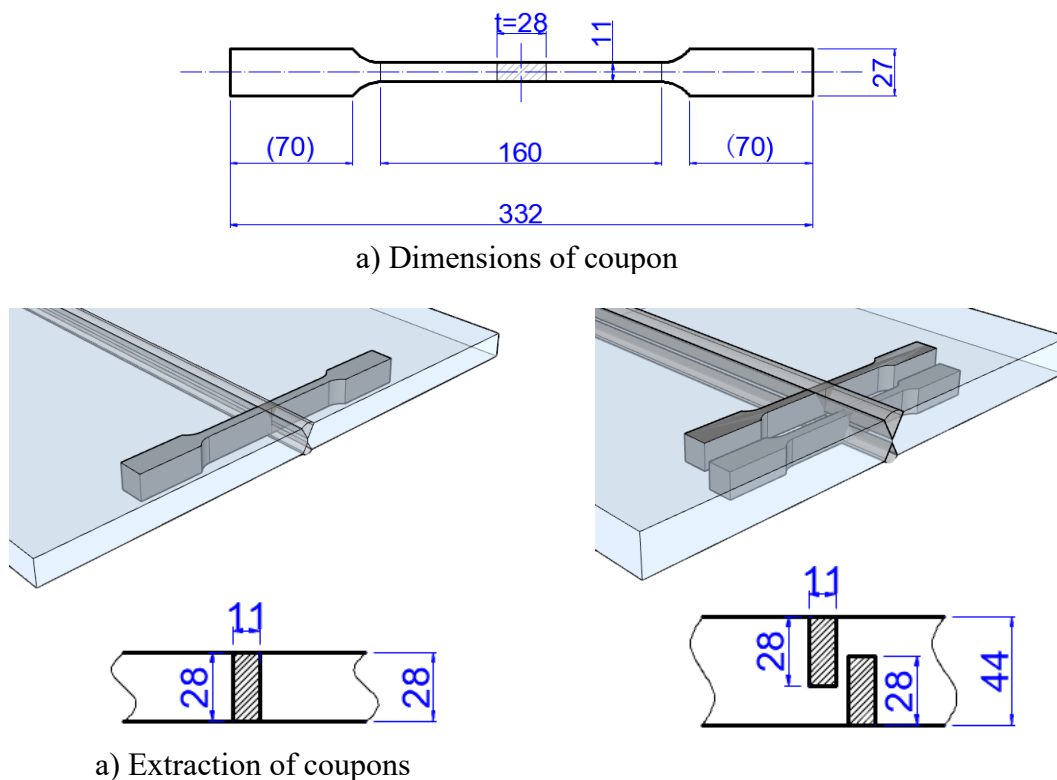
Figure 3.16 Extraction locations and dimensions of Q620 TM tensile test coupons
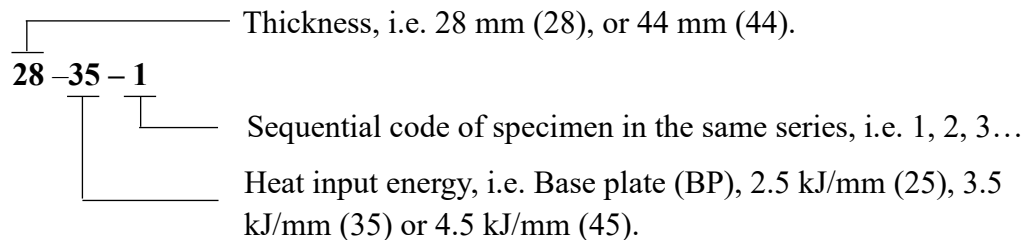
Figure 3.17 Designation system of tensile tests on coupons of Q620 TM butt-welded

sections

3.4.2   Test program

Table 3.12 shows the test program of the tensile tests on the 28 and the 44 mm welded sections together with corresponding control groups. Typical coupons before test are illustrated in Figure 3.18. The test set-up and instrumentation are the same with those adopted for the tensile tests of the S690 QT steel presented in Section 3.3.3.

Table 3.12 Test program of tensile test on coupons of 28 and 44 mm thick welded sections

Test series	Thickness (mm)	Cross sectional dimension (mm × mm)	Gauge length (mm)	Quantity	Remarks
28-BP	28	28 × 11	100	2	1 with DIC
28-25		28 × 11	100	2	1 with DIC
28-35		28 × 11	100	2	-
28-45		28 × 11	100	2	1 with DIC
44-BP	44	28 × 11	100	2	1 with DIC
44-25		28 × 11	100	4	1 with DIC
44-35		28 × 11	100	4	-
44-45		28 × 11	100	4	1 with DIC

Notes: $L = 5.65 \times \sqrt{A_0}$, where $A_0 = 28 \times 11$

After etching

After painting for DIC measurement

Figure 3.18 Typical coupons of Q620 butt-welded connections before test

It should be noted that the extensometer with a gauge length of 100 mm was set in the middle of the coupon to cover the HAZs and the fusion zone.

3.4.3　Test results

A total of 22 coupons were tested and the fractured coupons are demonstrated in Figure 3.19. The measured mechanical properties of the 28 and the 44 mm thick base plates and their welded sections under three heat input energy are summarized in Table 3.13. Figures 3.20 and 3.21 plot the measured stress-strain curves of the 28 and the 44 mm

thick steel plates respectively. It is shown that the curves follow closely among all those with the same heat input energy group, and hence, the results are shown to be consistent. There is no obvious yield plateau in the measured stress-strain curves, thus, the 0.2% proof strength is adopted as the yield strengths of all the coupons.

a) 28 mm thick sections   b) 44 mm thick sections

Fractured at HAZ

c) Typical fracture mode of coupons from 28 mm thick section

Fractured at HAZ

d) Typical fracture mode of coupons from 44 mm thick section

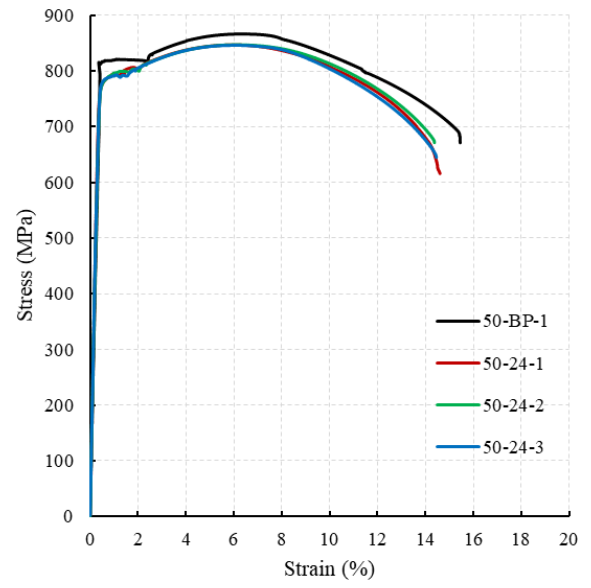Figure 3.19 Fractured coupons of Q620 TM 28 and 44 mm the butt-welded sections

Table 3.13 Measured mechanical properties of 28 and 44 mm thick base plates and
their welded sections

| Specimen	Young's Modulus, E (kN/mm²)	Yield strength, f_y (N/mm²)	Tensile strength, f_u (N/mm²)	f_y/f_u	Elongation at fracture ε_f (%)	Fracture position
28-BP-1	212	637	767	0.83	20.1	-
28-BP-2	215	637	766	0.83	20.7	-
28-25-1	211	655	744	0.88	17.0	HAZ
28-25-2	218	668	746	0.90	16.8	HAZ
28-35-1	220	643	730	0.88	19.1	HAZ
28-35-2	215	650	734	0.89	16.1	HAZ
28-45-1	220	644	726	0.89	16.2	HAZ
28-45-2	206	645	725	0.89	17.1	HAZ
44-BP-1	216	633	774	0.82	20.1	-
44-BP-2	213	626	771	0.81	19.5	-
44-25-1	219	660	750	0.88	16.3	HAZ
44-25-2	217	666	762	0.87	12.4	HAZ
44-25-3	216	660	753	0.88	14.8	HAZ
44-25-4	220	660	762	0.87	14.2	HAZ
44-35-1	215	660	753	0.88	15.9	HAZ
44-35-2	210	653	747	0.87	13.5	HAZ
44-35-3	216	652	743	0.88	15.2	HAZ
44-35-4	214	659	750	0.88	15.3	HAZ
44-45-1	218	650	741	0.88	14.4	HAZ
44-45-2	209	652	742	0.88	13.9	HAZ
44-45-3	206	656	743	0.88	15.0	HAZ
44-45-4	218	658	751	0.88	14.6	HAZ
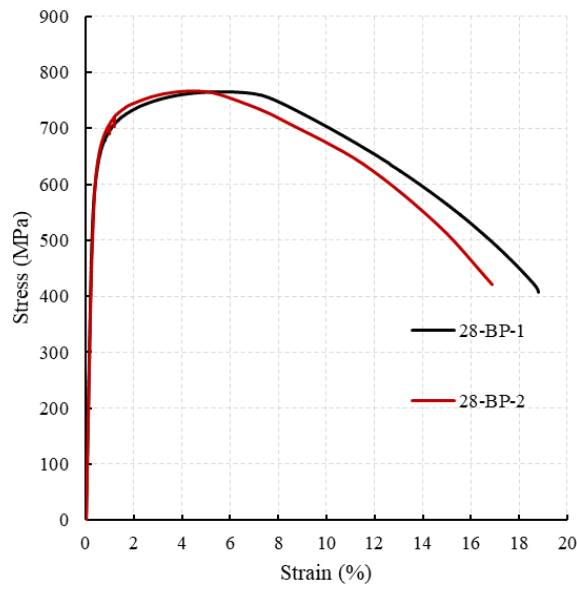
a) Base plate
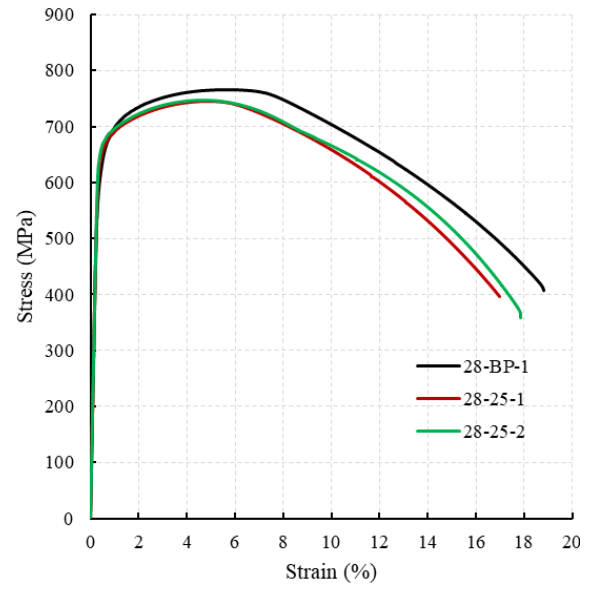
b) q= 2.5kJ/mm
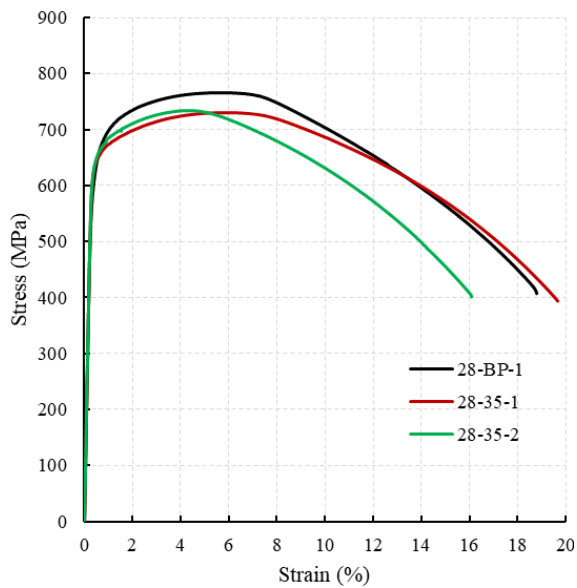
c) q=3.5 kJ/mm
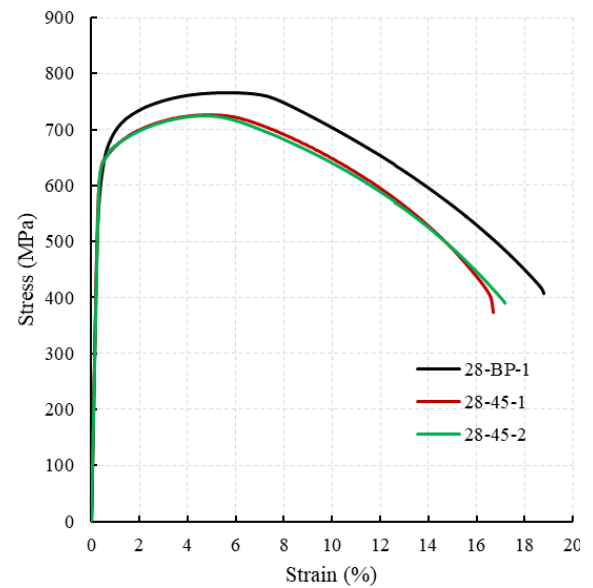
d) q=4.5 kJ/mm

Figure 3.20 Full-range stress-strain curves of the coupons of the 28 mm thick butt-welded sections

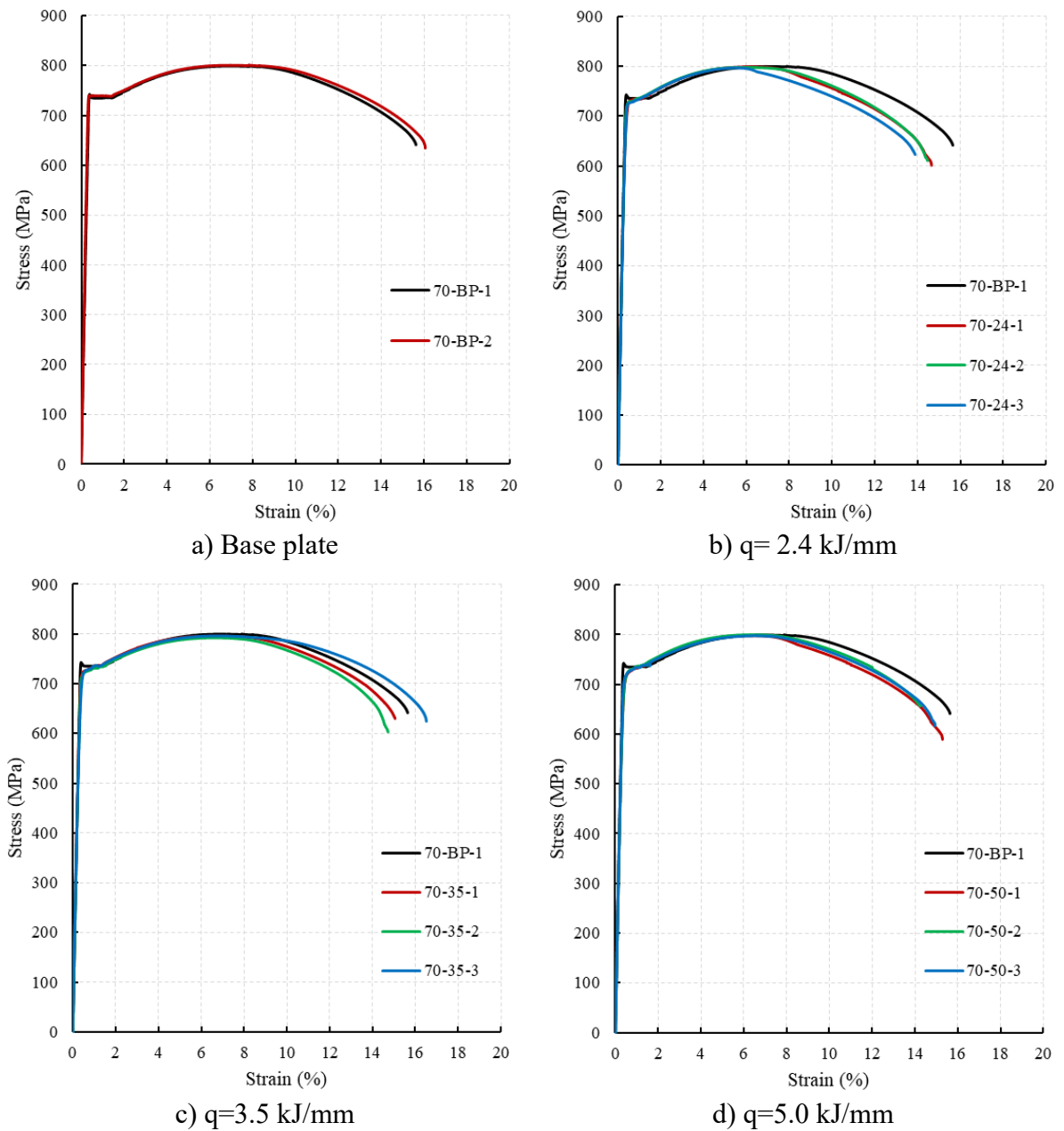a) Base plate

b) q= 2.5kJ/mm

c) q=3.5 kJ/mm

d) q=4.5 kJ/mm
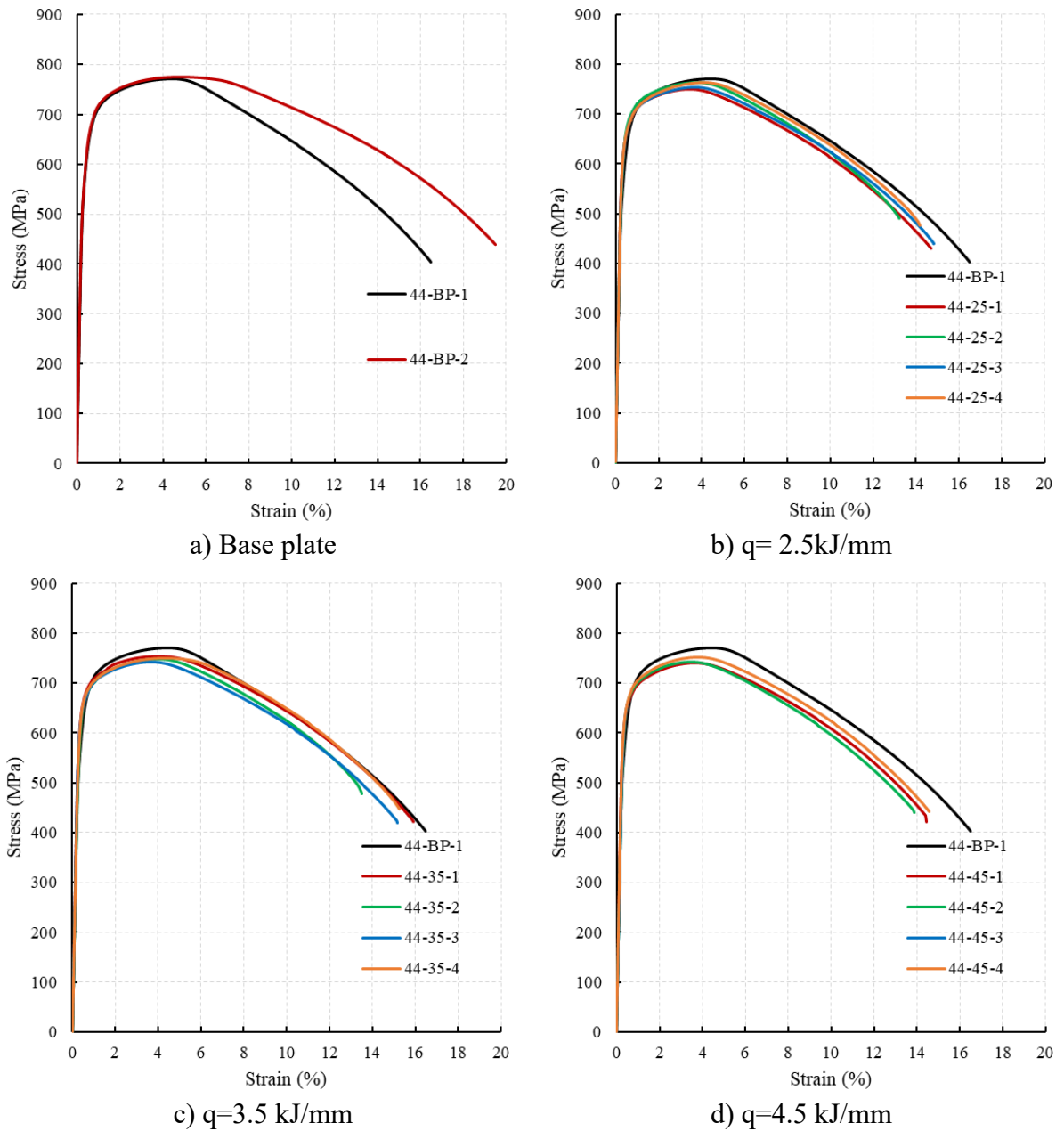
Figure 3.21 Full-range stress-strain curves of the coupons of the 44 mm thick butt-welded sections

It is shown that:

1) As shown in Figure 3.22 b) and c), the mechanical properties of the welded sections change significantly, when compared with those of the base plates. Both the yield and the tensile strengths of the welded sections decrease when the heat input energy is increased as shown in Tables 3.14 and 3.15. It is evident in these cases that

reductions to the strengths of the base plates due to the effects of welding is significant.

2) The measured yield strengths of the 28 mm thick welded sections were shown to vary from 645 to 662 N/mm^2, i.e. 4% larger than that of the base plates. Similarly, the measured yield strengths of the 44 mm thick welded sections were shown to vary from 654 to 662 N/mm^2, i.e. nearly 5% larger than that of the base plates. As shown in Figures 3.23 b) and 3.24 b), the linear elastic ranges of the 28 and the 44 mm base plates end at around 500 and 400 N/mm^2, respectively, while the yield strength of the weld metal is 626 N/mm^2 as demonstrated in Figure 3.25 and the linear elastic range ends at 600 N/mm^2.

3) The measured tensile strengths of the 28 mm thick welded sections were shown to vary from 726 to 745 N/mm^2, i.e., about 5% of that of the base plates. While the measured tensile strengths of the 44 mm thick welded sections were shown to vary from 744 to 757 N/mm^2, i.e., about 4% of that of the base plates. There is still a certain reduction in the tensile strengths of the welded sections.

4) According to GB 50661 (CABP, 2011), the tensile strength of any coupon of welded sections shall not be less than the corresponding specified minimum tensile strength of the base plate. In this case, it should be 710 and 690 N/mm^2 according to GB/T 1591 for 28 and 44 mm thick Q620 TM steel plates, respectively. As shown in Table 3.14, all the welded sections with a wide range of heat input energy are shown to possess qualified mechanical properties.
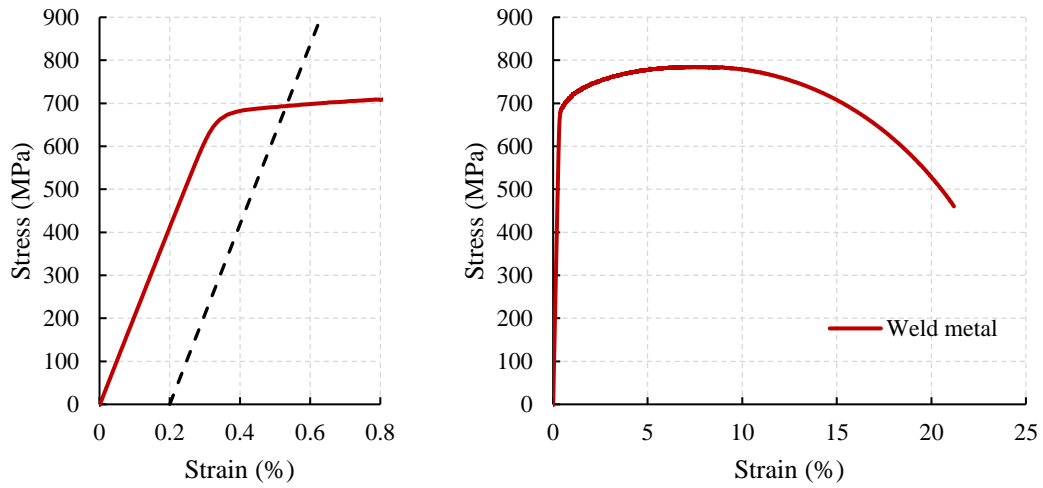
a) Test results of weld metal
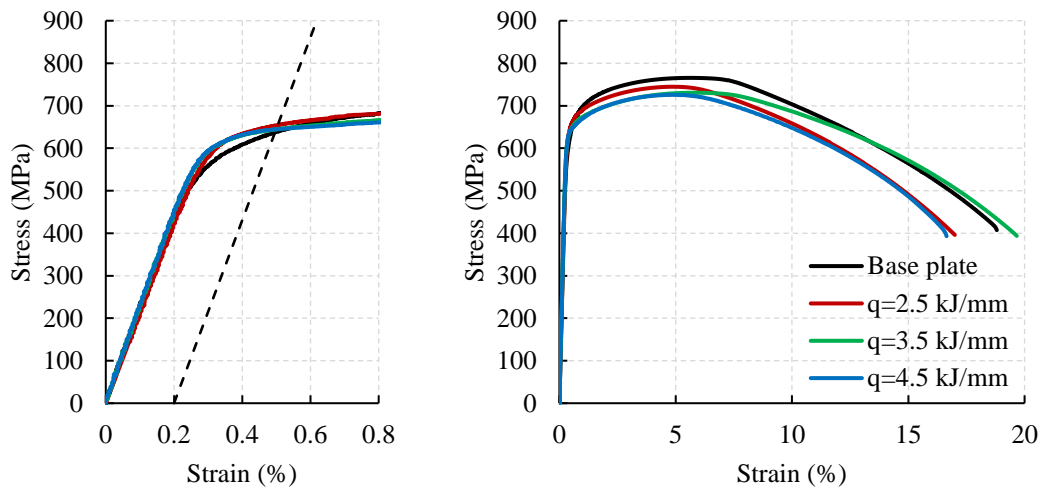
b) Test results of 28 mm thick sections
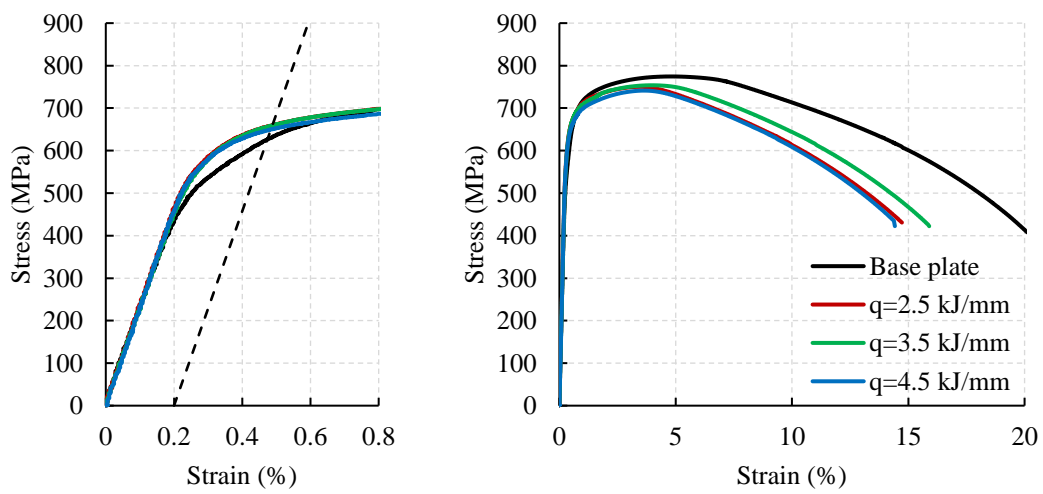
c) Test results of 44 mm thick sections

Figure 3.22 Test results of Q620 TM 28 mm sections

Table 3.14 Average mechanical properties of welded sections

Thickness (mm)	Heat input (kJ/mm)	f_y (N/mm²)	f_u (N/mm²)	Elongation at fracture (%)
28	Base plate	637	767	20.4
	2.5	662	745	16.9
	3.5	647	732	17.6
	4.5	645	726	16.7
44	Base plate	630	773	19.8
	2.5	662	757	14.4
	3.5	656	748	15.0
	4.5	654	744	14.5

Table 3.15 Reduction factors of mechanical properties of welded sections

Thickness (mm)	Heat input (kJ/mm)	$\dfrac{f_y}{f_{y-BP}}$	$\dfrac{f_u}{f_{u-BP}}$	$\dfrac{\varepsilon_L}{\varepsilon_{L-BP}}$
28	2.5	1.04	0.97	0.83
	3.5	1.02	0.95	0.86
	4.5	1.01	0.95	0.82
44	2.5	1.05	0.98	0.73
	3.5	1.04	0.97	0.76
	4.5	1.04	0.96	0.73

Note:

f_{y-BP}, f_{u-BP} are the yield strength and the tensile strength of the base plate.

ε_{L-BP} is the elongation at fracture of the base plate.

3.5 Test results with DIC

As mentioned in the previous two sections, 12 coupons were tested with DIC for measurements of surface strain fields and they are listed as follow. Figure 3.23 shows the four sampling points on a typical engineering stress-strain curve of a typical coupon for further demonstration of measured strain field.

Point ① is well within the elastic range with a stress of about 300 MPa,

Point ② is close to the yield strength,

Point ③ is close to the tensile strength of the steel, and

Point ④ is close to the elongation at fracture.

It should be noted that the sampling frequency is 30s, so that the images captured were close to target stresses as much as practically feasible. Unfortunately, the necking or the fracture region may locate outside the target region shot by cameras during DIC measurement.
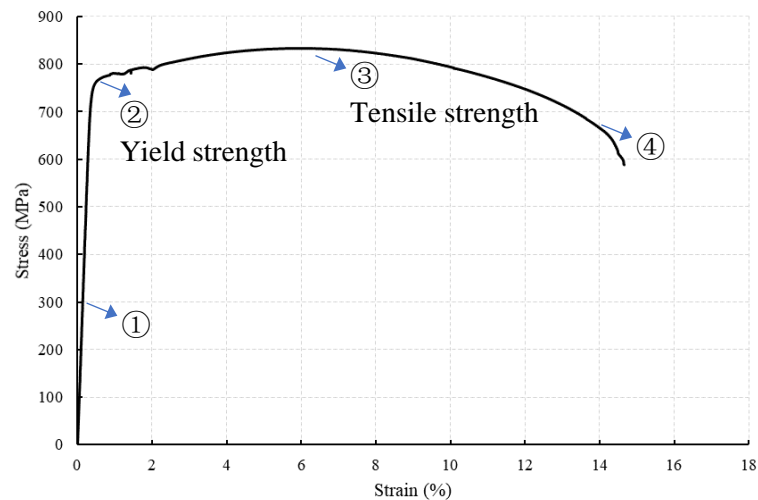
Figure 3.23 Sampling points along a stress-strain curve

3.5.1　S690 QT 50 and 70 mm base plate and welded sections

The true principal strains along the longitudinal direction of the coupons of the S690 QT 50 mm and the S690 QT 70 mm base plates and welded sections with different heat input energy under tension are plotted in Figures 3.24 and 3.25.

For the base plate:

1) Figures 3.24 a) and 3.25 a) show the coupons of the 50 and the 70 mm thick base plate respectively. A uniformly distributed strain field is obtained for deformations according to Points ①, ② and ③ with necking.

2) In Point ④, the strain distribution after necking is shown to be symmetric, and the symmetry plane is perpendicular to the longitudinal direction of the coupon, as shown in Figure 3.25 a).

For those coupons of the welded sections, the strains are still shown to distribute uniformly at a stress level of 300 N/mm^2 according to Points ① in Figure 3.24 b), and c), as well as Figure 3.25 b) and c). Situations become different when the deformations are increased to Point ②. It should be noted that the weld metal has a smaller yield strength when compared with that of the base plate, a slightly larger strain level is found, when compared with other parts of the welded section. What's more, the HAZ adjacent to the fusion zone also shows a larger strain level when compared with the other parts.

However, significant differences in the strain distributions of the coupons become apparent when the deformations reach Point ③:

1) The partially grain-refined HAZ (PGRHAZ), with non-uniform grain sizes and non-uniform strength, is the weakest part in a weld joint and it has the largest strain level

according to Figure 3.27 b) and c), and Figure 3.28 b) and c).

2) The coarse-grain HAZ (CGHAZ) which lies adjacent to the fusion zone has large grain sizes and higher strength when compared with those of the other parts in HAZ and the base plate. So, a smaller strain of CGHAZ region is detected in the weld joint, when compared with those of the other parts.
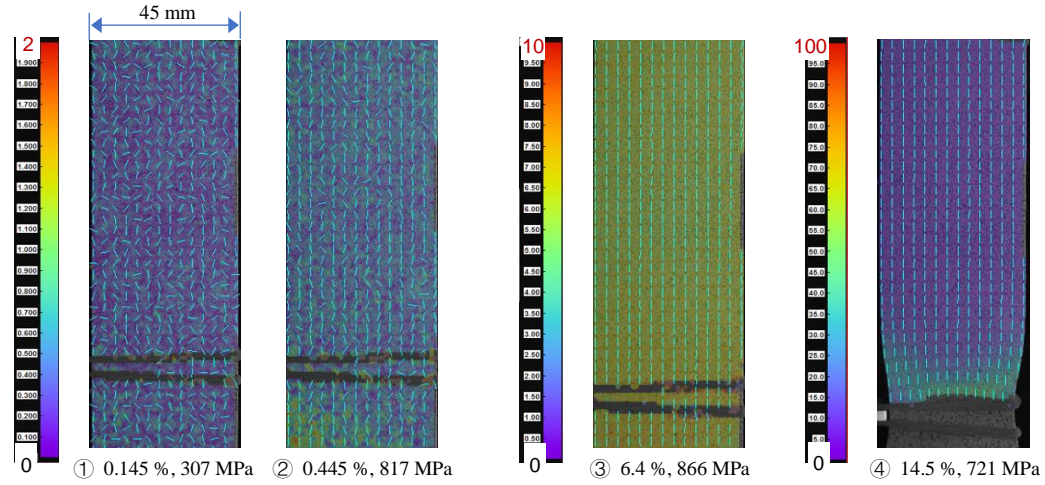
a) Coupon 50-BP-1
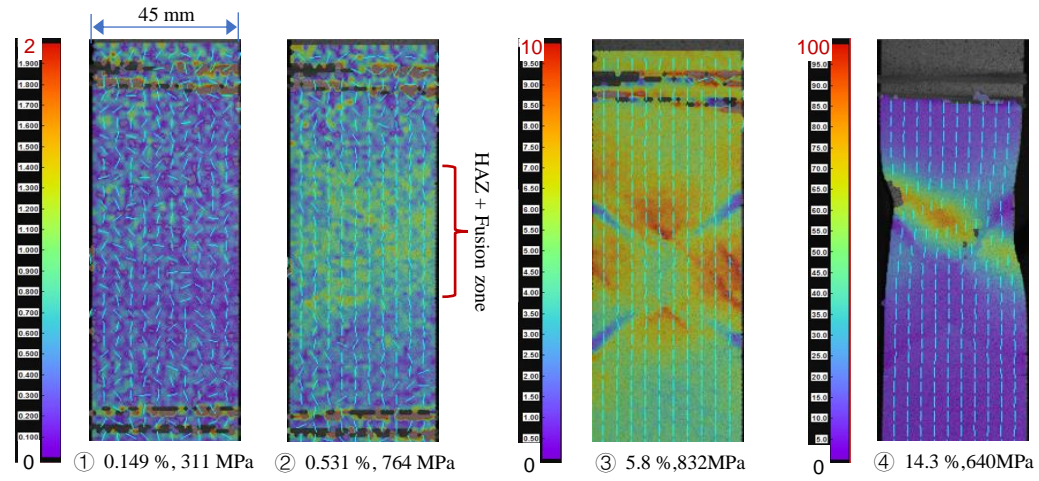
b) Coupon 50-24-1
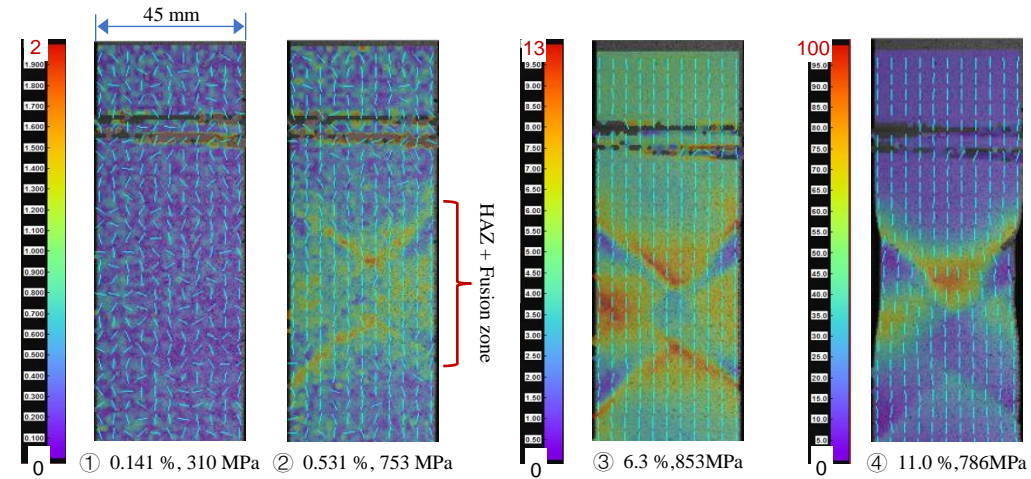
c) Coupon 50-50-1

Figure 3.24 Longitudinal strain fields of the coupons of S690 QT 50 mm thick base

plates and welded sections under tension
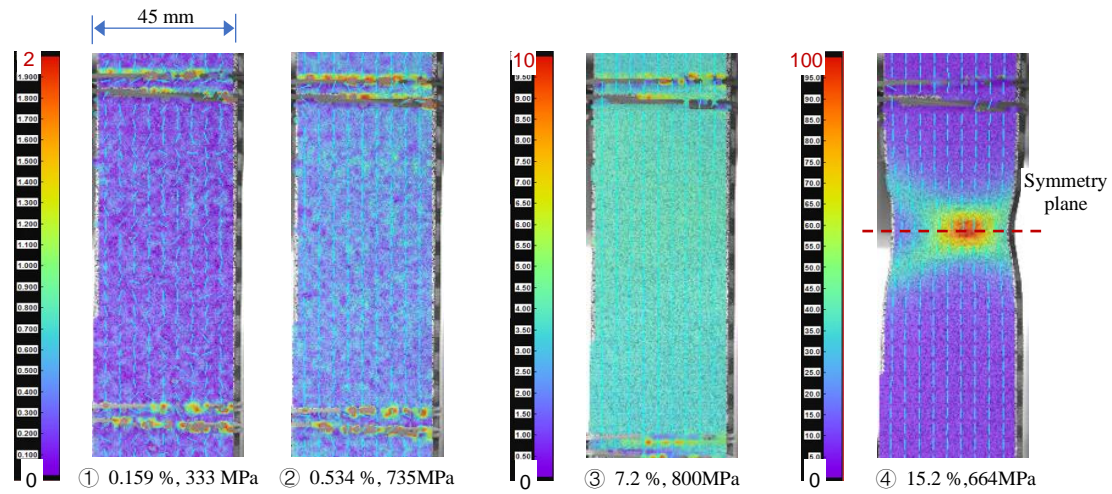
a) Coupon 70-BP-1
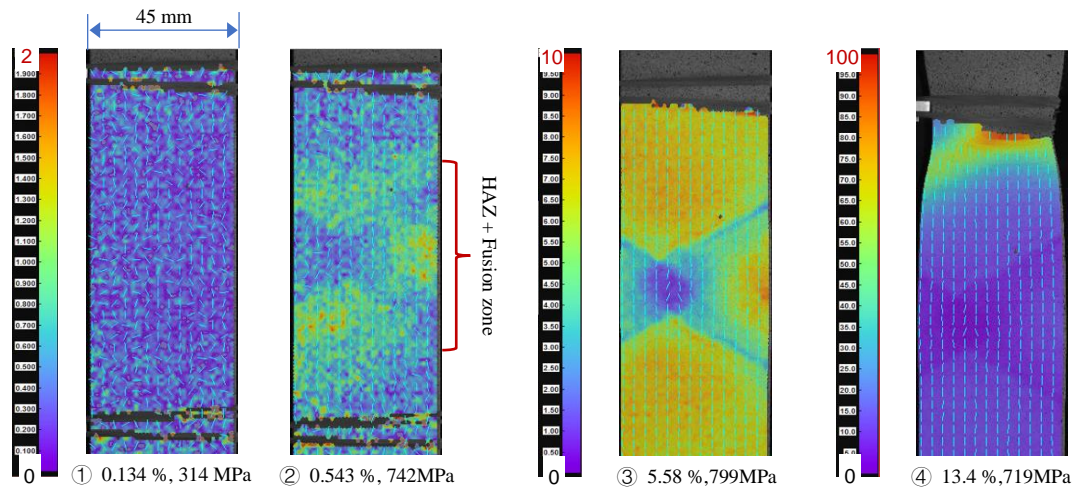
b) Coupon 70-24-1
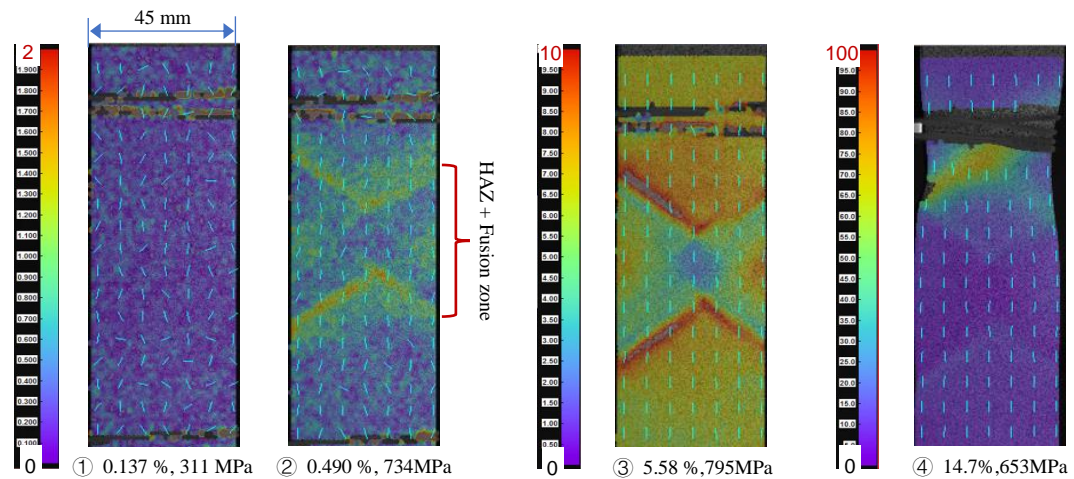
c) Coupon 70-50-1

Figure 3.25 Longitudinal strain field of coupons of S690 QT 70 mm thick base plates and welded sections under tension

3.5.2　Q620 TMCP 28 and 44 mm base plate and welded sections

The surface longitudinal strain fields of the Q620 TM 28 mm and the Q620 TM 44 mm base plates and the welded sections are presented in Figures 3.29 and 3.30. It is noticeable that these results will be further used for comparison with FEM results of the Q620 TM welded sections under tension in later chapter.

For the base plate:

1) Figures 3.26 a) and 3.27 a) show the coupons of the 28 and the 44 mm thick base plate respectively. A uniformly distributed strain field is obtained for deformations according to Points ①, ② and ③ with necking.

2) In Point ④, the strain distribution after necking is shown to be symmetric, and the symmetry plane is perpendicular to the longitudinal direction of the coupon, as shown in Figures 3.26 a) and 3.27 a).

For those coupons of the welded sections, the strains are still shown to distribute uniformly at a stress level of 300 N/mm^2 according to Points ① in Figure 3.26 b), and c), as well as Figure 3.27 b) and c). Situations become different when the deformations are increased to Point ②. It should be noted that the weld metal has a larger yield strength when compared with that of the base plates, a slightly smaller strain level is found, when compared with other parts of the welded section. What's more, the HAZ adjacent to the fusion zone shows a larger strain level when compared with the other parts.

However, significant differences in the strain distributions of the coupons become apparent when the deformations reach Point ③. The partially grain-refined HAZ (PGRHAZ), with non-uniform grain sizes and non-uniform strength, is the weakest part

68

in a weld joint and it has the largest strain level according to Figure 3.26 b) and c), and Figure 3.27 b) and c). However, the coarse-grain HAZ (CGHAZ) is not that obvious as there is no significant 'blue region', which stands for a low strain level, in the HAZ.

a) Coupon 28-BP-1

b) Coupon 28-25-1

c) Coupon 28-45-1

Figure 3.26 Longitudinal strain fields of coupons of Q620 TM 28 mm thick base

plates and welded sections under tension
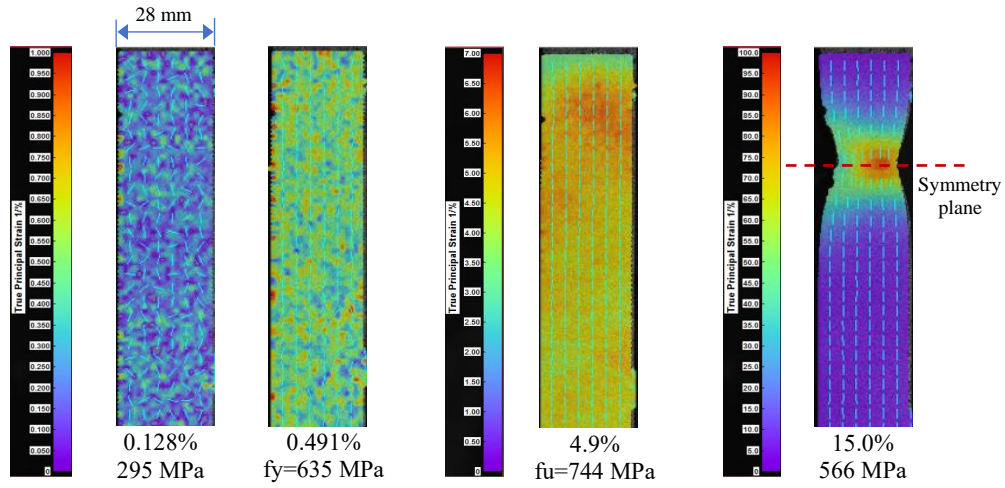
a) Coupon 44-BP-1
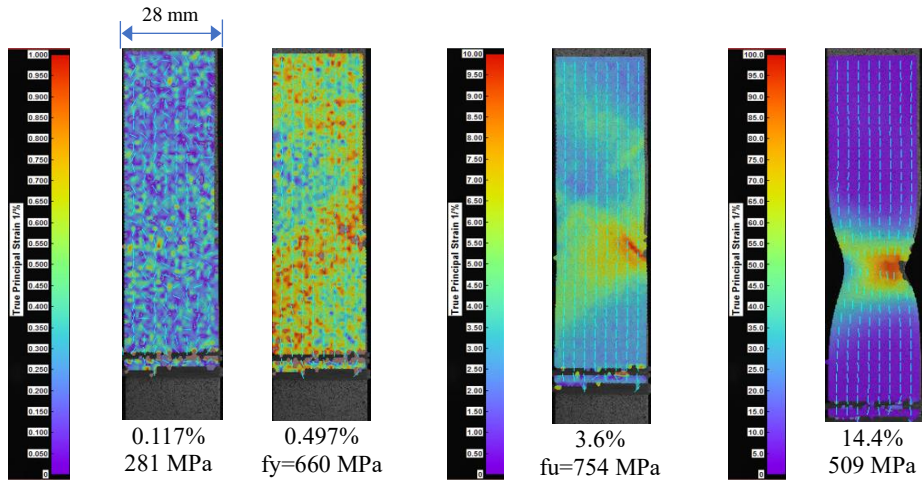
b) Coupon 44-25-1
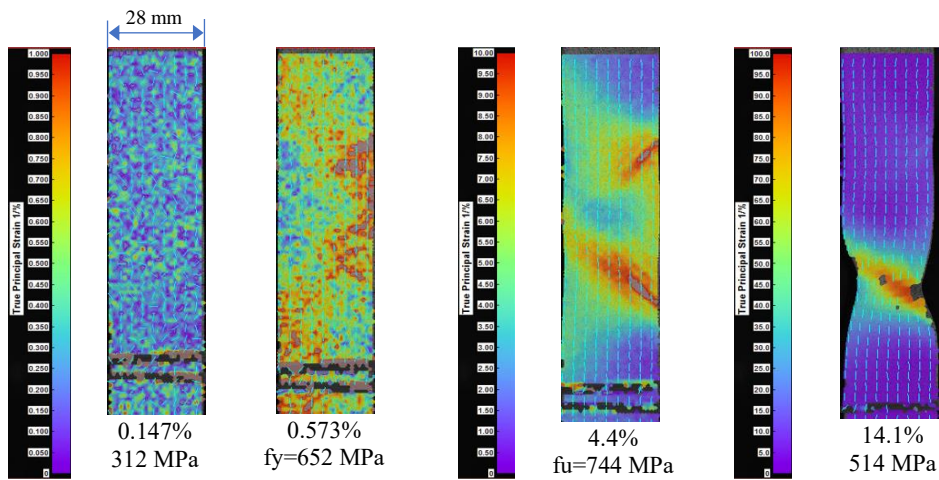
c) Coupon 44-45-1

Figure 3.27 Longitudinal strain fields of coupons of Q620 TM 44 mm thick base

plates and welded sections under tension

It is found that:

1) In a welded section under tension, the strain distribution is non-uniformed when compared with the base plate, as there are various regions, i.e. the HAZ and the fusion zone, with different mechanical properties.

2) By comparing the strain distribution between coupons of QT sections to those of TM sections, the 'blue region' in HAZ is less significant in HAZ of TM section, which indicates that the strength of coarse-grain HAZ in the HAZ of TM welded sections is less significant when comparing with that of QT steel.

| a) Coupon 50-24-1 | b) Coupon 50-50-1 | c) Coupon 70-24-1 | d) Coupon 70-50-1 |
| e) Coupon 28-25-1 | f) Coupon 28-45-1 | g) Coupon 44-25-1 | h) Coupon 44-45-1 |
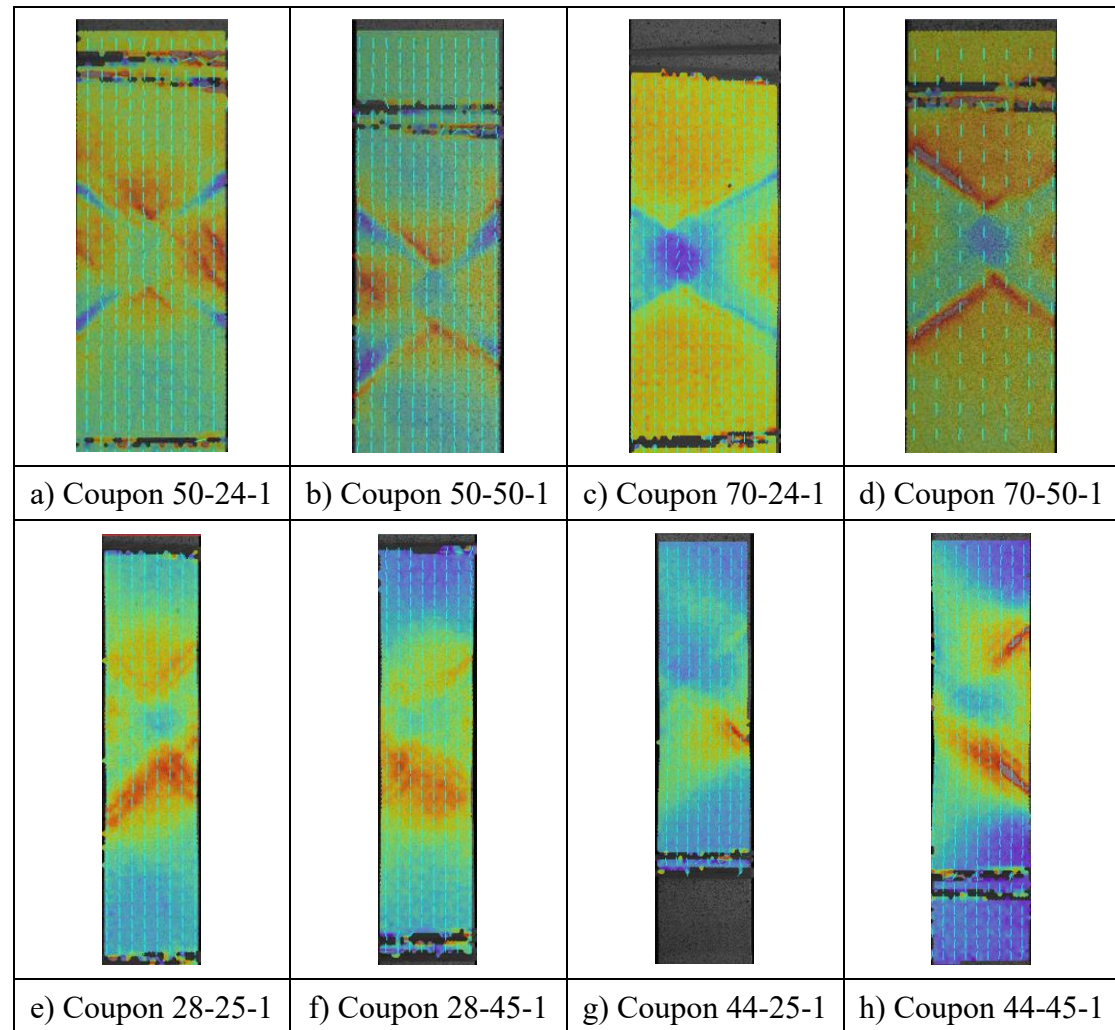
Figure 3.28 Comparison of strain fields among different coupons

3.6 Metallographic analyses

Metallographic analyses were conducted on both the S690 QT and the Q620 TM base plates and their welded sections to investigate the microstructures and their changes caused by welding. Scanning Electron Microscope (SEM) was used to capture high resolution images of various regions in the vicinities of the heat-affected-zones of the welded sections.

3.6.1 Examination program

Metallographic analysis was conducted on both the S690 QT and the Q620 TM steel base plates and their welded sections, and an examination program is listed in Table 3.16.

Table 3.16 Examination program of metallographic analysis

Delivery condition	Thickness (mm)	Heat energy input (kJ/mm)			
QT	50	Base plate	2.4	3.5	5.0
TM	28	Base plate	2.5	3.5	4.5

3.6.2 Examination set-up and instrumentation

As shown in Figure 3.28, a Tescan VEGA3 SEM system was employed in this study. The locations of sampling points are shown in Figure 3.29, and the coarse-grain HAZ (CGHAZ), the fine grain HAZ (FGHAZ), the inter-critical HAZ (ICHAZ), the subcritical HAZ (SCHAZ) and also the base plate are investigated.

73

Figure 3.29 Tescan VEGA3 SEM
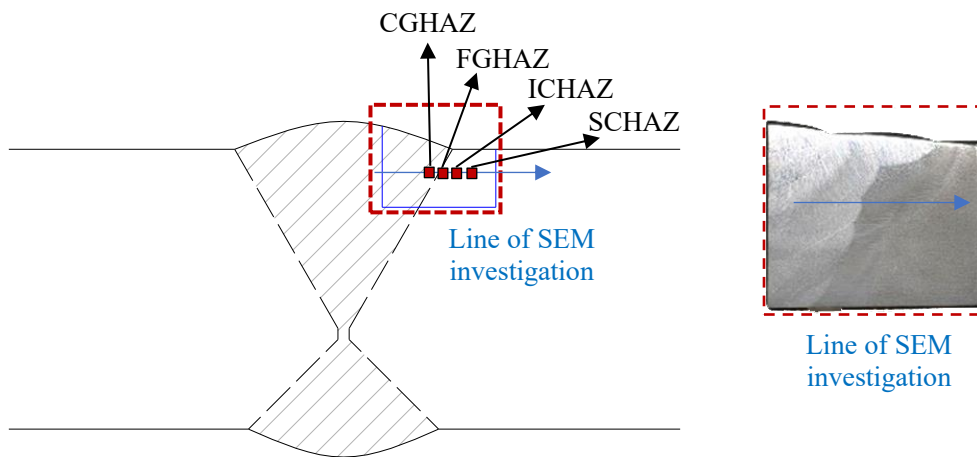
Figure 3.30 Locations of sampling points

3.6.3   Examination results

3.6.3.1 S690 QT 50mm welded sections

In a typical welding process, a HAZ may be readily sub-divided into four regions in accordance with the peak temperature experienced during a thermal cycle imposed by a welding process:

➢   Coarse grain HAZ (CGHAZ), which is formed by heating the steel to a high

temperature above the critical phase-transformation point Ac3;

➢ Fine grain HAZ (FGHAZ), which is also formed by heating the steel to a temperature above the critical phase-transformation point Ac3, but yet lower than that in CGHAZ;

➢ Inter-critical HAZ (ICHAZ), which is formed by heating the steel to a temperature between the critical phase-transformation points Ac1 and Ac3 and

➢ Subcritical HAZ (SCHAZ), which is often refered to a re-tempering region.

The SEM micrographs of HAZ of specimen 50-24 are shown in Figure 3.30. The CGHAZ and the FGHAZ are regions that are entirely transformed into austenite due to the high peak temperature in the thermal cycle.

a) It should be noted that during the cooling process, the solidification phase in the CGHAZ transformed into a microstructure with a mixture of martensite and bainite.

b) The FGHAZ usually has the most reasonable grain structure. The microstructure of the FGHAZ also consists of martensite and bainite but with smaller grain sizes compared with those in the CGHAZ.

c) Figure 3.30 (c) presents the microstructure in the ICHAZ. In this region, the steel was partially transformed into austenite during the heating process, and then, transformed into a microstructure with a mixture of martensite, bainite and ferrite after cooling down.

d) The SCHAZ is the region exposed to a thermal cycle with a peak temperature below Ac1. In figure 3.30 (d), some cementite particles caused by carbide diffusion at a relatively low temperature can be observed.

e) The S690 QT steel base plates are mainly composed of tempered martensite with a

small amount of bainite as shown in Figure 3.30 (e).

The microstructures of the 50 mm thick welded sections with heat input energy of 3.5 and 5.0 kJ/mm are shown in Figures 3.31 and 3.32 respectively. The microstructure changes in the HAZ are similar among the welded sections with different heat input. By comparing the CGHAZ in those welded sections with increasing heat input energy, i.e., Figures 3.30 a), 3.32 a) and 3.32 a), the grain sizes become larger as the smaller cooling rates are allowed for grain growth.
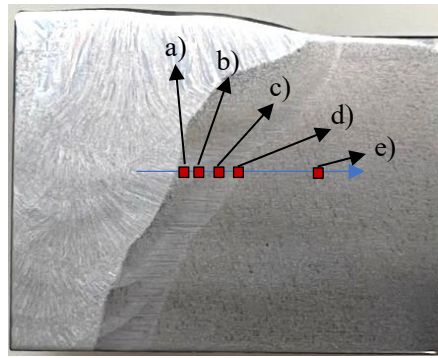
q = 2.4 kJ/mm
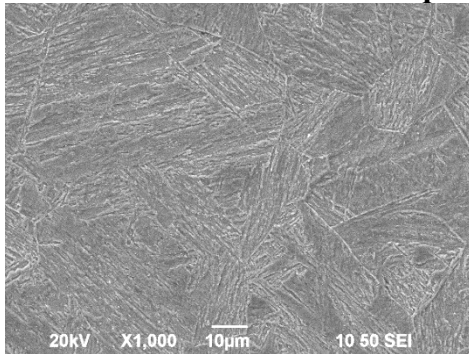
a) CGHAZ
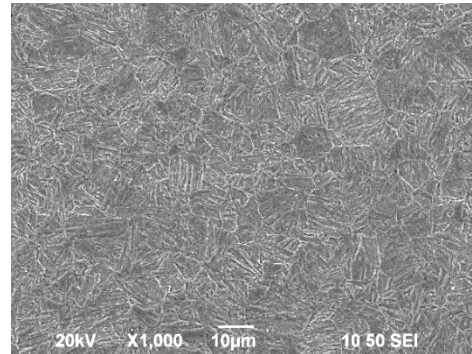
b) FGHAZ
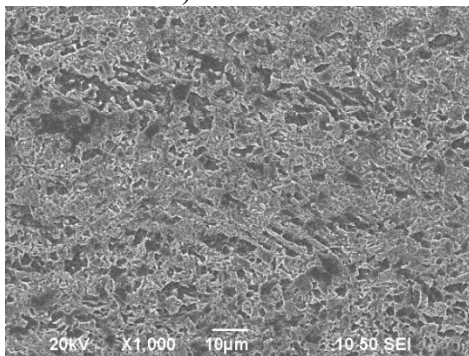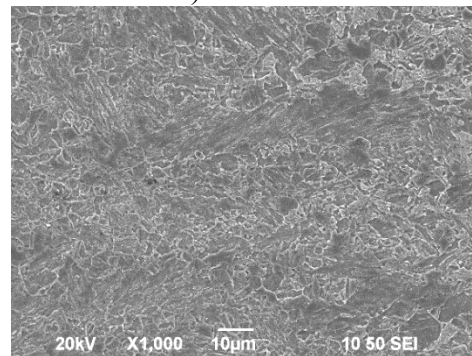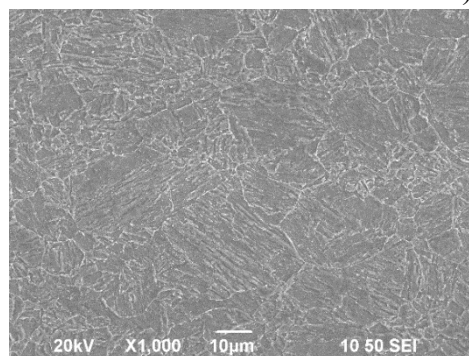
c) ICHAZ

d) SCHAZ

e) Base metal

Figure 3.31 SEM images of S690 QT 50 mm thick welded sections: q=2.4 kJ/mm
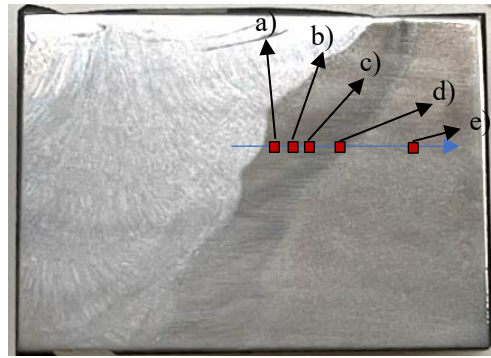
q = 3.5 kJ/mm
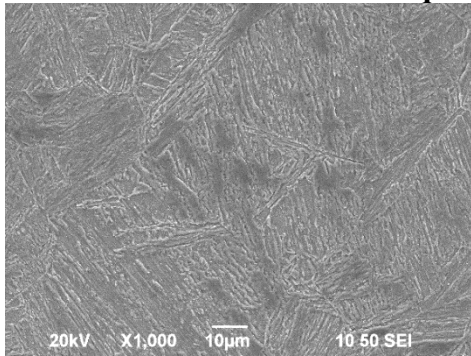
a) CGHAZ
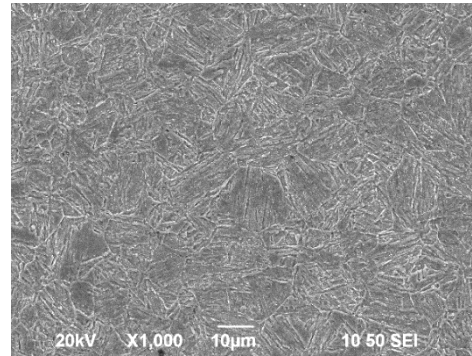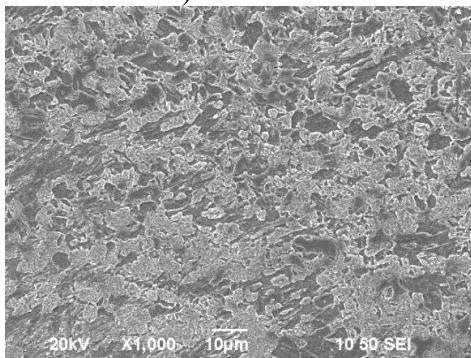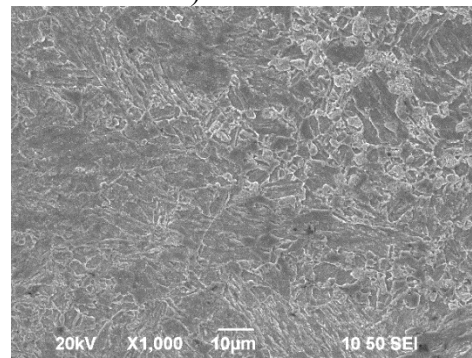
b) FGHAZ
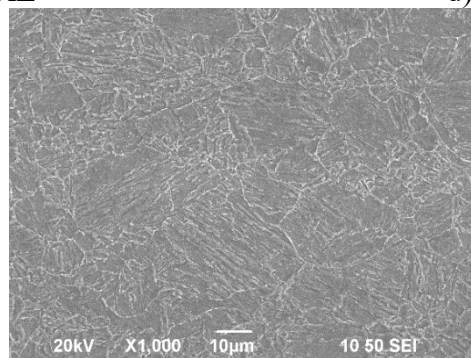
c) ICHAZ

d) SCHAZ

e) Base metal

Figure 3.32 SEM images of S690 QT 50 mm thick welded sections: q=3.5 kJ/mm
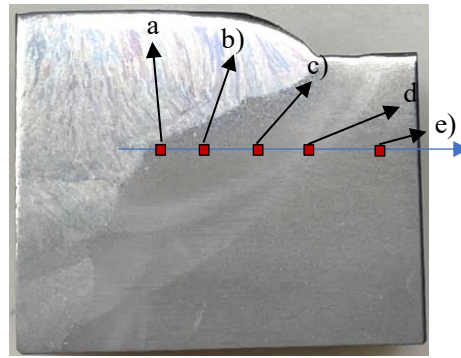
q = 5.0 kJ/mm
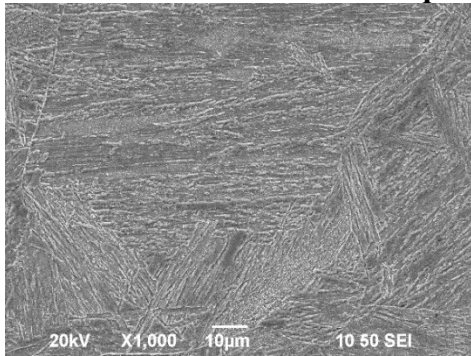
a) CGHAZ
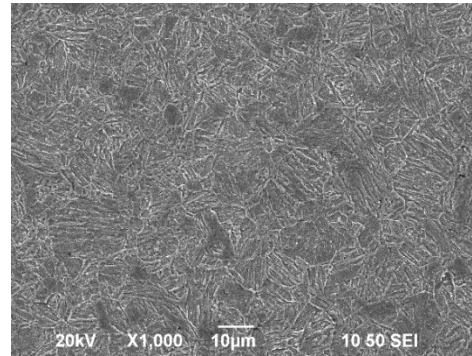
b) FGHAZ
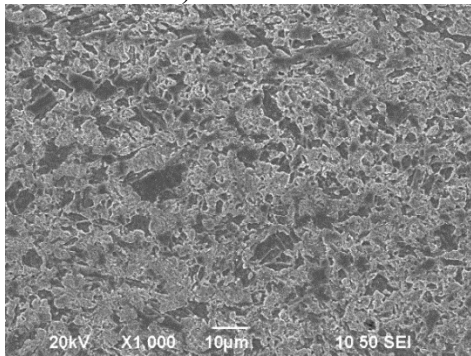
c) ICHAZ
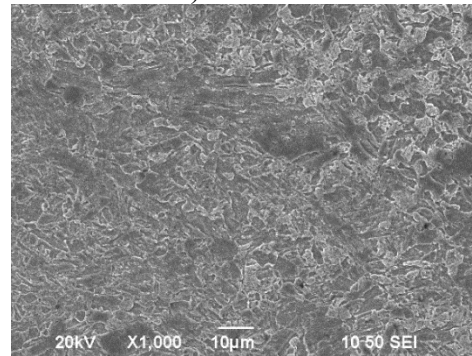
d) SCHAZ
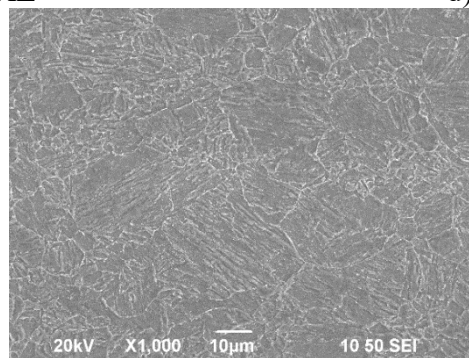
e) Base metal

Figure 3.33 SEM images of S690 QT 50 mm thick welded sections: q=5.0 kJ/mm

q = 2.4 kJ/mm			
a) CGHAZ	b) FGHAZ	c) ICHAZ	d) SCHAZ
q = 3.5 kJ/mm			
a) CGHAZ	b) FGHAZ	c) ICHAZ	d) SCHAZ
q = 5.0 kJ/mm			
a) CGHAZ	b) FGHAZ	c) ICHAZ	d) SCHAZ
Base metal			
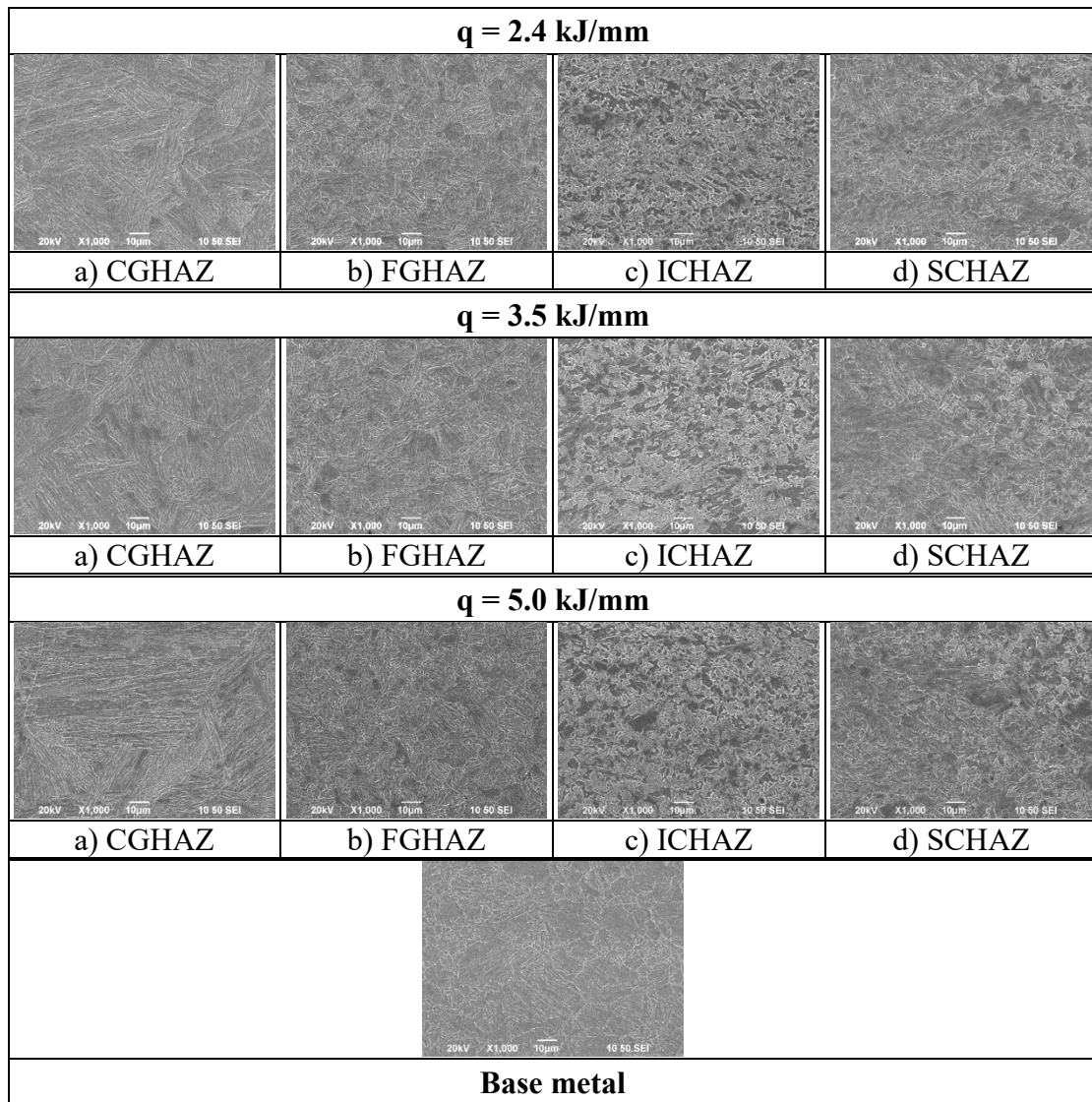
Figure 3.34 Comparison of SEM images between various heat input energies

3.6.3.2 Q620 TM 28mm welded sections

It should be noted that:

a) Figures 3.33 a) and b) show that the microstructures of the CGHAZ and the FGHAZ are mainly bainite with a small amount of ferrite and martensite. The grain sizes of the CGHAZ are much larger than those of the FGHAZ because the peak temperature in this region is extremely high, and close to the melting point of steel, resulting in an obvious coarsening of austenite grains.

b) For the microstructure of the ICHAZ, Figure 3.33 c) shows that more ferrite was formed during the welding process. The microstructure of the SCHAZ obtained by SEM is shown in Figure 3.33 d). Some cementite can be observed in this zone, which means that heating to temperatures around the critical point Ac1 promotes cementite nucleation and coagulation.

c) Typical microstructure of S620 TMCP steels mainly consists of bainite and ferrite as demonstrated in Figure 3.33 e).
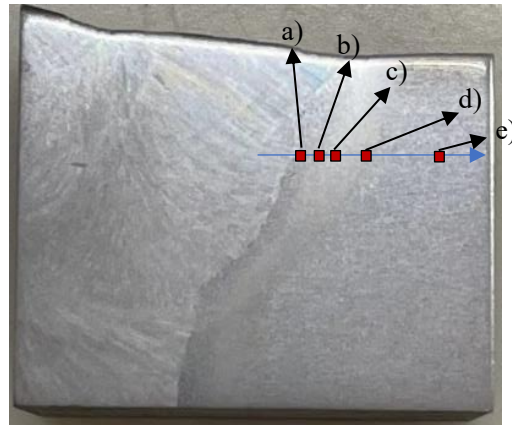
q = 2.5 kJ/mm
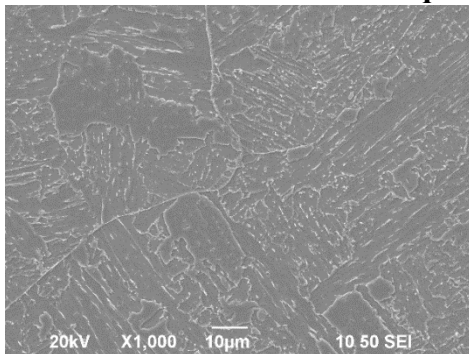
a) CGHAZ
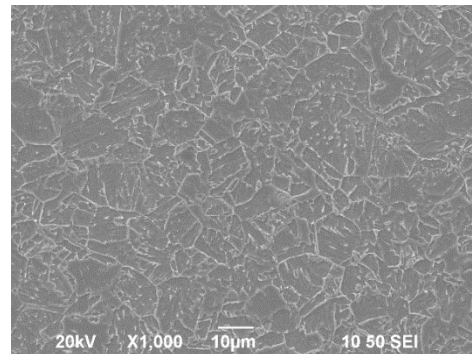
b) FGHAZ
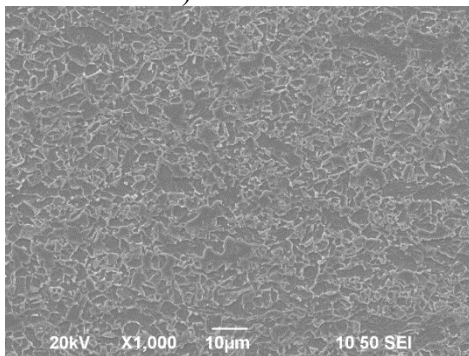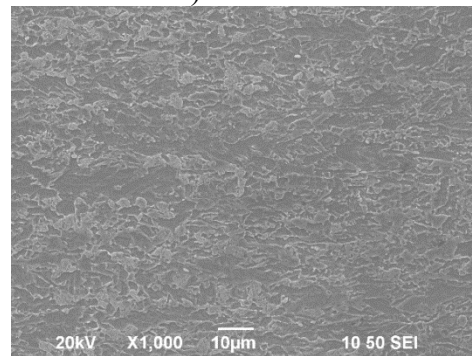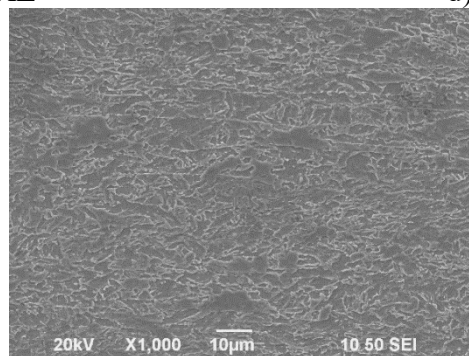
c) ICHAZ

d) SCHAZ

e) Base metal

Figure 3.35 SEM images of Q620 TM 28 mm thick welded sections: q=2.5 kJ/mm
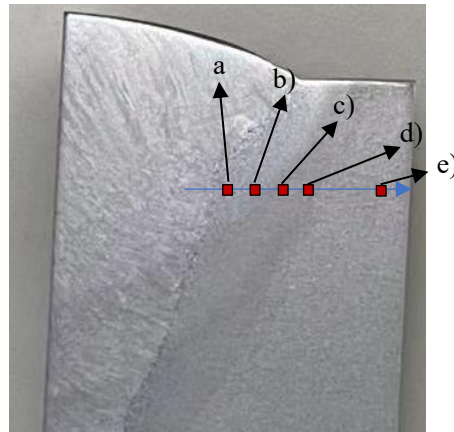
q = 3.5 kJ/mm
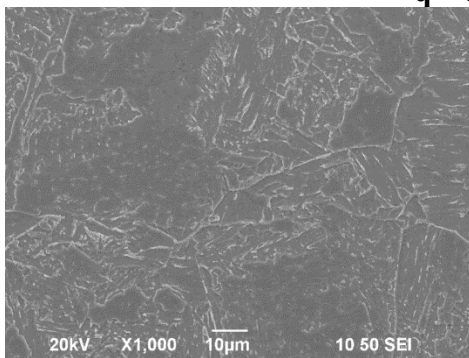
a) CGHAZ
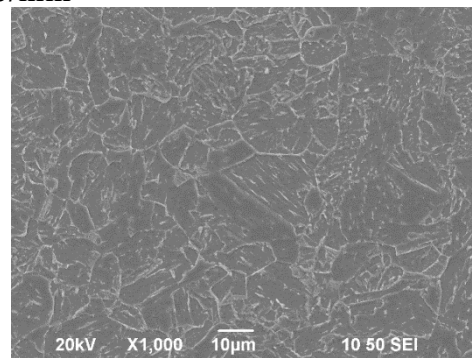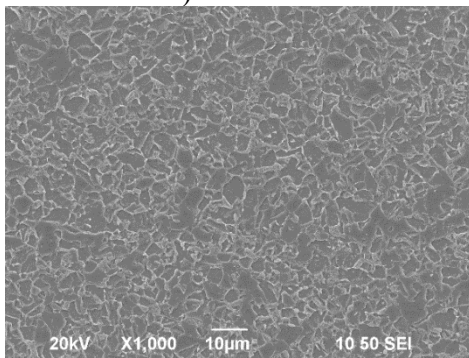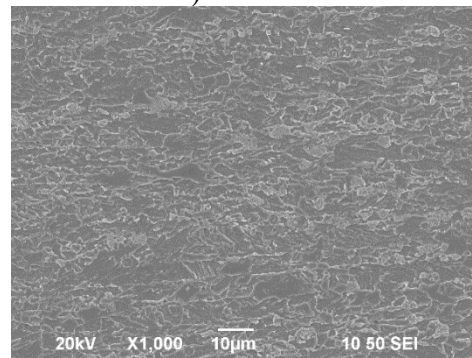
b) FGHAZ
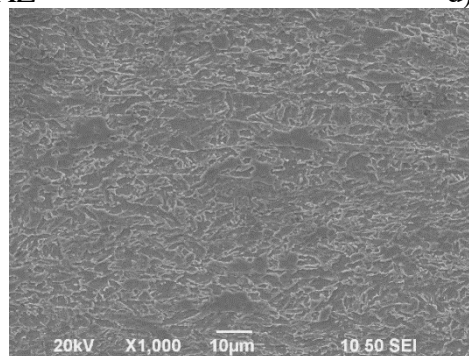
c) ICHAZ

d) SCHAZ

e) Base metal

Figure 3.36 SEM images of Q620 TM 28 mm thick welded sections: q=3.5 kJ/mm
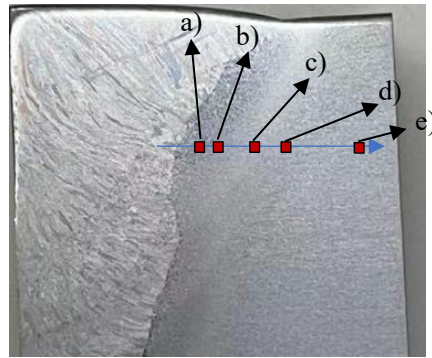
q = 4.5 kJ/mm
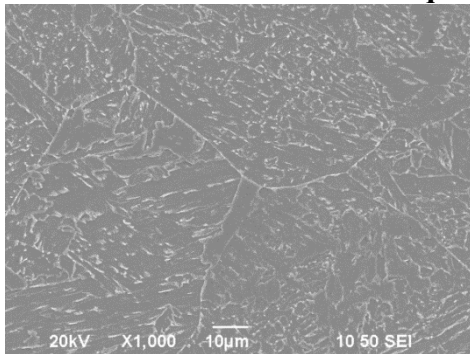
a) CGHAZ
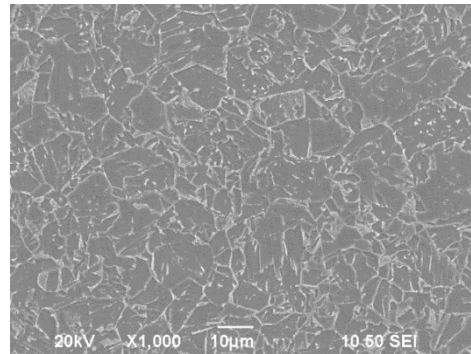
b) FGHAZ
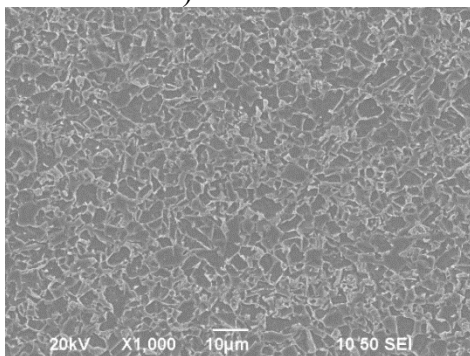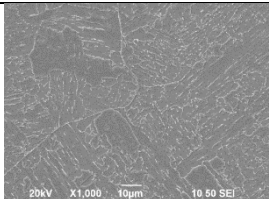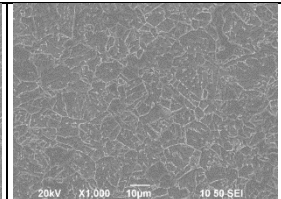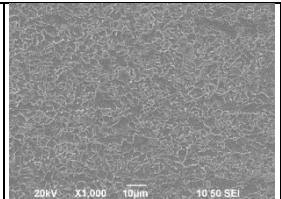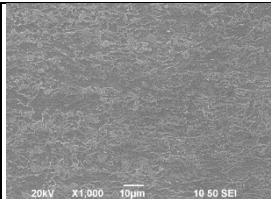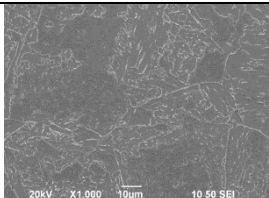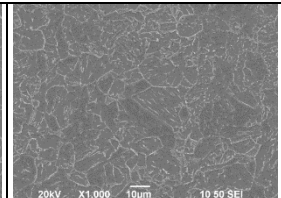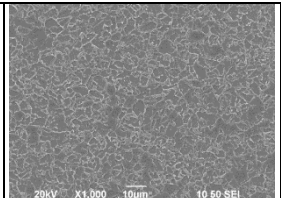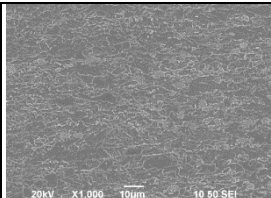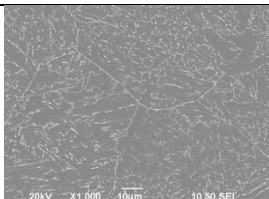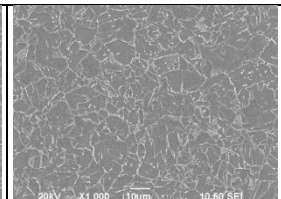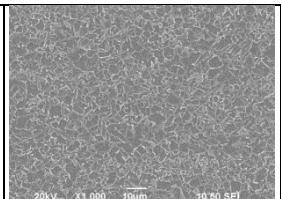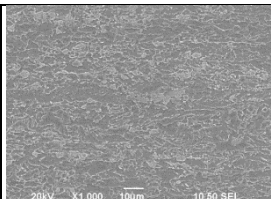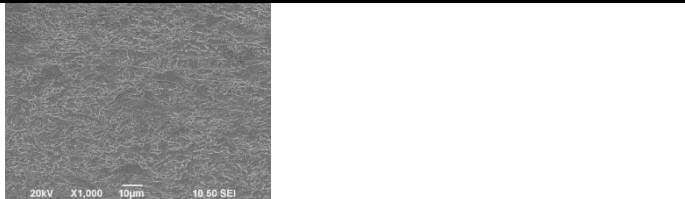
c) ICHAZ
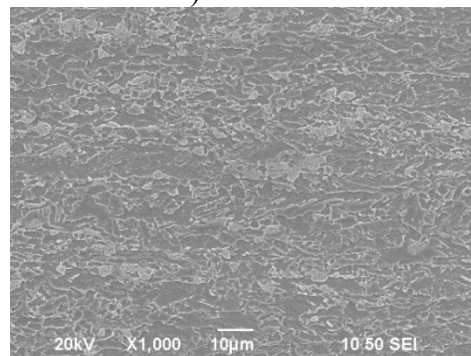
d) SCHAZ
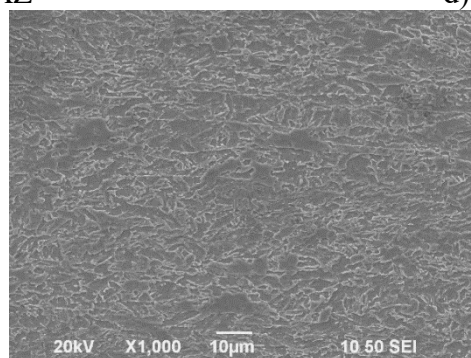
e) Base metal

Figure 3.37 SEM images of Q620 TM 28 mm thick welded sections: q=4.5 kJ/mm

q = 2.5 kJ/mm			
a) CGHAZ	b) FGHAZ	c) ICHAZ	d) SCHAZ
q = 3.5 kJ/mm			
a) CGHAZ	b) FGHAZ	c) ICHAZ	d) SCHAZ
q = 4.5 kJ/mm			
a) CGHAZ	b) FGHAZ	c) ICHAZ	d) SCHAZ
Base metal			

3.7 Conclusions

In this chapter, a total of 56 monotonic tensile tests on standard coupons from both the S690 QT and the Q620 TM base plates and their welded sections were conducted to investigate the welding effects onto the mechanical properties of these steels. Detailed examinations on the deformation characteristic of these coupons were reported. SEM was used to illustrate the changes of microstructures within the HAZ.

1. There is no difference in the mechanical properties at those coupons extracted from different locations within the thickness of the S690 QT 50mm steel plates. However, for those of the 70mm steel plates, reductions in both the yield and the tensile strengths of those coupons extracted from the middle layers at 7.1% and 6.6% respectively were found, when compared with those results of the top and the bottom layers. This demonstrates that the modern metallurgical technology is able to produce high strength steel thick plates up to 50 mm thick with homogenous strength.

2. There are only small reductions in the yield and the tensile strengths of the S690 QT steel welded sections when compared with their base plates. For the Q620 TM steel welded sections, the reductions are significant. However, the measured tensile strengths of both QT and TM welded sections with various heat input energies in this study satisfy the strength requirements stipulated in EN ISO 15614-1 and GB 50661, respectively.

3. The range of heat input energy varies from 2.4 to 5.0 kJ/mm in this study, and it is considered to cover the heat input energy commonly used in practice with a single wire SAW process. Hence, it is considered that application of these parameters for welding these S690 QT and Q620 TM thick sections with existing welding technology is highly acceptable.

4. Compared with the S690 QT 16mm thick welded sections tested by LIU (2018), the mechanical properties of both the S690 QT and the Q620 TM welded sections reported here do not vary significantly with a wide range of heat input energy during welding. With the increase in the plate thickness, the reduction factors of these welded sections on both the yield and the tensile strengths become larger, and this means that the effect of welding onto their mechanical properties becomes less significant. This is readily explained that with the increase of the plate thickness, the cooling rate of the welded sections after welding becomes faster, and recrystallization of the microstructures can only take plate in a short time. More detailed information may be found in Chapter 6.

5. As shown in the DIC results, the strain distributions of these welded sections under tension are quite different from those of the base plates as there are various zones with different mechanical properties within the welded sections in the vicinity of the heat-affected zones in a welded section.

It should be noted that:

a) For the QT welded sections, the CGHAZ with large grain sizes martensite has a higher strength than the other part so their longitudinal strains under tension in this region is the lowest, while the strength of SCHAZ with cementite particles inside the grains are reduced compared with those of the base plates.

b) For the TMCP welded sections, the CGHAZ and the FGHAZ with small amounts of martensite may not be strengthened, when compared with the base plates, and the longitudinal strain fields also indicated that there is not obvious strengthened region. A softened region of ICHAZ, which consists of more ferrite, were detected successfully.

Chapter 4. Experimental and numerical investigation of residual stresses of S690 QT 50 mm thick welded sections

4.1 Introduction

This chapter presents a systematic experimental and numerical investigation into the residual stresses of the S690 QT 50 mm thick butt-welded sections, and the following tasks are carried out:

a) Temperature measurement of the welded sections during welding

The welding parameters, such as current, voltage and welding speed of the SAW process, were measured carefully, while thermocouples were set used for the measurement of temperature history during the welding.

b) Residual stress measurement of the welded sections after welding

The hole-drilling method according to GB/T 31310 was adopted to measure the surface residual stresses of the welded sections. As the residual stresses inside the steel plates could not be measured directly, a local material removal method was adopted to remove the top layer, and then, the bottom layer of the welded sections. Then, the hole-drilling method was applied on the newly formed surfaces. It should be noted that as there was stress release after material removal, the measured residual stresses on each of the newly formed surfaces did not represent the actual stress state of the welded sections before the material removal. Thus, finite element technique was employed to simulate these processes, and to determine the initial residual stresses throughout the thicknesses of these welded sections.

c) Numerical simulation on welding

Sequentially coupled thermomechanical analysis was used in this study as it allows for a calibration process on the temperatures measured during welding. Heat transfer analysis was first carried out and calibrated with the measured temperature distribution

history. Both the film and the radiation coefficients were adjusted until the predicted temperature data were compared well with the measured ones. In the mechanical analysis, the local material removal processes were simulated and their effects on the initial residual stresses were predicted for comparison with the measured ones.

d) Comparison between measured and predicted results

The simulated residual stresses within the welded sections after material removal were compared with the measured ones. These two sets of data agree well with each other, then the simulated residual stresses before material removal were considered to be accurately predicted. With this series of experiments and simulations, the residual stresses within the thicknesses of the welded sections were then readily determined.

Two heat input energy, 2.4 and 5.0 kJ/mm, adopted during the submerged arc welding (SAW) were selected, and these values were considered to cover a wide range of heat input energy in practical welding.

Stress has 6 components and each of them acts in a different direction and on a different plane. Considering that usually, it is the longitudinal residual stresses that dominate the structural performance in a welded section, and also, only the longitudinal residual stress pattern is given design standards. Hence, the experimental and numerical investigations in this chapter focus on the residual stress in the longitudinal direction.

4.2 Temperature measurement

4.2.1 Measurement program

In this experimental investigation, a total of two butt-welded sections were welded, and the measurement program with dimensions of the welded sections is shown in Table 4.1. It should be noted that the plates for welding were cut by a flame torch though flame cutting may induce significant residual stress in the steel plates. Then the plates were further divided into two parts by wire cutting, as shown in Figure 4.1. This process was generally considered not to induce any significant residual stresses. Then, beveling was carried out onto the newly formed edges. The joint details of the S690 QT 50 mm thick plates are illustrated in Figure 4.2.

Table 4.1 Measurement program

Designation	Thickness (mm)	Length L (mm)	Width W (mm)	Welding method	Heat input energy (kJ/mm)
RS50-24	50	1000	500	GMAW for root SAW for the rest	2.4
RS50-50					5.0

a) Wire cut along the centerline   b) Beveling for weld groove
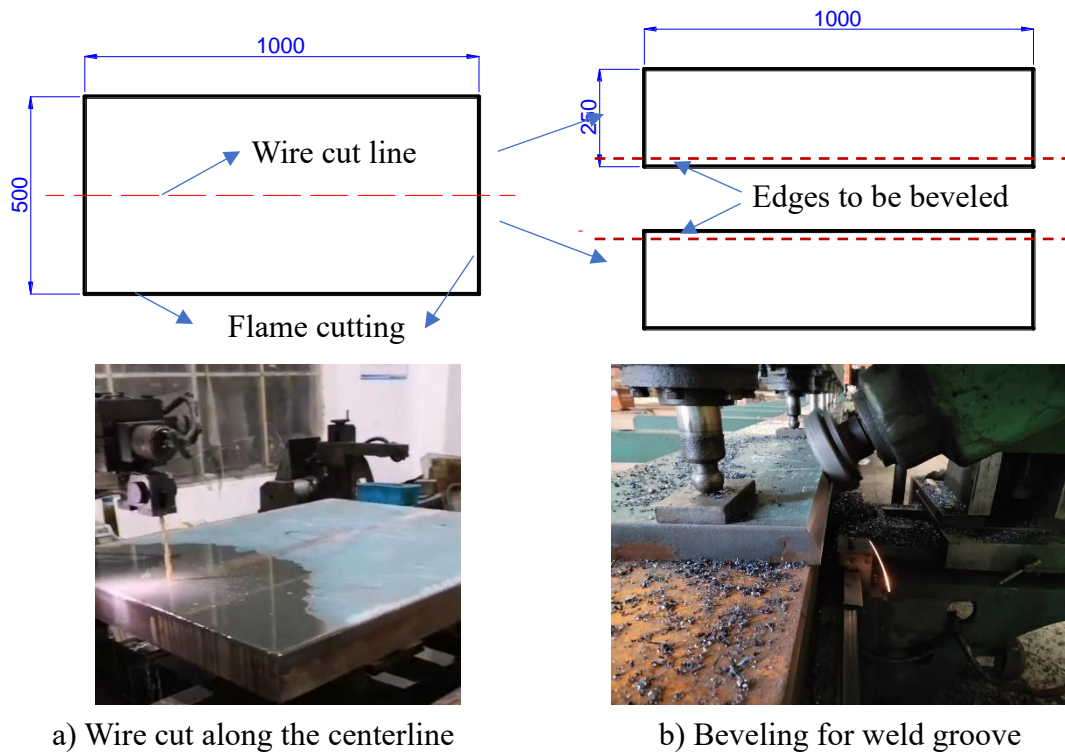
Figure 4.1 Edge preparation

a) Dimensions of the plates

Section A-A

b) Joint details
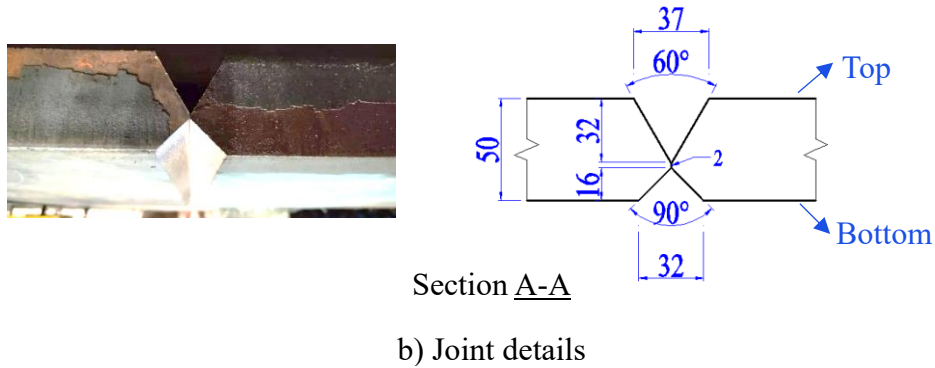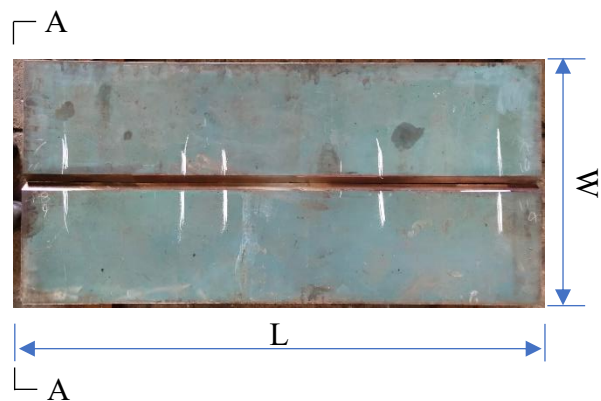
Figure 4.2 Butt-welded sections with an X-shaped groove

Various steps of the welding process are illustrated in Figure 4.3:

a) Run-on plates were first fixed at both ends to allow a fully developed arc at the beginning as well as the end of the welding process. Tick welds were provided at the back side groove to connect these two plates tightly.

b) Preheating was carried out with two heating panels, and the temperatures of the steel plates were measured by a hand-held infrared temperature probe. The minimum preheat temperature was 120 °C for these S690 QT 50 mm thick sections.

c) Thermocouples for temperature measurements were spot welded onto specific locations adjacent to the groove. These temperatures were recorded continuously with a data logger.

d) Manual welding was carried for the first pass, and the heat input energy of the manual welding was kept to vary within a small range only by an experienced welder.

e) Then, the SAW process was used for the other passes with specific heat input energy shown in Table 4.1.

f) After welding of the top side, the welded section was turned over, and carbon arc gouging was applied to remove the edge and the incomplete welding penetration.

g) Again, the SAW process was used to complete the welding of the joint, and post-weld heat treatment (PWHT) was conducted subsequently.

Turn over

a) Welding of run-on plate

b) Pre-heating with heating blankets

c) Thermocouples were spot welded

Turn over

d) Manual welding for the 1st pass
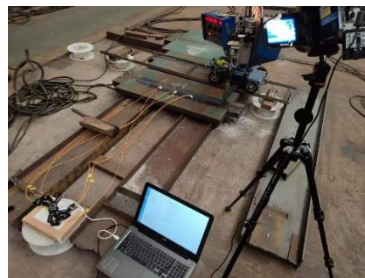
e) SAW for the rest
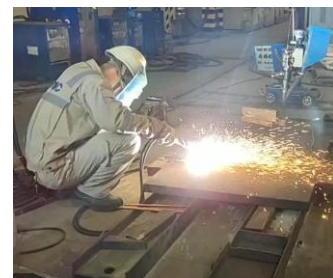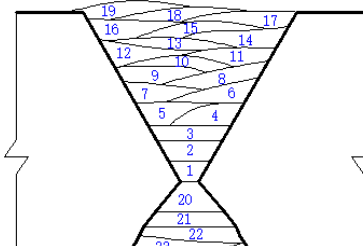
f) Carbon arc gouging

Figure 4.3 Typical welding process of the 50 mm thick butt welded sections

The voltage and the current of the SAW process were determined after several trial runs. This combination of the current and the voltage at 620A and 32V, respectively, is considered to be suitable for a wide range of heat input energy, i.e. from 2.0 kJ/mm to 5.0 kJ/mm. The recorded welding parameters during the welding of these two sections are summarized in Tables 4.2 and 4.3.

Table 4.2 Welding parameters of Section RS50-24

Top surface, ambient temperature: 7 ℃						Bottom surface, ambient temperature: 13 ℃					
Pass	Weld method	Voltage (V)	Current (A)	Weld speed (mm/s)	Heat input energy (kJ/mm)	Pass	Weld method	Voltage (V)	Current (A)	Weld speed (mm/s)	Heat input energy (kJ/mm)
1	Manual	27-32	144-146	1.89	1.81	1		31.8-32.3	550-555	5.7	2.95
2		31.7-32.3	554-559	6.40	2.6	2		31.5-32.0	647-651	7.9	2.40
3		31.7-32.2	614-618	7.86	2.40	3		---	---		
4		---	---			4		31.5-32.2	620-625		
5		31.7-32.3	617-621			5		---	---		
6		---	---			6		31.6-32.2	622-627		
7		---	---			7	SAW	---	---		
8		31.6-32.2	619-623			8		31.8-32.5	621-625		
9		---	---			9		---	---		
10	SAW	31.8-32.4	619-623			10		31.9-32.6	623-628		
11		---	---			11		---	---		
12		31.7-32.2	617-622			12		31.8-32.5	619-623		
13		---	---			13		---	---		
14		31.7-32.3	617-622								
15		---	---								
16		31.9-32.4	619-622								
17		---	---								
18		31.8-32.5	618-624								
19		---	---								

Welding pass schedule of RS50-24

Table 4.3 Welding parameters of Section RS50-50

Top surface, ambient temperature: 7 ℃						Bottom surface, ambient temperature: 7 ℃					
Pass	Weld method	Voltage (V)	Current (A)	Weld speed (mm/s)	Heat input energy (kJ/mm)	Pass	Weld method	Voltage (V)	Current (A)	Weld speed (mm/s)	Heat input energy (kJ/mm)
1	Manual	27-32	144-146	1.89	1.81	1		31.7-32.3	658-602	6.28	2.90
2	SAW	31.5-32.1	550-556	6.29	2.65	2	SAW	32.0-32.6	621-623	3.76	5.03
3		31.7-32.5	618-623	3.75	5.03	3		31.9-32.5	619-624		
4		31.9-32.6	619-623			4		---	---		
5		---	---			5		32.1-32.7	618-623		
6		31.9-32.5	618-623			6					
7		---	---								
8		32.0-32.6	620-624								
9		---	---								

Note: '---' means not recorded
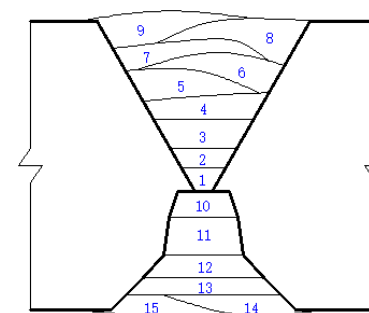
Welding pass schedule of RS50-50

4.2.2　Measurement set-up and instrumentation

A certified Type-K thermocouple, Model WI0100, was used in this study to measure the transient surface temperatures, and a portable welding machine, WU0200 Mini Thermocouple Welding Unit, was employed to spot weld thermocouples directly onto the surfaces of the steel plates. In addition, a mud material, ETL HT Putty, was used to cover the exposed surfaces of the thermocouples in order to provide a stable working environment. It should be noted that during the welding, six isolated thermal data ports (Phidgets TMP1100), a hub (Phidgets HUB0000_0) and a computer were used to acquire electrical signals going through the thermocouples, and these signals were converted into temperature values in the unit of Celsius degree. This isolated data logger system can provide steady and reliable measurement without interference. The equipment used in this test are shown in Figure 4.4.

a) Thermocouple wire

b) Spot welding unit

c) ETL HT Putty

d) Phidgets data logger

Figure 4.4 Equipment for temperature measurement

Figure 4.5 illustrates the thermocouple arrangement for temperature measurements during the welding process. For each welded section, a total of 6 thermocouples were

attached to the top surface of the steel plate adjacent to the welding groove. Two thermocouples (P1 & P2) were arranged at a distance of 10 mm and 20 mm apart from the edge of the groove, and two repeated series of thermocouples (P3 & P4, and P5 & P6) were attached along the groove at a spacing of 200 mm.
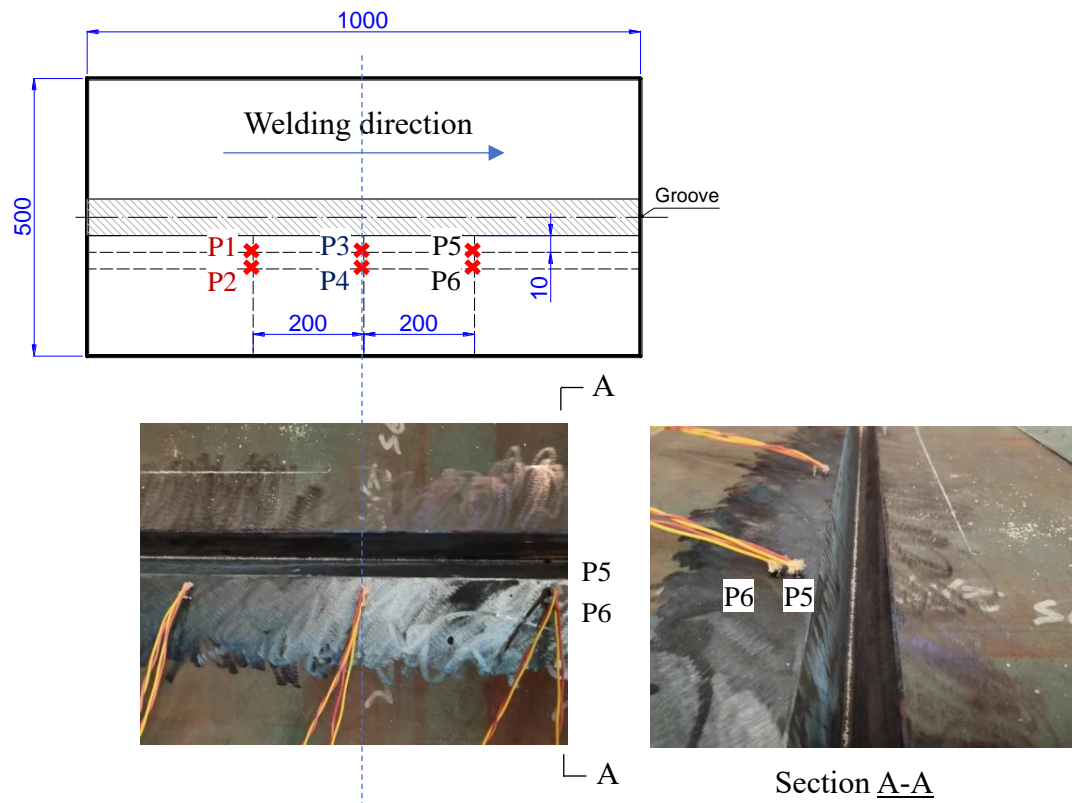
Figure 4.5 Arrangement of thermocouples along the groove of the welded section

Thermocouple P6 after weld pass 13 in Section RS50-24, and both Thermocouples P5 and P6 after weld pass 4 in Section RS50-54 were replaced for measurement of $t_{8/5}$ with another Type-K thermocouple, Model XC4-K-24 with a maximum working temperature at 1200 °C. Unfortunately, these measurements failed as the surface of the weld metal was covered with solidified slag after welding, and thermocouple XC4-K-24 was also buried in this slag after welding of some passes.

4.2.3   Temperature measurement results

The measured transient temperature history of six thermocouples, namely P1 to P6, of two welded sections are shown in Figure 4.6. It should be noted that the first pass was carried out with manual welding, and there were several pauses due to running out of electrodes. So, the measured temperatures of weld pass 1 were not considered in the further analysis. Typical temperature histories of Sections RS50-24 and RS50-50 at the top surfaces are shown in Figure 4.7 for clarity.

The maximum temperatures captured by each thermocouple during each weld pass are summarized in Tables 4.4 and 4.5. It is found that the measured temperatures at the same longitudinal lines are close to each other during the same weld pass. It should be noted that as pre-heating was carried out before the thermocouples were attached, so the temperatures at the starting point were found to be about 150 °C.
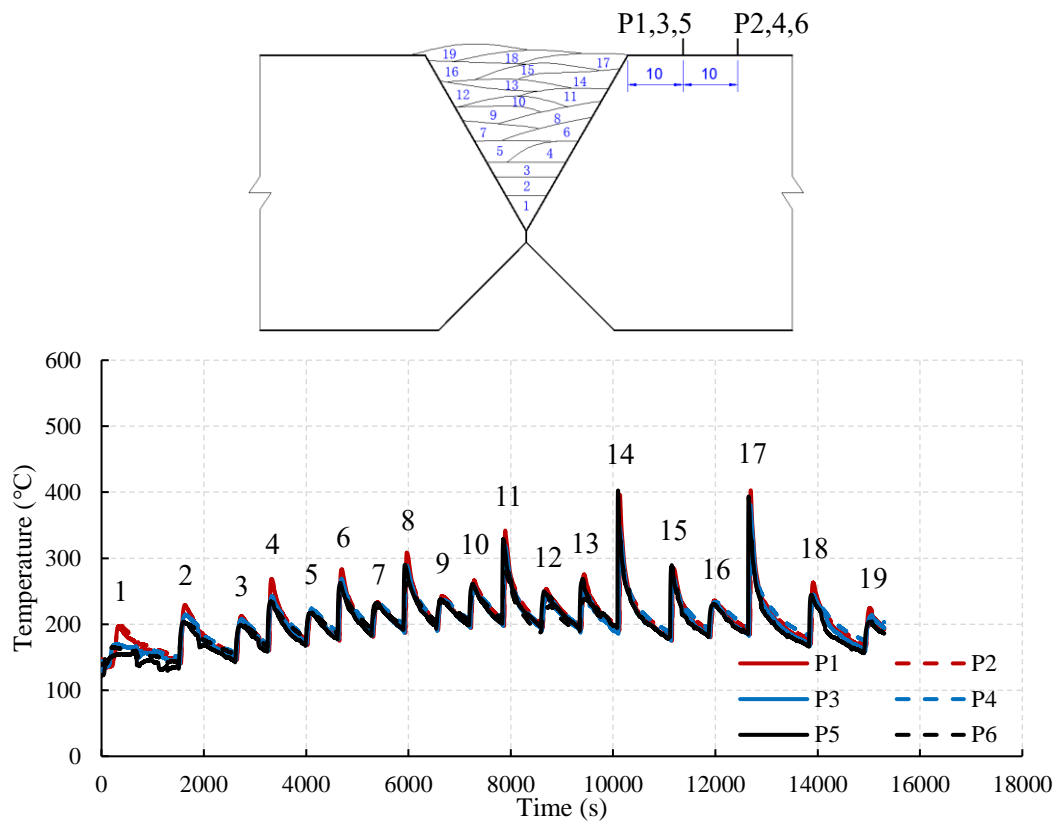
a) Section RS50-24
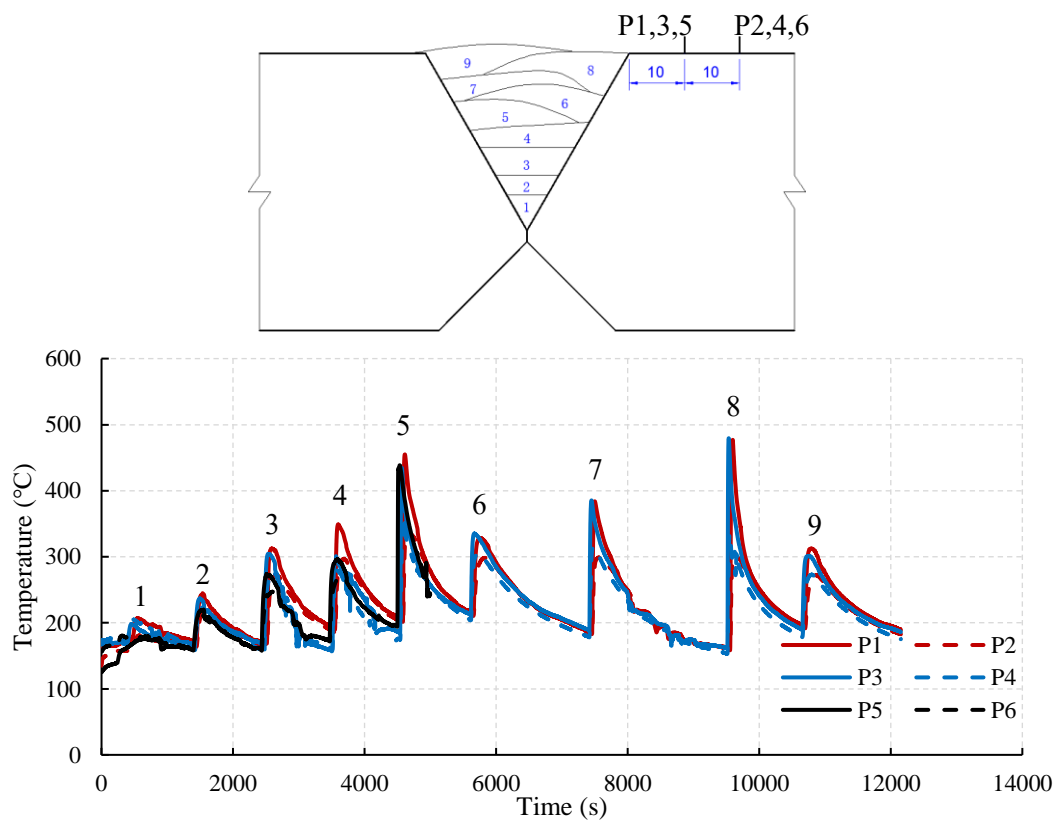
b) Section RS50-50

Figure 4.6 Measured transient temperature histories at the top surfaces

Table 4.4 Measured maximum temperatures (°C) of each pass of Section RS50-24

Pass	Thermocouple					
	P1	P3	P5	P2	P4	P6
1	-	-	-	-	-	-
2	229	214	203	225	213	201
3	212	208	198	209	204	198
4	268	242	234	254	232	226
5	221	224	217	220	222	217
6	283	269	262	268	253	248
7	233	249	231	231	230	224
8	308	288	288	284	269	261
9	241	237	237	242	236	233
10	266	257	261	258	251	247
11	342	318	328	302	287	280
12	253	243	248	244	240	228
13	275	251	268	253	245	237
14	396	347	402	306	287	-
15	284	270	290	261	252	-
16	235	233	231	232	233	-
17	403	380	393	302	294	-
18	263	244	244	241	236	-
19	224	210	205	211	213	-

Table 4.5 Measured maximum temperatures (°C) of each pass of Section RS50-50

Pass	Thermocouple					
	P1	P3	P5	P2	P4	P6
1	-	-	-	-	-	-
2	245	234	220	217	213	211
3	312	303	273	271	264	247
4	349	300	296	296	270	270
5	453	433	439	339	343	-
6	327	335	-	298	293	-
7	381	385	-	299	304	-
8	476	478	-	299	324	-
9	312	301	-	271	263	-
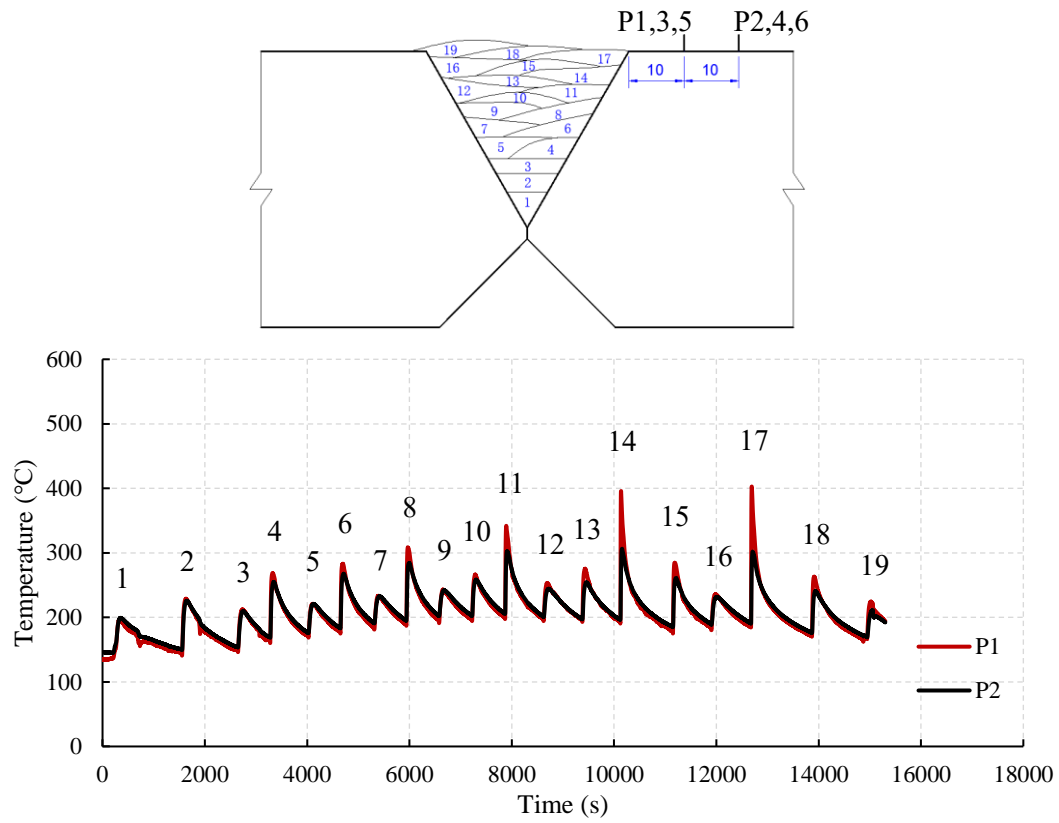
a) Section RS50-24
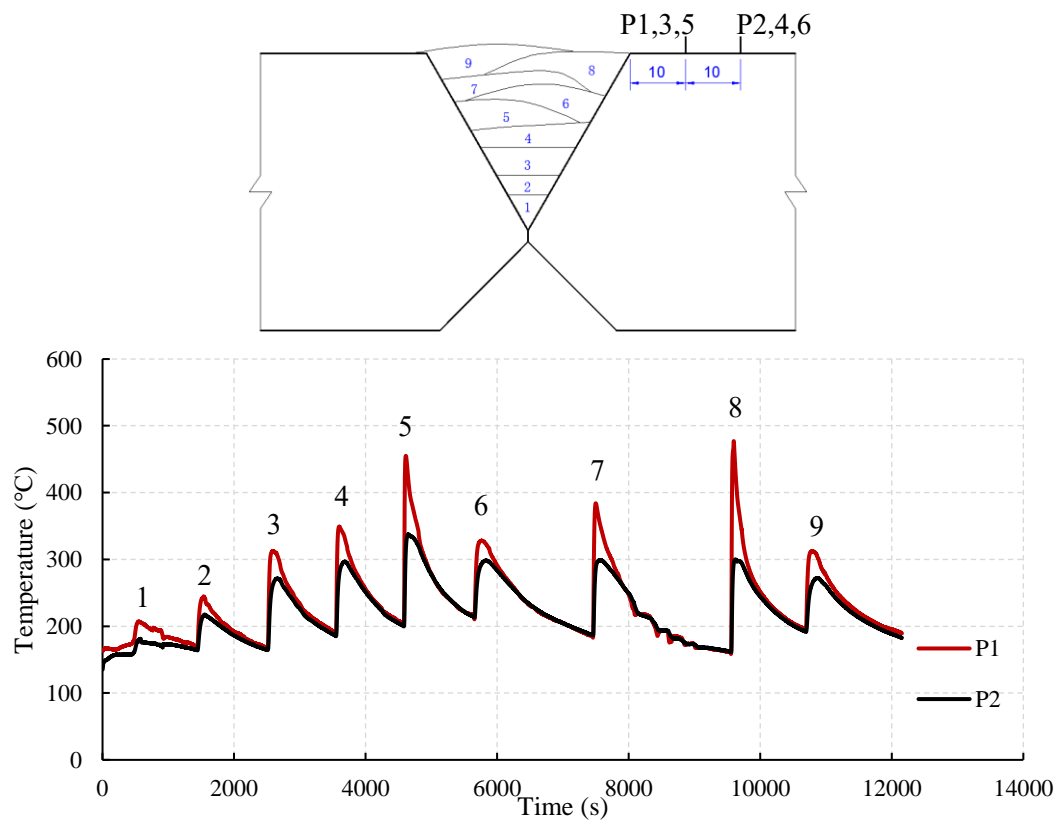
b) Section RS50-50

Figure 4.7 Typical measured temperature history

4.3 Residual stress measurement

4.3.1 Measurement program

In order to measure the welding induced residual stresses of these welded sections, the hole-drilling method was adopted, and strain rosettes were systematically attached onto the steel plates. The measurement program of the residual stresses is shown in Table 4.3. It should be noted that the welded sections were cut using a water jet, each with a length of 300 mm for easy handling.

Table 4.6 Measurement program of residual stresses

Section	Top			Bottom		
	Surface	Layer 1	Layer 2	Surface	Layer 1	Layer 2
RS50-24	11	6	6	11	6	6
RS50-50	11	6	6	11	6	6

The rosette arrangement on the top and the bottom surfaces is shown in Figure 4.8. The spacing between the rosettes in the transverse direction was 10 mm in the region adjacent to the edges of the fusion zone as the residual stresses were expected to be reduced dramatically within this region. As the distance increased, the spacing between the rosettes was increased accordingly to 25 mm. It should be noted that the width of the fusion zone at the top and the bottom surfaces was not the same, so the rosettes 1 to 10 on both surfaces were not aligned vertically in the thickness direction.

In order to evaluate the residual stresses caused by flame cutting, one strain rosette was provided at a small distance to the edges of the steel plates for measurement.

D = 18 mm for Section RS50-24
D = 23 mm for Section RS50-50
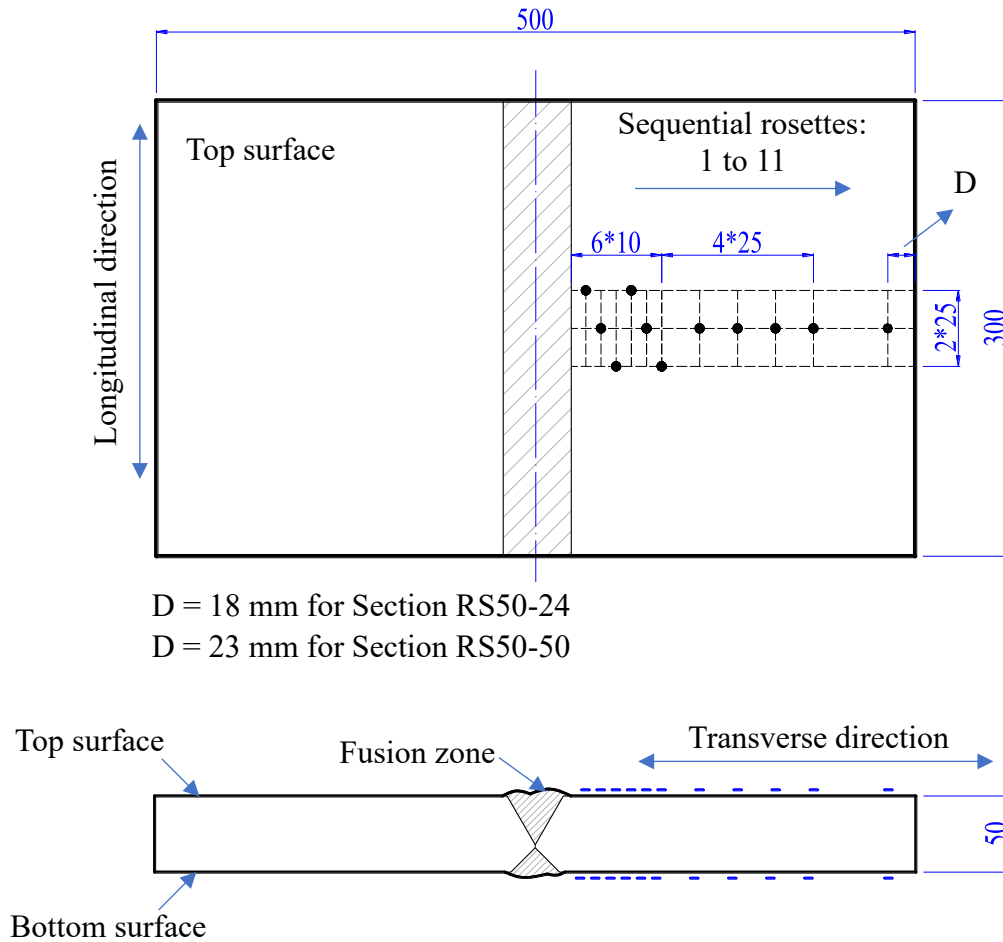
Figure 4.8 Rosette arrangement pattern on top and bottom surfaces

As shown in Figure 4.9, after the measurement of residual stresses on both the top and the bottom surfaces, a milling process was conducted carefully to remove the steel material from a local region with a thickness of 10 mm at both the top and the bottom surfaces of the steel plates, and strain rosettes were provided onto the newly formed surfaces. The residual stresses on the newly formed surfaces of the welded sections were subsequently measured.
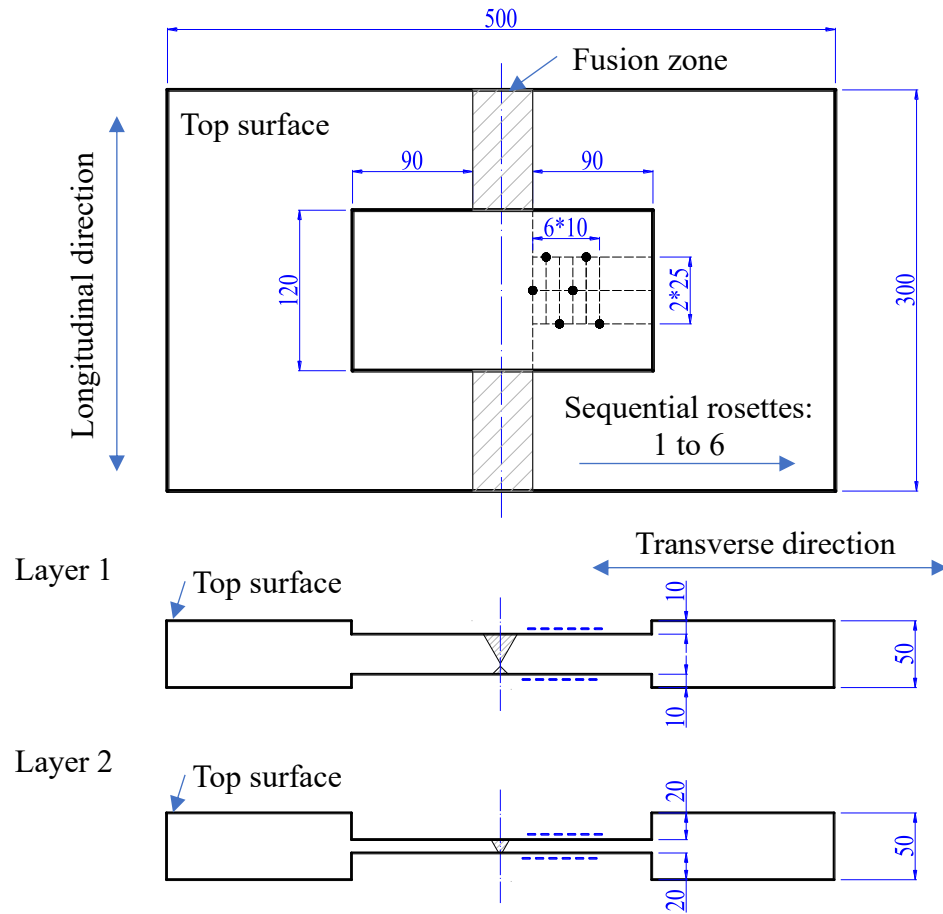
Figure 4.9 Rosette arrangement pattern after milling

To demonstrate the arrangement of strain rosettes of the whole section, the cross sectional distribution of rosettes of two sections are illustrated in Figure 4.10.

a) Section RS50-24

b) Section RS50-50
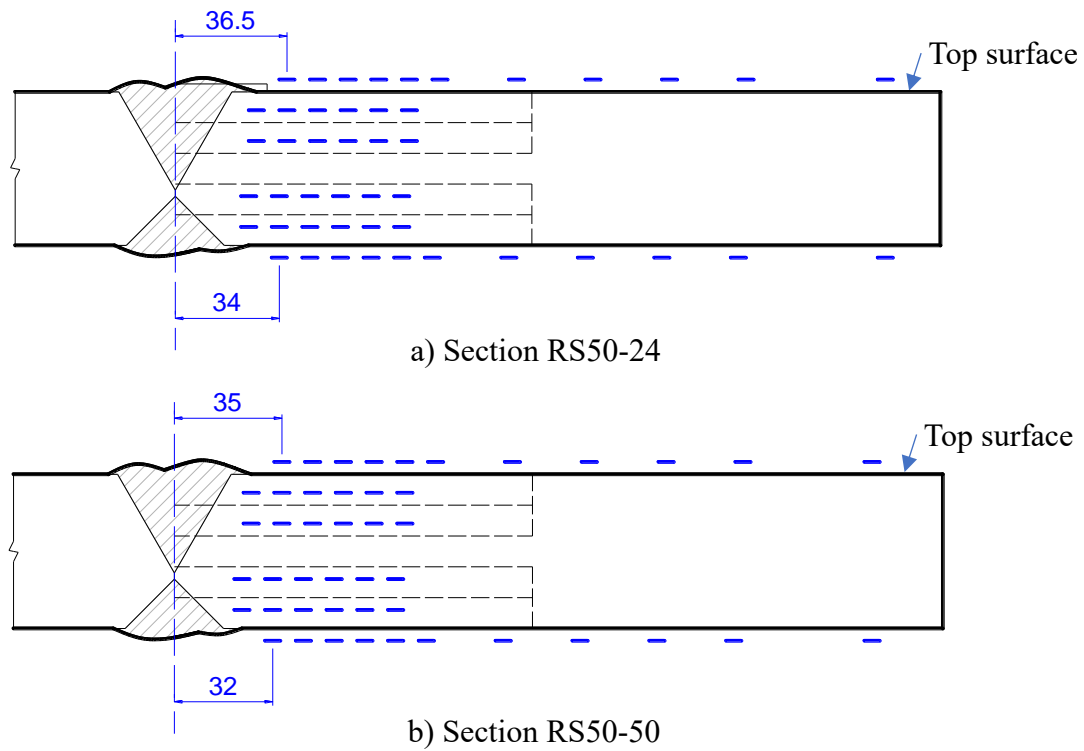
Figure 4.10 Cross sectional distribution of rosettes

It should be noted that the residual stresses of the fusion zone cannot be measured with the hole-drilling method as the calibrated coefficients of the fusion zone cannot be obtained with sufficient accuracy. Although a specimen with specified dimensions should be used for the calibration process according to Appendix A in GB/T 31310, the volume of the fusion zone is too small to be machined into a test specimen. Hence, no rosette was provided onto the fusion zone in this measurement.

4.3.2 Measurement set-up and instrumentation

The set-up of the residual stress measurement is shown in Figure 4.11. A JHZK hole-drilling machine and Type-A strain rosettes, according to GB/T 31310, were employed. The JHZK hole-drilling machine was carefully maneuvered so that the line of drilling was aligned with the center of the target rosette with the help of a magnifying lens. Then, an electric-driven drilling unit was properly installed for the drilling process. It should be noted that during the drilling process, a hole with a depth of 1.8 mm was

made in a continuous process. A rosette before and after the hole-drilling process is shown in Figure 4.12.
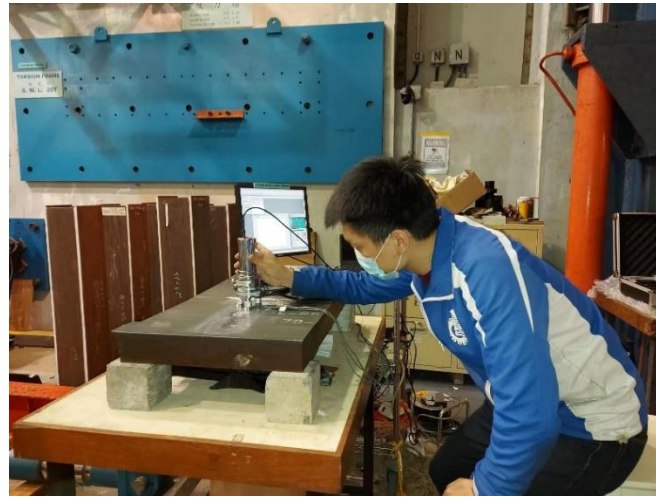
Figure 4.11 Set-up of hole-drilling process
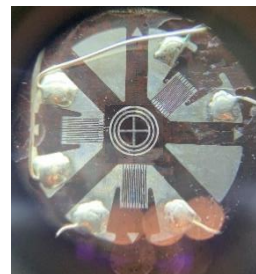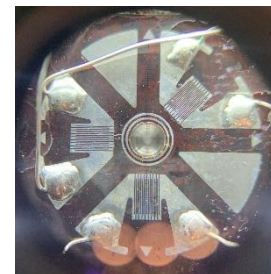
Before drilling   After drilling

Figure 4.12 A JHZK hole-drilling system

After the measurement on both the top and the bottom surfaces, a milling process was employed to remove local steel material, a large amount of coolant was provided during milling to reduce any heating effect onto the welded sections caused by the milling process, as shown in Figure 4.13 a). After the removal process, hole-drilling was carried out onto the newly formed surfaces, as shown in Figure 4.13 b). The whole process of

material removal and hole-drilling were performed twice so that both the residual stresses on Layer 1 and Layer 2 were measured.

a) Milling for material removal   b) Hole-drilling on the newly formed surface

Figure 4.13 Residual stress measurement after material removal

4.3.3 Measurement results

The residual stresses were calculated based on two calibrated coefficients, namely Coefficients A and B, together with the released strains recorded after hole-drilling. Both coefficients A and B of S690 QT 50 mm thick steel plates were calibrated according to Appendix A in GB/T 31310, and their values are given in Table 4.7. Figure 4.14 illustrates the order of rosettes on different layers, namely the top surface (T), the first and the second layers under the top surface (T-L1 and T-L2), the bottom surface (B), and the first and the second layers under the bottom surface (B-L1 and B-L2).

Table 4.7 Coefficients A and B of S690 QT 50 mm thick plates under different stress levels

Thickness (mm)	Stress level	A	B
50	0.1 to 0.6 σ_{yield}	-0.4445	-0.8246
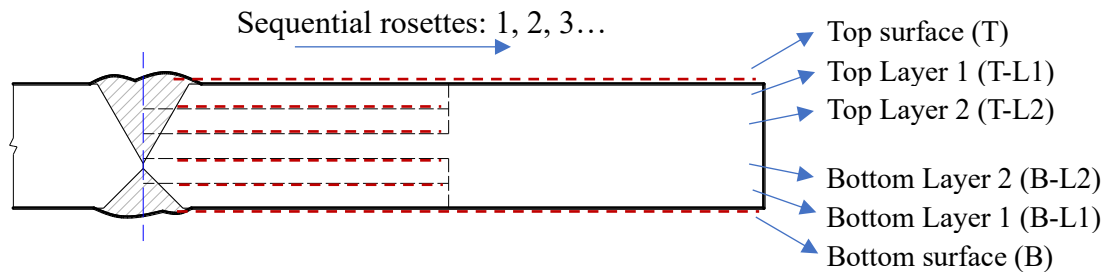
Figure 4.14 Rosette orders and different layers

The measured longitudinal residual stresses of both Surfaces T and B, and Layers T-L1 and B-L1 and T-L2 and B-L2 of Section RS50-24 are listed in Tables 4.8, 4.9 and 4.10, respectively, and the distributions of residual stresses onto various layers are plotted in Figures 4.15. The measured longitudinal residual stresses of both Surfaces T and B, and Layers T-L1 and B-L1 and T-L2 and B-L2 of Section RS50-50 are listed in Tables 4.11, 4.12 and 4.13, respectively, and the distributions of residual stresses are plotted in Figures 4.16. It is found that:

1) There are only small differences between measured residual stresses on the top and the bottom surfaces in each section.

2) The released residual stresses on Layers 1 and 2 in each figure are also very close to each other. This may indicate that the internal residual stresses on the top and the bottom surfaces before milling are also very close to each other.

It should be noted that the last data in each series of the Top and the Bottom surfaces gave the residual stresses of the free edge after flame-cutting, and hence, tensile residual stresses were measured.

For Layers 1 and 2, significant tensile stresses were found at Layers T-L1-1, B-L1-1, T-L2-1 and B-L2-1 of both welded sections, as these points were close to the fusion zones, while the compressive stresses were found to be within 100 N/mm^2 at the rest.

Table 4.8 Residual stresses on Top and Bottom surfaces of Section RS50-24

Rosette	Residual stress (N/mm^2)	Rosette	Residual stress (N/mm^2)
T-1	-148.1	B-1	-66.8
T-2	-187.6	B-2	-142.0
T-3	-183.0	B-3	-137.2
T-4	-247.1	B-4	-167.7
T-5	-151.9	B-5	-111.5
T-6	-156.1	B-6	-161.3
T-7	-180.6	B-7	-136.1
T-8	-76.3	B-8	-163.4
T-9	-124.2	B-9	-156.2
T-10	-188.6	B-10	-171.3
T-11	100.0	B-11	124.7

Table 4.9 Residual stresses on Top and Bottom Layers 1 of Section RS50-24

Rosette	Residual stress (N/mm^2)	Rosette	Residual stress (N/mm^2)
T-L1-1	385.4	B-L1-1	335.5
T-L1-2	-5.8	B-L1-2	-1.4
T-L1-3	-61.5	B-L1-3	-58.8
T-L1-4	-78.2	B-L1-4	-53.4
T-L1-5	-61.5	B-L1-5	-60.7
T-L1-6	-80.2	B-L1-6	-77.1

Table 4.10 Residual stresses on Top and Bottom Layers 2 of Section RS50-24

Rosette	Residual stress (N/mm^2)	Rosette	Residual stress (N/mm^2)
T-L2-1	100.3	B-L2-1	0.8
T-L2-2	-20.3	B-L2-2	-20.6
T-L2-3	-60.8	B-L2-3	-38.8
T-L2-4	-25.6	B-L2-4	-33.4
T-L2-5	-45.6	B-L2-5	-40.7
T-L2-6	-60.4	B-L2-6	-57.1

Table 4.11 Residual stresses onto Top and Bottom surfaces of Section RS50-50

Rosette	Residual stress (N/mm²)	Rosette	Residual stress (N/mm²)
T-1	-1.7	B-1	-72.2
T-2	-176.5	B-2	-114.7
T-3	-195.0	B-3	-95.7
T-4	-236.7	B-4	-141.4
T-5	-224.2	B-5	-137.5
T-6	-215.7	B-6	-179.9
T-7	-225.2	B-7	-142.5
T-8	-224.1	B-8	-194.6
T-9	-200.6	B-9	-160.9
T-10	-150.2	B-10	-170.2
T-11	80.2	B-11	150.5

Table 4.12 Residual stresses on Top and Bottom Layers 1 of Section RS50-50

Rosette	Residual stress (N/mm²)	Rosette	Residual stress (N/mm²)
T-L1-1	402.3	B-L1-1	327.2
T-L1-2	9.8	B-L1-2	-26.3
T-L1-3	-70.9	B-L1-3	-54.3
T-L1-4	-86.1	B-L1-4	-61.0
T-L1-5	-70.7	B-L1-5	-43.8
T-L1-6	-72.8	B-L1-6	-47.3

Table 4.13 Residual stresses on Top and Bottom Layers 2 of Section RS50-50

Rosette	Residual stress (N/mm²)	Rosette	Residual stress (N/mm²)
T-L2-1	100.9	B-L2-1	98.3
T-L2-2	-20	B-L2-2	-26.3
T-L2-3	-50.9	B-L2-3	-62.3
T-L2-4	-66.1	B-L2-4	-69.0
T-L2-5	-50.7	B-L2-5	-51.8
T-L2-6	-52.8	B-L2-6	-55.3
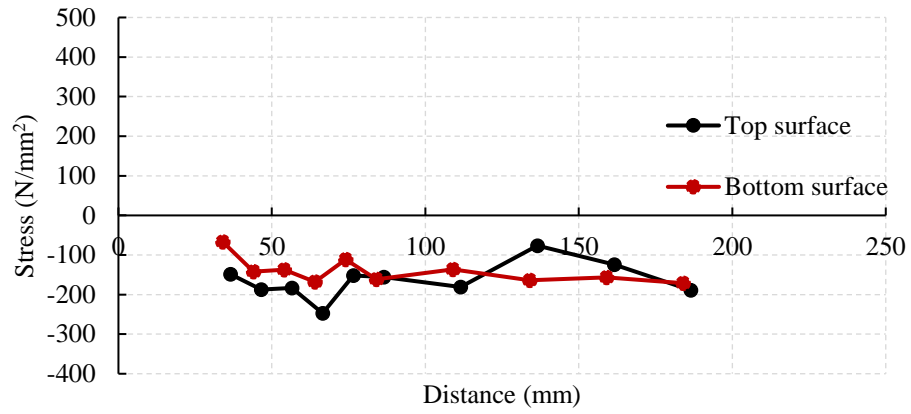
a) Top and bottom surfaces
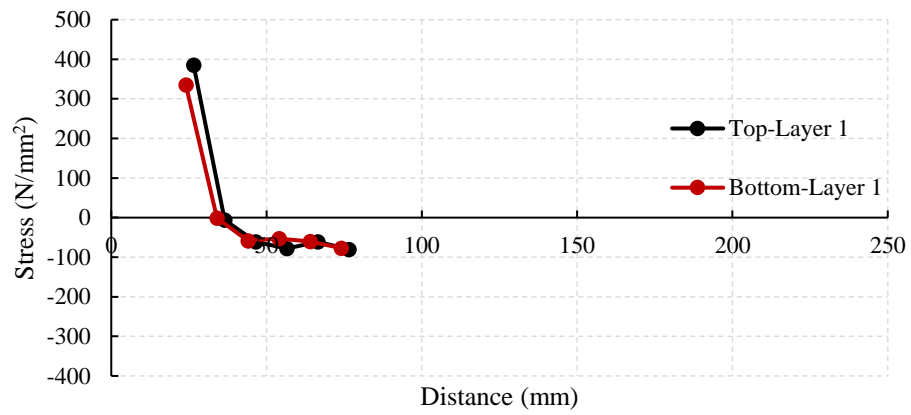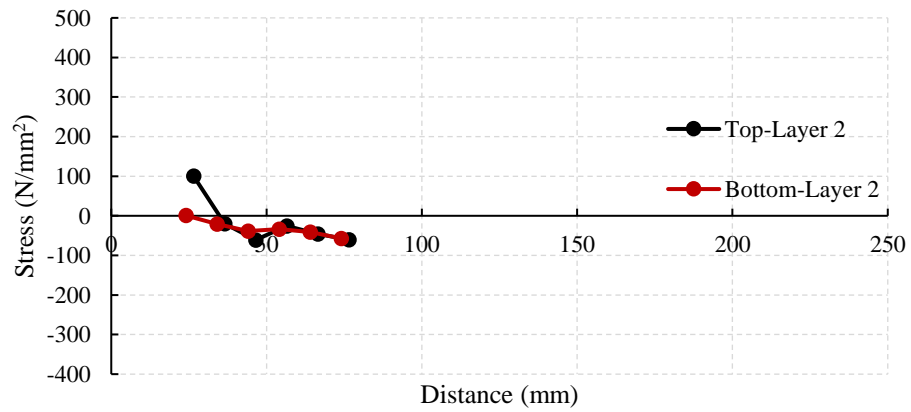
b) Layer 1

c) Layer 2

Figure 4.15 Residual stress distribution of Section RS50-24
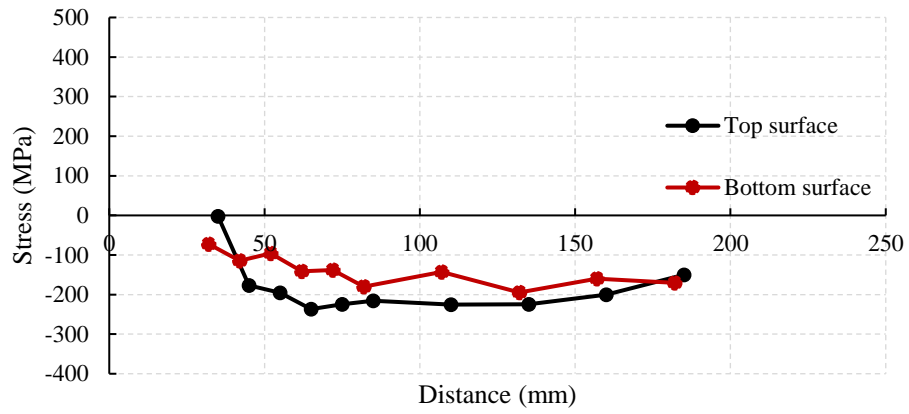
a) Top and bottom surfaces
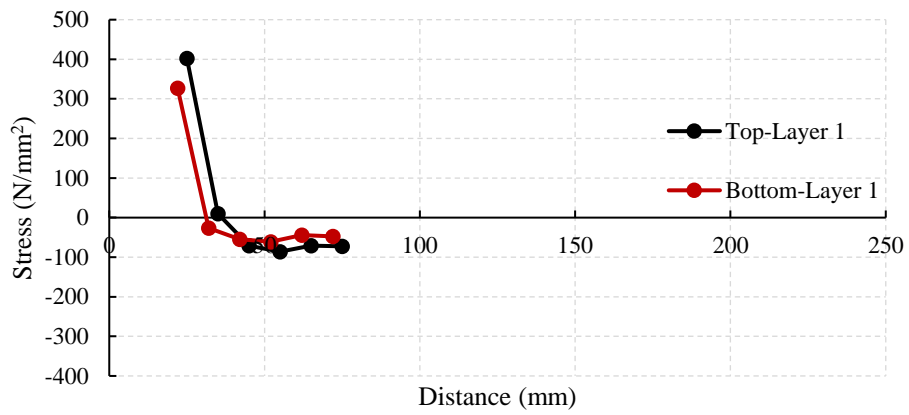
b) Layer 1
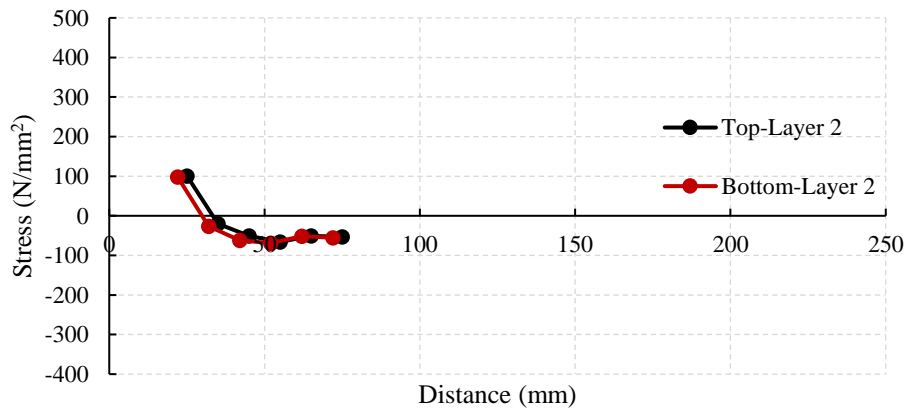
c) Layer 2

Figure 4.16 Residual stress distribution of Section RS50-50

4.4 Numerical simulation of residual stresses

The finite element models (FEM) of the welding process were established using ABAQUS. The measured results, i.e. temperature history and residual stresses, onto various layers described in Section 4.3 were used to calibrate the models in this section.

The sequentially coupled thermo-mechanical analysis was employed in these simulations. Firstly, the heat transfer model was carefully calibrated against the measured transient temperature history of each weld run. Then, the simulated temperature distribution history, together with the mechanical material properties and appropriate boundary conditions were provided into the mechanical analysis model to calculate the residual stresses. Figure 4.17 illustrates the flow chart of the 3D sequentially coupled thermo-mechanical analysis for the welded sections.
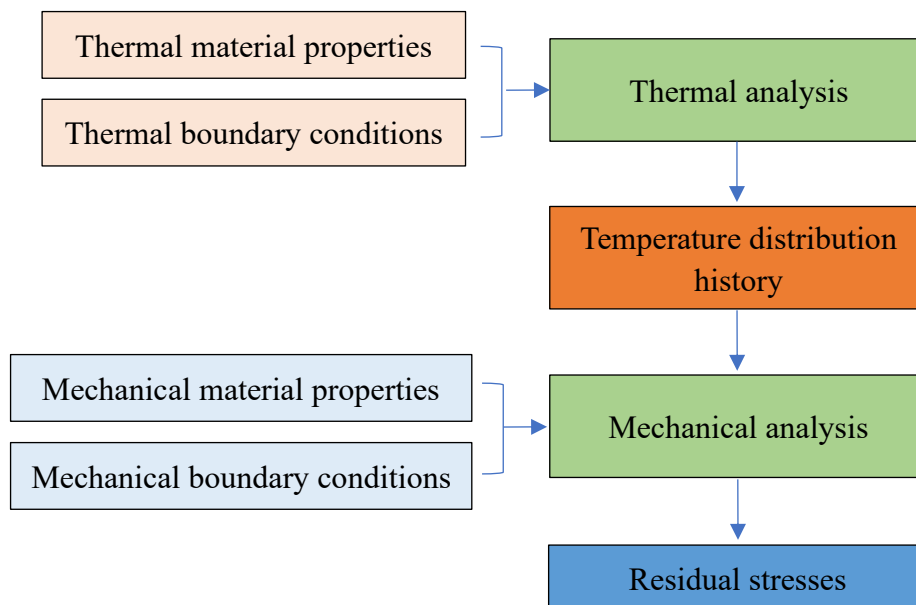
Figure 4.17 Flow chart of the sequentially coupled thermo-mechanical analysis

4.4.1 Modelling process

Figure 4.18 illustrates 3D models established for the modelling. Considering the plate thickness and the dimensions of the butt welded section, a graded meshing strategy is adopted. The weld bead and its adjacent areas are believed to suffer from large temperature gradients and significant residual stresses. Hence, a locally refined mesh is used in these areas. The cross-sectional views of the finite element models of the welded sections with heat input energy of 2.4 and 5.0 kJ/mm adopted during welding are shown in Figure 4.18 b) and c), respectively, and each weld pass is highlighted with a different color. The weld passes have been configured according to the measured sizes and their locations during the welding process.

a) Overall view

Top surface
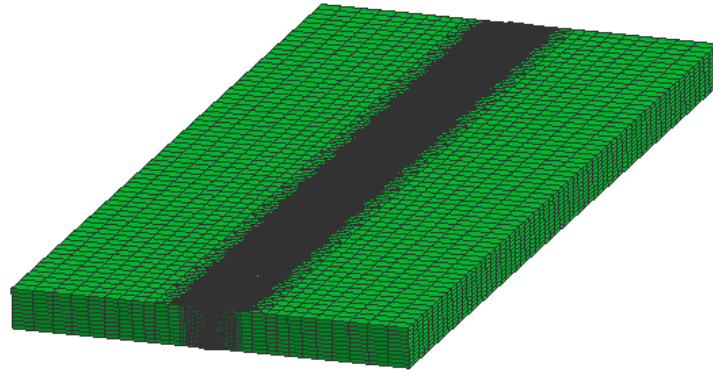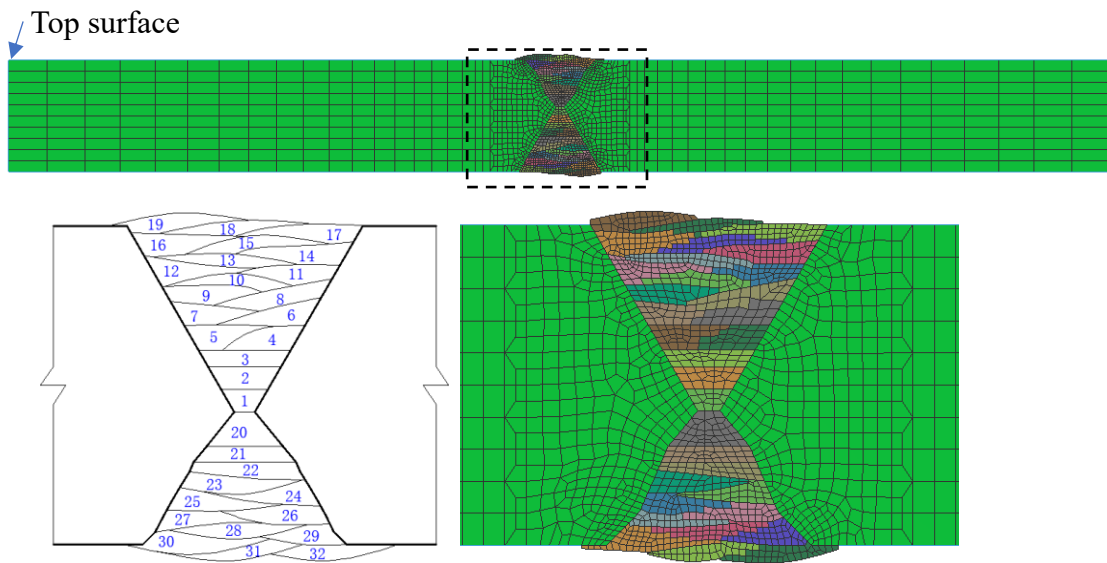
b) Cross sectional view of Section RS50-24

Top surface
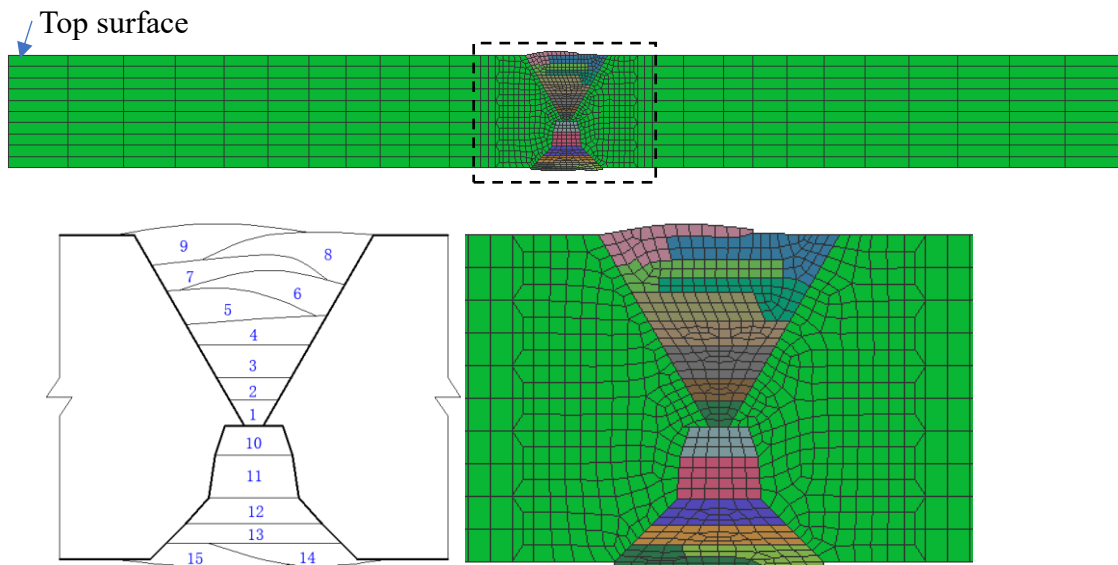
c) Cross sectional view of Section RS50-50

Figure 4.18 3D models of S690 QT 50mm thick welded sections

4.4.2 Element type

3D linear hexahedral elements with eight nodes are used in the models, as shown in Figure 4.19, that is elements DC3D8 which is employed for the thermal analysis. It should be noted that the corresponding elements C3D8R with reduced integration schemes is employed for the mechanical analysis. As both the nodal numbers and the degrees of freedom of these two solid elements are identical, compatibility of the heat transfer and the mechanical models can be readily satisfied.
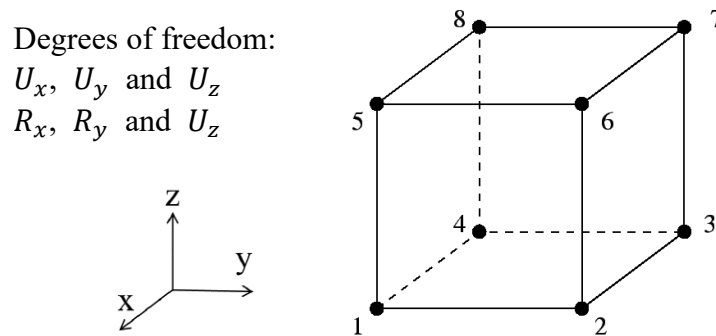
Figure 4.19 Typical 8-noded linear solid element in ABAQUS Elements C3D8R and DC3D8

4.4.3 Boundary conditions

a) Thermal boundary condition

Convection and radiation are considered to be the primary sources of heat loss in the welding of two sections in this study, so the film coefficient and the coefficient of emissivity should be defined carefully. However, these two parameters change significantly with the surface conditions of the steel plates, so several trial analyses of welding of Section RS50-50 were carried out, and then calibrated with the measured temperature history. The film coefficient and the coefficient of emissivity after calibration are taken to be 25 W/m^2/K and 0.8, respectively.

b) Mechanical boundary condition

The boundary conditions in the finite element models were defined according to the test set-up, as shown in Figure 4.20. These two steel plates were fixed by run-on plates at both ends so that the degrees of freedom are fixed in both directions in the plane of the welded sections at Points 1 to 4. In order to fix the welded section in the reference space, U_z at Points 1 and 2 were also fixed.
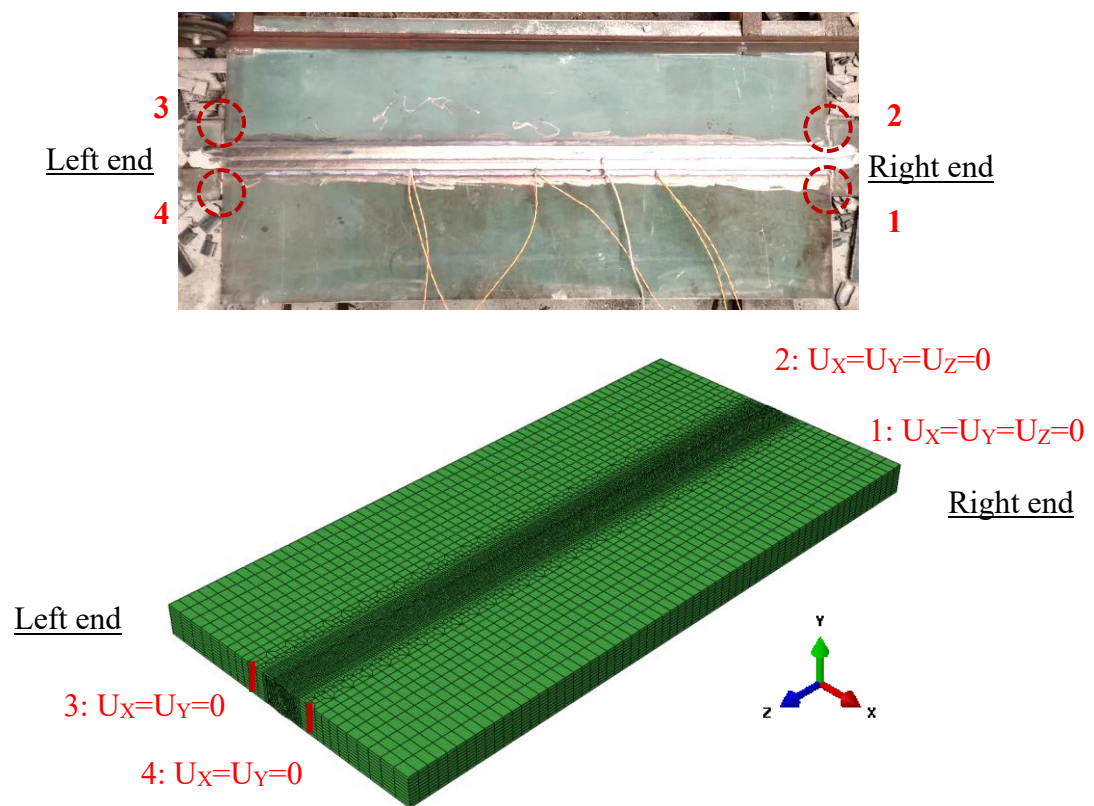
Figure 4.20 Boundary conditions of the mechanical models

4.4.4 Thermal material properties

Temperature-dependent parameters, including the thermal conductivity λ and the heat specific c of S690 steel, are considered to be different from those of the normal grade steel given in Eurocode 3. These two parameters of the S690 steel reported by E. Steau (2020) and Sun (2009) are adopted, as shown in Figure 4.21. It should be noted that the

conductivity after 1500 °C was set to be three times the conductivity at room temperature as the conductivity value of the molten metal is unknown. This is helpful to limit the maximum temperature of the simulated fusion zone of the welded sections to a reasonable range after several trial analyses.
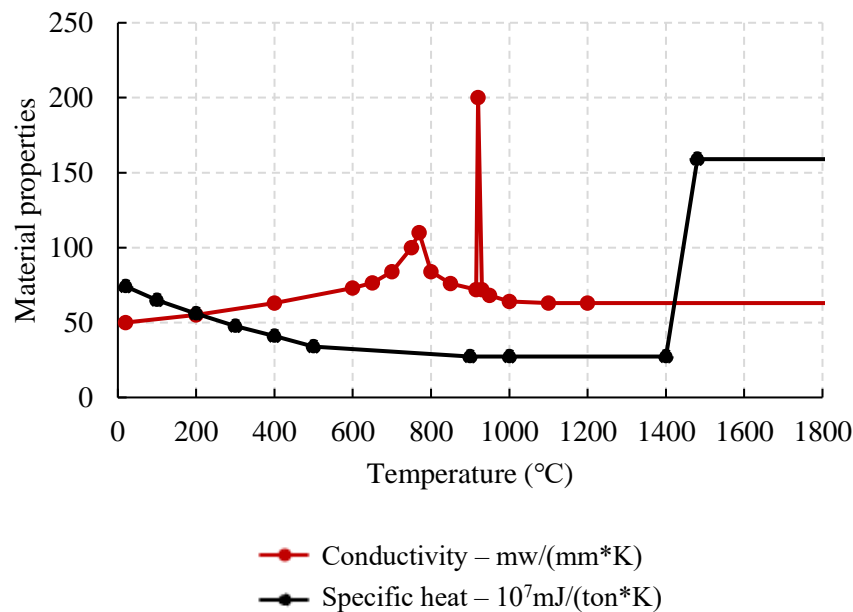
Figure 4.21 Thermal material properties of S690 steel

4.4.5 Mechanical properties

a) Thermal expansion

It is believed that the expansion and contraction of the base plates and the weld metal are the main causes of the welding induced residual stresses and deformations (MacDonald, 2011; Masubuchi, 2001). So the thermal expansion behaviour of the base plates and the weld metal were carefully tested with a Quenching and Deformation Dilatometer (Linseis Messgeräte GmbH).

Typical dimensions of test specimens used in dilatometer tests are shown in Figure 4.22 a). A thermocouple was spot-welded on the surface of the specimen with a tick welder

(Figure 4.22 b), and the measured temperatures were under control during the test. The specimen was heated to 900°C, which is the maximum operating of this dilatometer machine, with a heating rate of 50°C/s. Three repeat tests were carried out according to the test program shown in Table 4.14. A transducer was attached to the specimen for measurement of elongation during the heating process (Figure 4.22 d). The tests were conducted in a vacuum environment to prevent any oxidization of the test specimen.

a) Test specimen

b) Tick welder

c) L78 RITA Quenching and Deformation Dilatometer

d) Heating unit
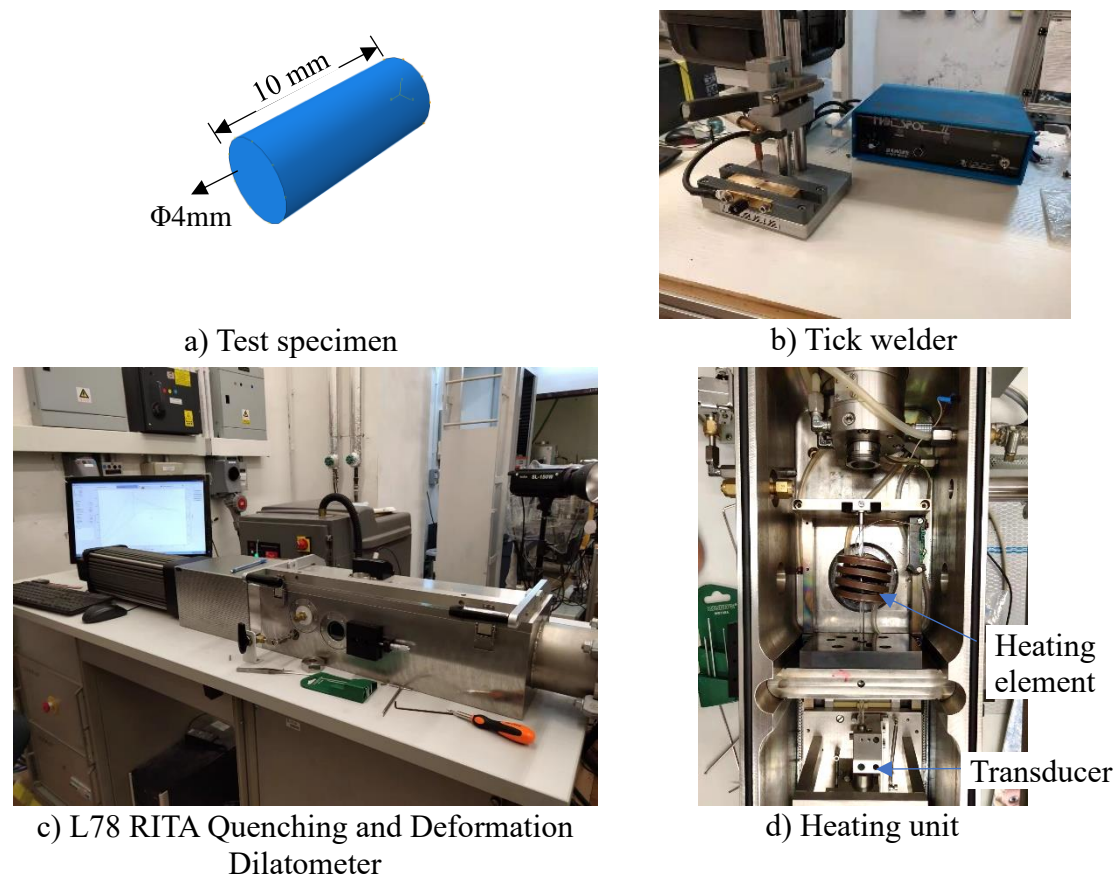
Figure 4.22 Dilatometer test

Table 4.14 Test program of dilatometer test

Material	Number	Heating rate (°C/s)	Max temperature (°C)	Number of specimens
Base metal	BP	50	900	3
Weld metal	WM	50	900	3

The test results are summarized in Figure 4.23. The base plate is shown to have an

elongation larger than that of the weld metal before 800 °C, and an obvious volume shrinkage is detected when the temperature rises above 700 °C due to phase changes. Also, it is found that the elongation predicted by Eurocode 3 is larger than those measured values of the base plate and the weld metal when the temperature goes beyond 700 °C.
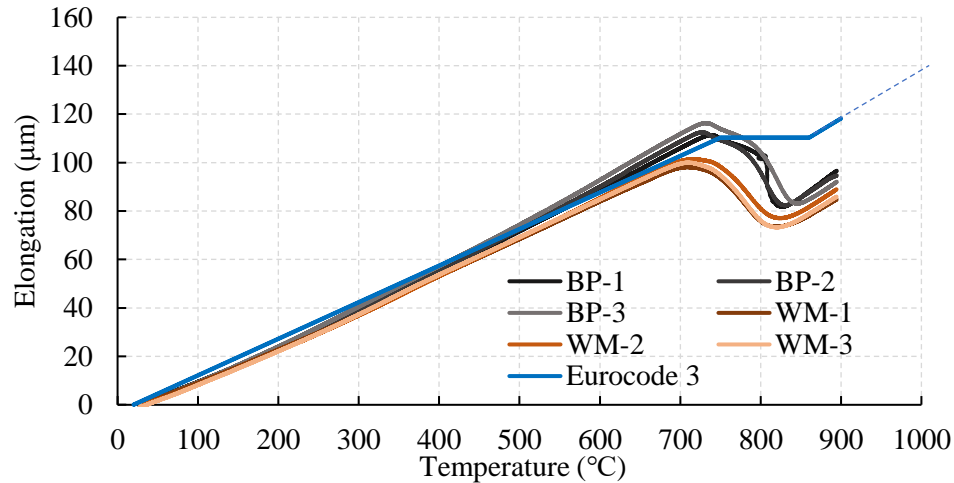
Figure 4.23 Test results

Typical simplified thermal expansion patterns for both the base plate and the weld metal were proposed based on the dilatometer test results for subsequent FEM analyses, as shown in Figure 4.24 a), considering that the thermal elongation predicted by EC 3 ends at 1200 °C, these two simplified thermal expansion patterns are also extended to 1200 °C. The corresponding thermal expansion coefficients are derived and plotted in Figure 4.24 b).
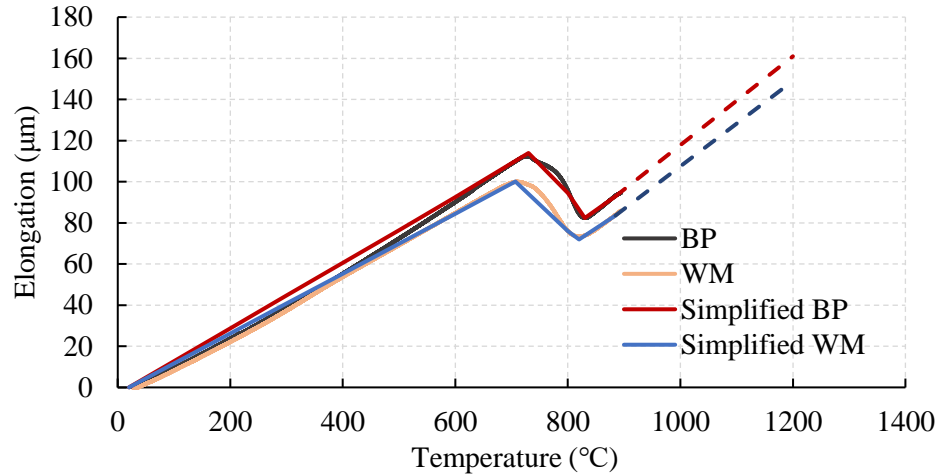
a) Simplified thermal elongation
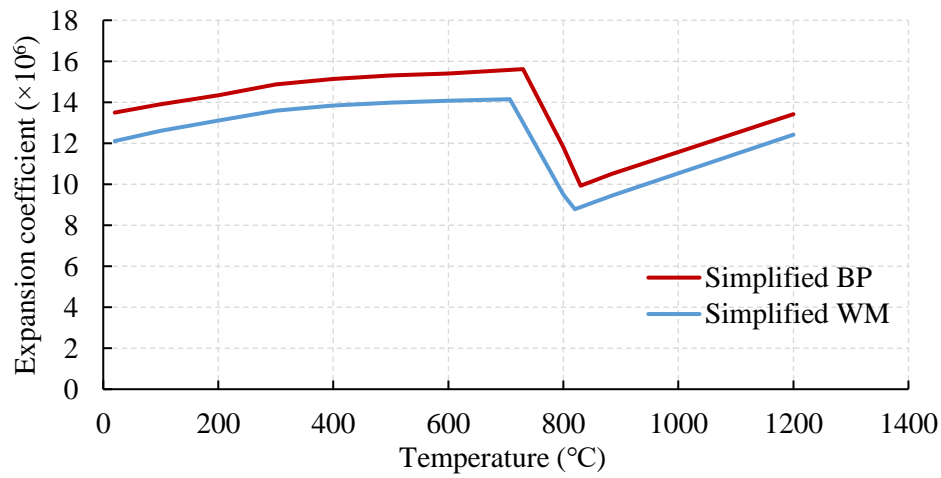
b) Corresponding thermal expansion coefficient

Figure 4.24 Simplified thermal expansion patterns

b) Mechanical properties at elevated temperature

According to previous studies on the mechanical properties of the S690 steel at elevated temperatures given by Wang (2018) and Qiang (2012), the reduction factors to the elastic modulus of S690 steel are similar to those given in Eurocode 3, but the reduction factors to the yield strengths given in Eurocode 3 are found to be significantly larger than measured values. Hence, the reduction factors to the elastic modulus E, the yield strength f_y, and the tensile strength f_u of the S690 steel in this project follow the results given by Wang (2018), as shown in Figure 4.25.
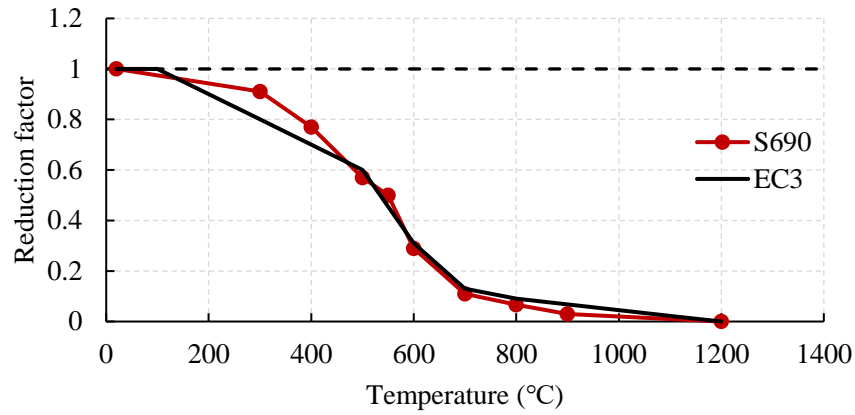
a) Young's modulus E
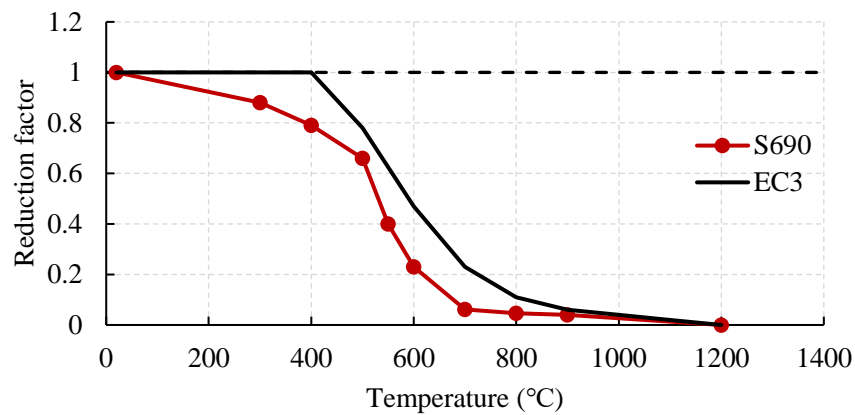
b) Yield strength f_y
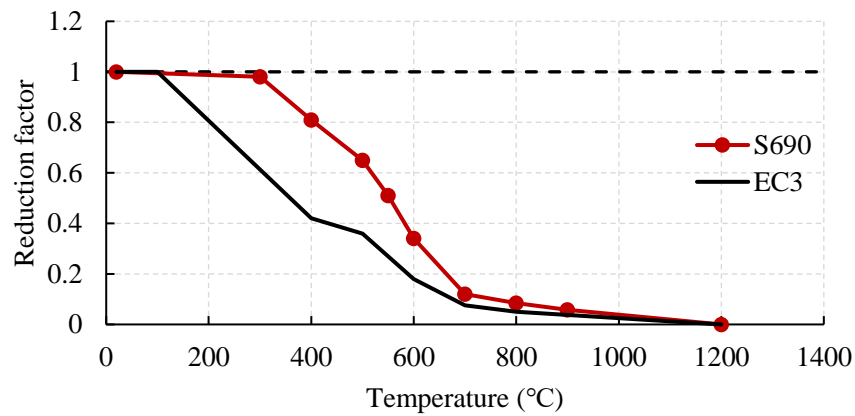
c) Tensile strength f_u

Figure 4.25 Reduction factors to mechanical properties of S690 steel

c) **True stress-strain curves at room temperature**

Both the true stress-strain relationships of the base plate and the weld metal were considered in the simulation process, and they followed the same reduction factors at

the elevated temperature shown in Figure 4.25. In order to simplify the computation process, a tri-linear true stress-strain model was adopted for these two steel materials, as shown in Figure 4.26.
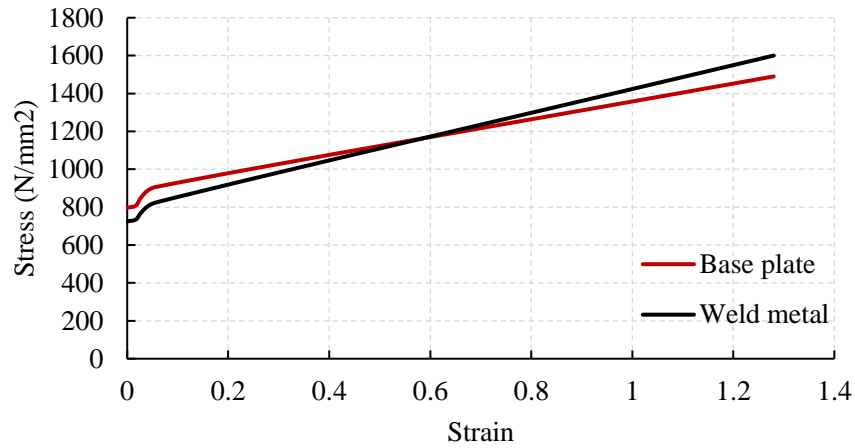
Figure 4.26 True stress-strain curves of base plate and weld metal

4.4.6 Heat source model

A double ellipsoidal heat source model (Goldak, 1984) was used in this study to define the energy distribution of a moving heat source. Figure 4.27 illustrates both the dimensions and the distribution pattern of the heat source.
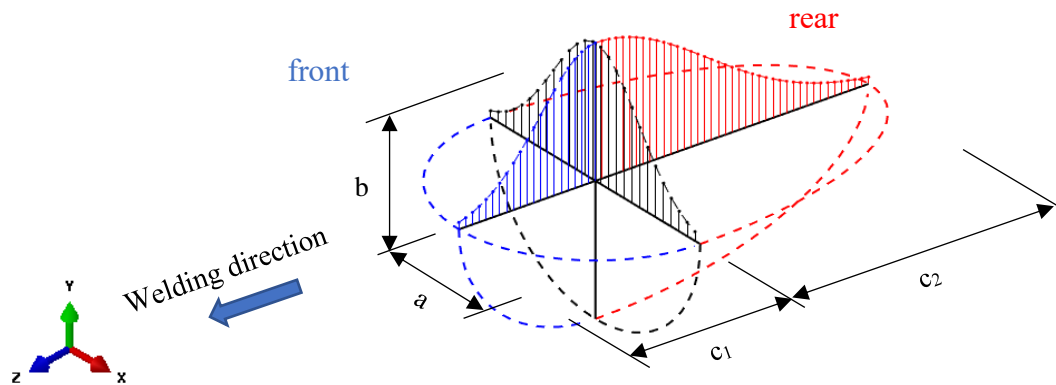
Figure 4.27 Double ellipsoidal heat source model

The heat flux distributed in both the front and the rear, q_1 and q_2, are computed respectively as follows:

$$\begin{cases} q_1(x,y,z) = \dfrac{6\sqrt{3}f_f Q}{a_1 bc\pi\sqrt{\pi}}\exp\left(-\dfrac{3x^2}{a^2}\right)\exp\left(-\dfrac{3y^2}{b^2}\right)\exp\left(-\dfrac{3z^2}{c_1{}^2}\right) \\[2mm] q_2(x,y,z) = \dfrac{6\sqrt{3}f_r Q}{a_2 bc\pi\sqrt{\pi}}\exp\left(-\dfrac{3x^2}{a^2}\right)\exp\left(-\dfrac{3y^2}{b^2}\right)\exp\left(-\dfrac{3z^2}{c_2{}^2}\right) \end{cases}$$

where q_1 and q_2 are the volumetric heat flux in the front and the rear respectively [W/m³];

$a, b,\ c_1$ and c_2 are semi-axes of the double ellipsoid [m];

Q is the total heat input energy during welding [J];

x, y, and z are the local coordinates; and

f_f and f_r are fractions illustrating energy distribution, and $f_f + f_r = 2$.

In this study, the welding efficiency η is considered to be 0.95 and 0.85 for the SAW and the GMAW, respectively.

It should be noted that the geometry parameters of the double ellipsoidal heat model were adjusted to make sure that the simulated fusion zone was close to the practical welding. So, some trial runs were carried out to calibrate these geometry parameters.

4.4.7   Initial residual stress before welding

The initial residual stresses after flame cutting should not be ignored in a welding simulation process, as reported by several researchers (Jokiaho, 2017; Wang 2012). Large tensile residual stresses, which may be larger than the yield strengths of the base plate, were found in small regions adjacent to the cutting edges.

Jokiaho (2017) measured the flame-cutting induced residual stresses of a S355 60 mm thick steel plate with a minimum yield strength of 325 N/mm² and a tensile strength of

470 N/mm². The result is shown in Figure 4.28 a), and a tensile residual stress at 300 N/mm² is found at the free edge. ECCS (1976) summarized typical residual stress patterns, as shown in Figure 4.28 b). It is obvious that the patterns of these flame-cutting-induced residual stresses are quite similar to one another. Hence, a high tensile residual stress at the free edge is found, and it decreases sharply to zero, then a compressive residual stress occurs.

The simplified residual stress pattern given by ECCS was adopted as the initial residual stress field in this study, as shown in Figure 4.29. A maximum tensile residual stress of 800 N/mm², which is the yield strength of base plate, is assigned along the free edge, and compressive stresses at the rest of the plate are assigned to be 40 N/mm² according to force equilibrium.
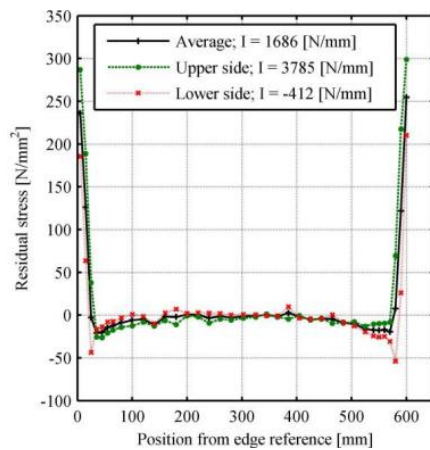
a) Residual stress distribution of
S355 60 mm thick steel plate
(Jokiaho, 2017)
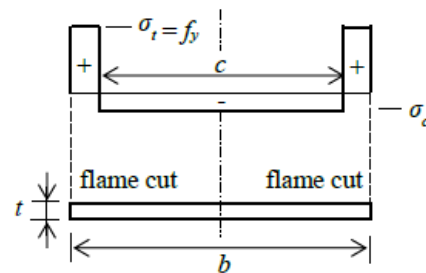
b) Residual stress distribution of
flame cut plates
(ECCS, 1976)

Figure 4.28 Residual stresses induced by flame cutting
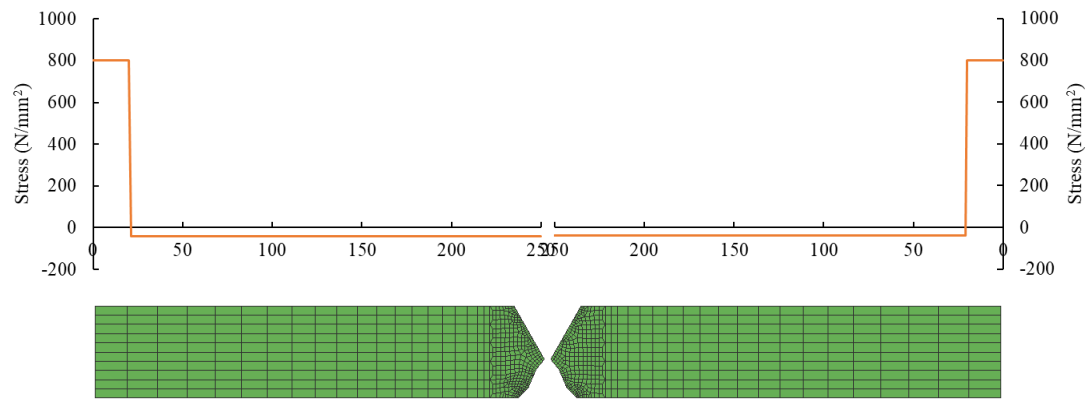
Figure 4.29 Initial residual stress before welding

All the analyses have been completed successfully in a modern desktop computer with Intel i7 CPU and RAM of 32 GB. The total running time for the sequentially coupled thermomechanical analyses for Models RS50-24 and 50-50 welded sections are 88 and 58 days, respectively.

4.4.8 Temperature results

a) Section RS50-24

The transient surface temperature history was measured with three pairs of thermocouples, and the measured results were found to be quite consistent among these pairs of thermocouples.
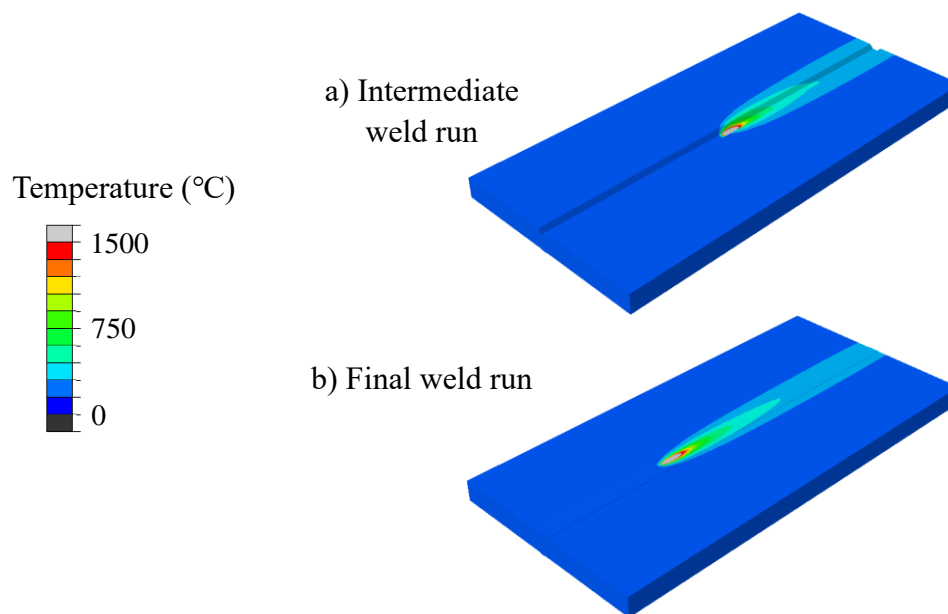
Figure 4.30 Typical predicted temperature field of Section RS50-24

Figure 4.30 shows typical temperature distributions during welding of Section RS50-24. Both the measured and the simulated temperature history at Location P1 are plotted together onto the same graph for direct comparison, as shown in Figure 4.31 b). Similarly, the measured and the simulated temperatures of Location P2 are also plotted together in Figure 4.31 c). Tables 4.15 and 4.16 summarize the maximum temperatures measured and simulated at various welding passes.

It is found that the measured and the simulated results agree with each other well, and the maximum discrepancy at Location P1 is merely 69 ℃ at weld pass 11 while the maximum discrepancy at Location P2 is merely -13 ℃ at weld pass 2. These

127

discrepancies are considered to be very small. Hence, Model RS50-24 is demonstrated be to able to predict the temperature history of the welding process with a high degree of accuracy.
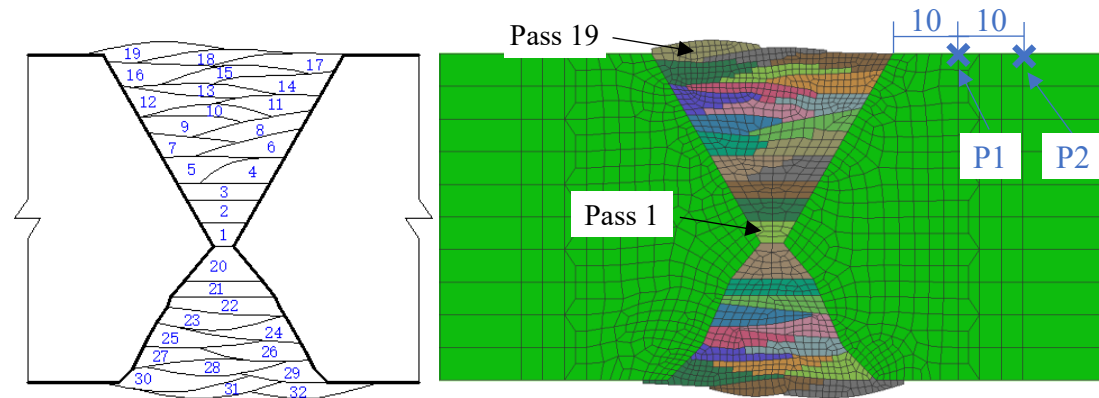
a) Locations P1 and P2
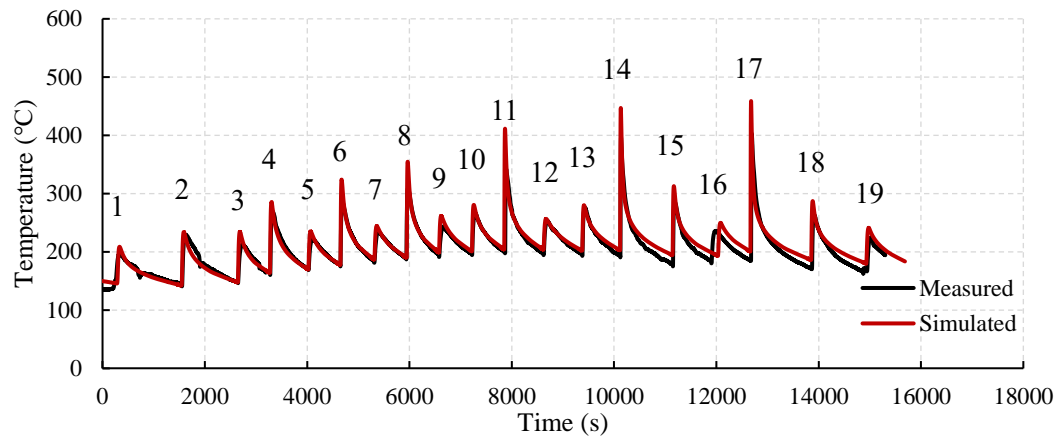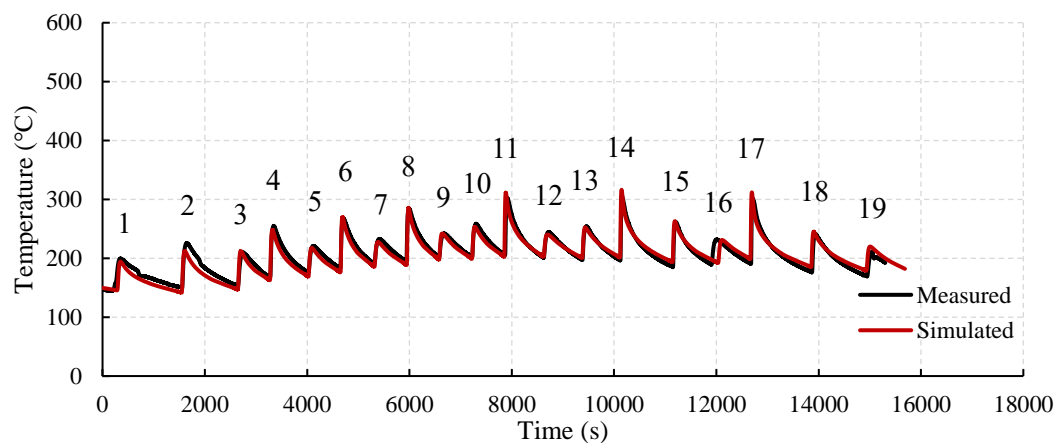
b) Location P1

c) Location P2

Figure 4.31 Comparison of measured and simulated temperature history of Section RS50-24

Table 4.15 Comparison of maximum temperatures at Location P1 of Section RS50-24

Weld pass	Measured	Simulated	Discrepancy	Error
1	-	-	-	-
2	229	232	3	1.3%
3	212	232	20	9.4%
4	268	285	17	6.3%
5	221	234	13	5.9%
6	283	323	40	14.1%
7	233	242	9	3.9%
8	308	353	45	14.6%
9	241	261	20	8.3%
10	266	280	14	5.3%
11	342	411	69	20.2%
12	253	256	3	1.2%
13	275	278	3	1.1%
14	396	446	50	12.6%
15	284	311	27	9.5%
16	235	250	15	6.4%
17	403	458	55	13.6%
18	263	286	23	8.7%
19	224	241	17	7.6%

Average: 8.3%

Table 4.16 Comparison of maximum temperatures at Location P2 of Section RS50-24

Weld pass	Measured	Simulated	Discrepancy	Error
1	-	-	-	-
2	225	212	-13	-5.8%
3	209	212	3	1.4%
4	254	247	-7	-2.8%
5	220	217	-3	-1.4%
6	268	268	0	0.0%
7	231	227	-4	-1.7%
8	284	286	2	0.7%
9	242	239	-3	-1.2%
10	258	253	-5	-1.9%
11	302	311	9	3.0%
12	244	239	-5	-2.0%
13	253	252	-1	-0.4%
14	306	314	8	2.6%
15	261	262	1	0.4%
16	232	230	-2	-0.9%
17	302	311	9	3.0%
18	241	244	3	1.2%
19	211	218	7	3.3%

Average: 1.9%

b) Section RS50-50

The transient surface temperature history was measured with three pairs of thermocouples, and the measured results were found to be quite consistent among these pairs of thermocouples.
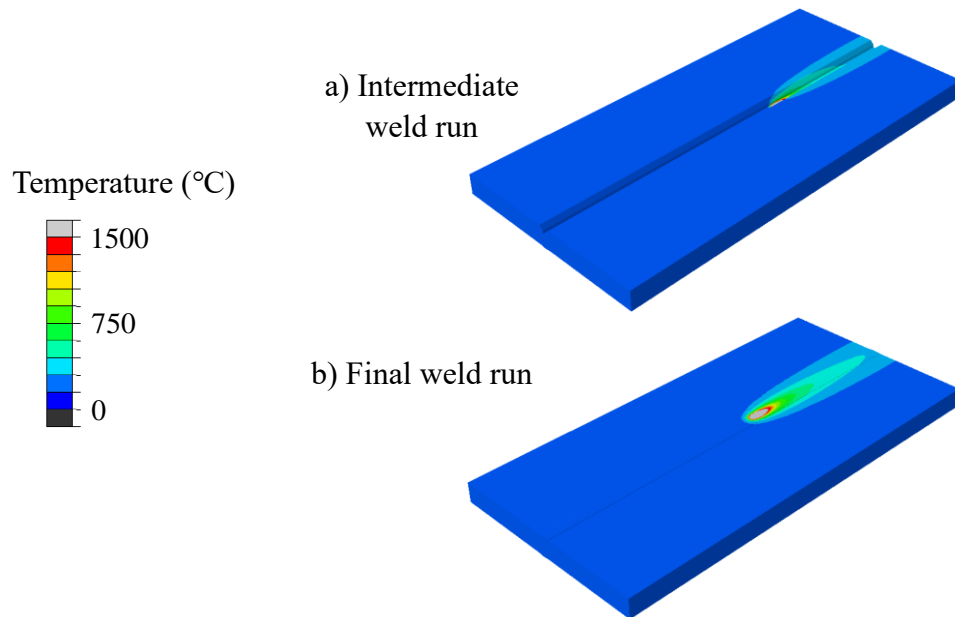
Figure 4.32 Typical predicted temperature distribution of Section RS50-50

Figure 4.32 shows typical temperature distributions during welding of Section RS50-50. Both the measured and the simulated temperature history at Location P1 are plotted together onto the same graph for direct comparison, as shown in Figure 4.33 b). Similarly, the measured and the simulated temperatures of Location P2 are also plotted together in Figure 4.33 c). Tables 4.17 and 4.18 summarize the maximum temperatures measured and simulated at various welding passes.

It is found that the measured and the simulated results agree with each other well, and the maximum discrepancy at Location P1 is merely 57 °C at weld pass 8, and the maximum discrepancy at Location P2 is merely 51 °C at weld pass 8. These discrepancies are considered to be very small. Hence, Model RS50-50 is demonstrated

to be able to predict the temperature history of the welding process with a high degree of accuracy.
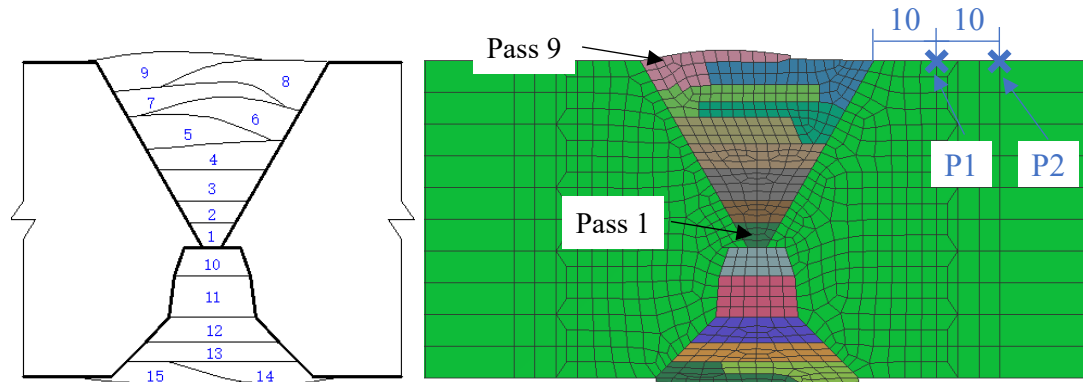
a) Locations P1 and P2
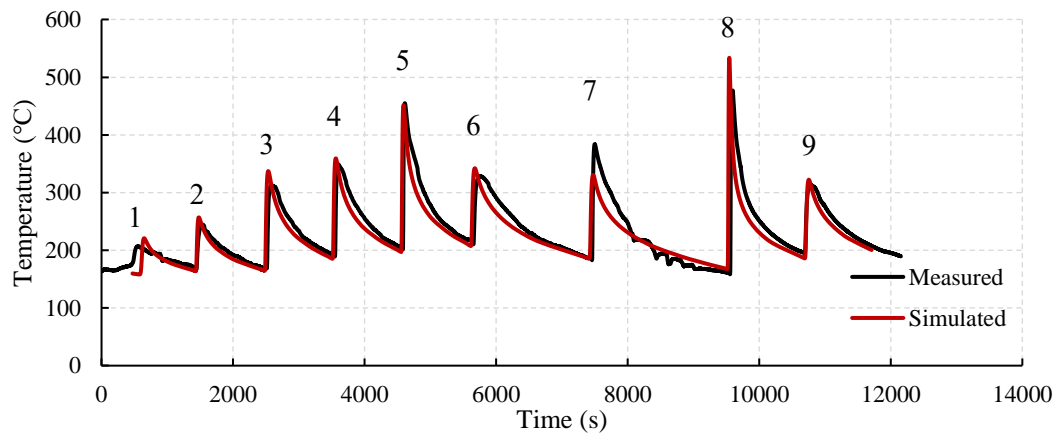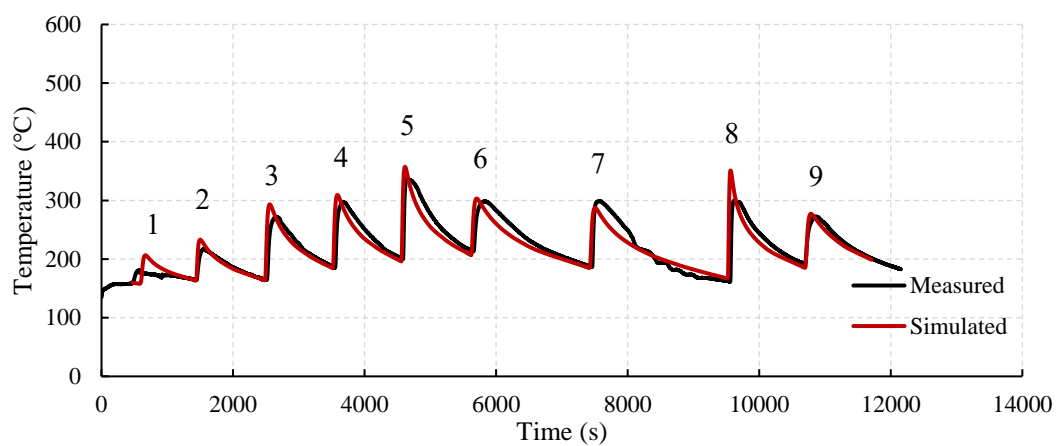
b) Location P1

c) Location P2

Figure 4.33 Comparison of measured and simulated temperature history of Section RS50-50

Table 4.17 Comparison of maximum temperatures at Location P1 of Section RS50-50

Weld pass	Measured	Simulated	Discrepancy	Error
1	-	-	-	-
2	245	256	11	4.5%
3	312	335	23	7.4%
4	349	359	10	2.9%
5	453	451	-2	-0.4%
6	327	341	14	4.3%
7	381	331	-50	-13.1%
8	476	533	57	12.0%
9	312	320	8	2.6%
			Average:	5.9%

Table 4.18 Comparison of maximum temperatures at Location P2 of Section RS50-50

Weld pass	Measured	Simulated	Discrepancy	Error
1	-	-	-	-
2	217	232	15	6.9%
3	271	290	19	7.0%
4	296	309	13	4.4%
5	339	356	17	5.0%
6	298	302	4	1.3%
7	299	288	-11	-3.7%
8	299	350	51	17.1%
9	271	276	5	1.8%
			Average:	5.9%

133

4.4.9 Mechanical results

a) Section RS50-24

Figure 4.34 plots the residual stress distributions of the whole section and also of the welded section after the cutting and milling process. Large localized tensile residual stresses are found in the fusion zone and adjacent areas, and small compressive residual stresses are found in the other part.

Figure 4.35 illustrates the residual stress distributions of the cross-section in the middle of Section RS50-24. The simulated surface residual stresses at both the top and the bottom surfaces at Step b are extracted and compared with tested results, as shown in Figure 4.36. Both the simulated and the measured results are shown to be very close to one another.

It is also noticeable that the simulated residual stresses in the fusion zone at the top surface is much higher than those at the bottom surface. This can be explained as the weldment at the top acted as constraints during the contraction of the weldment at the bottom, so the tensile stresses at the top surface were increased accordingly.

Step a. Welded section after welding   Step b. Welded section after cutting

Step c. Welded section after
milling Layer 1

Step d. Welded section after
milling Layer 2
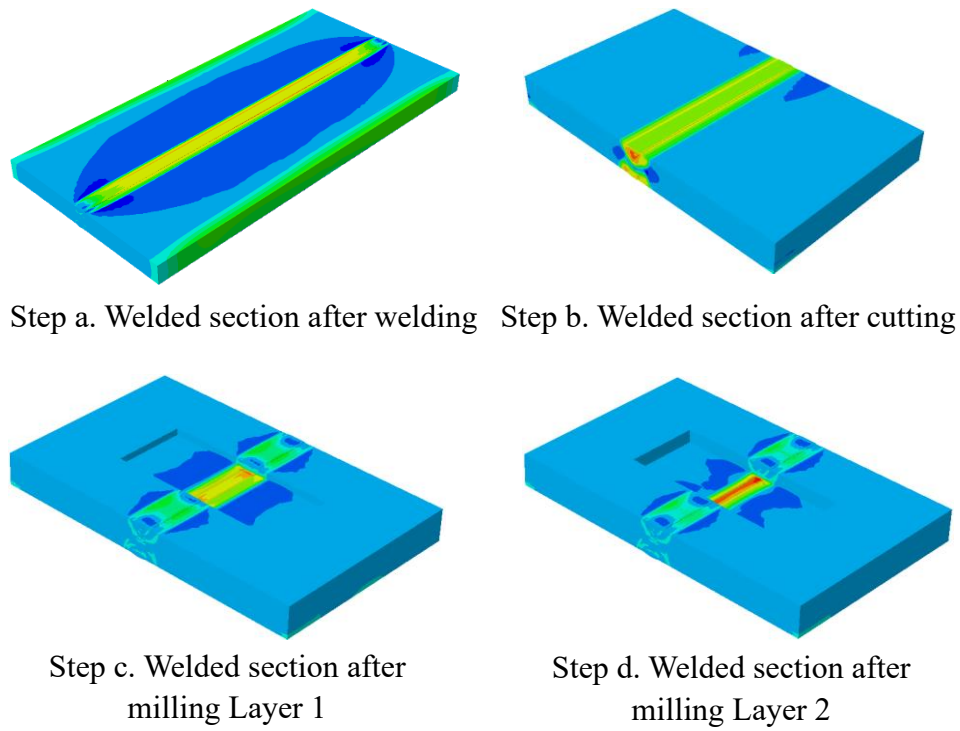
Figure 4.34 Residual stress distribution of Section RS50-24

Step a. Welded section after welding

Step b. Welded section after cutting

Step c. Welded section after milling Layer 1

Step d. Welded section after milling Layer 2
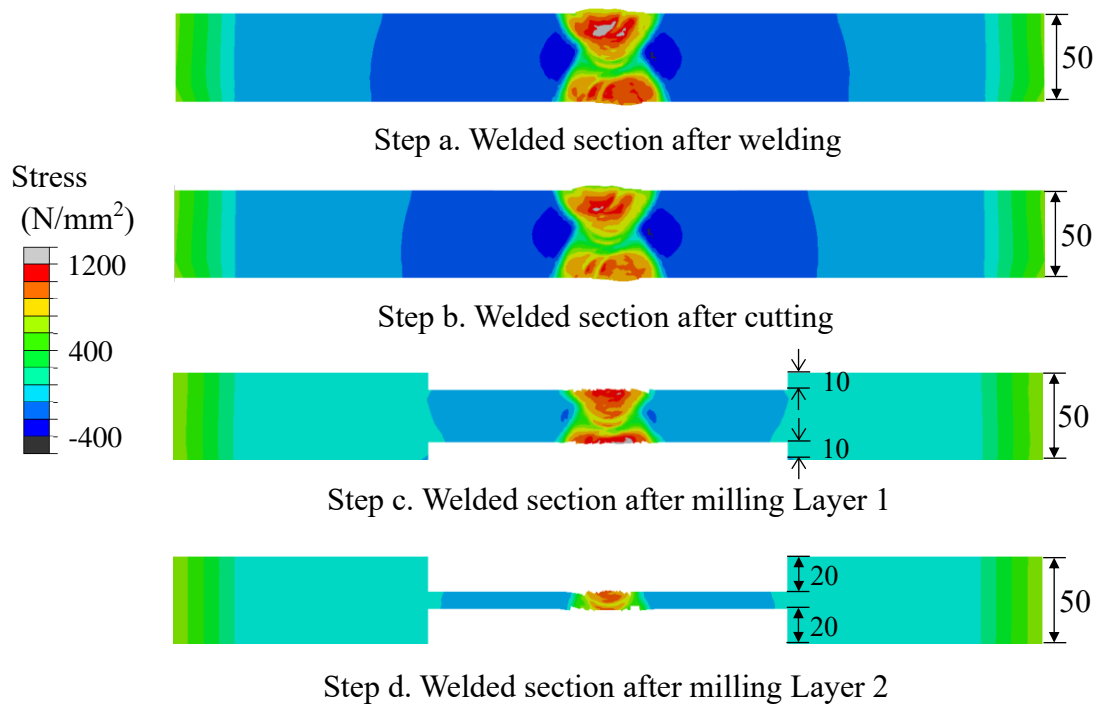
Figure 4.35 Cross sectional distributions of residual stresses of Section RS50-24
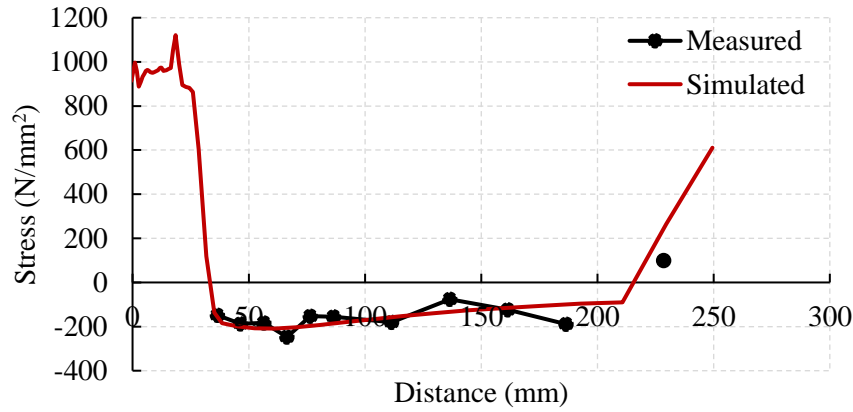
a) Simulated and measured residual stresses on the top surface
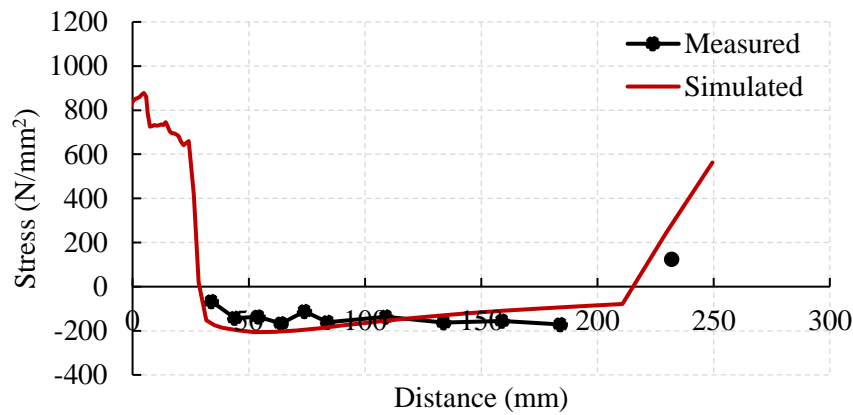
b) Simulated and measured residual stresses on the bottom surface

Figure 4.36 Comparison of surface residual stresses of Section RS50-24

The released residual stresses after the milling process at Steps c and d of both the measured and the simulated results were further compared. Figure 4.37 a) and b) plot the residual stresses after machining of Layer 1 under the top and the bottom surfaces, respectively, while comparison of Layer 2 is shown in Figure 4.37 c) and d). Since the simulated and measured results are shown to be in good agreement, the finite element model is shown to have accurately predicted the residual stresses after milling and stress release. Hence, it is considered that the finite element model can accurately predict the residual stresses before milling and stress release.
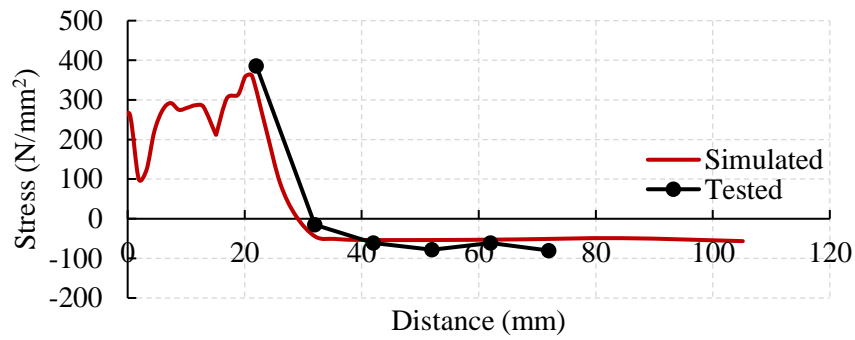
a) Layer 1 under the top surface
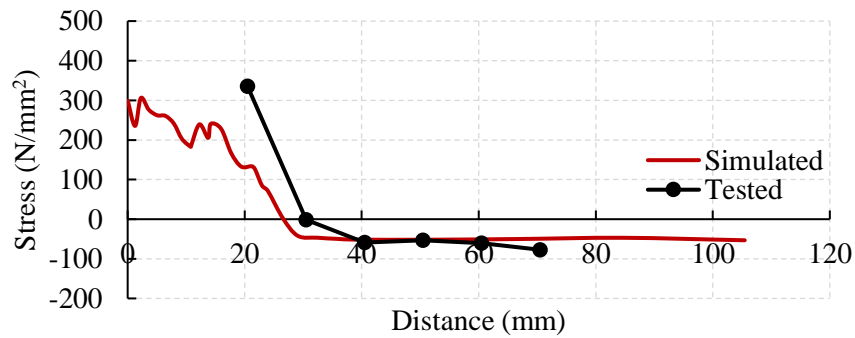
b) Layer 1 under the bottom surface
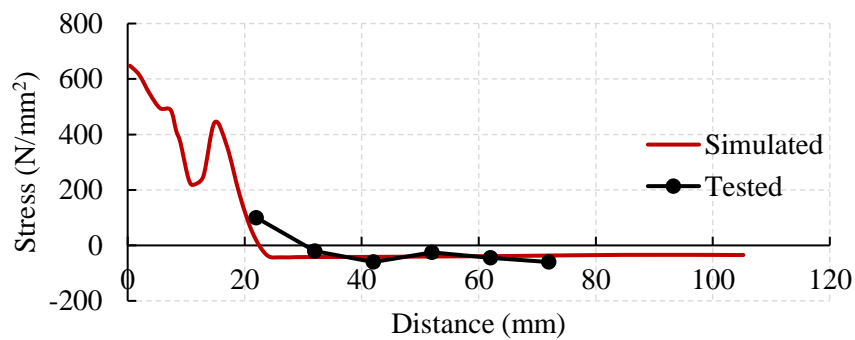
c) Layer 2 under the top surface
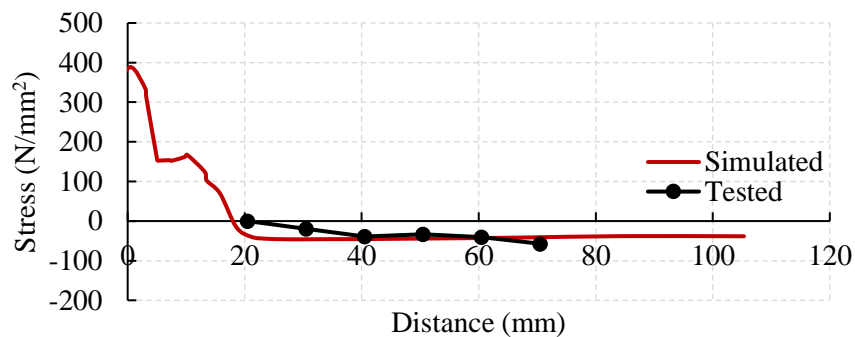
d) Layer 2 under the bottom surface

Figure 4.37 Comparison of residual stress after milling of Section RS50-24

The through-thickness variations of the residual stresses of Section RS50-24 before milling and material removal are plotted in Figure 4.38.

It is shown that the variations of the compressive residual stresses along the thickness direction is very small. For the tensile stresses, due to an X shape groove, the width of the fusion zone becomes smaller when it goes from the top and the bottom surface to the middle one, and the width of the tensile stress region changes with the width of the fusion zone. This can be explained as it is the contraction of the fusion zone that leads to the formation of the tensile residual stresses.

In addition, there is only a little difference in the variation of the residual stresses along the y-axis, so the residual stresses may be considered symmetrical.
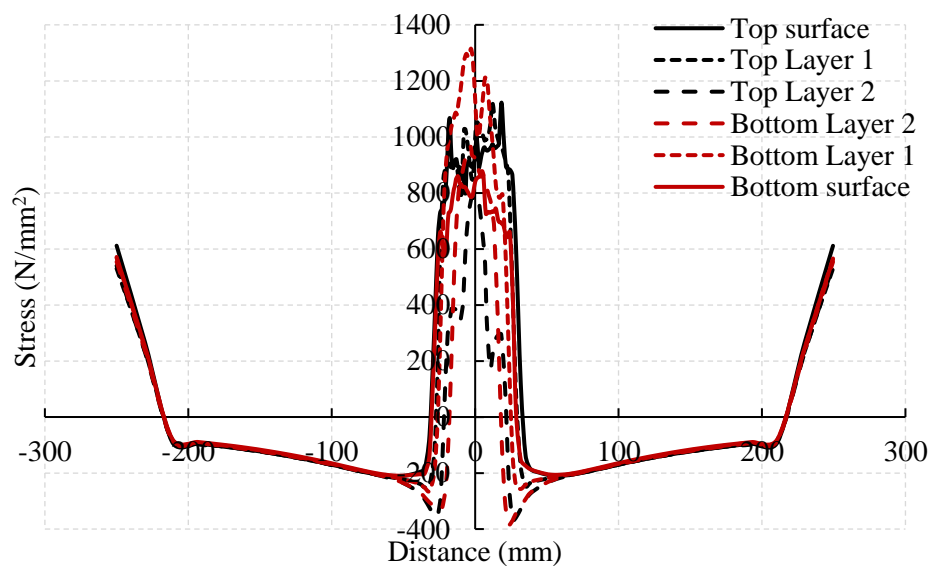
Figure 4.38 Through thickness variations of residual stresses

b) RS50-50

Figure 4.39 plots the residual stress distributions of the whole section and also of the welded section after the cutting and milling process. Large localized tensile residual stresses are found in the fusion zone and adjacent areas, and small compressive residual stresses are found in the other parts.

Figure 4.40 illustrates the residual stress distributions of the cross-section in the middle of Section RS50-50. The simulated surface residual stresses at both the top and the bottom surfaces at Step b are extracted and compared with tested results, as shown in Figure 4.41. Both the simulated and the measured results are shown to be very close to one another.

It is also noticeable that the simulated residual stresses in the fusion zone at the top surface is much higher than those at the bottom surface. This can be explained as the weldment at the top acted as constraints during the contraction of the weldment at the bottom, so the tensile stresses at the top surface were increased accordingly.

Step a. Welded section after welding   Step b. Welded section after cutting

c) Welded section after milling   d) Welded section after
Layer 1   milling Layer 2
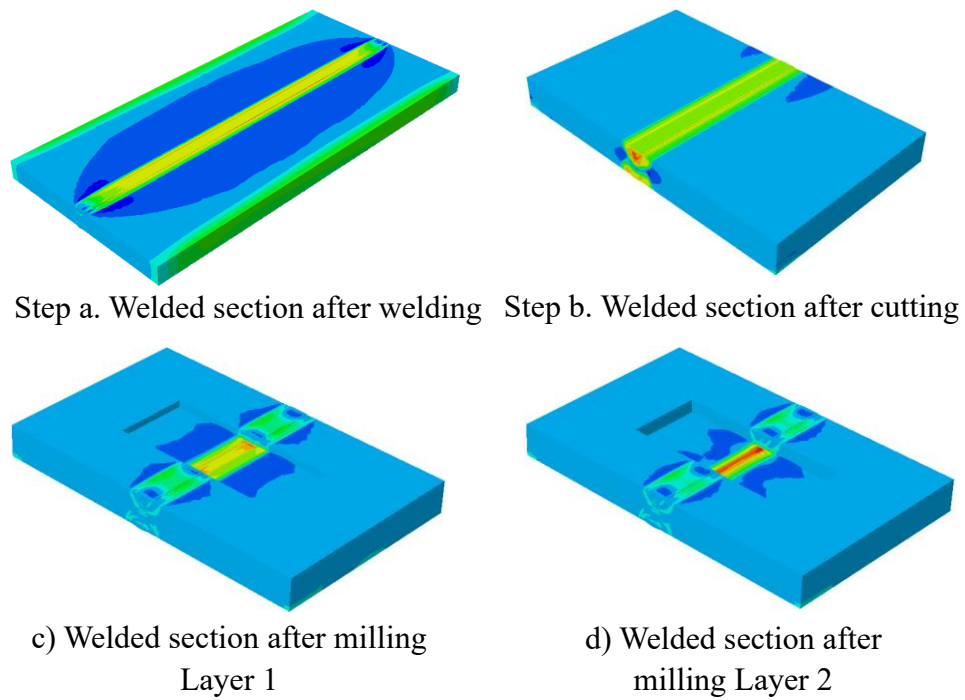
Figure 4.39 Residual stress distributions of Section RS50-50
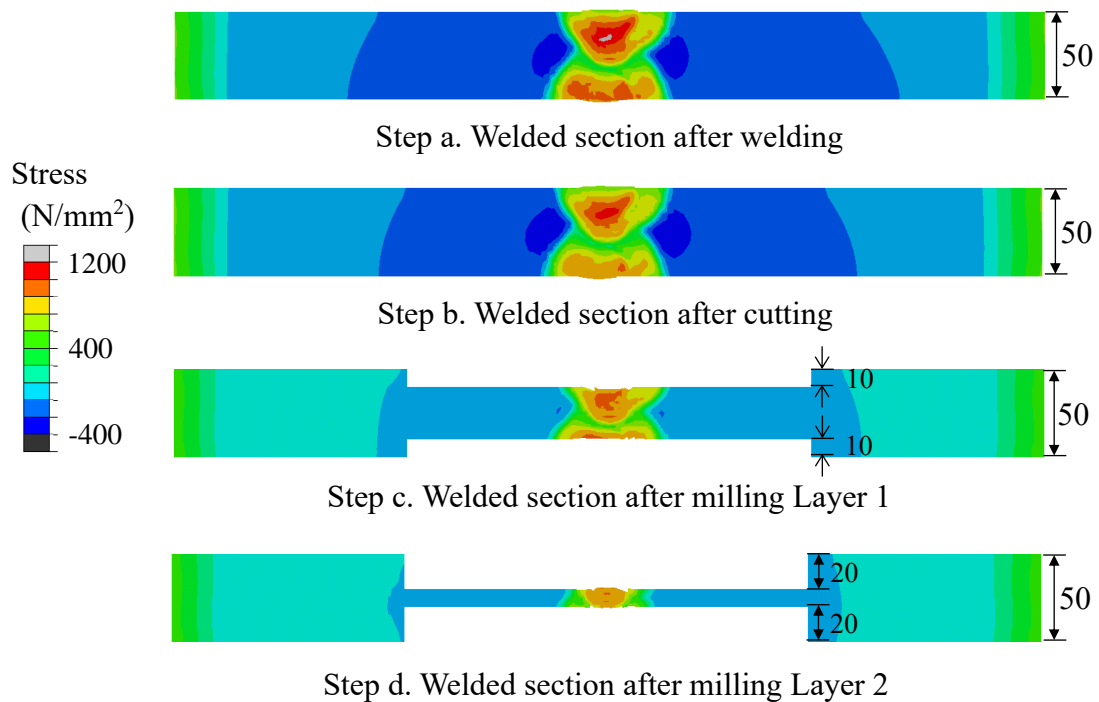
Figure 4.40 Cross sectional distributions of residual stresses of Section RS50-50
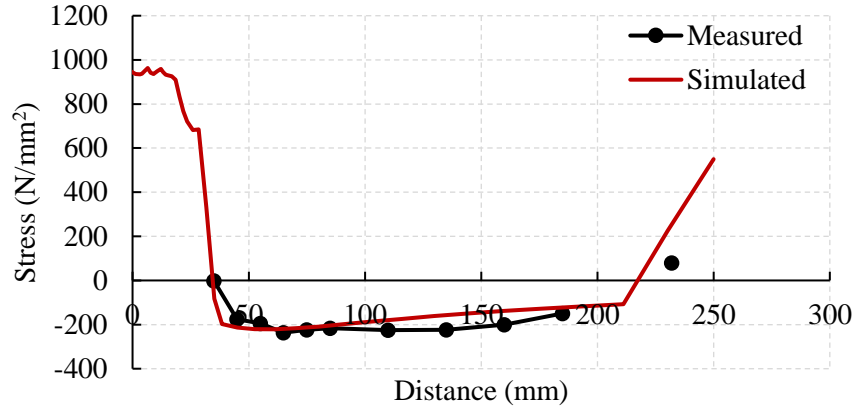
a) Simulated and measured residual stresses on the top surfaces
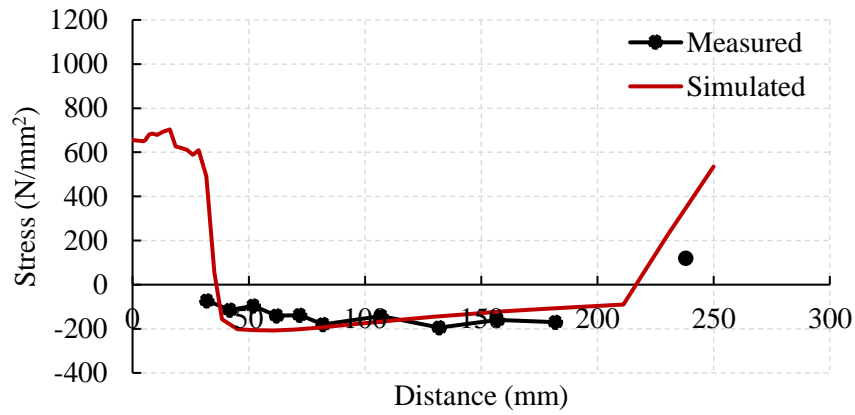
b) Simulated and measured residual stresses on the bottom surfaces

Figure 4.41 Comparison of surface residual stresses of Section RS50-50

The released residual stresses after the milling process at Steps c and d of both the measured and the simulated results were further compared. Figure 4.42 a) and b) plot the residual stresses after machining of Layer 1 under the top and the bottom surfaces, respectively, while comparison of Layer 2 is shown in Figure 4.42 c) and d). Since the simulated and measured results are shown to be in good agreement, the finite element model is shown to have accurately predicted the residual stresses after milling and stress release. Hence, it is considered that the finite element model can accurately predict the residual stresses before milling and stress release.
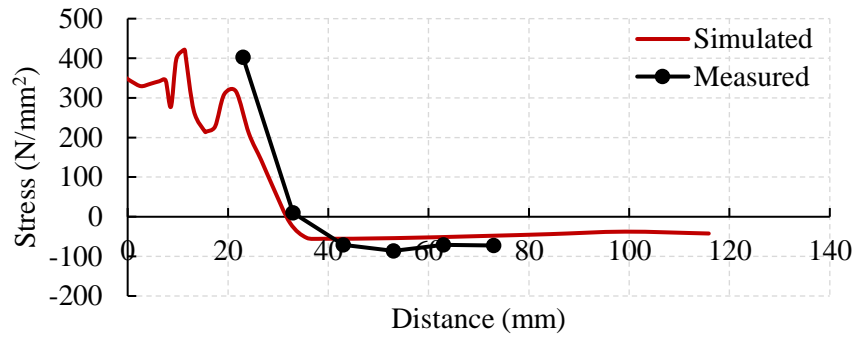
a) Layer 1 under the top surface
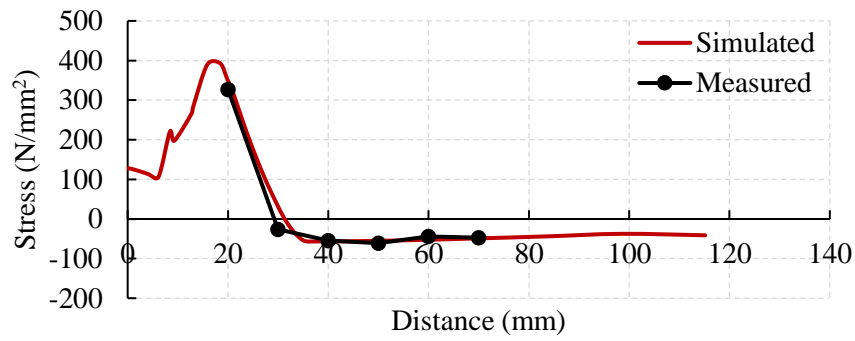
b) Layer 1 under the bottom surface
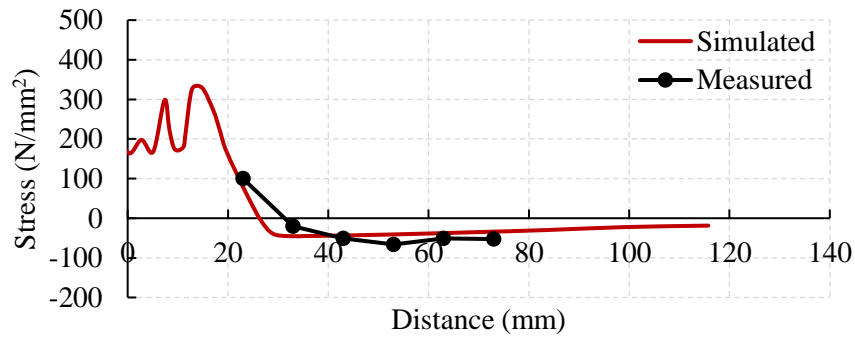
c) Layer 2 under the top surface
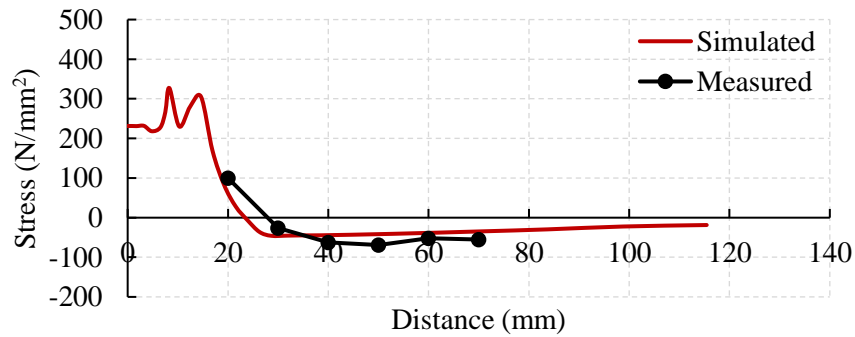
d) Layer 2 under the bottom surface

Figure 4.42 Comparison of residual stresses after milling of Section RS50-50

The through-thickness variations of the residual stresses of Section RS50-50 before milling and material removal are plotted in Figure 4.43.

It is shown that the variations of the compressive residual stresses along the thickness direction is very small. For the tensile stresses, due to an X shape groove, the width of the fusion zone becomes smaller when it goes from the top and the bottom surface to the middle one, and the width of the tensile stress region changes with the width of the fusion zone. This can be explained as it is the contraction of the fusion zone that leads to the formation of the tensile residual stresses.

In addition, there is only a little difference in the variation of the residual stresses along the y-axis, so the residual stresses may be considered symmetrical.
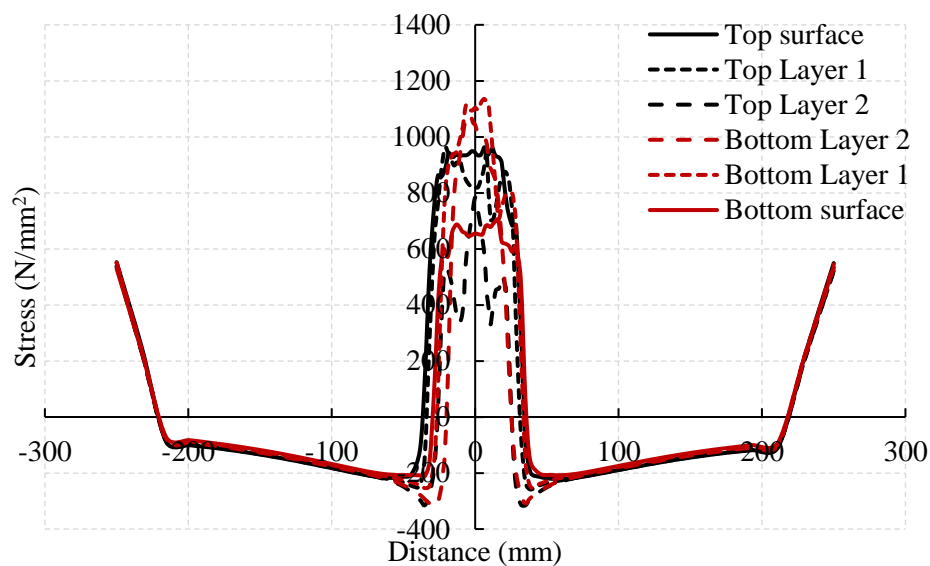
Figure 4.43 Through thickness variations of residual stresses

4.5 Comparison with S690 16mm thick welded sections

In order to compare the residual stresses between 16 mm thick weld sections and 50 mm thick weld sections, numerical simulations were carried out to investigate the residual stresses in S690 QT 16mm thick butt-welded section. Detailed numerical results are presented in this section.

Two sections with heat input energy of 1.0 and 2.0 kJ/mm, namely Sections RS16-10 and RS16-20, were prepared as shown in Figure 4.44. The width and the length of these welded sections were taken to be 10 and 20 times the plate thickness, which are the same as those of the 50 mm welded sections. The joint design of these 16 mm thick sections and the volume of each weld pass were set according to a trial welding.

a) Overall view

Number of weld passes = 5

b) Cross-section A-A of Section RS16-10

Number of weld passes = 3

b) Cross-section A-A of Section RS16-20
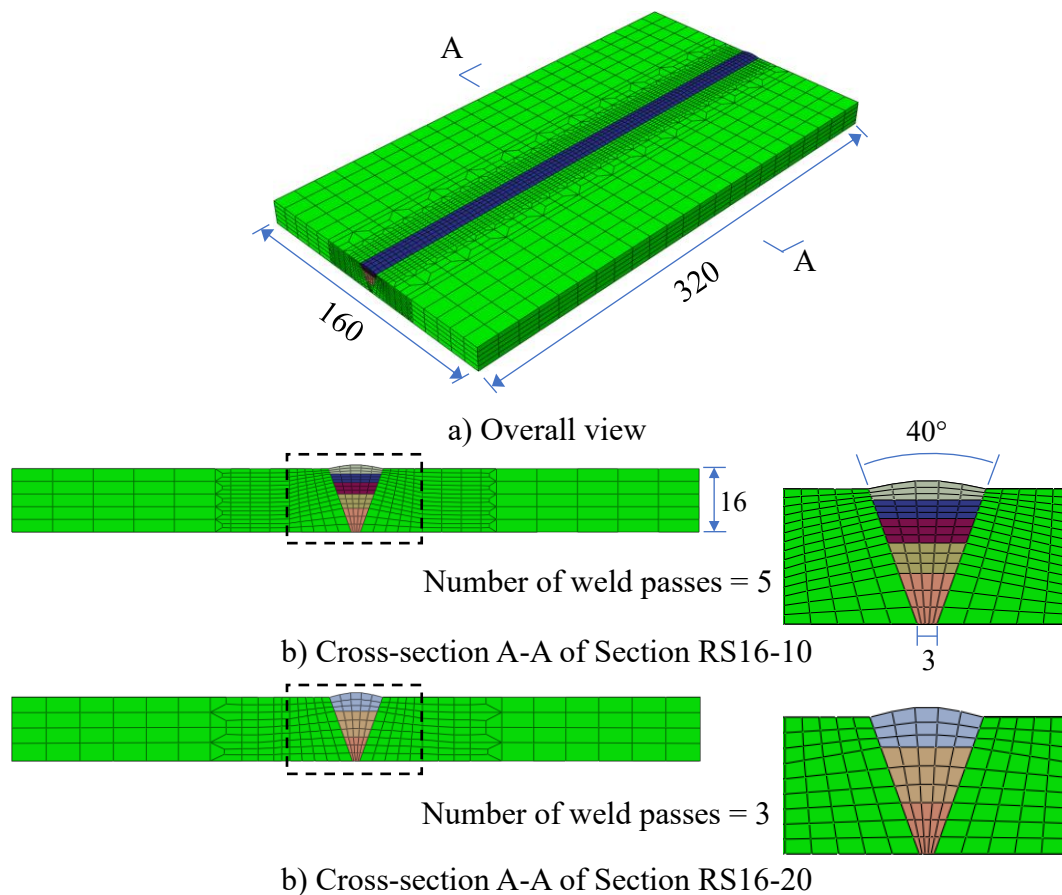
Figure 4.44 3D model of 16 mm thick weld sections

The welding parameters were also chosen based on the trial welding as shown in Table 4.19. It should be noted that the heat input energy of the first pass of Section RS16-20 was set to be 1.0 kJ/mm as such a weld joint does not allow for a higher heat input energy.

Table 4.19 Welding parameters of 16 mm thick welded sections

Section	Pass	Current (A)	Voltage (V)	Speed (mm/s)	Heat input energy (kJ/mm)
RS16-10	1 - 5	200	26	4.4	1.0
RS16-20	1	200	26	4.4	1.0
	2 & 3	240	28	2.8	2.0

In order to make a direct comparison, the material properties of the 16 mm thick plate were set to be the same as those of the 50 mm thick plate. Also, same boundary conditions were adopted in the models of these 16 mm thick welded sections. Sequentially coupled thermomechanical analyses were carried out and typical simulated temperature fields and longitudinal surface residual stresses are shown in Figures 4.45 and 4.46, respectively.

a) Section RS16-10

Temperature (°C)

1500

750

0

b) Section RS16-20
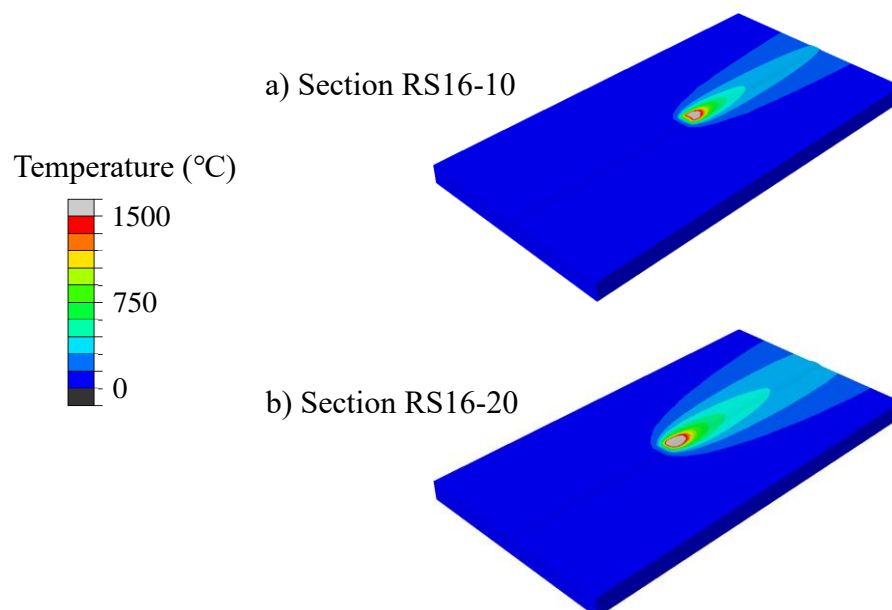
Figure 4.45 Typical predicted temperature field of final run

145
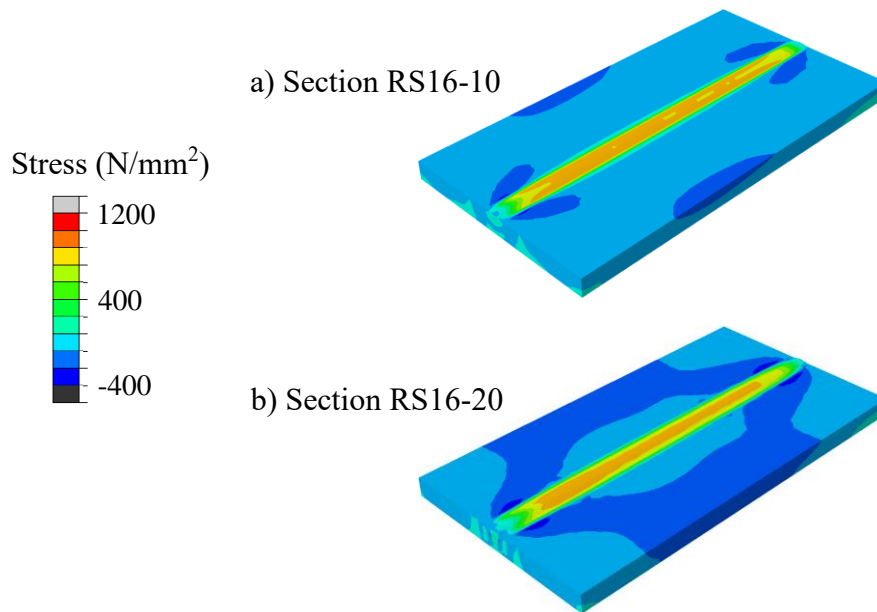
Figure 4.46 Residual stress field after welding

The cross sectional residual stress distributions at the mid-length of these two sections were extracted as shown in Figure 4.47. Similar to those 50 mm thick welded sections, the following are found in the models of these 16 mm thick welded sections:

a) Large localized tensile residual stresses are found in the region adjacent to the fusion zones, and these tensile residual stresses change sharply through the thickness direction.

b) The differences in surrounding compressive residual stresses among various layers are small. The differences in compressive residual stresses between the top surface to the middle layer, and the top surface to the bottom surface at a distance of 40 mm are about 18 and 48 N/mm^2 for Section RS16-10, respectively, and 22 and 49 N/mm^2 for Section RS16-10, respectively. Hence, it is reasonable to assume the distributions of residual stresses to be constant throughout the thickness direction.
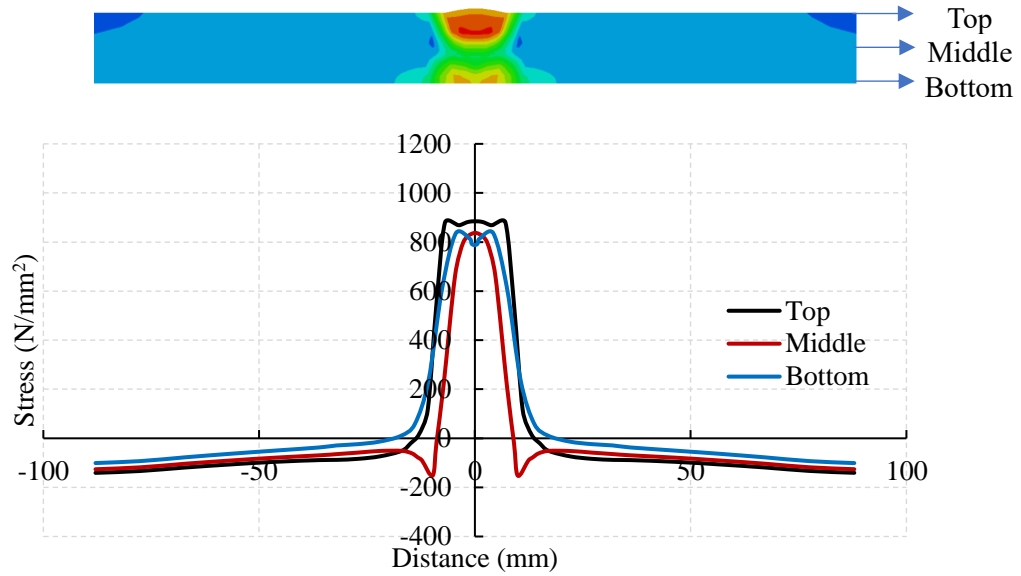
a) Section RS16-10
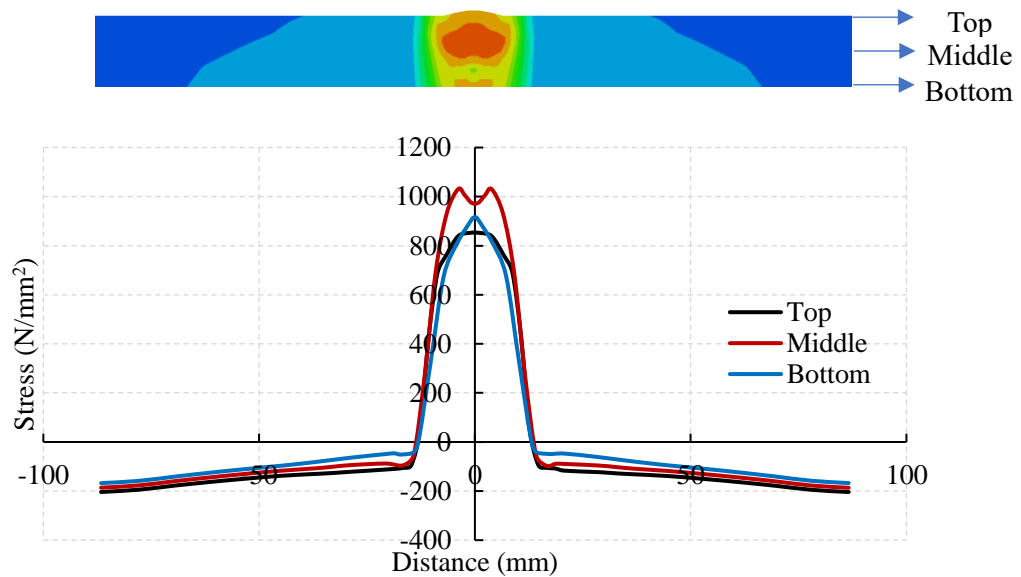
b) Section RS16-20

Figure 4.47 Residual stress distributions in various layers

4.5.1 Effect of heat input energy

It should be noted that the heat input of 2.4 kJ/mm is quite a small value in the SAW process while 5.0 kJ/mm goes beyond the upper limit of a single wire SAW machine. It is considered that Sections RS50-24 and RS50-50 in this chapter can represent a wide range of heat input energy used in practice.

In order to allow for effective comparison between these welded sections, the distance in a residual stress-distance curve is normalized respective to their respective plate widths. Considering that the tensile residual stresses change sharply in the area adjacent to the fusion zones in both the transverse and the through thickness direction, the area under curve (AUC) of these stresses outside the tensile residual stress regions are summarized and compared.

Shown in Figure 4.48, the residual stresses of 6 layers of Section RS16-10, namely L1 to L6, are extracted and the AUC of these compressive residual stresses are calculated. In order to sum up the residual stresses of each layer, a weight factor is provided according to their covered area. Hence, the weight factors of L1 and L6 are both 0.1, and the weight factors of L2 to L5 are 0.2. Based on these, the residual stresses of Section RS16-10 after summing up is calculated as:

$-84.6 \times 0.1 + -82.4 \times 0.2 + -78.5 \times 0.2 + -66.3 \times 0.2 + -52.3 \times 0.2 + -46.7 \times 0.1$

$= -69.0 \text{ N/mm}^2$

By applying this method, the stress levels of the other three sections are compared in Table 4.20. It should be noted that there are only 4 layers of elements in Section RS16-20, so only 5 layers of residual stresses were extracted. It is found that:

1) Within the same plate thickness, the increasing heat input energy leads to an increase in residual stresses. However, when the plate thick increases from 16 mm to 50 mm, the effect of increasing heat input energy becomes less significant. When the heat input energy is doubled, the residual stresses in the 16 mm thick welded sections increase by 55% while in the 50 mm thick welded sections, an increase of merely 9.4% is found.

2) The residual stresses of 50 mm thick welded sections are larger than those of 16 mm thick welded section with a heat input energy of 1.0 kJ/mm but smaller than

that with 2.0 kJ/mm.
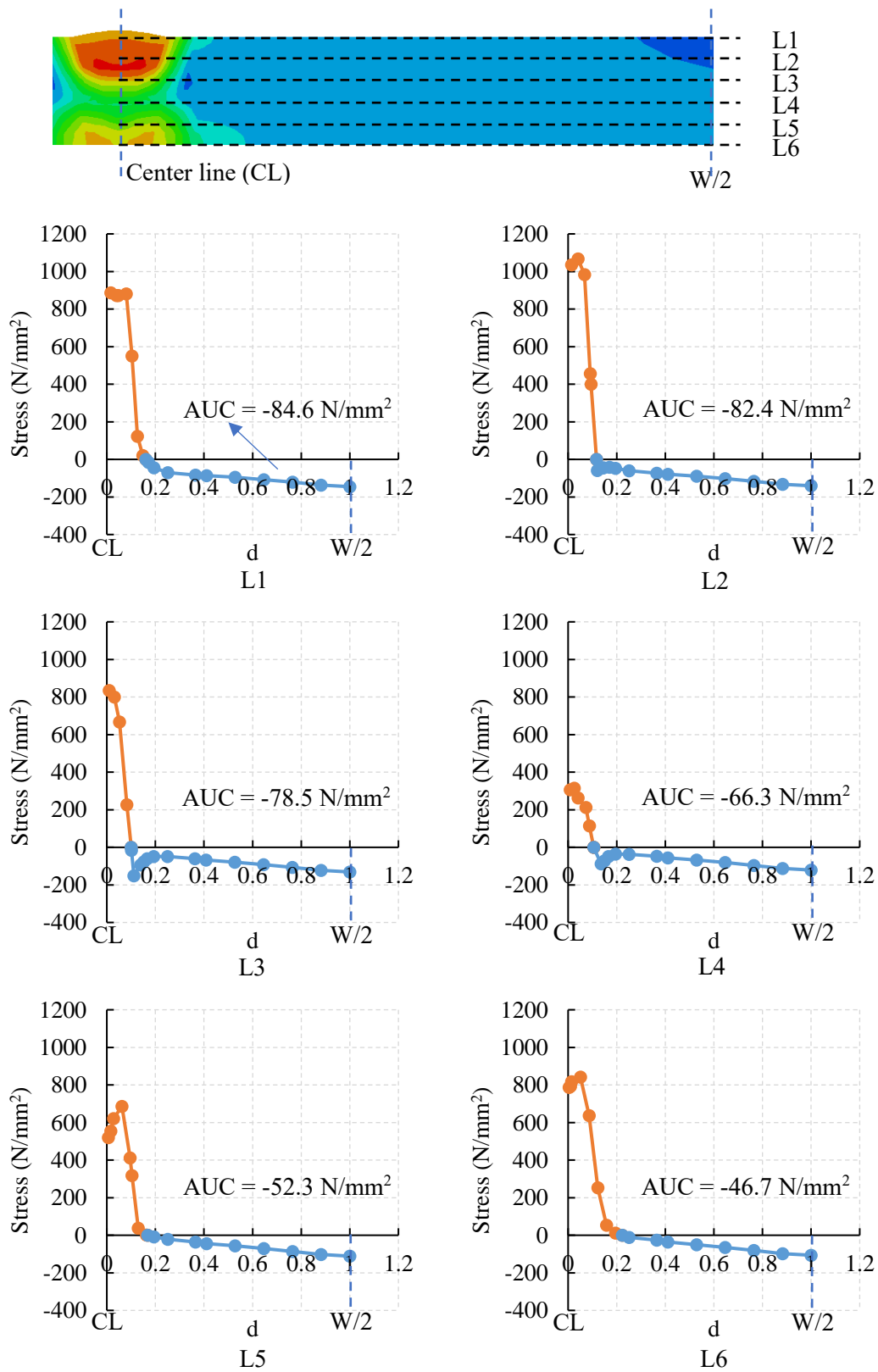
Figure 4.48 Calculation of AUC in various layers of Section RS16-10

Table 4.20 Comparison of compressive residual stress level

Layer	Section RS16-10		Section RS16-20		Section RS50-24		Section RS50-50	
	AUC (N/mm^2)	Weight	AUC (N/mm^2)	Weight	AUC (N/mm^2)	Weight	AUC (N/mm^2)	Weight
L1	-84.6	0.1	-124.6	0.125	-63.64	0.1	-82.6	0.1
L2	-82.4	0.2	-118.4	0.25	-75.0	0.2	-89.5	0.2
L3	-78.5	0.2	-108.4	0.25	-89.7	0.2	-98.1	0.2
L4	-66.3	0.2	-95.2	0.25	-92.8	0.2	-93.4	0.2
L5	-52.3	0.2	-106.9	0.125	-75.2	0.2	-77.8	0.2
L6	-46.7	0.1	-	-	-65.7	0.1	-70.2	0.1
Sum	-69.0 N/mm^2		-106.9 N/mm^2		-79.5 N/mm^2		-87.0 N/mm^2	

4.5.2 Comparison with existing standards

BS 7910 gives an equation for prediction of welding-induced residual stresses in ferrite steel plates with thicknesses varying from 24 to 300 mm. The profiles are suitable for a distance of ±1.5W from the weld center line, where W is the weld width. It is noticeable that the distribution of residual stresses along the thickness direction is considered to be constant, and also, there is no difference in the residual stresses under various heat input energy as illustrated in BS 7910.

$$\frac{\sigma_R^L}{\sigma_Y} = 1$$

where σ_R^L is the longitudinal residual stress, and

σ_Y is the smaller value of either the yield strength of the base plate or that of the weld metal.

Although the tensile residual stresses change sharply with a large stress gradient, the variation of compressive residual stresses in different layers is small, as shown in previous sections. Hence, it is reasonable to assume that the distributions of these

residual stresses along the thickness direction is constant.

The widths of the tensile stress zones are ±0.71W and ±0.84W for Sections RS50-24 and RS50-50, respectively, and ±0.73W and ±0.79W for those of Sections RS16-10 and RS16-20, respectively. Hence, the width predicted with BS 7910, that is ±1.5W, is overestimated when compared with these models, as shown in Figure 4.49.
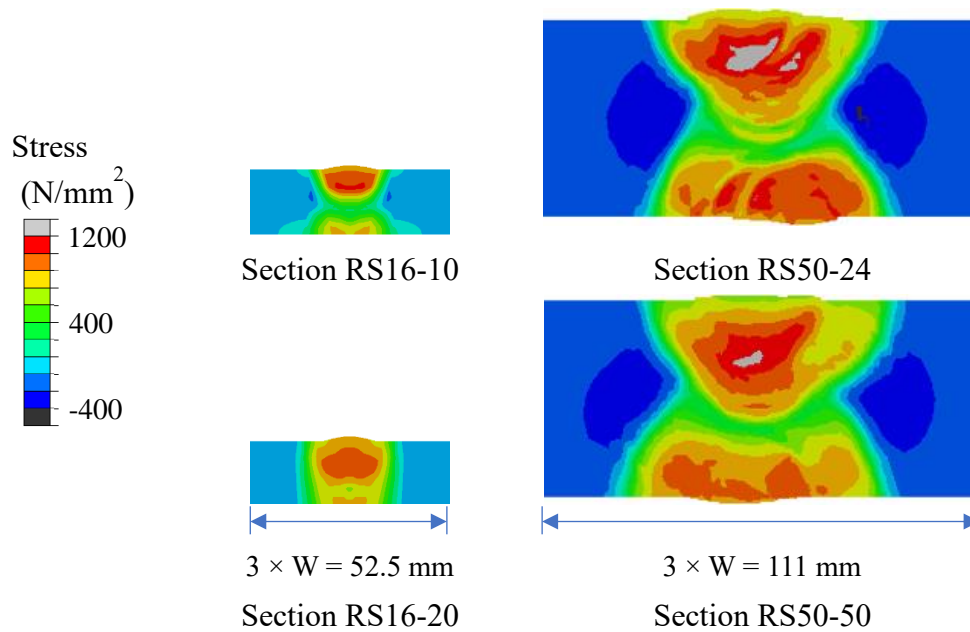
Figure 4.49 Width of tensile stress region

Then, the stress level given by BS7910 is compared with the simulation results. The stress level is set to be the yield strength of weld metal, that is 687 N/mm^2 in this case, and the suitable width is±1.5W. As shown in Table 4.21, such a prediction is conservative as it leads to at least a 75% of increment of residual stress.

Table 4.21 Update of prediction of residual stress given by BS7910

Section	RS16-10	RS16-20	RS50-24	RS50-50
Compressive residual stress (N/mm^2)	69	106.9	79.5	87
1×weld width (mm)	26.25	26.25	55.5	55.5
Normalized width	0.298	0.298	0.222	0.222
Calculated tensile residual stress (N/mm^2)	204.9	204.9	152.5	152.5
Comparison	197%	92%	92%	75%

The effect of increasing heat input energy on residual stress becomes less significant with an increase in the plate thickness. The results given in Section 4.4 show that there is only a 9.4% difference in compressive residual stresses between Sections RS50-24 and RS50-50. The prediction that there is no difference in the residual stresses under various heat input energy is highly acceptable.

4.6 Conclusions

In this chapter, the residual stress distribution of S690 QT 50 mm sections with two heat input energies, i.e. 2.4 and 5.0 kJ/mm, were investigated. The residual stresses inside the welded section can not be measured directly, so the temperature histories during welding, residual stresses on the top and bottom surfaces and the residual stresses after the local material removal method were used to calibrate the FEM. In this way, the residual stresses inside the welded sections can be extracted from the FEM. Then, the results were compared with 16 mm thick welded sections. It is found that:

1. There is small difference in the compressive residual stress level of different layers of both two S690 QT 50 mm sections under different heat input energy. For these 16 mm thick welded sections, the difference becomes significant. While the width of the tensile residual stress region is highly related to the width of the fusion zone, so there is a small difference in stress level and distribution of tensile residual stresses.

2. Heat input energy has a negligible effect on the residual stress level of S690 QT 50 mm thick welded sections. Such a finding will help simplify the analysis of the structural performance of welded members fabricated with thick plates, as the effect of heat input energy can be neglected.

3. The residual stress level of these 50 mm thick welded sections is found to be larger than that of 16 mm thick welded section with heat input energy of 1.0 kJ/mm but smaller than that with 2.0 kJ/mm.

4. Predicted residual stresses given by Standard BS 7910, that is ±1.5W, has been proved to overestimate the width of the tensile residual stress region and it provides a 75% margin in residual stress.

Chapter 5. Modelling of standard tensile tests of S690 QT and Q620 TM welded sections

5.1 Introduction

In Chapter 3, the effects of welding onto the structural behavior of both the S690 QT and the Q620 TM high strength steel under tension were investigated experimentally, and these test results have been compared with test results of S690 QT 16mm thick welded sections reported by LIU (2018). A significant reduction in the tensile strengths of the Q620 TM welded sections was found, and the reduction factors were considered to be related to the heat input energy during welding. This is readily explained with a change in the microstructures of the high strength steel plates. The transient temperature history during welding is found to have significant impacts on the microstructures of a HAZ of the welded section.

However, a systematic experimental investigation into the effects of welding onto the mechanical properties of HSS welded sections is often time consuming, and lots of resources are needed, i.e., welding of steel plates, machining of test coupons, and testing. Thus, a finite element simulation is considered to be able to reduce the workload of this whole process. For example, the effect of heat input energy on the mechanical properties of the steel plates is obtained with the simulation first, and then, the predicted results are checked with experimental results. This technique can be further used on welded members, together with a simulation of welding-induced residual stresses as shown in Chapter 4. Hence, the effects of welding onto the structural responses of a welded member are studied numerically.

Simulation of the welded sections under loading is challenging as several regions of the welded sections, i.e. the base metal, the HAZ, and the fusion zone, possess different mechanical properties. While the HAZ can be further divided into several sub-zones, as illustrated in Chapter 3, and the mechanical properties of each sub-zone change

154

continuously. Also, the heat input energy during welding influences both the mechanical properties and the dimensions of each sub-zone.

In this chapter, a Critical Sub-Zone method is proposed for the finite element simulation of the welded sections under loading. Some simplifications are made, and only the most critical sub-zone within the HAZ is considered in this proposed solution. The following two key points should be solved:

1) the mechanical properties of each sub-zone within the HAZ of a welded section, and
2) the location and dimensions of the most critical sub-zone within the HAZ of a welded section.

The S690 QT 16mm thick welded sections as well as the Q620 TM 28 and 44 mm thick welded sections under tension were simulated, and the results were verified with the measured ones given by LIU (2018), and also the results reported in Chapter 3. With this proposed solution, the simulation of the structural responses of the welded members become possible even with limited computing resources.

5.2 Mechanical properties of sub-zones in HAZ of S690 QT 16 mm thick steel

5.2.1 Heat treatment

In order to obtain the mechanical properties of various sub-zones in the HAZ of the S690 QT 16 mm thick welded sections, a thermal mechanical physical simulation process was performed to prepare heat-treated coupons of the S690 QT steel under designed temperature history. Two key parameters, the maximum temperature (T_{max}), and the cooling time from 800 to 500 °C ($t_{8/5}$), were selected to define a specific temperature history for a heat treatment procedure. The $t_{8/5}$ was defined according to a pilot study on 16 mm thick welded sections and the values of $t_{8/5}$ were found to be 5.5 s, 12.4 s and 22.0 s for heat input energy, q, at 1.0, 1.5 and 2.0 kJ/mm, respectively. The mechanical properties of these welded sections have been tested by LIU (2018).

It should be noted that a funnel-shaped coupon was used for the heat treatment, and subsequently for the tensile tests to make sure that most of the deformation takes place in the middle of the coupon under tension, which is also the heat-treated portion with a designed transient temperature history. Typical dimensions of the coupons are shown in Figure 5.1.
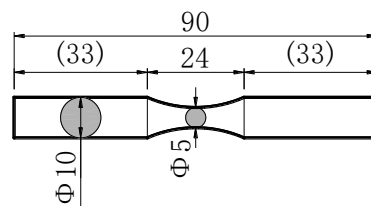
Figure 5.1 Dimension of coupons

A designation system for the heat treatment process is shown in Figure 5.2.

```
┌──────────────────── Maximum temperature, i.e. 1320 °C (1320) …
│        ┌─────────── t8/5: i.e. 5.5 s (5.5), 12.4 s (12.4) …
│        │
1320 – 5.5
```
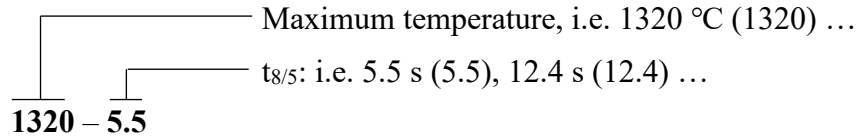
Figure 5.2 Designation system of heat treatment

5.2.1.1 Test program

A total of 24 coupons were heat-treated according to the designed heating-cooling curves with various maximum temperatures T_{max} and cooling time $t_{8/5}$, and the test program of the heat treatment is summarized in Table 5.1.

Table 5.1 Test program of heat treatment on S690 QT steel coupons

Coupons	Max temperature T_{max} (°C)	Heating rate, $R_{heating}$ (°C/s)	Top time t_{top} (s)	Cooling time $t_{8/5}$ (s)
5.5-1320	1320	100	1	5.5
5.5-1050	1050	100	1	5.5
5.5-850	850	100	1	5.5
5.5-800	800	100	1	5.5
5.5-750	750	100	1	5.5
5.5-700	700	100	1	5.5
5.5-600	600	100	1	5.5
5.5-500	500	100	1	5.5
12.4-1320	1320	100	1	12.4
12.4-1050	1050	100	1	12.4
12.4-850	850	100	1	12.4
12.4-800	800	100	1	12.4
12.4-750	750	100	1	12.4
12.4-700	700	100	1	12.4
12.4-600	600	100	1	12.4
12.4-500	500	100	1	12.4
22.0-1320	1320	100	1	22.0
22.0-1050	1050	100	1	22.0

22.0-850	850	100	1	22.0
22.0-800	800	100	1	22.0
22.0-750	750	100	1	22.0
22.0-700	700	100	1	22.0
22.0-600	600	100	1	22.0
22.0-500	500	100	1	22.0

Figure 5.3 Typical heating-cooling curve

5.2.1.2 Heat treatment process

Gleeble 3800 Thermal Mechanical Physical Simulation System as shown in Figure 5.4 a) was used to carry out the heat treatment process. For each coupon, a thermocouple was tick-welded at the center of the coupon for measurement of temperature changes. Figure 5.4 b) illustrates the coupon clamped in the chamber. Figure 5.5 shows the measured temperature history against the design values, and it is shown that the designed values of both T_{max} and $t_{8/5}$ have been achieved successfully. All the heat treatment processes were conducted in a vacuum environment to prevent any oxidation of the surfaces of the steel coupons at high temperatures. Figure 5.6 illustrates typical coupons before and after heat treatment.

a) Gleeble 3800 system
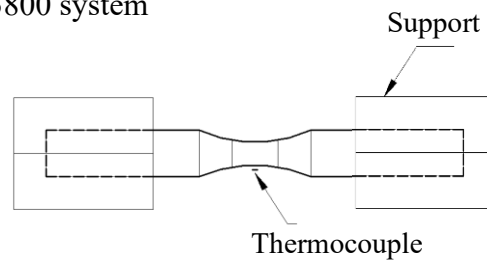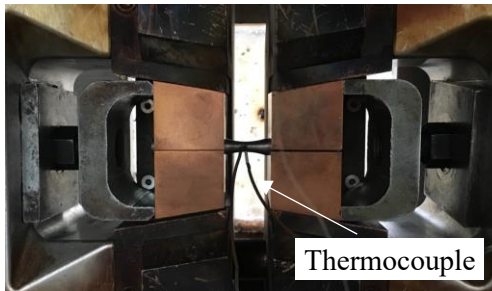
b) A detailed view of the coupon installed inside the chamber

Figure 5.4 Heat treatment to QT coupons

a) $t_{8/5}$ = 5.5 s

b) $t_{8/5}$ = 12.4 s

c) $t_{8/5}$ = 22.0 s
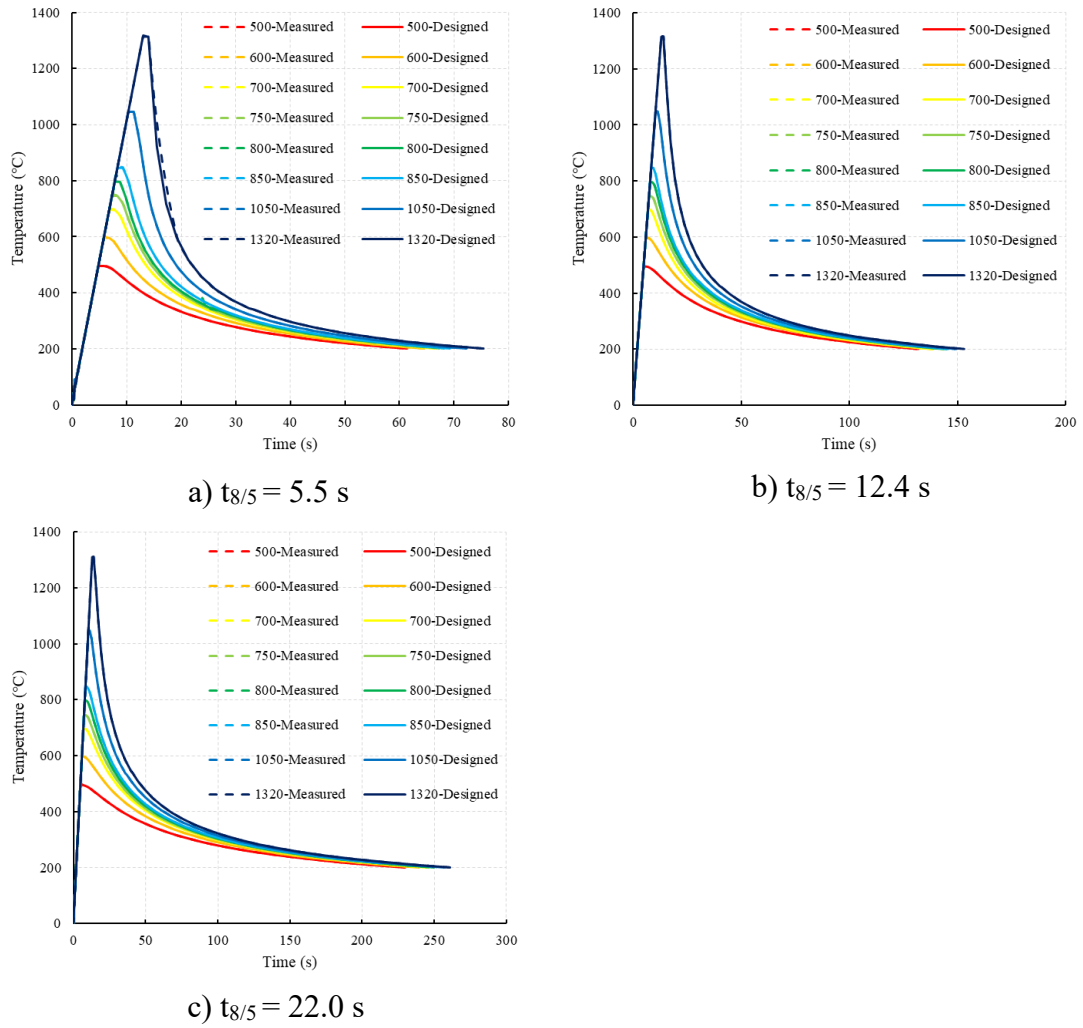
Figure 5.5 Comparison of measured and designed temperature history

a) Before heat treatment

b) After heat treatment

Figure 5.6 Typical coupons before and after heat treatment

5.2.2 Tensile tests

Typical test set-up and instrumentation of the tensile tests are shown in Figure 5.7. Monotonic tensile tests of 24 heat-treated coupons and one reference coupon of the base plate were conducted with INSTRON 8800. The gauge length of the extensometer was 10 mm. In each test, a Photographic Deformation Analysis (PDA) method was used to capture the instantaneous diameter of the coupon during the test to derive the true stress-strain relationship of the heat-treated coupon.
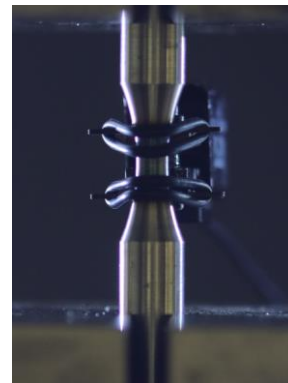
a) Typical set-up   b) Attachment of an extensometer

Figure 5.7 Test set-up for monotonic tensile tests

5.2.2.1 Test results

Figure 5.8 shows typical fracture location of these heat-treated coupons under tension. All the coupons fractured at the central parts of the funnel-shaped coupons with the minimum cross-sectional areas. Hence, all these coupons with specific designed temperature history have been tested successfully.
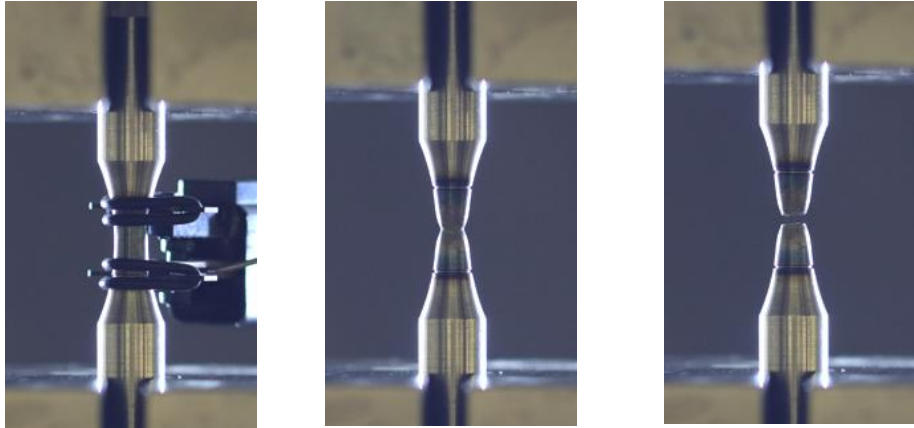
Figure 5.8 Typical fracture of a heat-treated coupon under tension

The measured stress-strain curves and their key mechanical properties are presented in Figure 5.9 and Table 5.2, respectively. The curves are classified according to the cooling time $t_{8/5}$, which means that in each group of these coupons, they have the same $t_{8/5}$ but different T_{max}. It is shown that:

Owing to different T_{max} and $t_{8/5}$, microstructural change took place at the central portion of these funnel-shaped coupons. According to their continous cooling transfomation characteristices, different phases of the steel were formed according to various cooling time $t_{8/5}$. For those coupons with high T_{max} and small $t_{8/5}$, martensite was formed in the coupons which possessed high strengths up to 1200 N/mm^2. Other phases, such as tempered martensite, and dual phase martensite and ferrite were also formed. As these phases possessed lower strength, these phases controlled mechanical properties of the HAZ, and hence, of those of the welded connections. It should be noted that

1) These three curves follow the same trend, i.e. there are no changes in their tensile strengths before T_{max} exceeds 700 °C. This is readily explained as the lower critical temperature (Ac$_1$) of this S690 QT steel is 735 °C, i.e. when a phase change starts. This will lead to a change in their mechanical properties of the steel.

Then, with an increase in T_{max}, the tensile strengths of the coupons within each

162

group decrease, and become smaller than that of the base plate. The decrease ends at 750, 800, and 800 °C for those coupons having $t_{8/5}$ equals 5.5, 12.4 and 22.0 s, respectively. After this, the tensile strengths of the coupons in each group increase with an increasing T_{max}.

2) Comparison the tensile strengths of these heat-treated coupons with that of the base metal presented in Figure 5.10 shows that the range of T_{max} for those heat-treated coupons with tensile strengths smaller than that of the base plate increases with an increase in $t_{8/5}$. Also, the reduction of the tensile strengths becomes more significant for a given T_{max} with an increase in $t_{8/5}$.

3) As also shown in Figure 5.10, it is obvious that when $t_{8/5}$ equals 5.5 s, the coupon with T_{max} of 750 °C has the smallest tensile strength. While for those coupons with $t_{8/5}$ equal to 12.4 s and 22.0 s, the coupons with T_{max} of 800 °C have the smallest tensile strengths. Thus, 750 °C is considered to be the most critical T_{max} in a HAZ with continuously changing temperature when $t_{8/5}$ equals 5.5 s. When the $t_{8/5}$ goes beyond 12.4 s, the most critical T_{max} is found to be 800 °C.
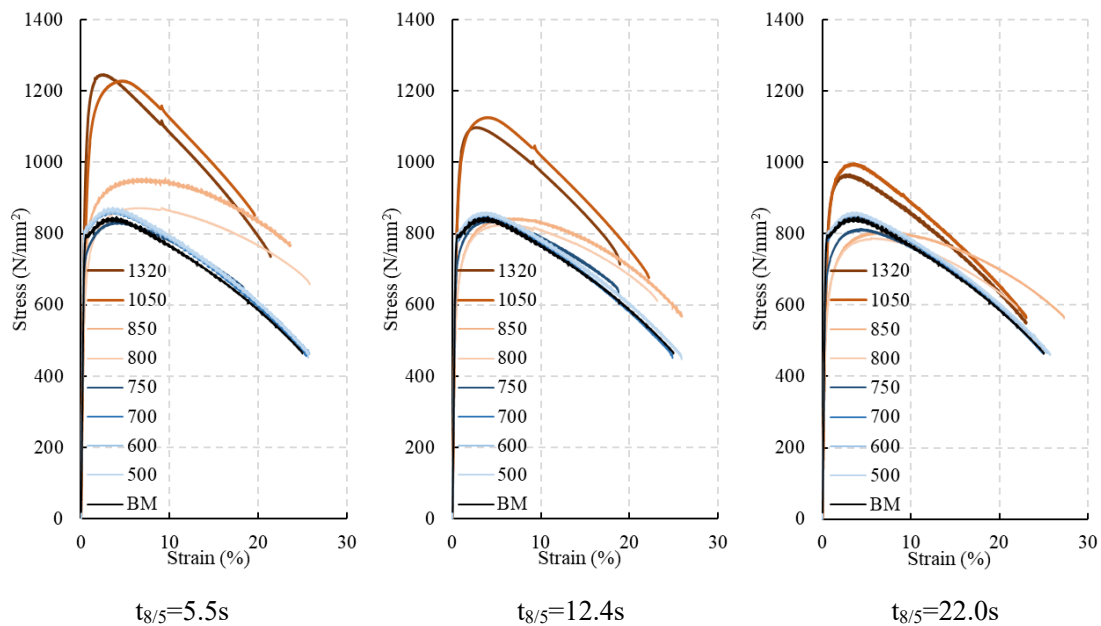
Figure 5.9 Measured stress-strain curves of S690 QT heat-treated coupons

Table 5.2 Measured mechanical properties of S690 QT heat-treated coupons

#	Young's Modulus (kN/mm^2)	Yield strength (N/mm^2)	Tensile strength (N/mm^2)
Base plate	242	790	852
5.5-1320	250	1025	1246
5.5-1050	203	893	1229
5.5-850	203	718	957
5.5-800	182	595	853
5.5-750	224	731	833
5.5-700	224	805	865
5.5-600	224	811	866
5.5-500	219	812	873
12.4-1320	213	896	1098
12.4-1050	210	830	1122
12.4-850	184	610	844
12.4-800	201	594	826
12.4-750	214	707	839
12.4-700	223	780	847
12.4-600	224	777	855
12.4-500	229	799	861
22.0-1320	197	787	966
22.0-1050	200	760	997
22.0-850	167	586	805
22.0-800	172	559	789
22.0-750	204	684	814
22.0-700	225	780	852
22.0-600	219	797	856
22.0-500	212	798	861
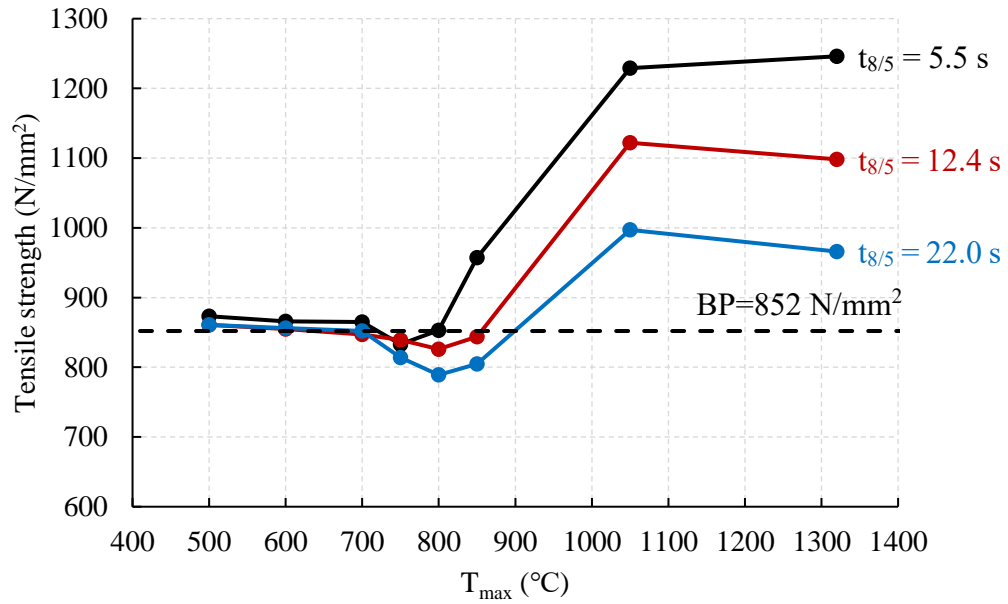
Figure 5.10 Variations of tensile strengths of S690 QT heat-treated coupons

5.2.3 The Critical Sub-Zone method

A complete description on the complete process of changes in the mechanical properties of the steel during welding is considered to be very difficult to simulate as many material data are needed to define the phase transformation during the heating-and-cooling process, and also to define specific microstructures. To simplify the simulation, any change in the microstructures of the steel plates are not considered. Instead, the modified mechanical properties of the steel plates are directly related to the temperature history of the welded sections, as shown in Figure 5.11.
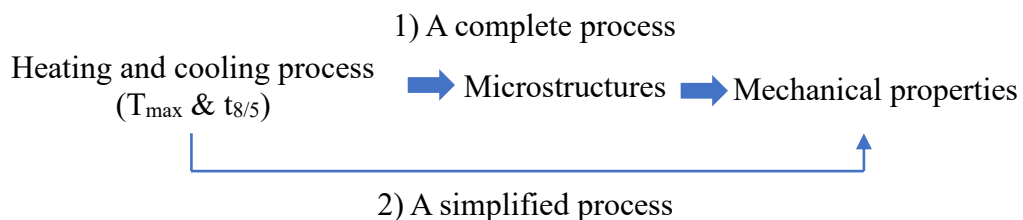
Figure 5.11 Simplification on changes in mechanical properties

a) Simplification 1: define of critical sub-zone

Temperatures change continuously within the HAZ of the welded sections, and this means that the microstructures, and hence, the corresponding mechanical properties of the steel grains within the HAZ change continuously. However, being restricted by the element sizes, the HAZ is divided into several regions, each with the same set of mechanical properties, and only the most critical one is considered in the numerical model.

A HAZ with $t_{8/5}$ = 22 s is set as an example of this simplification. As shown in Figure 5.12, only the critical sub-zone as marked with the black lines, is taken into consideration, and the tensile strength of the other part is set to be equal to the base plate (BP). The width of the critical sub-zone is determined by both the lower and the higher temperature boundaries, T_l and T_h, respectively.

With the simplification discussed above, for $t_{8/5} \geq 12.4$ s:

1) T_l is set to be constant in these heat treatment processes, because, as shown in Figure 5.12, there are no changes in the tensile strengths of those coupons with t_{max} under 700 °C, and hence, it is set to be the average of 700 °C and the most critical temperature, 800 °C, and this gives 750 °C.

2) As shown in Figure 5.10, T_h is always changing because the temperature range for those heat-treated coupons with tensile strengths smaller than those of the base plate increases with an increase of $t_{8/5}$. When $t_{8/5}$=22.0 s, the heat-treated coupon with T_{max} of 900 °C is considered to have a tensile strength equal to that of BP, so T_h is set to be the average of 800 °C and T_{BP} (900 °C). In this case, this gives 850 °C.

Similarly, for $t_{8/5}$ = 5.5 s, T_l is set to be the average of 700 and 750 °C, i.e. 725 °C, and T_h is the average of 750 °C and T_{BP} (800 °C), i.e. 775 °C.

166
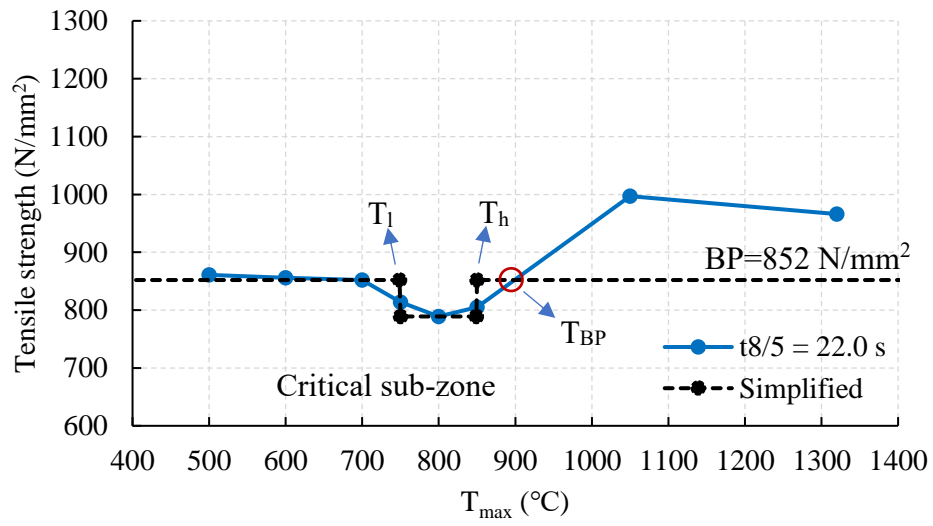
Figure 5.12 Modification of tensile strengths against T_{max} (°C)

5.3 Locations of critical sub-zones

Two S690 QT 16 mm thick welded sections with heat input energy of 1.0 and 2.0 kJ/mm, namely WS16-10 and WS16-20, were studied. The location of the critical sub-zone within the HAZ of a welded section depends heavily on the temperature distribution in the region adjacent to the weld line. The temperature changes sharply in this region, making it difficult to be measured accurately. So, the distribution of the critical sub-zone was simulated with a highly non-linear heat transfer analysis through finite element modelling. In order to determine the transient temperature history within these two welded sections effectively, 2-D heat transfer models were established according to the weld passes and welding parameters recorded by LIU, as shown in Figure 5.13.

a) Model WS16-10

b) Model WS16-20
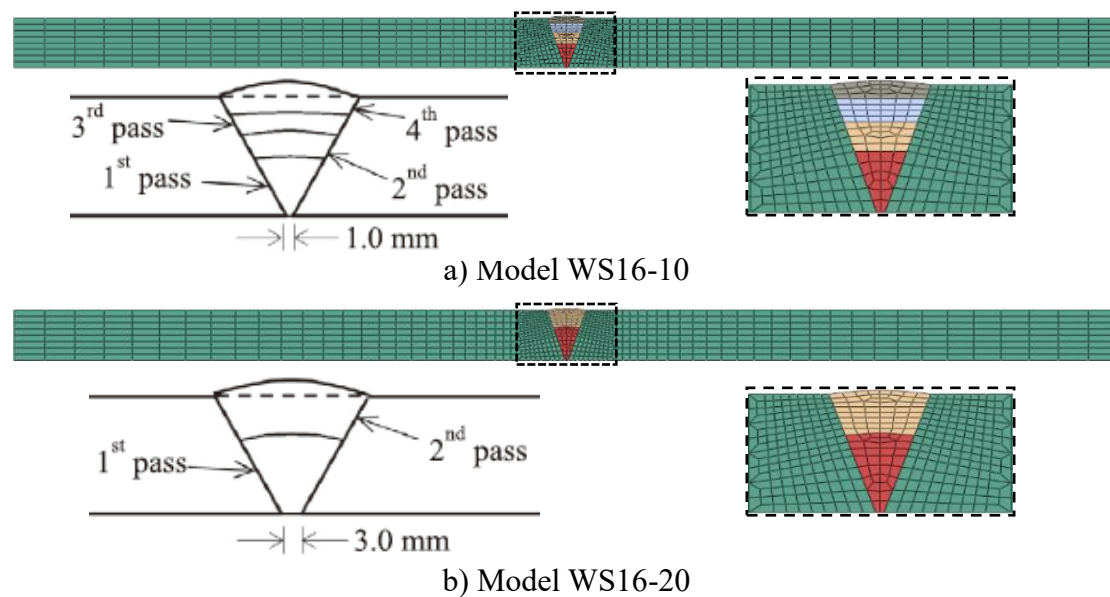
Figure 5.13 Heat transfer models of S690 welded sections

The cross sectional distributions of the temperature for each weld pass were extracted twice with different legends, as shown in Figure 5.14. The maximum temperatures for each legend were set to be 725 and 775 °C, which are the lower and the higher temperature boundaries, T_l and T_h, respectively, as defined in the last section. It should be noted that the temperature field shown in Figure 5.14 was selected to demonstrate that the maximum area of the grey region was achieved within each pass.

168

Then, the boundaries of the maximum temperatures in each cross section were extracted, and overlaid together. Weld pass 3 is taken as an example to be shown in Figure 5.15 a). By repeating the steps above, and overlaying repeatedly these cross sections of each pass together, the location of the critical sub-zone in the welded section is readily derived, as shown in Figure 5.15 c).

725 (T_l when t8/5 = 5.5s) 0	775 (T_h when t8/5 = 5.5s) 0
Legend	
a) Pass 1	
b) Pass 2	
d) Pass 3	
d) Pass 4	
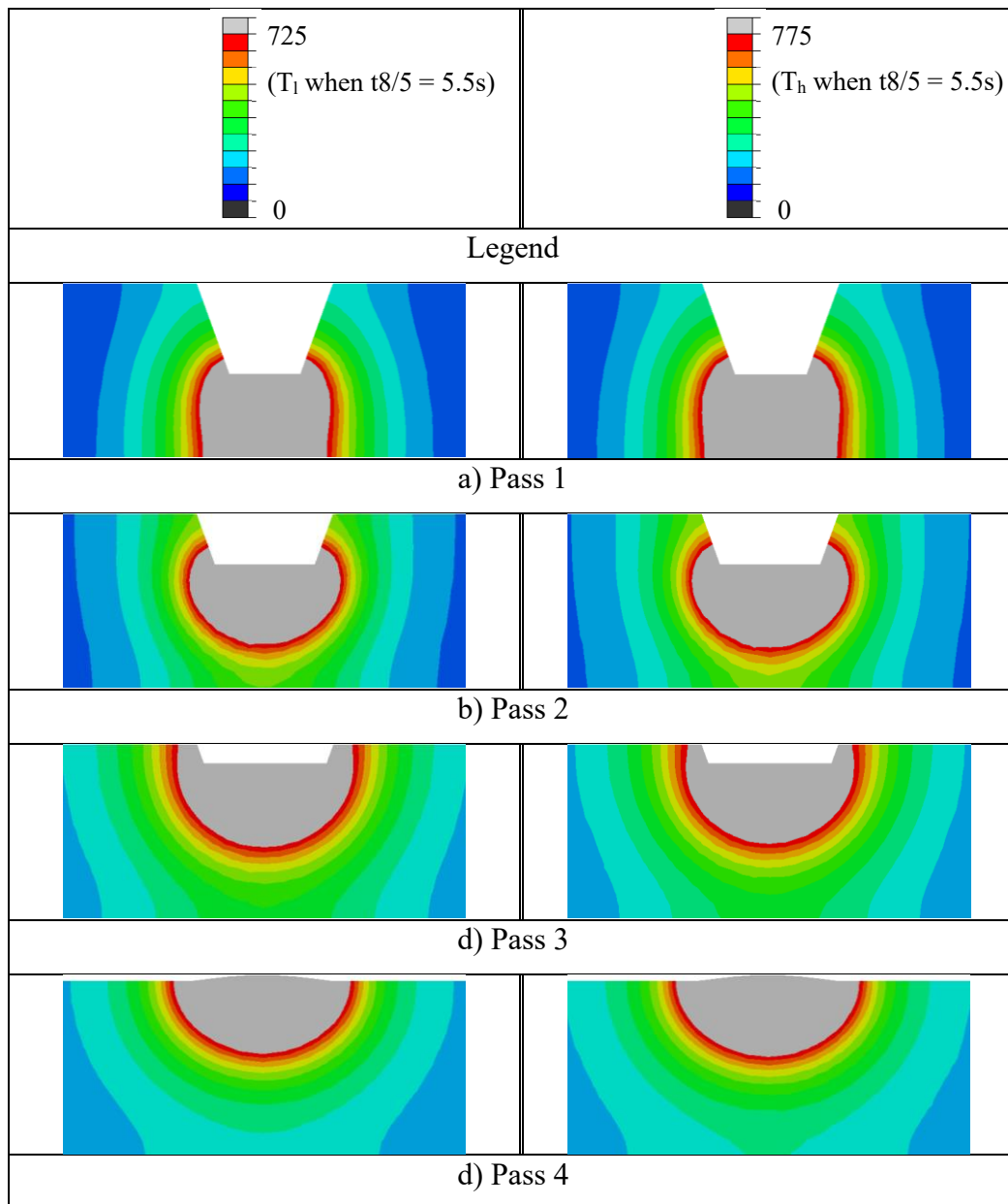
Figure 5.14 Cross sectional temperature distributions of Model WS16-10

169

725 °C   775 °C
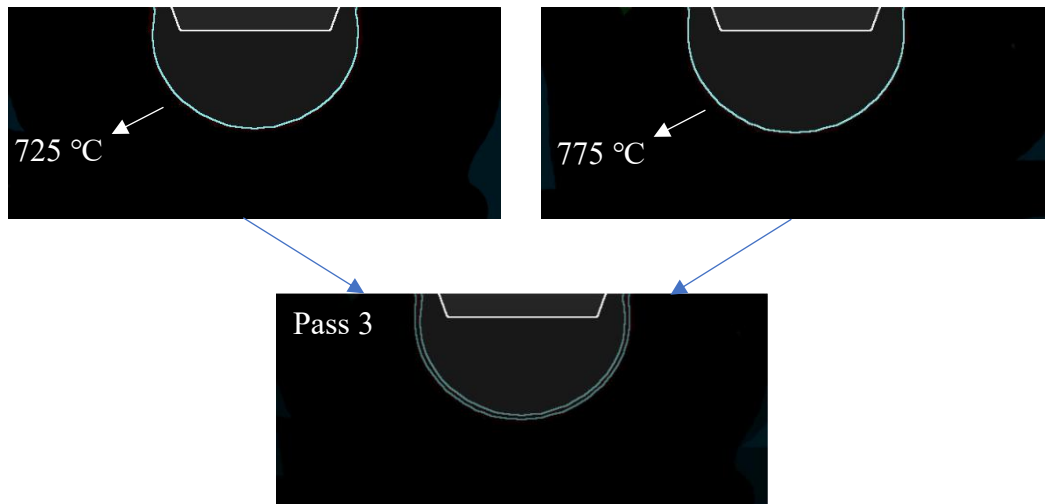
Pass 3

a) Critical sub-zone caused by weld pass 3

Pass 1   Pass 2

Pass 4
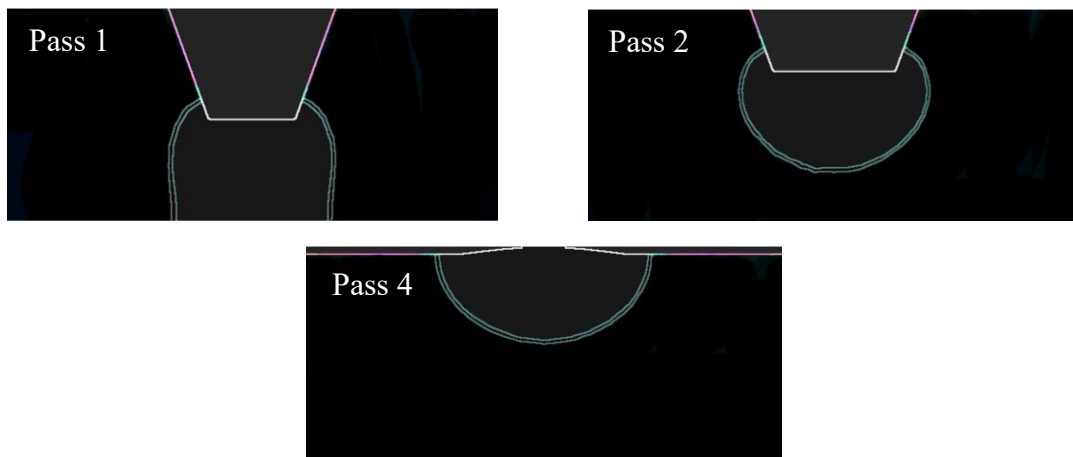
b) Critical sub-zone caused by other weld passes
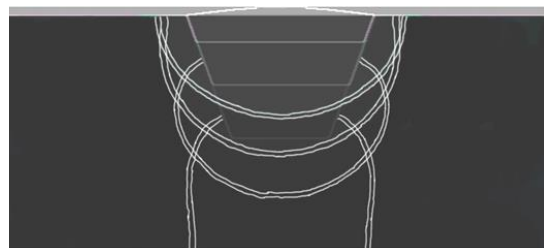
c) A complete image of various critical sub-zones

Figure 5.15 Overlaying of critical sub-zones in Model WS16-10

The process was carried out again, and the maximum temperatures for each of these legends were set to be 750 and 850 ℃ for Section WS16-20.

750 (T$_l$ when t8/5 = 22s) ... 0	850 (T$_h$ when t8/5 = 22s) ... 0
Legend	
a) Pass 1	
b) Pass 2	
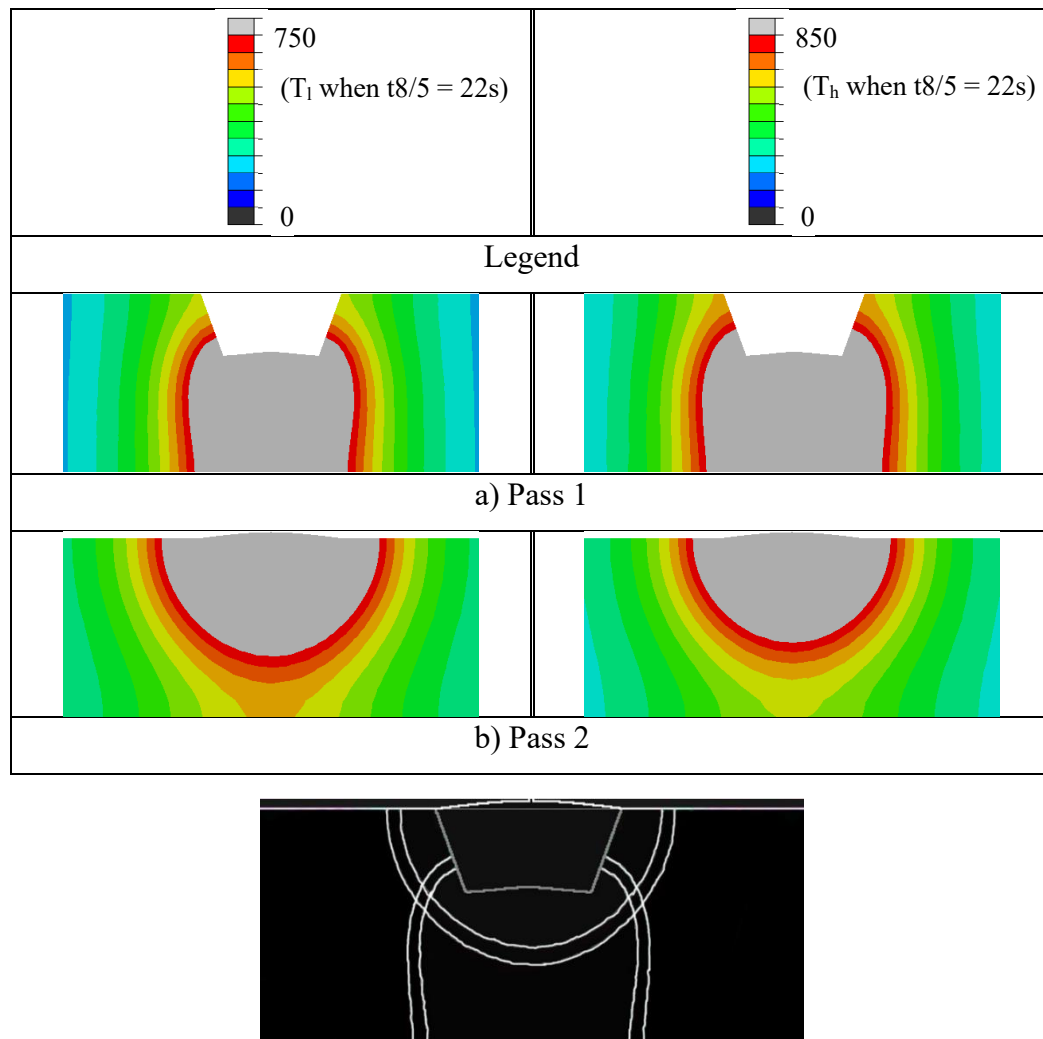
Figure 5.16 Allocating the critical sub-zone in Model WS16-20

5.3.1   Simplifications for the Critical Sub-Zone method

a) Simplification 2: $t_{8/5}$ in a welded section

It should be noted that the $t_{8/5}$ of all elements heated up in each pass in a welded section is not the same. However, their differences are typically small. Hence, it is considered to be acceptable for the HAZ under investigation to be produced with a constant heat input energy during welding, and the corresponding $t_{8/5}$ for all the elements are considered to be constant during the simulation process. As shown in Figure 5.17, the values of $t_{8/5}$ at different locations of weld passes 1 and 2 are illustrated to establish that the difference in $t_{8/5}$ of all these elments, and they are found to be within the range of 22 ± 1.8 s.

a) Legend

b) Weld pass 1

Weld pass 1

Point	P11	P12	P13
$t_{8/5}$ (s)	23.2	23.0	22.6

c) Weld pass 2

Weld pass 2

Point	P21	P22	P23
$t_{8/5}$ (s)	22.6	21.5	21.3
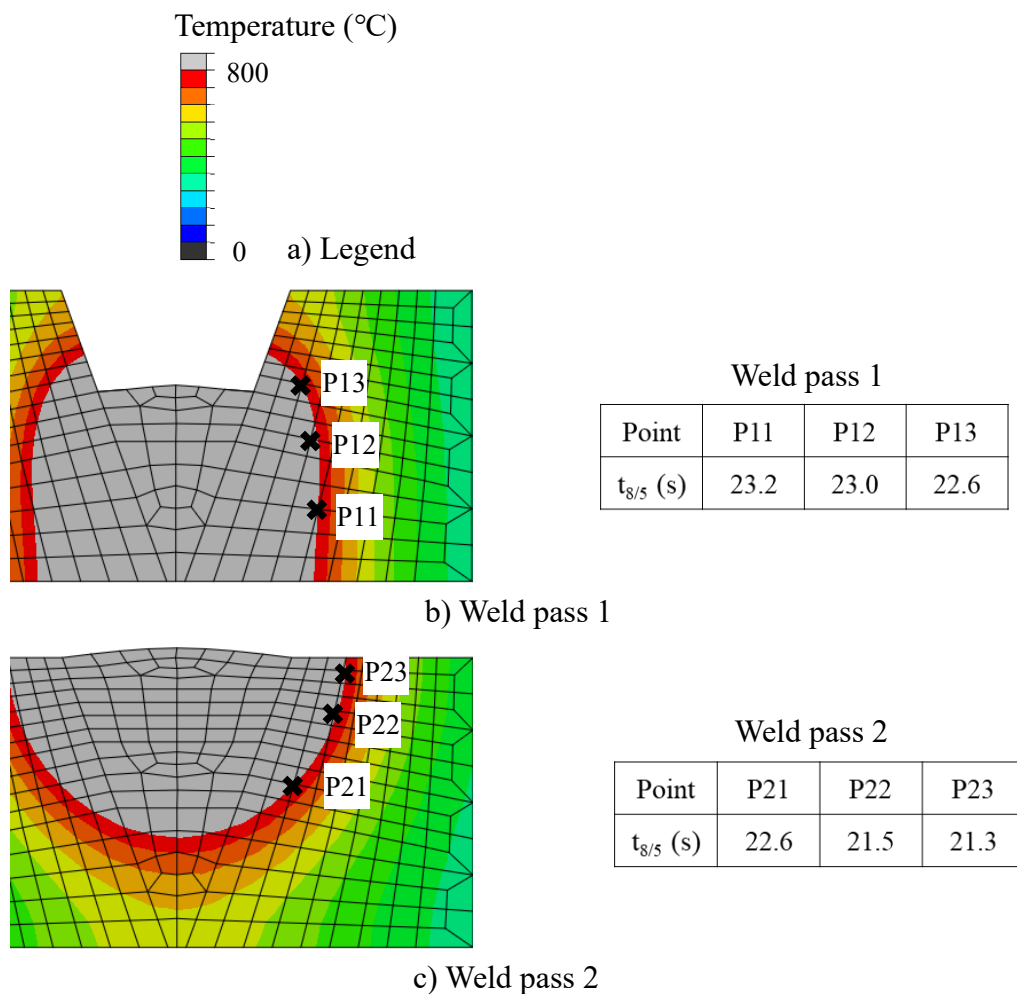
Figure 5.17 Typical $t_{8/5}$ values for various weld passes in Model WS16-20

b) Simplification 3: geometry of critical sub-zone

As shown in Figure 5.18, the coupons tested by LIU (2018) were extracted from the mid height of these welded sections. So, the critical sub-zones are simplified to have straignt edges, as highlighted in yellow for easy modeling, and the slopes of the critical sub-zones are assumed to follow those of the groove. As the groove and heat source were systematic along the center line of cross section, the critical sub-zones also located systematically. In Figure 5.18, a1 and a2 are the width of the critical sub-zone and the distance of the critical sub-zone to the groove, respectively, and they can be read from the overlayed figures.

a1=0.26 mm

a2=1.4 mm

Φ = 6 mm

Model WS16-10

a1=1.1 mm

a2=3.8 mm

Φ = 6 mm

Model WS16-20
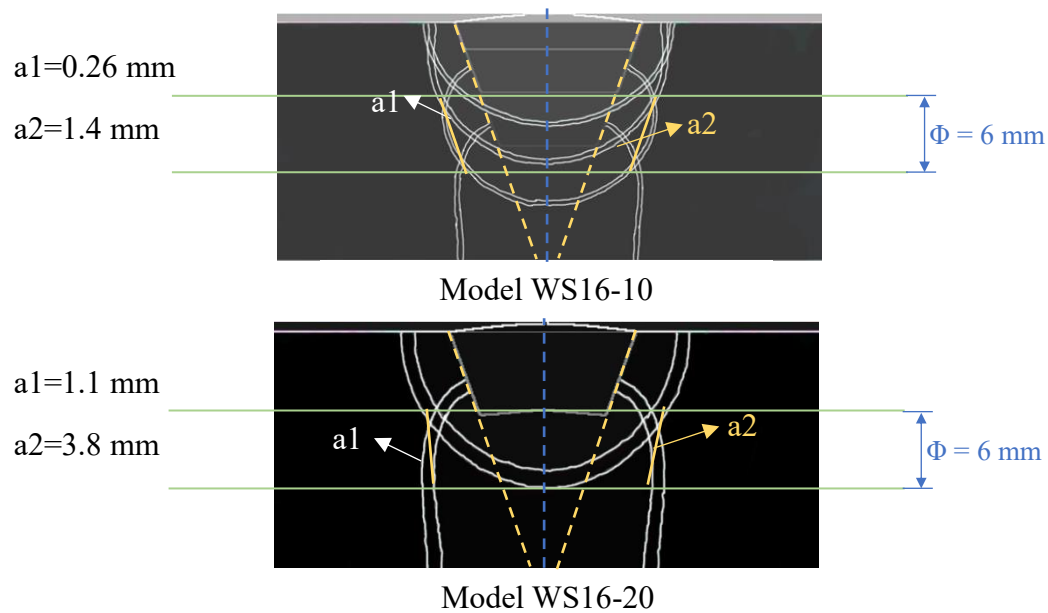
Figure 5.18 Simplification of critical sub-zones

5.4 Modeling of tensile tests on coupons of welded sections

Advanced finite element models have been developed to simulate the structural behavior of the welded sections of high strength steel plates. In modelling the HAZ of the welded sections, the proposed simplified critical sub-zones described in the last section, as shown in Figure 5.19, was adopted. The dimensions of the model is the same as those reported in LIU (2018).

a) Model S16-10

b) Model S16-20

■ Base plate   ■ Weld metal   ■ Critical sub-zone
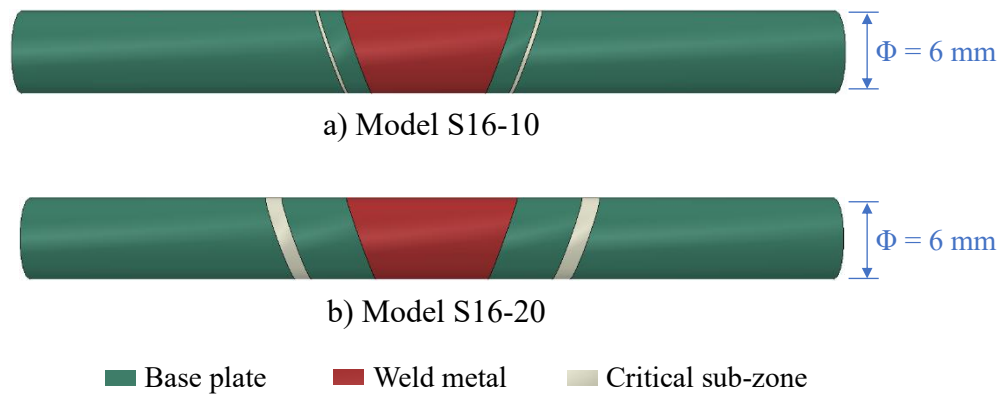
Figure 5.19 Finite element models of typical coupons of welded sections

5.4.1 Constitutive model of critical sub-zones

Being different from those standard coupons of both the base plate and the weld metal, the heat-treated coupon has non-standard geometry, and the width of the heat-treated region with homogenous microstructures is unknown. Hence, a sensitivity study is performed.

In this study, the width of the heat-treated region with homogenous microstructures is assumed to take up three different values, i.e. 1.0, 1.5 and 2.0 mm. Three different models, namely Models F-10, F-15 and F-20, were established according to various assumptions shown in Figure 5.20. Owing to symmetry, only one-eighth model of the coupon within the gauge length region was established to minimize computational resources. There are two parts in each model: the base plate (highlighted in white) and

the heat-treated region (highlighted in green). The true stress-strain curve of the base plate was obtained from test results of a standard tensile test.
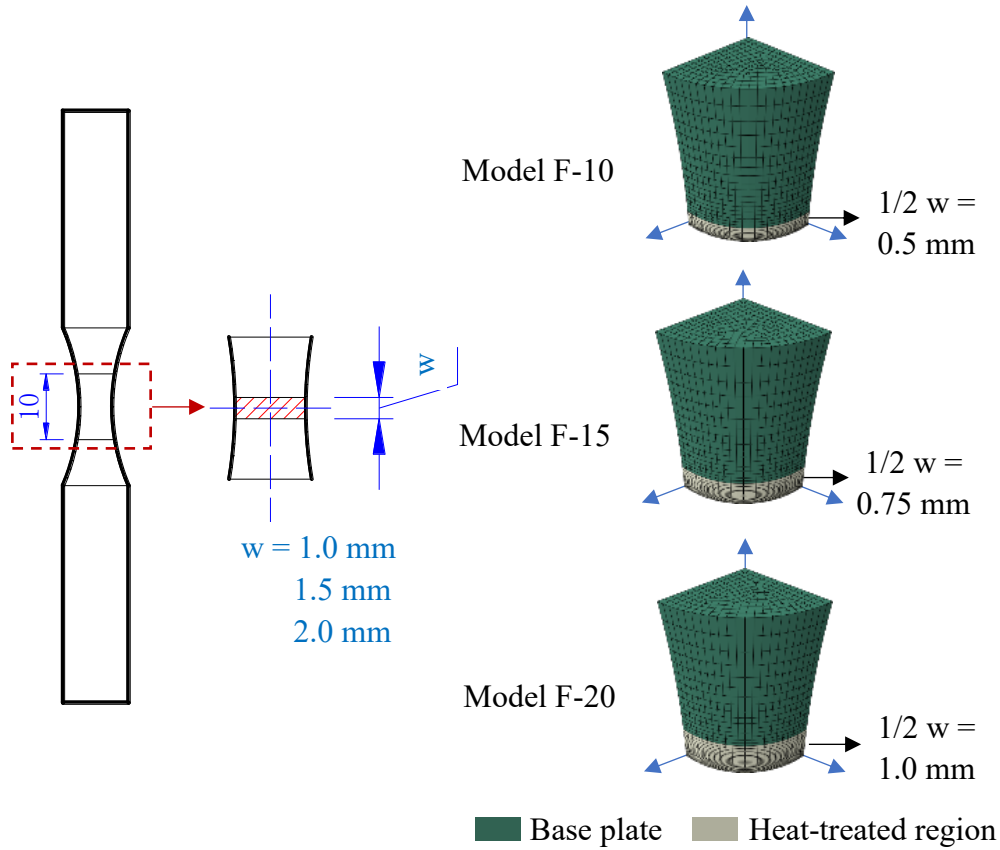
Figure 5.20 Finite element models of a funnel-shaped coupon

In order to derive the constitutive model of the funnel-shaped coupon, an iterative method proposed by Yao (2016) was employed, and details of the iterative method is shown in Figure 5.21:

1) The basic true stress-strain curve of the heat-treated coupon was derived from the traditional integration method, which is suitable for standard coupons.

2) Then, the basic true stress-strain (σ_t-ε_t) curve is updated as follows:

$$\sigma_{t(i+1)} = \left.\frac{F_{M(i)}}{F_{F(i)}}\right|_{V_{(i)}} \sigma_{t(i)}$$

where $\sigma_{t(i+1)}$ is the updated true stress

$F_{M(i)}$ is the measured force obtained in the test at displacement $V_{(i)}$

$F_{F(i)}$ is the predicted force calculated in the model at displacement $V_{(i)}$

$\sigma_{t(i)}$ is the Von Mises stress at the central node of the root cross section at displacement $V_{(i)}$

while $\varepsilon_{t(i+1)}$ is set to be the Von Mises strain at the central node of the root cross section at displacement $V_{(i)}$.

3) The true stress-strain (σ_t-ε_t) curve will be modified gradually, until the simulated force-displacement curve meets the measured one well.
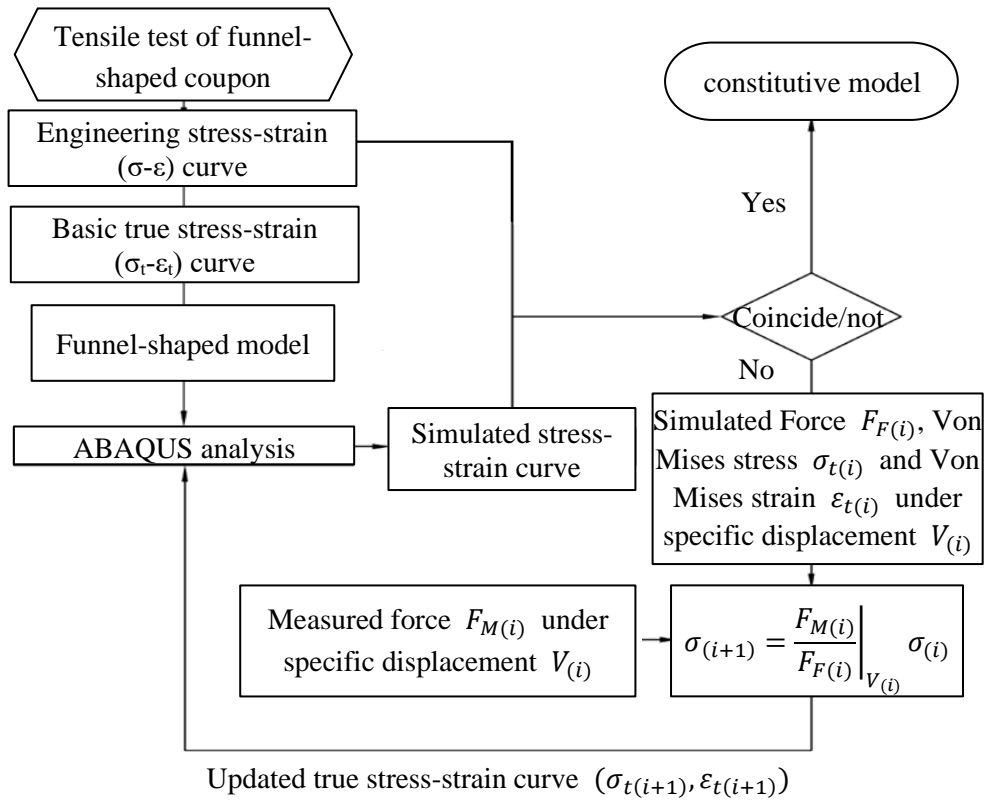
Figure 5.21 Iterative method for constitutive model of a funnel-shaped coupon

Take Coupon 22-800 as an example, by applying the iterative method with funnel-

shaped Models F-10, F-15 and F-20, three true stress-strain (σ_t-ε_t) curves, namely, True-F-10, True-F-15 and True-F-20, were obtained, and they are plotted in Figure 5.22.
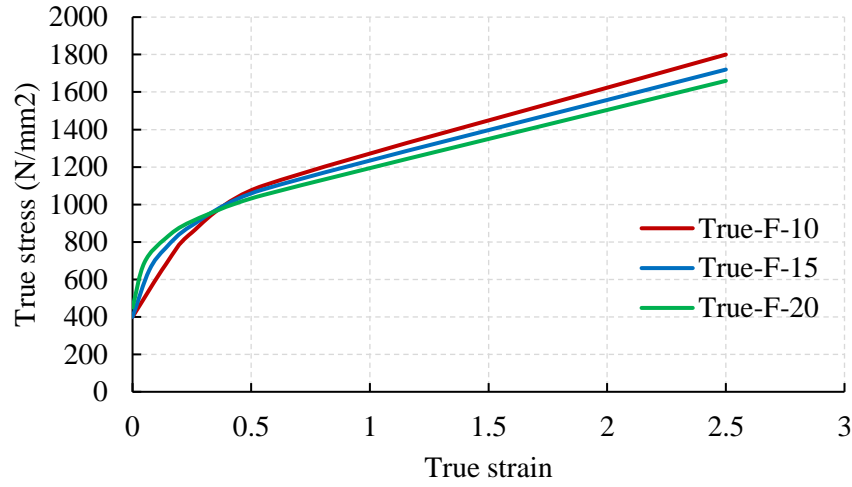
Figure 5.22 True stress-strain (σ_t-ε_t) curves of Coupon 22-800 obtained with iterative method

5.4.2   Simulation of tensile tests

By inputting these true stress-strain curves of Coupon 22-800 into Model 16-20 shown in Figure 5.19 b), the predicted tensile behavior of the coupon from Section WS16-20 can be obtained. The critical sub-zones in Models S16-20-F10, S16-20-F15 and S16-20-F20 were assigned to adopt the true stress-strain curves, True-F-10, True-F-15 and True-F-20, respectively. It should be noted that the gauge length was set at the middle of the coupon, that is, the HAZs at both sides and fusion zones was covered in the gauge length region.

Figure 5.23 shows the deformed meshes of the models at stress level about 580 N/mm^2, and it is found that necking takes place at the critical sub-zones of all the models successfully. A comparison of the engineering stress-strain (σ-ε) curves based on the measured and the predicted results is shown in Figure 5.24, while their tensile strengths are compared as shown in Table 5.3. It is obvious that Model S16-20-F10, which adopted the true stress-strain (σ_t-ε_t) curve True-F-10 based on Model F-10, gives the

177

best predicted results with only an error of 0.9% in the tensile strength.

Consequently, the width of the heat-treated region with constant mechanical properties in typical heat-treated coupons is taken rationally to be 1.0 mm. Hence, Model F-10 is readily employed to obtain the true stress-strain (σ_t-ε_t) curves of various coupons in the following sections.

a) Model S16-20-F10

b) Model S16-20-F15

c) Model S16-20-F20

■ Base plate   ■ Weld metal   ■ Critical sub-zone
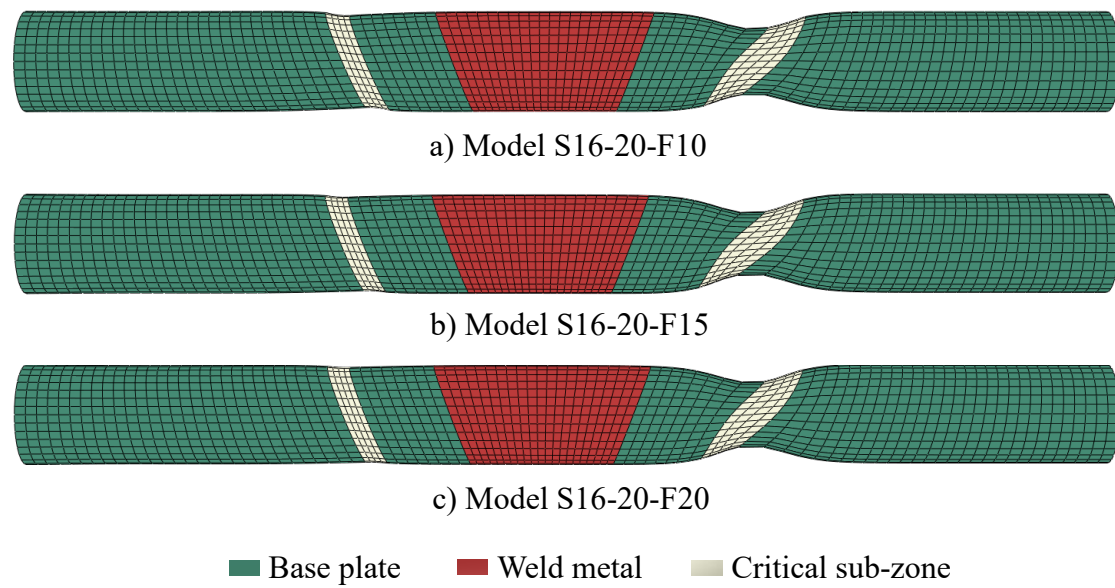
Figure 5.23 Deformed shapes of various models with critical sub-zones in HAZ
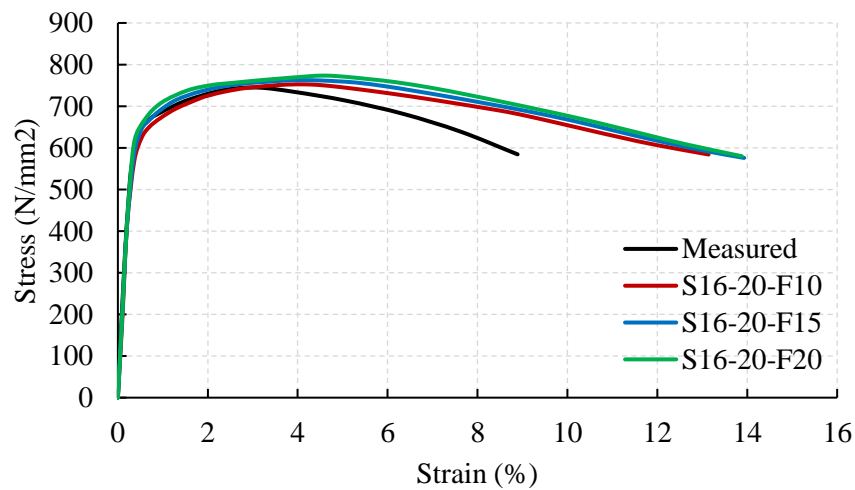
Figure 5.24 Comparison of measured and predicted engineering stress-strain curves of coupon S16-20 with various models

Table 5.3 Comparison of measured and predicted tensile strengths of Coupon S16-20

	True stress-strain of critical sub-zone	Tensile strength (N/mm^2)	Error (%)
Coupon S16-20	-	745	-
Model S16-20-F10	True-F-10	752	0.9
Model S16-20-F15	True-F-15	763	2.4
Model S16-20-F20	True-F-20	774	3.9

Through the iteration method, the true stress-strain (σ_t-ε_t) curves of Coupon 5.5-700 is obtained, and it is plotted in Figure 5.25.
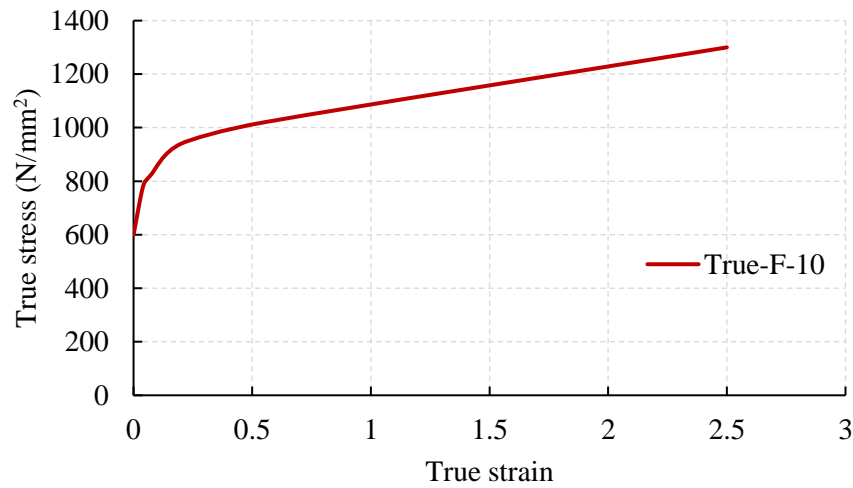
Figure 5.25 True stress-strain (σ_t-ε_t) curve of Coupon 5.5-700 obtained with iterative method with Model F-10

By inputting this true stress-strain (σ_t-ε_t) curve (shown in Figure 5.18 a) into Model 16-10, the predicted tensile behavior of the coupon from Section WS16-20 can be obtained. The necking takes place in a region adjacent to the critical sub-zone, and the deformed meshes with stress level about 524 N/mm^2 is shown in Figure 5.26. The simulated engineering stress-strain curve is compared with the measured one in Figure 5.27 and a good comparison between these two curves is achieved. The predicted tensile strength of the coupon is found to be 798 N/mm^2, and it compares well with that of the measured one, which is 808 N/mm^2, and an error of -1.2% is achieved.

179
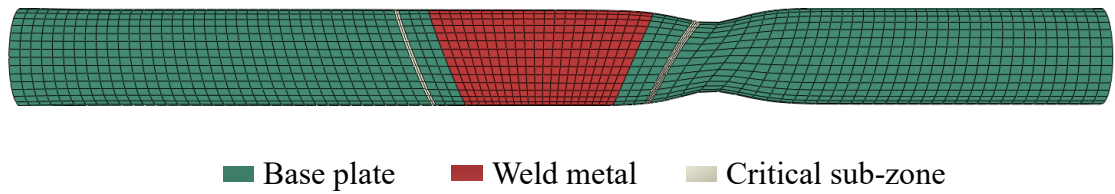
Figure 5.26 Deformed shapes of model with critical sub-zones in HAZ
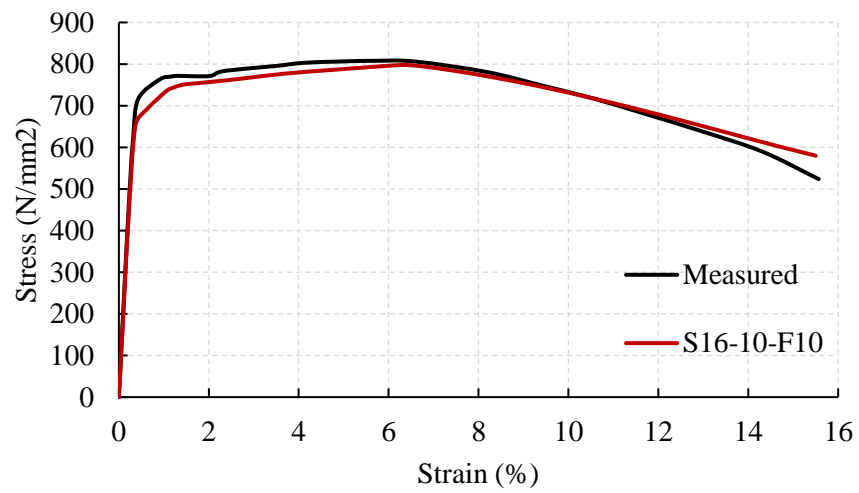
Figure 5.27 Comparison of measured and predicted engineering stress-strain (σ-ε)

curves of Coupon S16-10

5.4.3 Effect of gauge length regions in coupons of welded sections

In the tensile tests of the coupons of both the base plates and the welded sections reported by LIU (2018), strain gauges were used in the initial deformation stage to measure elongations up to 5%, and the yield strengths of these coupons were derived according to these data. However, such a setup is considered to lead to a significant difference in the yield strengths of a welded section when different gauge length regions are adopted.

Consider Model S16-20-F10 as an example. Two gauge length regions, namely GL-1 and GL-2, are set up in the model as shown in Figure 5.28, and the length of these two regions is 25 mm. Figure 5.29 shows a comparison of engineering stress-strain curves of the measured results to those of the predicted results according to the two cases of Regions GL-1 and GL-2. The corresponding yield strengths are found to be 647, 618 and 588 N/mm^2, respectively, and hence, the corresponding errors of these cases are 4.5% and 9.2% for cases of GL-1 and GL-2, respectively.

This is readily explained as there are several regions with different mechanical properties within a welded section, and these regions elongate with different strain levels when the welded section is under tension. This is clearly demonstrated in the DIC measurement results reported in Section 3.5 in Chapter 3. The differences in the proportion of different regions in the two cased of GL-1 and GL-2 leads to a different strain level under the same applied force.

In such tensile tests of coupons of welded sections, the author recommends using an extensometer and it should be placed to cover both HAZs around the weld metal.

181

a) Initial state

b) At stress level about 580 N/mm²
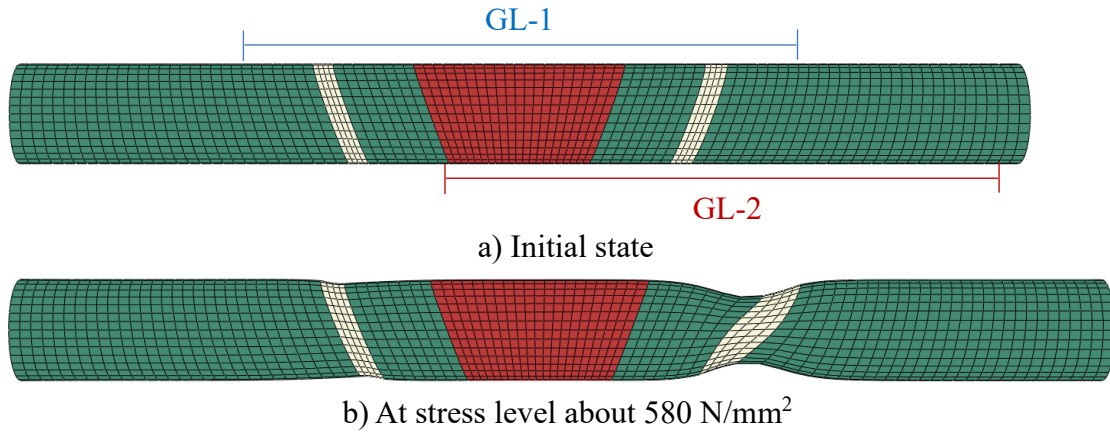
Figure 5.28 Different gauge length regions in typical coupon Model S16-20-F10
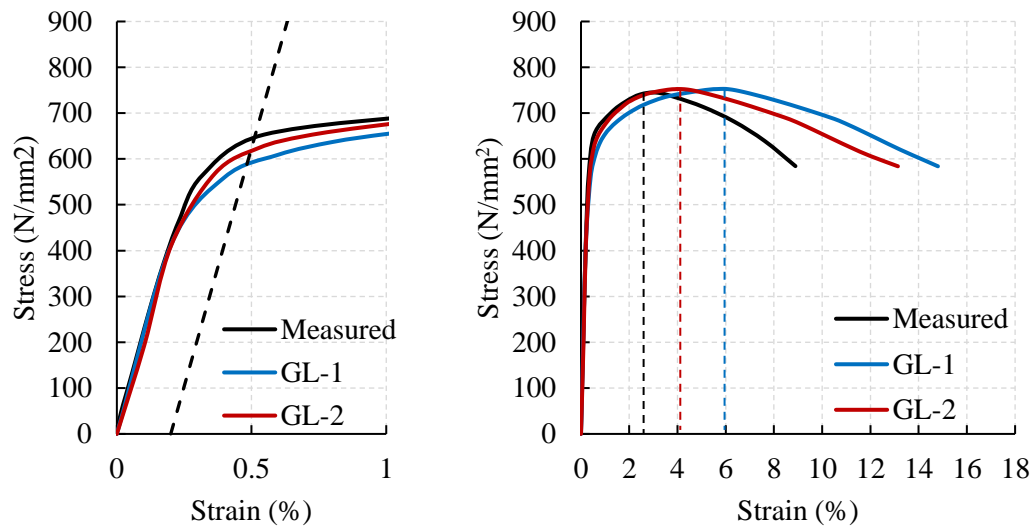
Figure 5.29 Comparison of engineering stress-strain curves of different gauge length

regions

Table 5.4 Comparison of measured and predicted mechanical properties

	Yield strength f_y (N/mm²)	Tensile strength f_u (N/mm²)	Ultimate strain at f_u (%)
Measured	647	745	3.1
GL-1	618	752	4.0
GL-2	588	752	5.9

5.4.4 Effect of distribution of critical sub-zones

In Model S16-20-F10, the inclination angle of the critical sub-zone is set to be 20°, which is the same as the groove of the welded section. In this section, the effect of the inclination angle is investigated. As shown in Figure 5.30, three models, namely, Models A-0, A-20 and A-40, each with an angle of 0°, 20° and 40°, respectively, were analyzed. The width of the critical sub-zone remains unchanged at 1.1 mm. Model A-20 is the same as Model S16-20-F10. A new designation system is used for these models for easy reference.

a) Model A-0

b) Model A-20

c) Model A-40
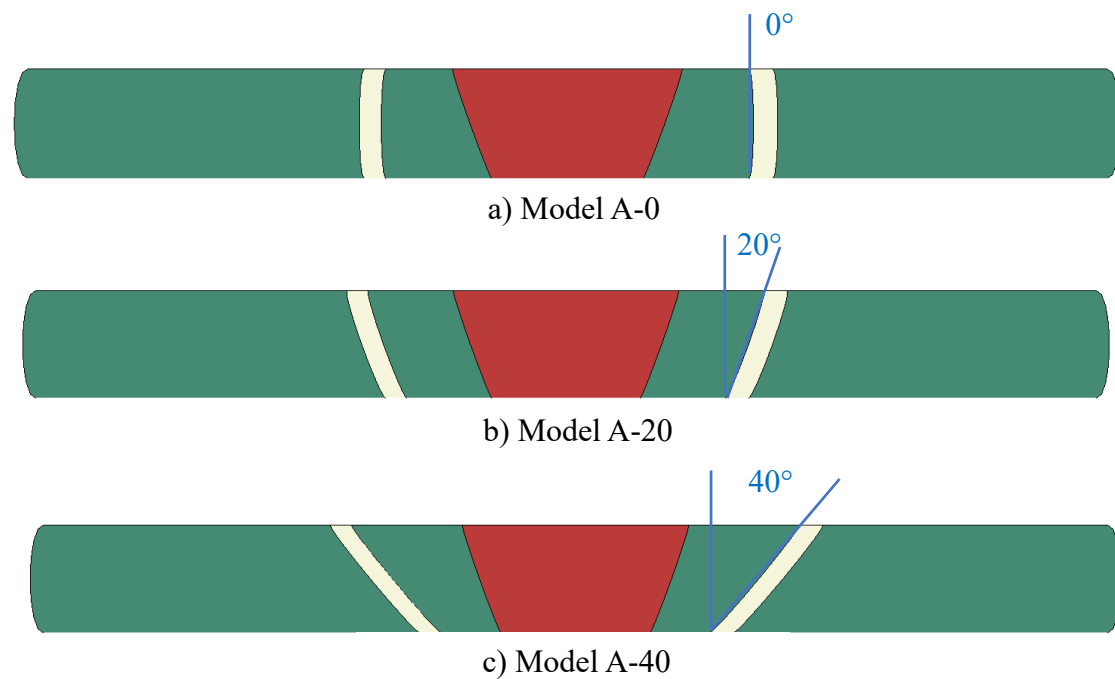
Figure 5.30 Models with various angles of critical sub-zones

The deformed meshes with stress level about 580 N/mm^2 are shown in Figure 5.31. The engineering stress-strain curves were extracted with Gauge Length region GL-2 shown in the last section, and they are plotted in Figure 5.32 for easy comparison. The tensile strengths of Models A-0, A-20 and A-40 are found to be 745, 752 and 767 N/mm^2, respectively, and there are only limited differences. So, setting the inclination angle of the critical sub-zone to be the same with that of the groove is able to provide satisfied results.

183

a) Model A-0

b) Model A-20

c) Model A-40
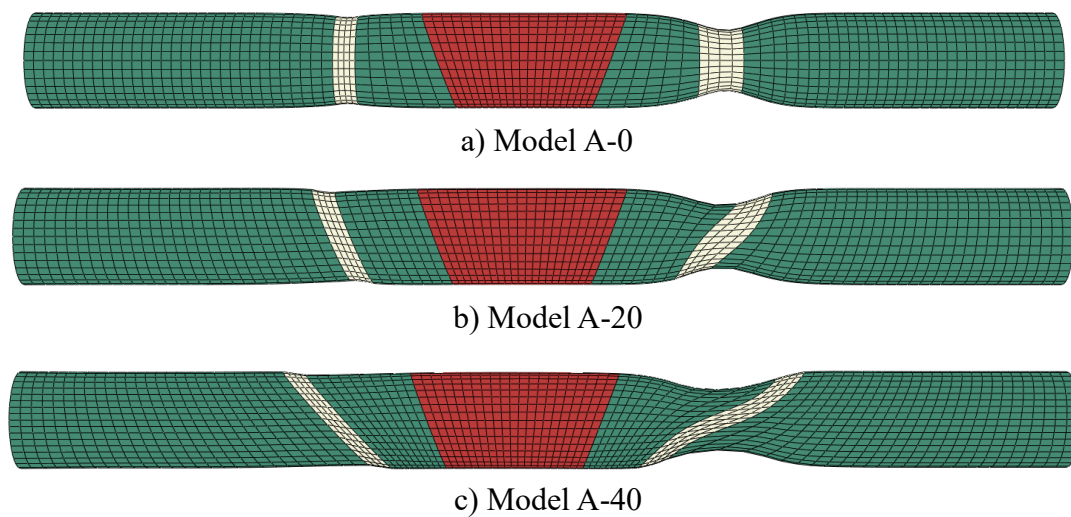
Figure 5.31 Simulated coupons after necking: inclination angles
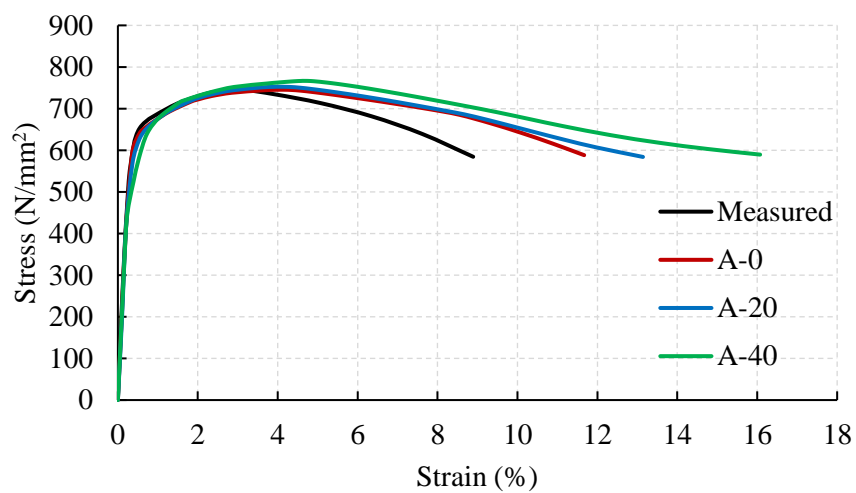
Figure 5.32 Comparison of engineering stress-strain curves: inclination angles

5.4.5 Effect of mesh size of critical sub-zones

In the previous sections, there were 4 layers of elements in the longitudinal direction of the coupon within the critical sub-zone. In this section, the mesh size of the critical sub-zone is investigated. As shown in Figure 5.33, three models, namely, Models M-1, M-2 and M-4, are built, and there are 1, 2 and 4 layers of elements in the critical sub-zone, respectively. Model M-4 is the same as Model S16-20-F10. A new designation system is used for these models for easy reference.

1.1 mm in width

| a) Model M-1 | b) Model M-2 | c) Model M-4 |
| element size: 1.1 mm | element size: 0.55 mm | element size: 0.275 mm |
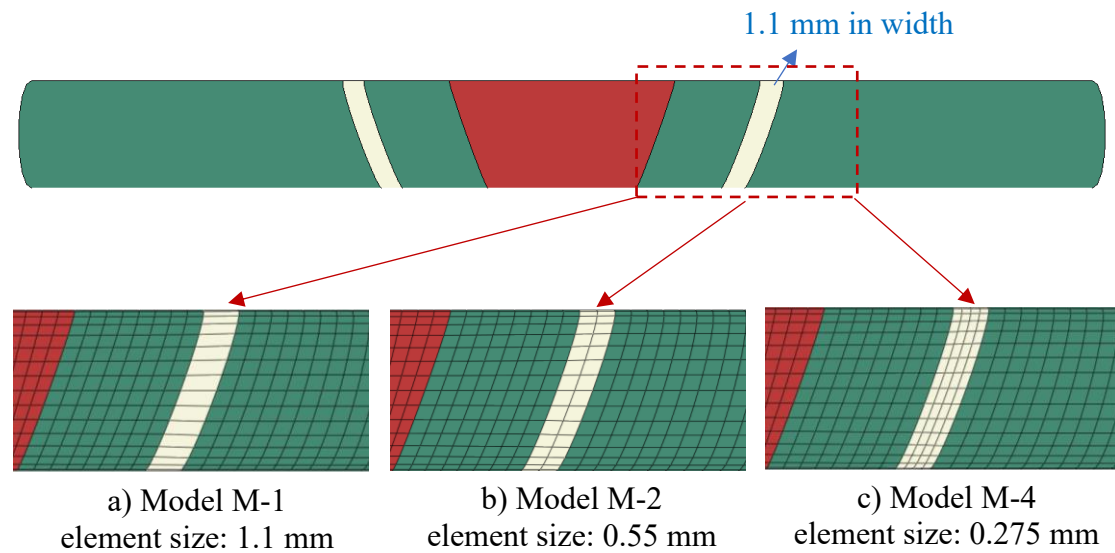
Figure 5.33 Models with various mesh sizes for the critical sub-zones

The simulated coupons at stress level about 580 N/mm^2 are shown in Figure 5.34. The stress-strain curves were extracted with Gauge length GL-2 shown in the last section, and these curves are plotted in Figure 5.35. The tensile strengths of models M-1, M-20 and M-40 are found to be 748, 752 and 753 N/mm^2, respectively. It is obvious that the differences in the results among these three models are neglectable.

a) M-1

b) M-2

c) M-4
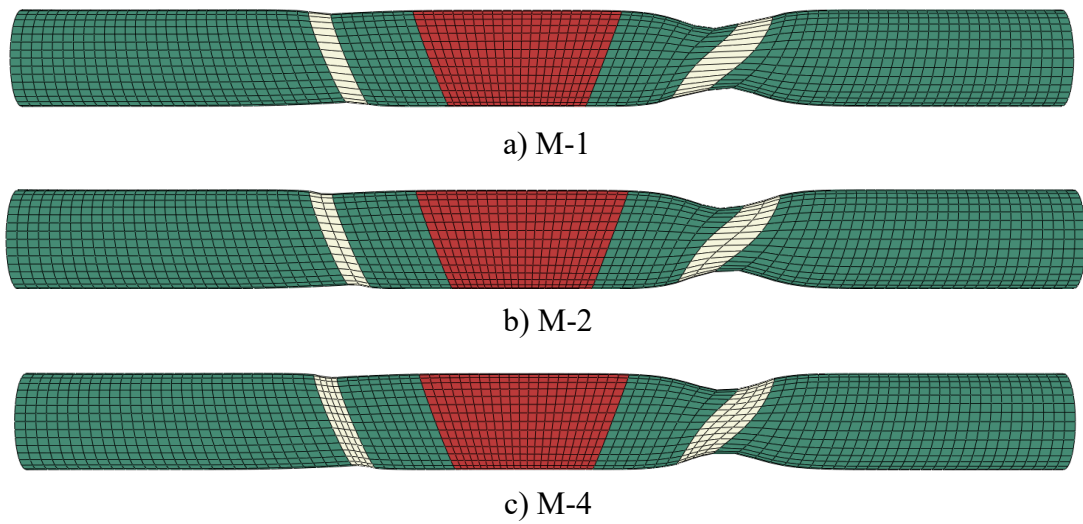
Figure 5.34 Simulated coupons after necking: element sizes
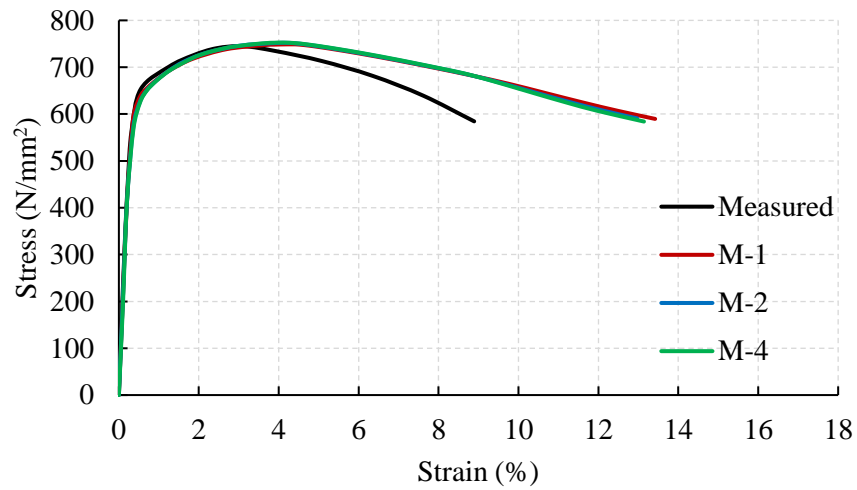
Figure 5.35 Comparison of engineering stress-strain curves: element sizes

5.5 Q620 TM 28 and 44 mm welded sections

In order to obtain the mechanical properties of the sub-zones in the HAZ of the Q620 TM 28 and 44 mm thick welded sections, and to make a direct comparison between the Q620 TM steel to the S690 QT steel, the same heat treatment processes were performed to prepare heat-treated coupons of the Q620 TM steel. Considering that the similar mechanical properties and microstructures between 28 mm thick and 44 mm thick plates, the coupons were only made from the Q620 TM 28 mm thick plates.

5.5.1 Heat treatment tests

A test program is shown in Table 5.5. The same set-up and instrumentation described in Section 5.2 are adopted.

Table 5.5 Test program of heat treatment on Q620 TM steel coupons

Coupons	Max Temperature T_{max} (°C)	Heating rate, $R_{heating}$ (°C/s)	Top time t_{top} (s)	$t_{8/5}$ (s)
5.5-1320	1320	100	1	5.5
5.5-1050	1050	100	1	5.5
5.5-850	850	100	1	5.5
5.5-800	800	100	1	5.5
5.5-750	750	100	1	5.5
5.5-700	700	100	1	5.5
5.5-600	600	100	1	5.5
5.5-500	500	100	1	5.5
12.4-1320	1320	100	1	12.4
12.4-1050	1050	100	1	12.4
12.4-850	850	100	1	12.4
12.4-800	800	100	1	12.4
12.4-750	750	100	1	12.4
12.4-700	700	100	1	12.4
12.4-600	600	100	1	12.4
12.4-500	500	100	1	12.4
22.0-1320	1320	100	1	22.0
22.0-1050	1050	100	1	22.0
22.0-850	850	100	1	22.0
22.0-800	800	100	1	22.0
22.0-750	750	100	1	22.0
22.0-700	700	100	1	22.0
22.0-600	600	100	1	22.0
22.0-500	500	100	1	22.0

All the heat-treatment processes were performed successfully. Tensile tests on these heat-treated coupons were conducted and the engineering stress-strain (σ-ε) curves of these coupons were plotted in Figure 5.36. Table 5.6 summarizes their measured mechanical properties. Unfortunately, the extensometer was not fixed properly during testing of Coupons 5.5-600 and 22.0-600, and their stress-strain curves were unable to be provided.

Figure 5.37 plots the tensile strengths of these heat-treated coupons against the maximum temperature, T_{max}. The curves are classified based on the cooling time $t_{8/5}$. Hence, in each group, the coupons have the same $t_{8/5}$ but different T_{max}. Similar to the S690 QT steel, the mechanical properties of the heat-treated coupons are highly dependent on the temperature history during heat treatment. It should be noted that:

1) There is no change in the tensile strength when T_{max} are below 500 °C. Then, with an increase in T_{max}, the tensile strengths in each group of the coupons decrease, and in many cases, they become smaller than that of the base plate. Such a decrease ends at 700 °C for each group.

   The lower critical temperature (Ac1) of the Q620 TM steel is 725 °C so there are phase changes when T_{max} exceeds 725 °C, which will lead to change of their mechanical properties. For T_{max} below 725 °C, diffusion of carbides occurs in the bainite, and the strength of bainite reduces with the diffusion of caribide.

2) Similar with the S690 QT steel, the range of T_{max} for heat-treated coupons with tensile strengths smaller than that of the base plate increases with an increase in $t_{8/5}$, and the reduction of tensile strengths becomes more significant for a given T_{max} with an increase in $t_{8/5}$.

3) Heat-treated coupons with T_{max} of 700 °C have the smallest tensile strength in each

189

group, and thus, 700 °C is considered to be the most critical T_{max} within the HAZ of the Q620 TM welded sections.
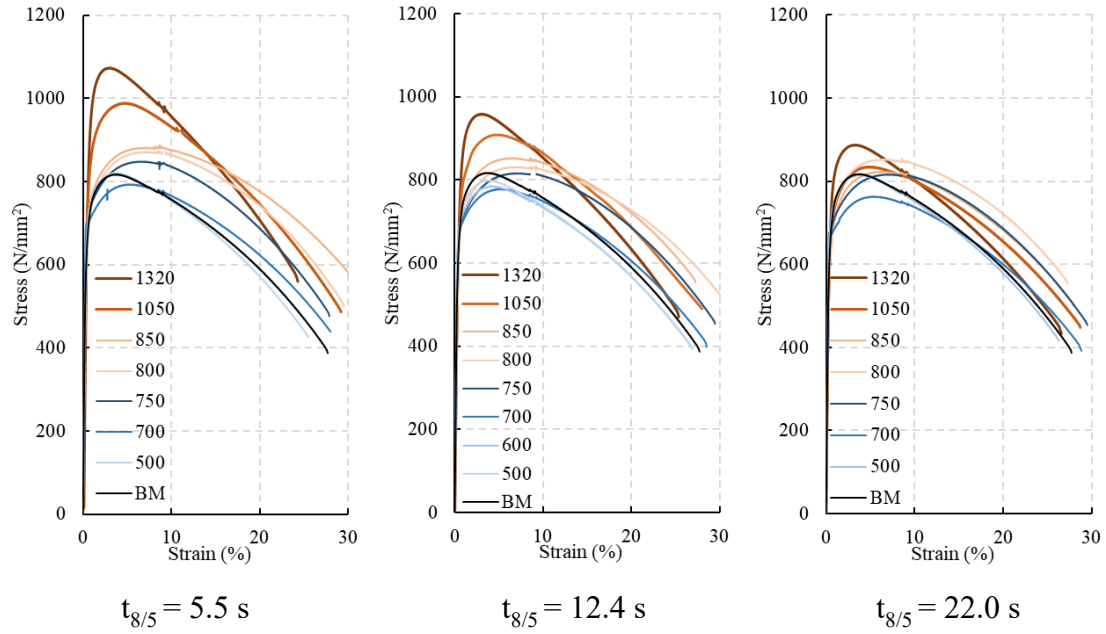
Figure 5.36 Measured stress-strain curves of Q620 TM heat-treated coupons

Table 5.6 Measured mechanical properties of Q620 TM heat-treated coupons

#	Young's Modulus (kN/mm^2)	Yield strength (N/mm^2)	Tensile strength (N/mm^2)
Base metal	245	650	817
5.5-1320	230	749	1073
5.5-1050	227	739	988
5.5-850	232	691	887
5.5-800	202	640	873
5.5-750	231	708	848
5.5-700	219	690	790
5.5-600	-	-	800
5.5-500	223	716	823
12.4-1320	216	726	959
12.4-1050	220	700	900
12.4-850	236	641	862
12.4-800	216	641	851
12.4-750	226	669	815
12.4-700	242	670	778
12.4-600	246	684	785
12.4-500	242	675	809
22.0-1320	218	705	887
22.0-1050	231	636	834
22.0-850	217	608	822
22.0-800	219	615	834
22.0-750	232	651	798
22.0-700	231	670	753
22.0-600	-	-	770
22.0-500	238	698	815
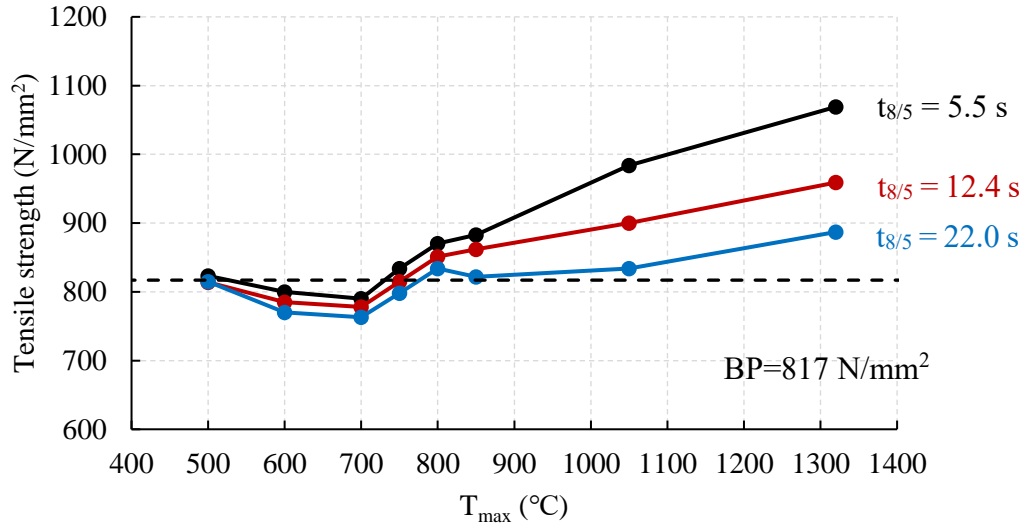
Figure 5.37 Summary of tensile strengths of Q620 TM heat-treated coupons

Simplification 1 is about setting both the lower and the higher temperature boundaries of the critical sub-zone. Cooling time $t_{8/5}$ at 22 s is set as an example for the Q620 TM steel (as shown in Figure 5.38). Considering that there is only a limited difference between the tensile strengths of Coupons 22-600 and 22-700, T_l is set to be the average of 500 °C and 600 °C, and this gives 550 °C. T_h is set to be the average of 700 °C and T_{BP} (774 °C), and this gives 737 °C.
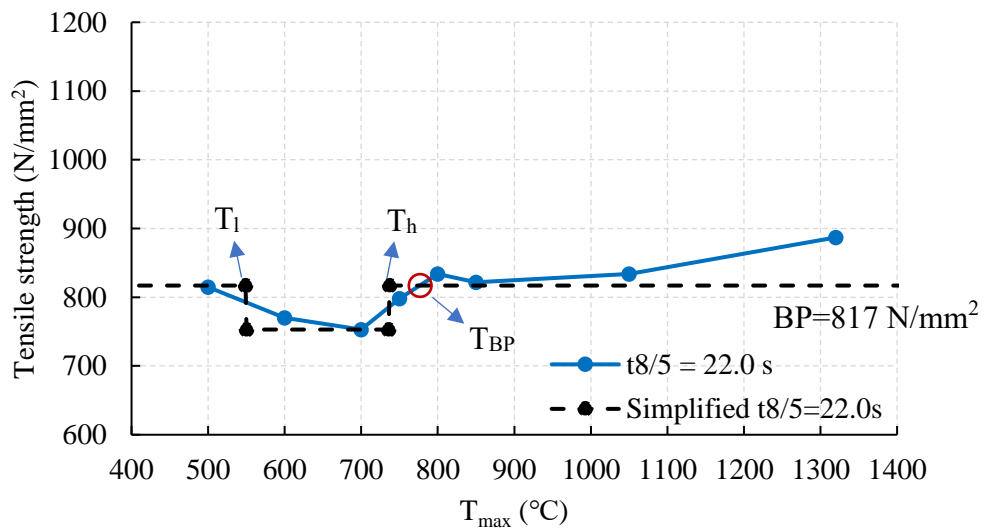
Figure 5.38 Simplified modification in tensile strengths against T_{max} (°C)

5.5.2 Comparison with S690 QT heat-treated coupons

In order to compare the test results of S690 QT heat-treated coupons to those of Q620 TM, the reduction factor of each coupon, which is the ratio of the tensile strength of heat-treated coupon over the tensile strength of the base plate, is plotted in Figure 5.39.

It is shown that:

1) For $t_{8/5}$ equals 5.5 and 12.4 s, the reduction factors for the tensile strengths of the TM steel at critical temperature are larger than these of the QT steel. When $t_{8/5}$ equals 22.0 s, the reduction factors at the critical temperature of the two steels are similar, that is 0.93.

2) The range of T_{max} with reduction factors smaller than 1.0 for the TM steel is larger than that for the QT steel.

Hence, it is reasonable to consider that if the same welding parameters are applied to both the QT and the TM welded sections under the same thickness, the latter will have a more significant reduction in their mechanical properties.
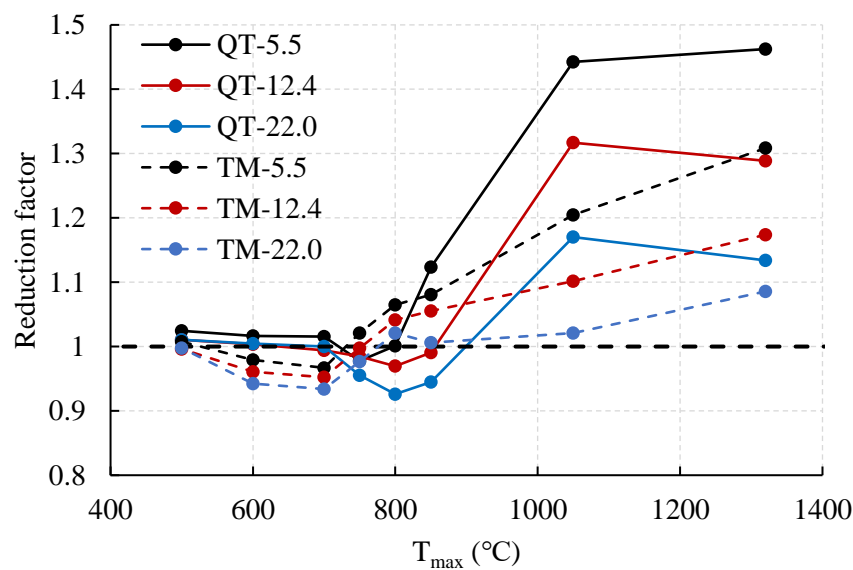
Figure 5.39 Comparison of tensile strengths of heat-treated coupons

5.5.3　Distribution of critical sub-zones

Four Q620 TM welded sections were studied in this section, and their welding parameters are reported in Table 5.7. Refer to Section 3.3 for details of the mechanical properties of these welded sections.

Table 5.7 Welding parameters of Q620 TM welded sections

Section	Thickness (mm)	Heat input energy (kJ/mm)	Voltage (V)	Current (A)	Travel speed (mm/s)	Number of passes
WS28-25	28	2.5	31.5-32.4	615-625	7.53	9
WS28-45		4.5			4.19	5
WS44-25	44	2.5	31.5-32.4	615-625	7.53	16
WS44-45		4.5			4.19	10

Same with these S690 QT welded sections, 2-D heat transfer models were established, as shown in Figure 5.40. Each weld pass was highlighted with a different color. A double ellipsoidal heat source was used to simulate the moving heat source. The thermal material properties of the TM steel are considered to be the same as those of the QT steel presented in Chapter 4.
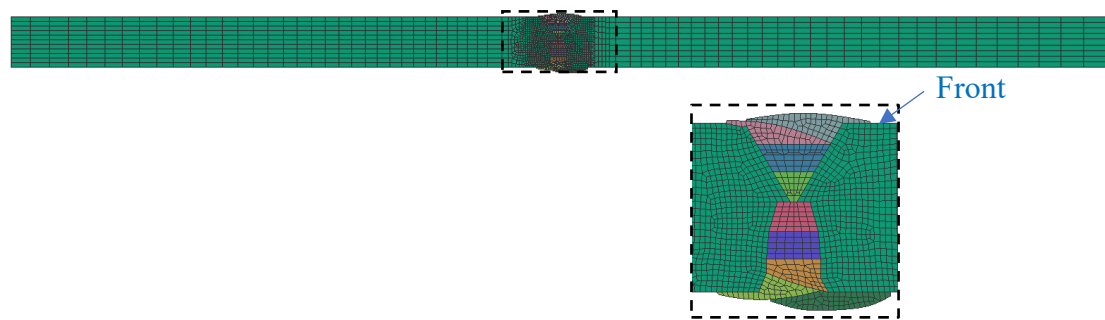
a) Section WS28-25
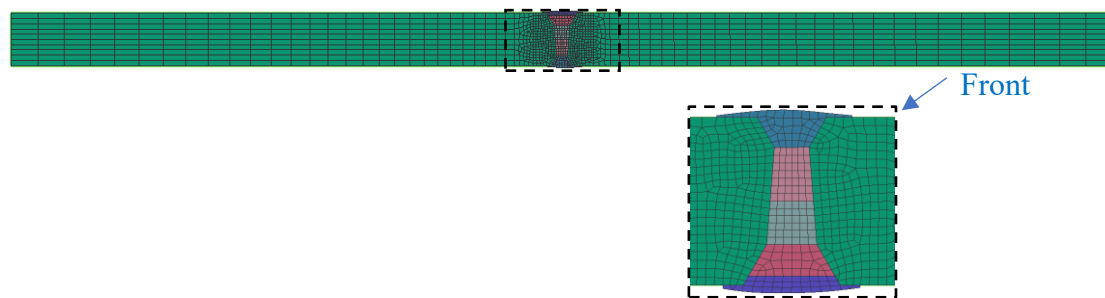
b) Section WS28-45
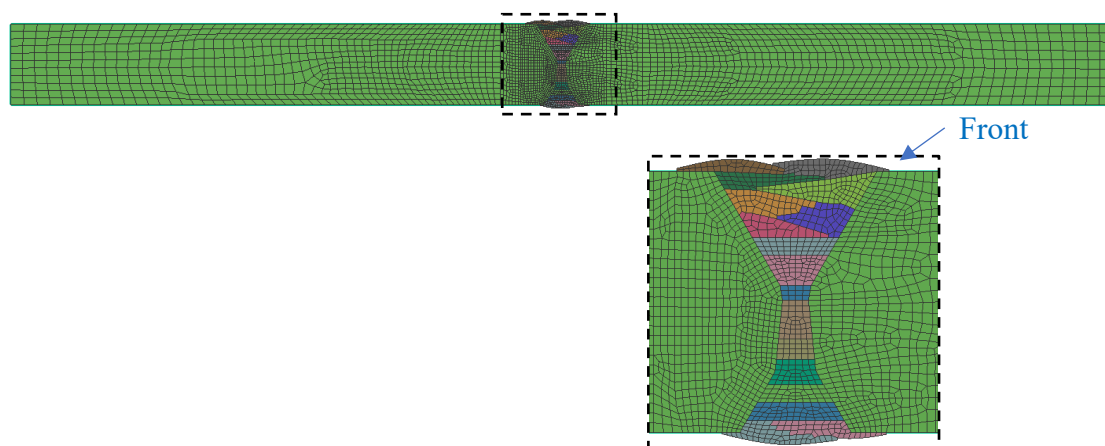
c) Section WS44-25
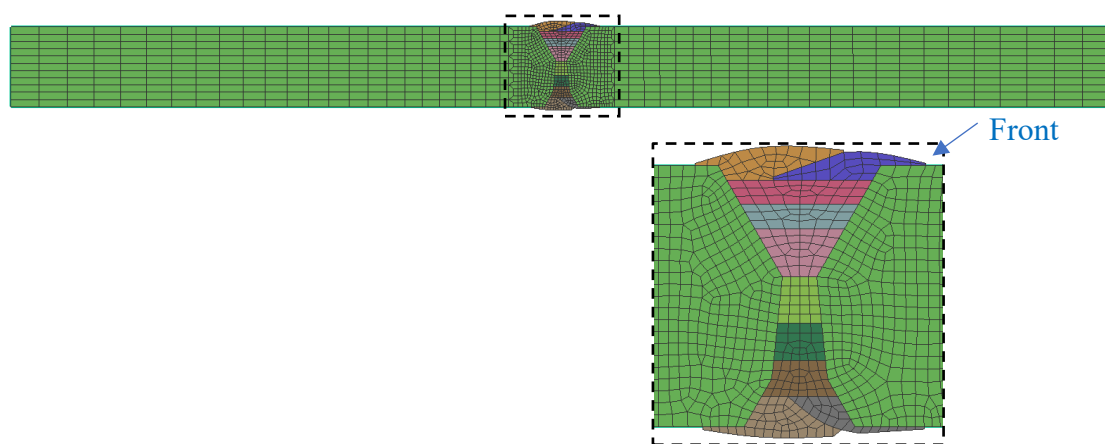
d) Section WS44-45

Figure 5.40 Heat transfer models of Q620 welded sections

The simulated cooling time $t_{8/5}$ of each welded section is extracted, and presented in Table 5.8. It is obvious that the $t_{8/5}$ in this table is not consistent with the values set in the heat treatment process. So, the mechanical properties of these heat-treated coupons with $t_{8/5}$ listed in Table 5.8 and lower and higher boundaries of the critical sub-zone, T_l and T_h, can not be obtained directly. To solve this, linear interpolation and extrapolation based on the $t_{8/5}$ is involved. Considering that there is only a small difference of $t_{8/5}$ between WS28-25 and WS44-25, i.e. ≤ 1 s, the $t_{8/5}$ of these two sections is set to be 17.4 s for easier handling.

Table 5.8 Simulated $t_{8/5}$ of Q620 TM welded sections

Section	Thickness (mm)	Heat input (kJ/mm)	$t_{8/5}$ (s)	Remarks
WS28-25	28	2.5	17.8	Simplified to 17.4 s
WS28-45		4.5	35	
WS44-25	44	2.5	17.0	Simplified to 17.4 s
WS44-45		4.5	24	

The critical temperature of this Q620 TM steel is 700 °C, so the mechanical properties of Coupons 17.4-700, 24-700 and 35-700 are needed for further analysis. The stress-strain curves of Coupons 12.4-700 and 22-700 are calculated with linear interpolation and extrapolation to get the stress-strain curves of these coupons, as shown in Figure 5.41. Then, these stress-strain curves are analyzed with the iterative method with Model F-10 to derive their true stress-strain (σ_t-ε_t) curves.

The true stress-strain (σ_t-ε_t) curves of Coupons 17.4-700, 24-700 and 35-700 together with true stress-strain (σ_t-ε_t) curves of the Q620 28 and 44 mm thick base plates, and of the weld metal are shown in Figure 5.42.
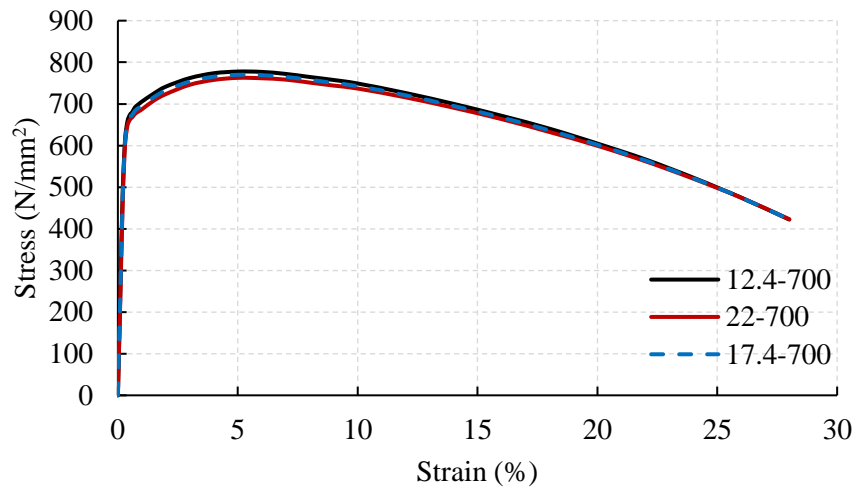
a) Coupon 17.4-700
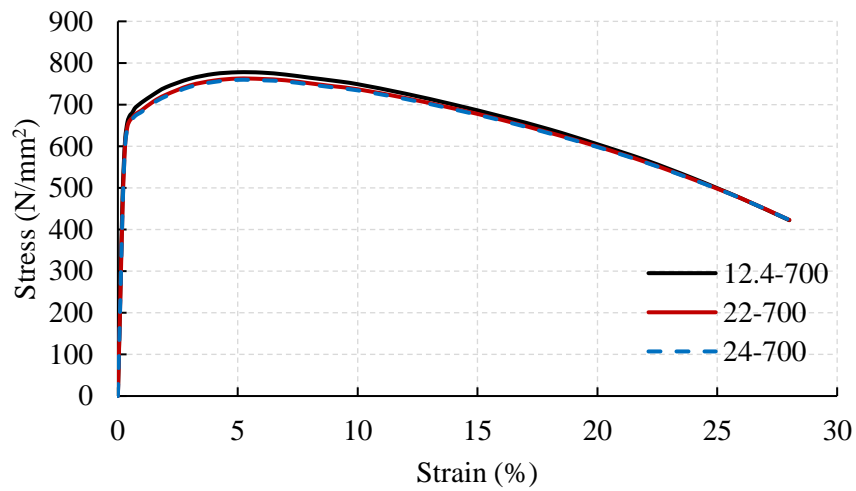
b) Coupon 24-700
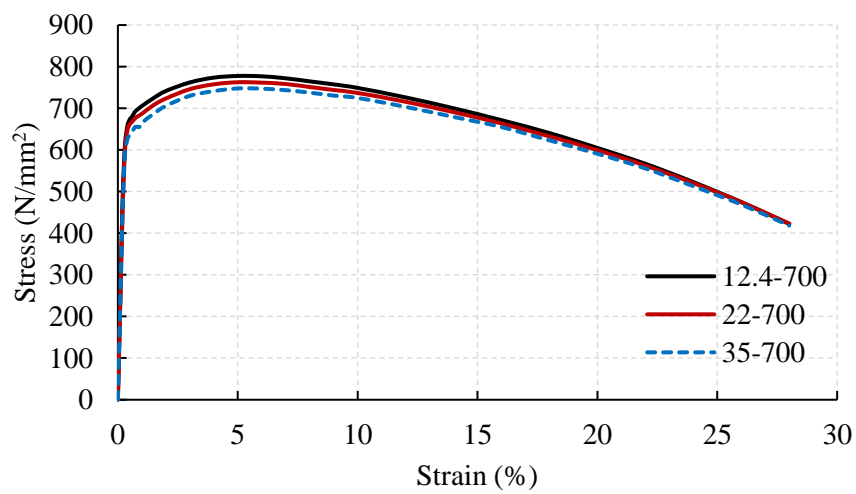
c) Coupon 35-700

Figure 5.41 Linear interpolation and extrapolation of engineering stress-strain curves
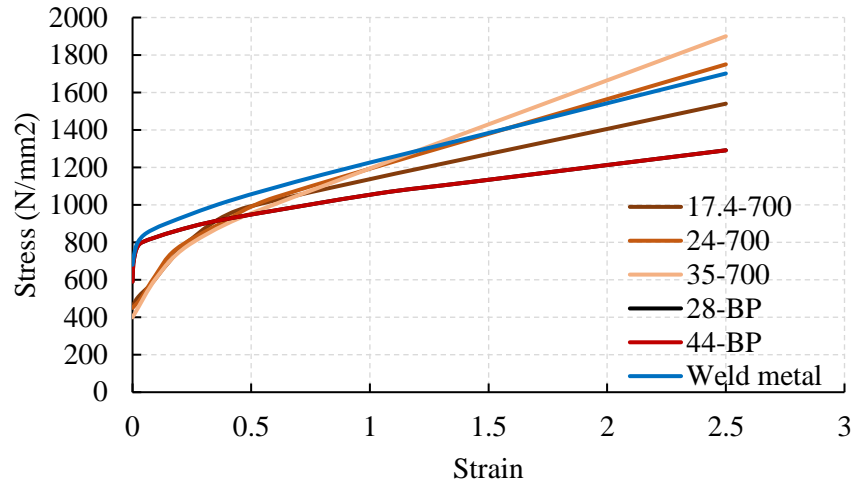
Figure 5.42 True stress-strain curves

Similar linear inerpolation and extrapolation was also adopted to derive both the lower and the higher temperature boundaries of the critical sub-zones. As shown in Table 5.9, T_l is set to be constant, that is 550 °C, and T_h is set to be the average value of 700 °C and T_{BP}, while T_{BP} is calculated with linear interpolation based on the test results of $t_{8/5}$ at 12.4 and 22.0.

Table 5.9 Temperature boundaries of critical sub-zones (°C)

Boundary	$t_{8/5}$ (s)				
	12.4	22.0	17.4	24	35
T_l	550	550	550	550	550
T_{BP}	750	774	757	779	804
T_h	725	737	729	740	752

Simplification 3: geometry of critical sub-zone

Then, these temperature boundaries of the critical sub-zones were extracted from the simulation results of each welded section. Compared with the 16 mm thick sections in the last section, there are more weld passes in the 28 and the 44 mm thick welded sections. Extracting and analyzing the temperature field of each pass is time-consuming,

198

so another simplification of simulation of these thick welded sections is made as follows. With a constant heat input energy during welding, the width of HAZ is assumed to be constant through the thickness direction of welded sections. Figure 5.43 shows the macrostructure of the 16 mm and the 70 mm thick welded sections. It is obvious that the width of their HAZs is constant, except the HAZ under the top and bottom surfaces of 70 mm welded sections shown in Figure 5.43 b). So, the width of critical sub-zones at 1/4 depth of welded sections through finite element modelling was set to be the width of critical sub-zones in a welded section.
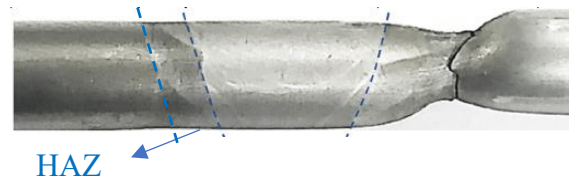
a) A deformed coupon of a 16 mm thick welded section by LIU(2018)

2.4 kJ/mm   5.0 kJ/mm
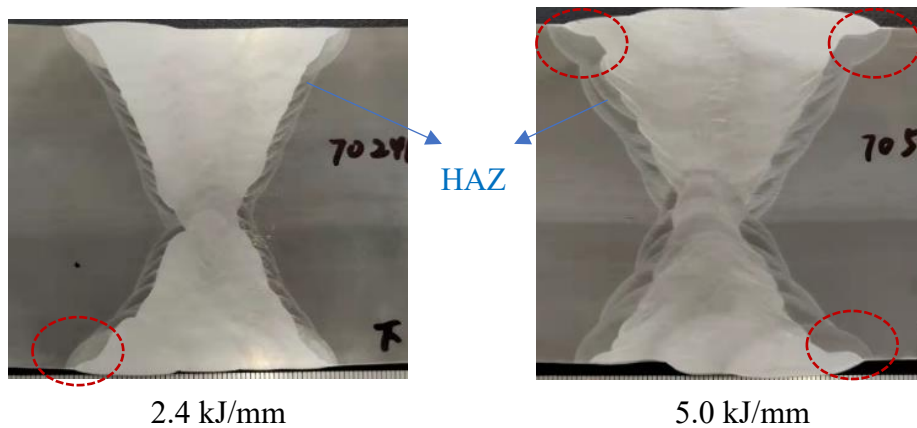
b) 70 mm thick welded sections

Figure 5.43 Macrostructures of welded sections

Figure 5.44 shows the numerical temperature boundaries of each welded section listed in Table 5.9, and the distance between each boundary was read from these figures. The width of the critical sub-zones in Sections WS28-25, WS28-45, WS44-25 and WS44-45 were found to be 2.6, 4.0, 1.8 and 3.7 mm, respectively.

199

| Distance between: | 1500 °C and 729 °C | 3.6 mm |
| | 729 °C and 550 °C | 2.6 mm |

a) Section WS28-25

| Distance between: | 1500 °C and 752 °C | 5.6 mm |
| | 752 °C and 550 °C | 4.0 mm |

b) Section WS28-45

| Distance between: | 1500 °C and 729 °C | 2.8 mm |
| | 729 °C and 550 °C | 1.8 mm |

c) Section WS44-25

| Distance between: | 1500 °C and 740 °C | 4.5 mm |
| | 740 °C and 550 °C | 3.7 mm |
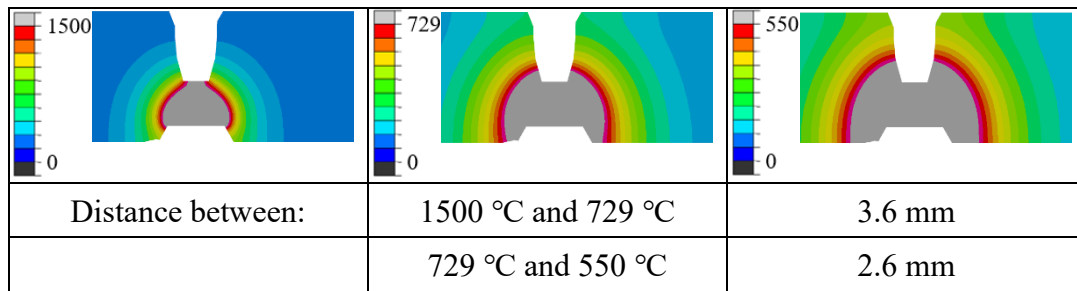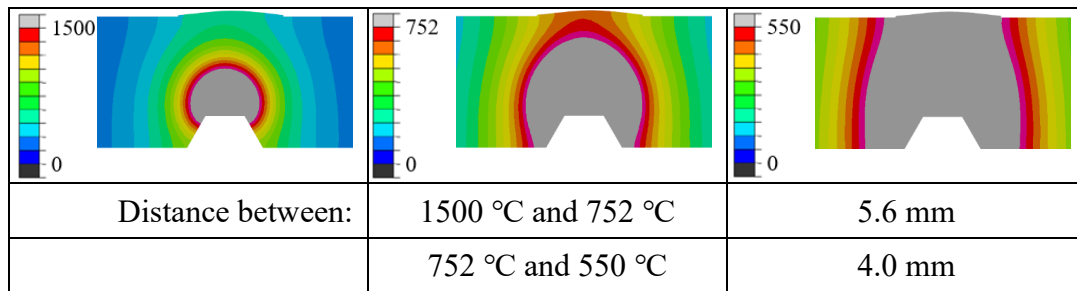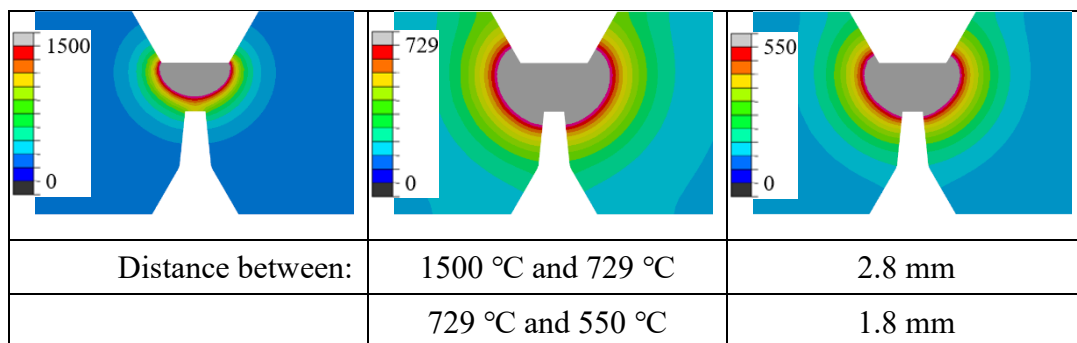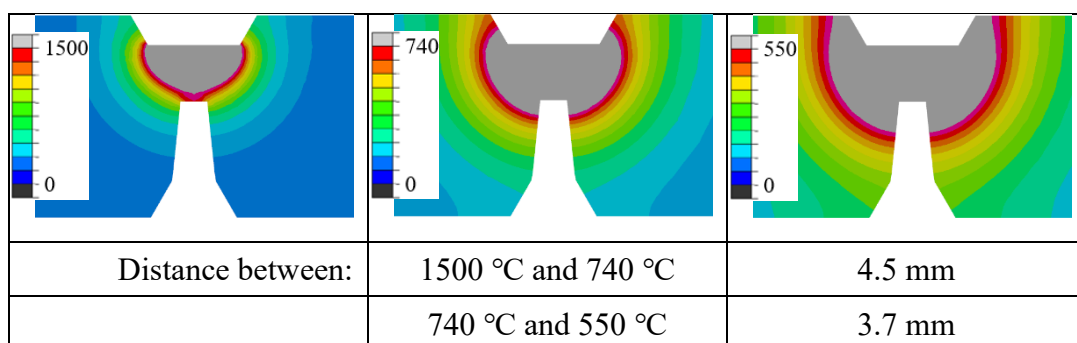
d) Section WS44-45

Figure 5.44 Boundaries of critical sub-zones obtained from FEM

A total of 4 models of the coupons were built based on these results, as shown in Figure 5.45. The mesh size of these coupons was about 2mm×2mm×2mm, while the mesh of these critical sub-zones was refined as there were four layers of elements in the longitudinal direction.

a) Model 28-25

b) Model 28-45

c) Model 44-25

d) Model 44-45

■ Base plate   ■ Weld metal   ▨ Critical sub-zone
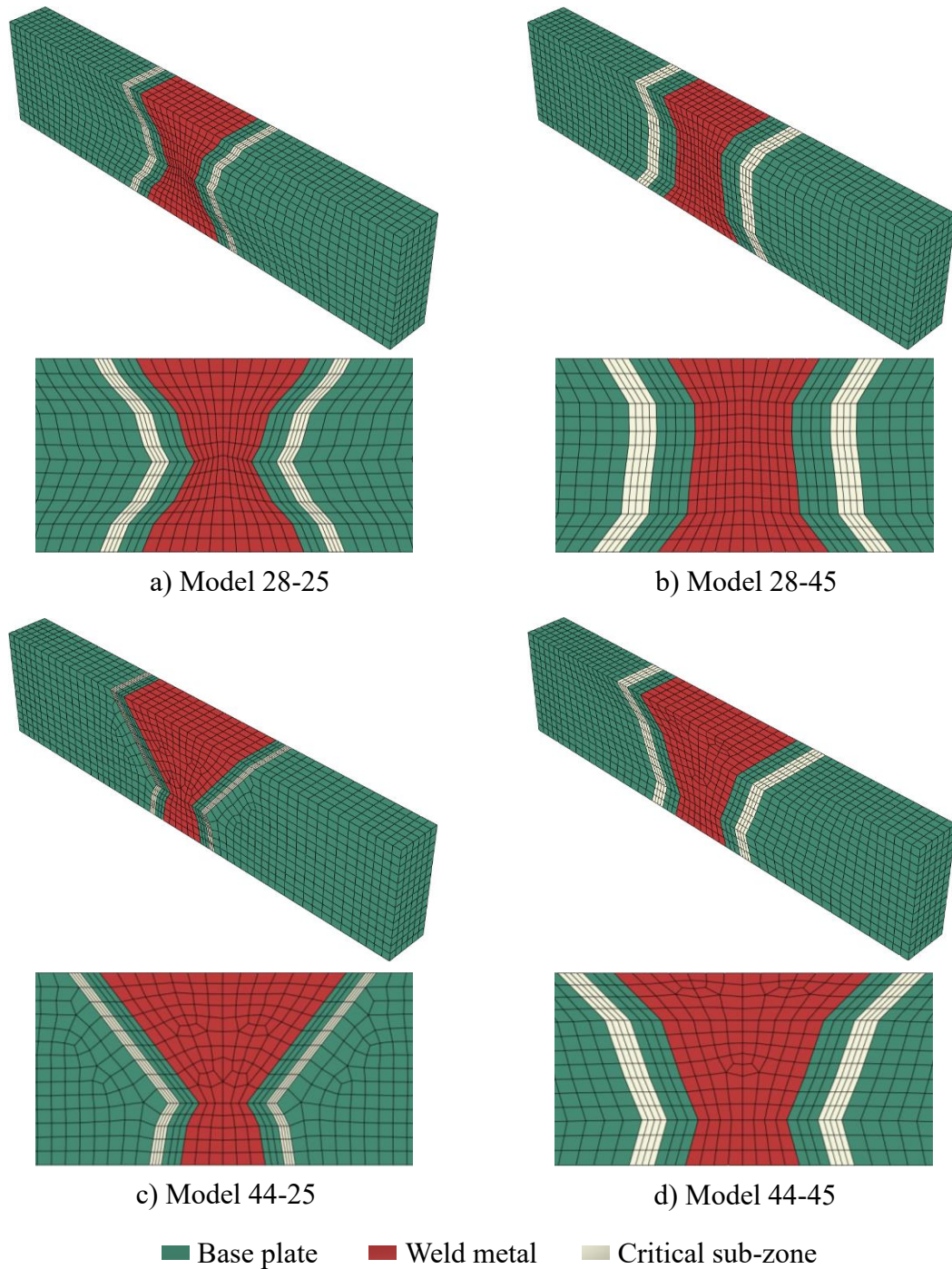
Figure 5.45 Modelling of coupons of welded sections

5.5.4 Simulation of tensile tests

Figure 5.46 shows the deformed meshes of various coupons at the last point of the predicted stress-strain curves shown in Figure 5.47. The tensile strengths of the measured and the predicted results were extracted, and listed in Table 5.10. It is obvious that a high level of accuracy in prediction of these stress-strain curves of these welded sections is successfully achieved. The errors of the predicted tensile strengths of all these coupons are well within 1%.
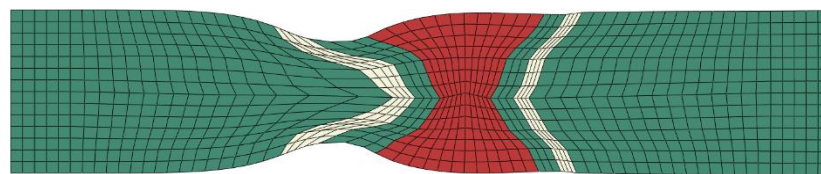
a) Model 28-25
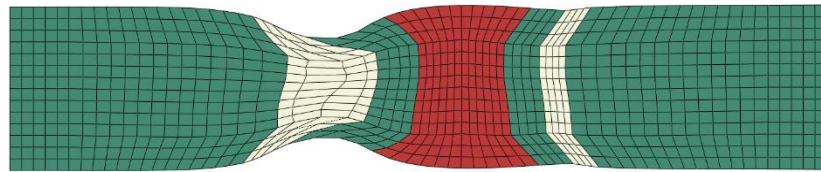
b) Model 28-45
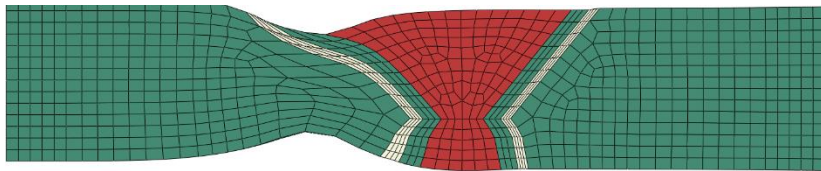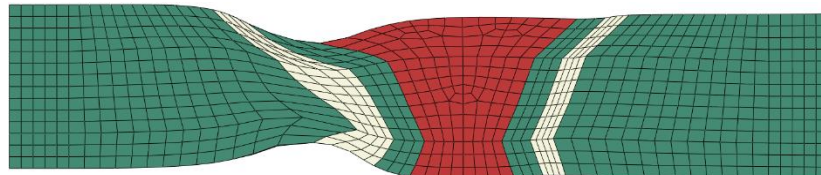
c) Model 44-25

d) Model 44-45

Figure 5.46 Deformed shapes of various models at strain level of 17%
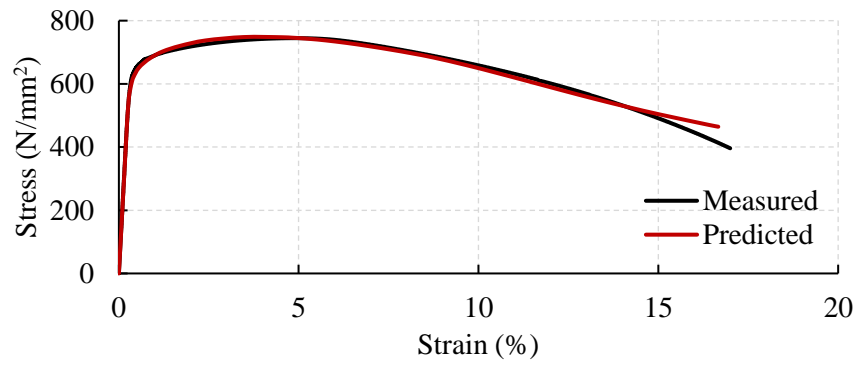
a) Coupon 28-25
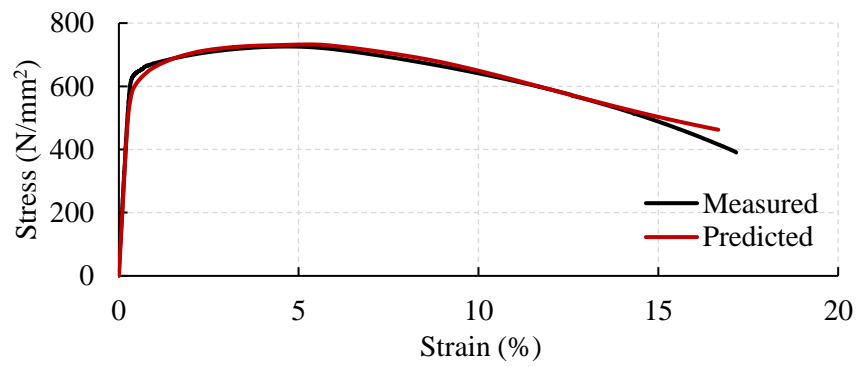
b) Coupon 28-45
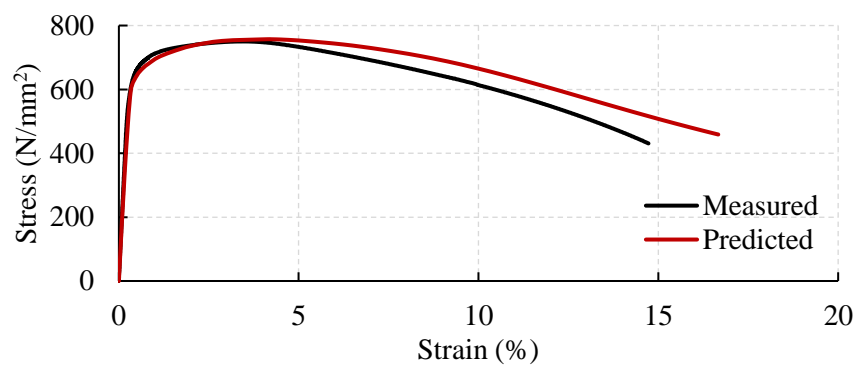
c) Coupon 44-25
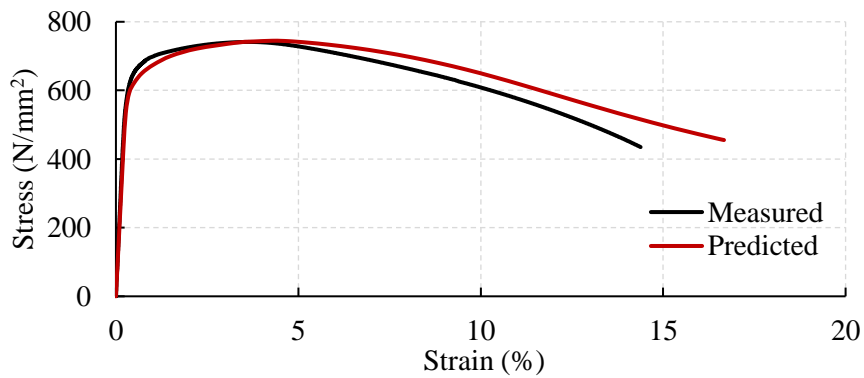
d) Coupon 44-45

Figure 5.47 Measured and predicted stress-strain curves

Table 5.10 Comparison of tensile strengths

Coupon	Tensile strength (N/mm^2)			Reduction factor	
	Measured	Predicted	Error (%)	Measured	Predicted
28-25	745	748	0.4	0.97	0.98
28-45	726	732	0.8	0.95	0.95
44-25	750	757	0.9	0.97	0.98
44-45	741	745	0.5	0.96	0.96

5.5.5 Effect of mesh size of critical sub-zones

The mesh size in the models above has been proven to be suitable for modeling thses coupons under tension. In order to further apply this Critical Sub-Zone method to a mesh of welded structural member, it is highly desirable to reduce the computational resources of thermo-mechanical analysis. The effect of mesh size of the critical sub-zone on the structural behavior of Coupon 28-45 is investigated in this section.

Three models, namely Models M-1, M-2 and M-4, were built, and there were 1, 2 and 4 layers of elements in the critical sub-zones in the longitudinal direction, respectively, as shown in Figure 5.48. The width of this critical sub-zone, according to Figure 5.44 b), is 4 mm. Model M-4 is the same as Model 28-45. A new designation system is used for these models for easy reference.

a) Model M-1   b) Model M-2   c) Model M-4
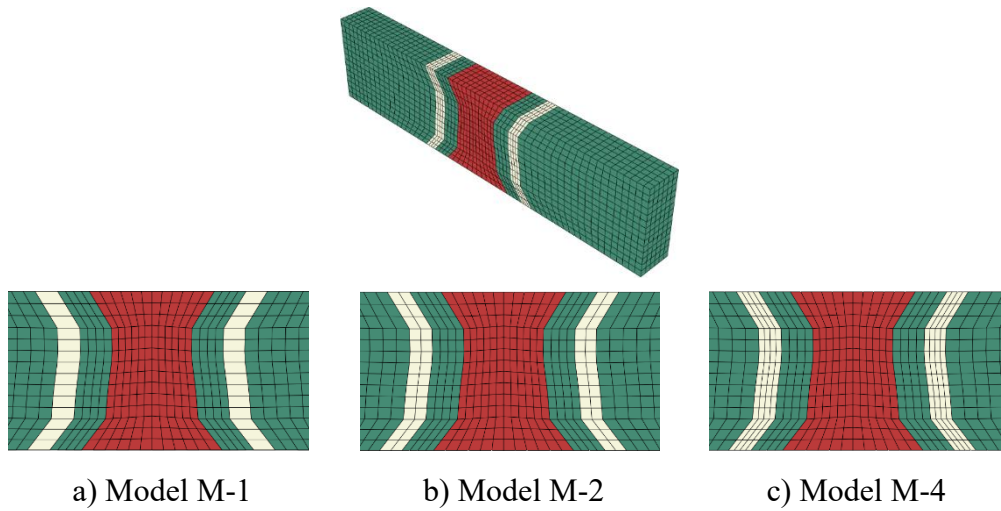
Figure 5.48 Models with various mesh sizes of critical sub-zones

The simulated coupons at maximum strain are shown in Figure 5.49 and the corresponding stress-strain curves are plotted in Figure 5.50. These stress-strain curves are shown to be close to each other and the tensile strengths of Models M-1 to M-4 are 731, 732 and 732 N/mm^2, respectively. Hence, the mesh size of the critical sub-zone within a range of 1 to 4 mm has a neglectable effect on the stress-strain curves of these models, and the element size up to 4 mm is considered to be adequate in the structural model.

a) Model M-1

b) Model M-2

c) Model M-4
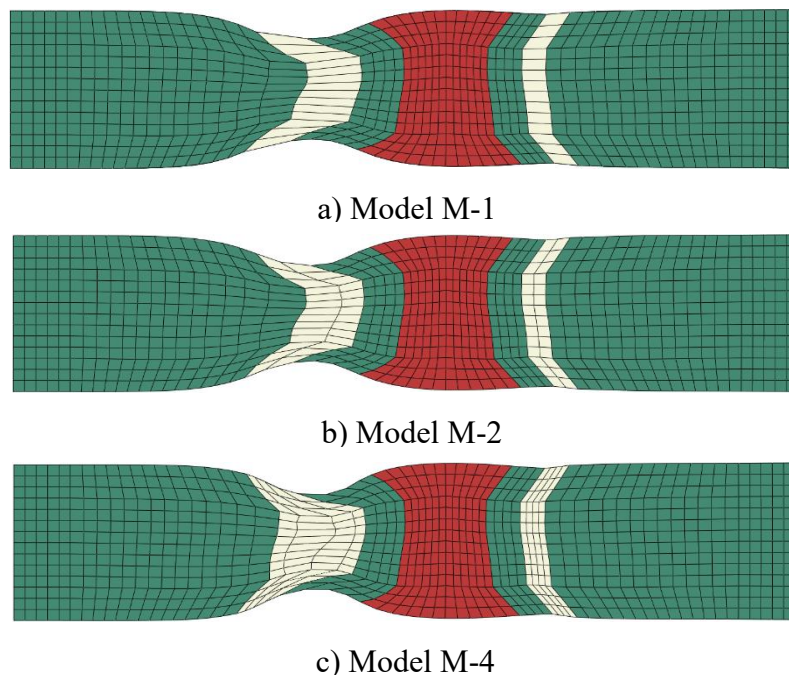
Figure 5.49 Deformed shapes of models with various mesh sizes in critical sub-zones
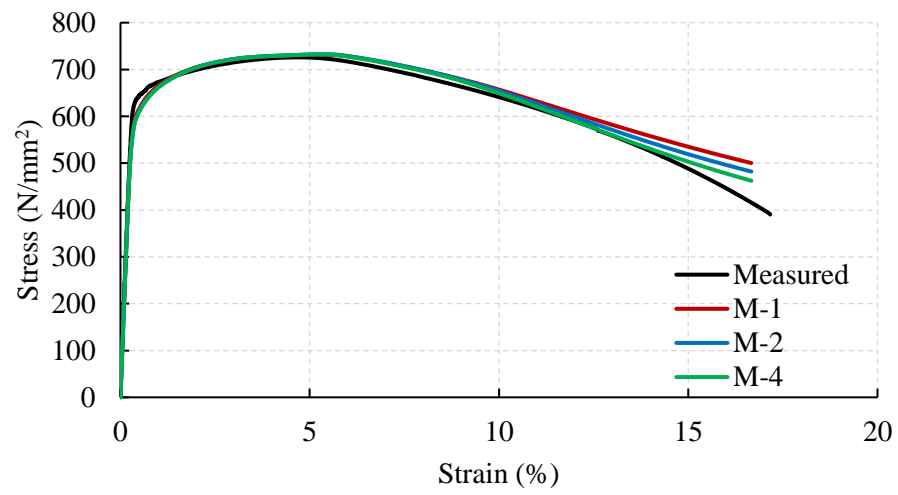
Figure 5.50 Comparsion of measured and predicted stress-strain curves

5.5.6 Comparison with DIC results

Strain fields of Coupons 28-25, 28-45, 44-25 and 44-45 were measured with DIC during tensile tests, and they are shown in Section 3.5 in Chapter 3. The longitudinal true strain field at a) tensile strength, and b) the last photo shot by DIC of the measured results and the predicted ones were compared in this section. Both the predicted distribution profile and the value of true strains meet the measured results well.

➢ **Coupon 28-25**

As shown in Figure 5.51 a), the predicted true strain distribution is found to be very similar to that of the measured results:

1) True strains at the critical sub-zone were found to be larger than those values in other parts in the welded sections in both the measured and the predicted results.

2) In the central portion of the fusion zone, the strain values were found to have smaller values than those of the surrounding weld metal, as shown in both the measured and the predicted results.

It is important to note the values of the true strains of the critical sub-zone. At first sight, the strain at the critical sub-zone measured by DIC is smaller than 10 % while the predicted value is larger than 10%, as a grey color is found in this region. After a detailed comparison, the strain values at the middle thickness of the measured and the predicted results (shown with black markers) are found to be 9.7% and 11.9%, respectively.

It should be noted that the distribution of critical sub-zones in simulation is simplified so that there is a difference in the distribution of large strain regions between those measured and those simulated ones.

207

As shown in Figure 5.51 b):

1) A quite similar necking profile was found between the measured and the predicted strain distributions.

2) The predicted location of the maximum strain was found to be fairly close to the observed fracture location in the tested coupons, indicating that the location of fracture is readily predicted.

Again, the predicted true strain was found to be larger than that given by DIC. Considering the difference in the distribution of the critical sub-zones, the maximum true strain was extracted and found to be 89.6% and 107.2% in the measured and the simulated sections, respectively, and their locations are highlighted with blackmarkers.

a) Strain at tensile strength

b) Strain at stress level about 507 N/mm^2
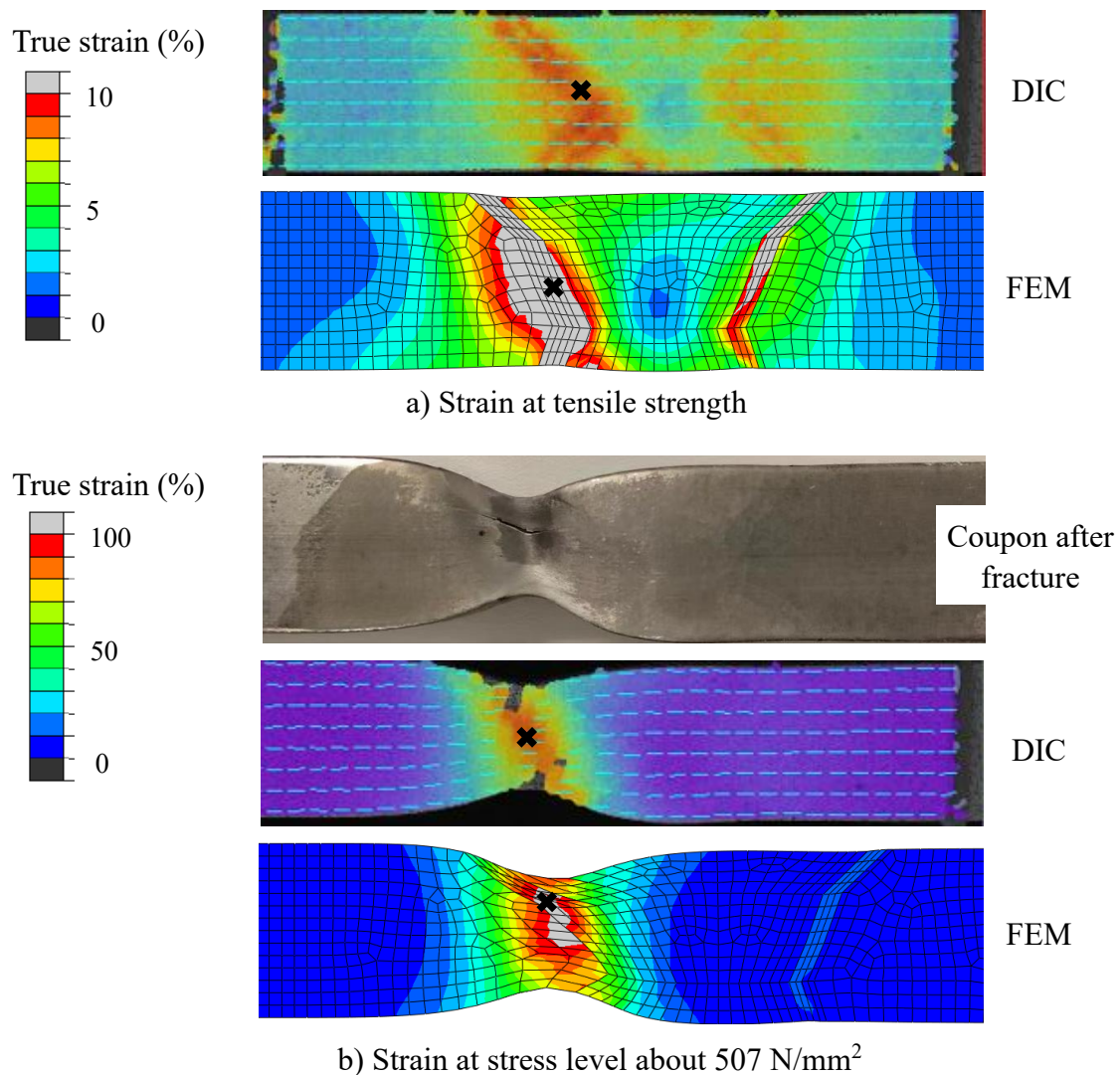
Figure 5.51 Measured and predicted true strain fields of Coupon 28-25

➤ **Coupon 28-45**

As shown in Figure 5.52 a), the predicted true strain distribution is found to be very similar to that of the measured results:

1) True strains at the critical sub-zone were found to be larger than those values in other parts in the welded sections in both the measured and the predicted results.

2) In the central portion of the fusion zone, the strain values were found to have smaller values than those of the surrounding weld metal, as shown in both the measured and the predicted results.

It is important to note the values of the true strains of the critical sub-zone. At first sight, the strain at the critical sub-zone measured by DIC is smaller than 10 % while the predicted value is larger than 10%, as a grey color is found in this region. After a detailed comparison, the strain values at the middle thickness of the measured and the predicted results (shown with black markers) are found to be 9.3% and 16.7%, respectively.

It should be noted that the distribution of critical sub-zones in simulation is simplified so that there is a difference in the distribution of large strain regions between those measured and those simulated ones.

As shown in Figure 5.52 b):

1) A quite similar necking profile was found between the measured and the predicted strain distributions.

2) The predicted location of the maximum strain was found to be fairly close to the observed fracture location in the tested coupons, indicating that the location of fracture is readily predicted.

Again, the predicted true strain was found to be larger than that given by DIC.

209

Considering the difference in the distribution of the critical sub-zones, the maximum true strain was extracted and found to be 81.8% and 119.2% in the measured and the simulated sections, respectively, and their locations are highlighted with blackmarkers.

a) True strain at tensile strength

b) True strain at stress level about 527 N/mm^2
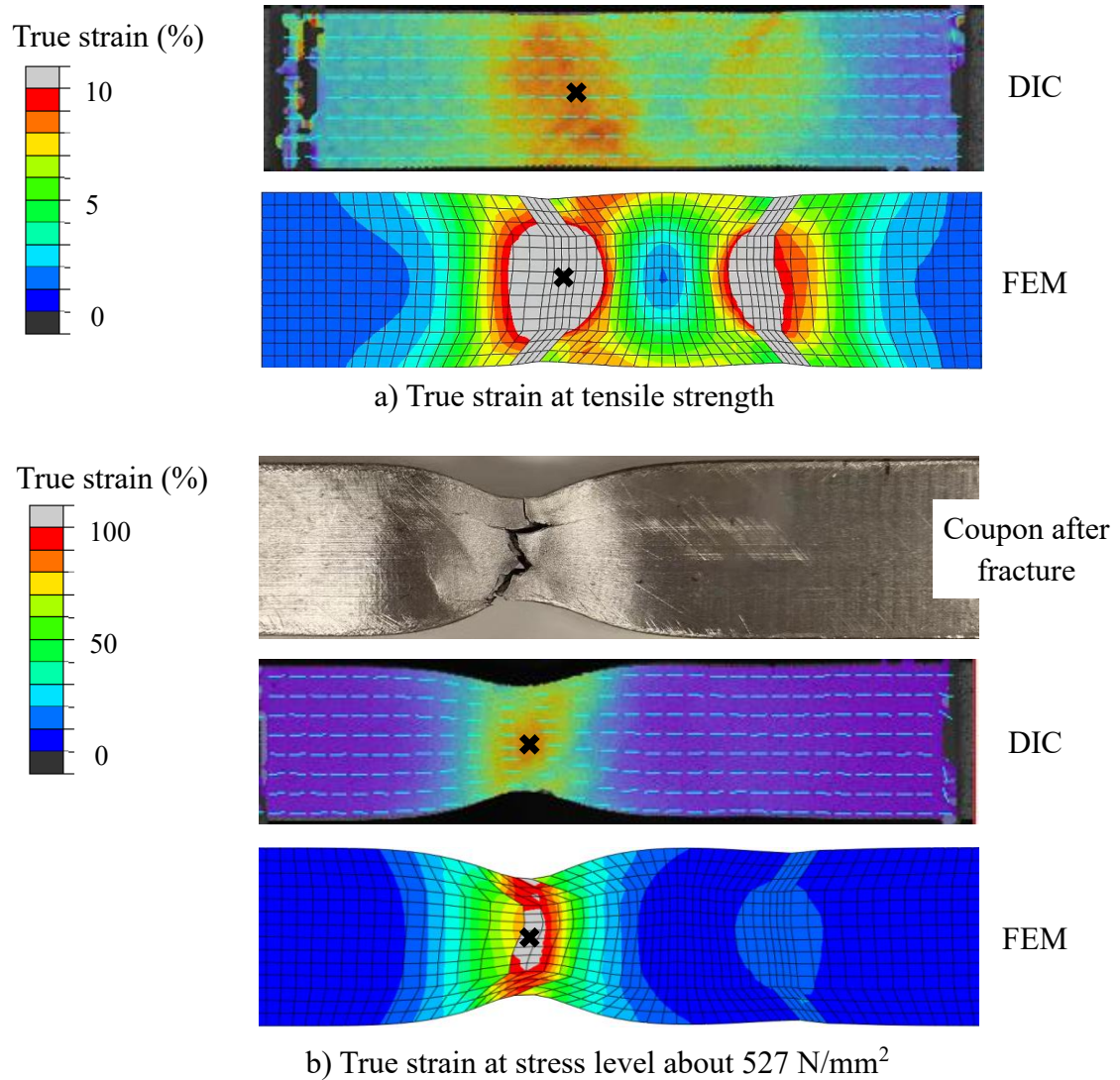
Figure 5.52 Measured and predicted true strain fields of Coupon 28-45

➢ **Coupon 44-25**

As shown in Figure 5.53 a), the predicted true strain distribution is found to be very similar to that of the measured results:

1) True strains at the critical sub-zone were found to be larger than those values in other parts in the welded sections in both the measured and the predicted results.

2) In the central portion of the fusion zone, the strain values were found to have smaller values than those of the surrounding weld metal, as shown in both the measured and the predicted results.

It is important to note the values of the true strains of the critical sub-zone. At first sight, the strain at the critical sub-zone measured by DIC is smaller than 10 % while the predicted value is larger than 10%, as a grey color is found in this region. After a detailed comparison, the strain values at the middle thickness of the measured and the predicted results (shown with black markers) are found to be 9.6% and 20.0%, respectively.

It should be noted that the distribution of critical sub-zones in simulation is simplified so that there is a difference in the distribution of large strain regions between those measured and those simulated ones.

As shown in Figure 5.53 b):

1) A quite similar necking profile was found between the measured and the predicted strain distributions.

2) The predicted location of the maximum strain was found to be fairly close to the observed fracture location in the tested coupons, indicating that the location of fracture is readily predicted.

Again, the predicted true strain was found to be larger than that given by DIC.

Considering the difference in the distribution of the critical sub-zones, the maximum true strain was extracted and found to be 91.5% and 105.8% in the measured and the simulated sections, respectively, and their locations are highlighted with blackmarkers.

a) Strain at tensile strength

b) Strain at stress level about 508 N/mm^2
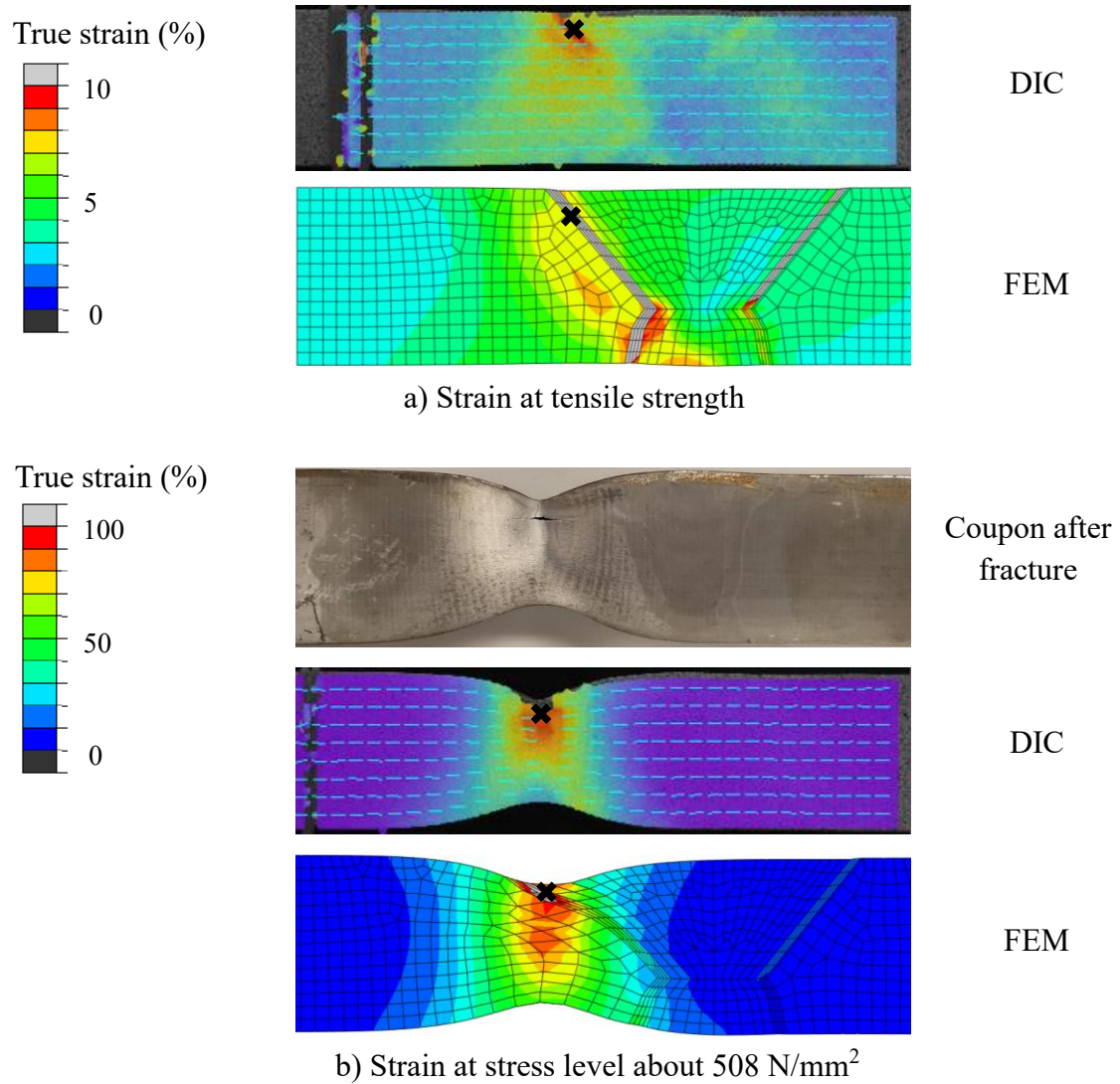
Figure 5.53 Measured and predicted true strain fields of Coupon 44-25

➢ **Coupon 44-45**

As shown in Figure 5.54 a), the predicted true strain distribution is found to be very similar to that of the measured results:

1) True strains at the critical sub-zone were found to be larger than those values in other parts in the welded sections in both the measured and the predicted results.

2) In the central portion of the fusion zone, the strain values were found to have smaller values than those of the surrounding weld metal, as shown in both the measured and the predicted results.

It is important to note the values of the true strains of the critical sub-zone. At first sight, the strain at the critical sub-zone measured by DIC is smaller than 10 % while the predicted value is larger than 10%, as a grey color is found in this region. After a detailed comparison, the strain values at the middle thickness of the measured and the predicted results (shown with black markers) are found to be 11.1% and 20.4%, respectively.

It should be noted that the distribution of critical sub-zones in simulation is simplified so that there is a difference in the distribution of large strain regions between those measured and those simulated ones.

As shown in Figure 5.54 b):

1) A quite similar necking profile was found between the measured and the predicted strain distributions.

2) The predicted location of the maximum strain was found to be fairly close to the observed fracture location in the tested coupons, indicating that the location of fracture is readily predicted.

Again, the predicted true strain was found to be larger than that given by DIC.

213

Considering the difference in the distribution of the critical sub-zones, the maximum true strain was extracted and found to be 90.7% and 104.4% in the measured and the simulated sections, respectively, and their locations are highlighted with blackmarkers.


a) Strain at tensile strength

b) Strain at stress level about 514 N/mm^2
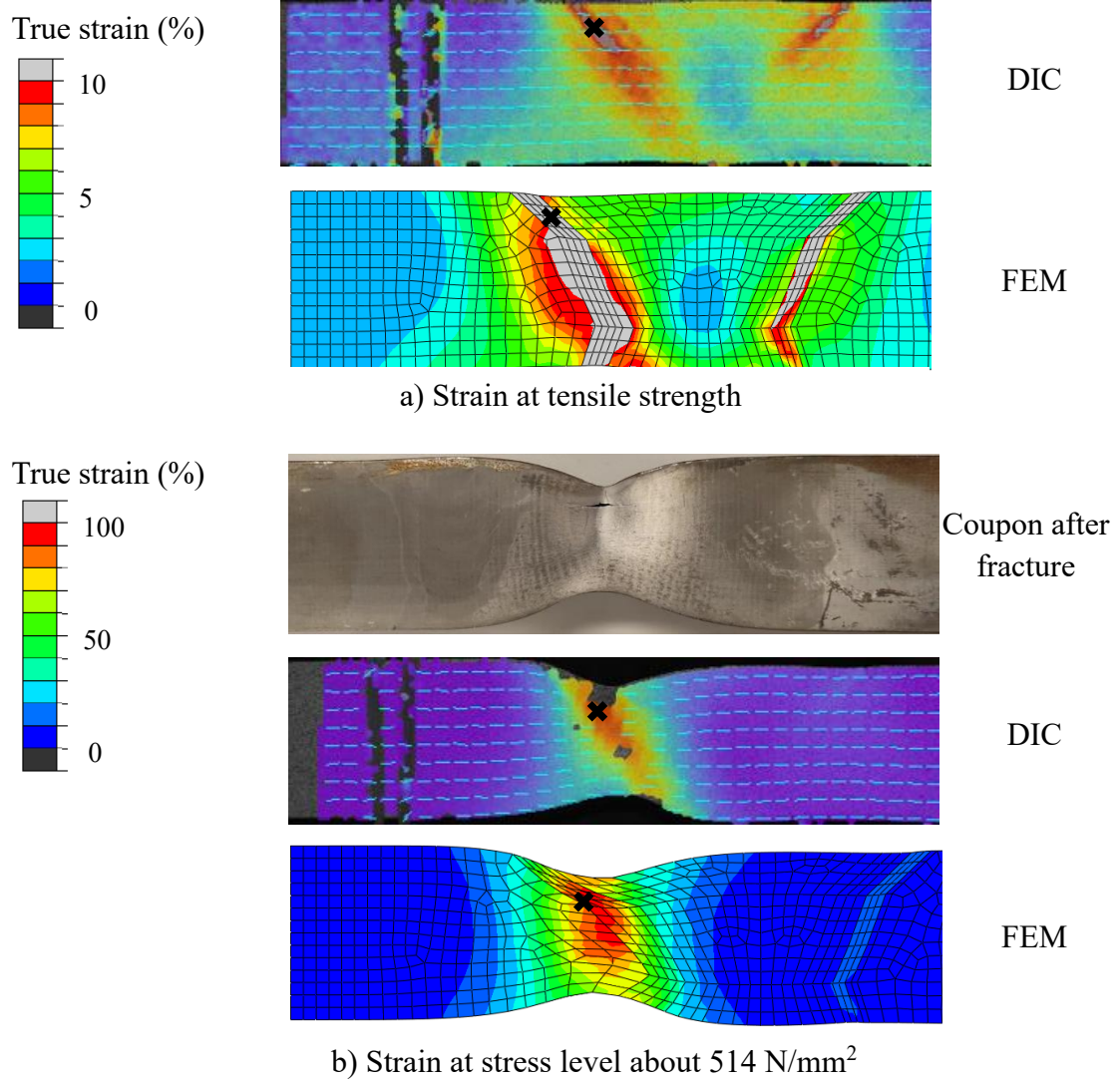
Figure 5.54 Measured and predicted true strain fields of Coupon 44-45

5.6 Conclusion

In this chapter, a Critical Sub-Zone method was proposed to simulate the structural behaviour of the coupons of high-strength steel welded sections under tension. The welded joint was simulated with the following three regions in a simplified manner: i) the weld metal, ii) the base plate, and iii) the critical sub-zone, and the following key issues were solved: a) mechanical properties of the critical sub-zones, and b) distributions of these critical sub-zones. It is demonstrated that the predicted stress-strain curves of both S690 QT and Q620 TM steel welded sections compare very well with those of the measured ones, although the microstructures in these two steel and their HAZs are quite different.

It is also found that in the modeling process, the effect of a) distribution of critical sub-zone, and b) mesh size in this region onto the simulated tensile strength is neglectable. Hence, this Critical Sub-Zone method is readily adopted to predict the structural response a large welded member with limited compute resources.

What's more, a systematic heat treatment process was carried out to investigate the mechanical property changes in HAZ of both S690 QT and Q620 TM steel welded sections. It is found that:

1) The most critical temperature, i.e. the heat treatment temperature that gives the smallest strength within one HAZ, for S690 QT and Q620 TM steel is found to be 800°C and 750°C, respectively.

2) Within a given $t_{8/5}$, the temperature range, which has a tensile strength in HAZ smaller than that of the base metal, for the TM steel is larger than that for the QT steel.

215

Chapter 6. Structural performance of TMCP 28 mm welded H-sections with different heat input energy under compression

6.1 Introduction

For high strength TM steels, large heating/cooling cycles induced during a practical welding process will trigger phase transformation, recrystallization, and grain growth in heat-affected-zones (HAZ) of their welded joints, which will lead to the reduction of mechanical properties as shown in Chapter 3. However, it becomes evident in many cases that reductions in various mechanical properties of these high strength welded members are found to be significantly less severe than anticipated. In general, there is a lack of systematic experimental evidence on such structural behavior of these welded members, in particular, with thick plates. Hence, an experimental investigation is undertaken to examine the structural behavior of high strength Q620 TM steel welded H-sections and their spliced welded H-sections under compression. An integrated model, which considers the effect of welding on residual stresses and changes in mechanical properties on the structural member, was proposed.

It should be noted that, the welding-induced residual stresses in thick sections have been simulated successfully, and a simplified simulation method on changes in the mechanical properties of these welded sections have also been proved to be accurate for these welded sections under tension. Considering that both residual stresses and changes in mechanical properties exist in a welded structure member, an integrated model is proposed to simulate the structural responses of these welded structure members.

The objective of this chapter includes:

a) To understand the structural behavior of the Q620 TM H-sections under compression.

b) To compare the cross-section resistances of the Q620 TM welded H-sections with welded splices with different heat input energy under compression.

c) To examine the effects of heat input energy on the structural performance of these Q620 TM welded H-sections with the proposed integrated model.

6.2 Fabrication process

A total of 6 stocky columns were designed, fabricated and tested under axial compression and details of these tests are presented as follows:

- ➢ 3 Q620 TM stocky columns, namely Sections H1, H2, H3.
- ➢ 3 Q620 TM spliced stocky columns, namely H3-25, H3-35, H3-45, with butt welded in the mid-heigh of these columns.

Typical cross-section dimensions of these welded H-sections are shown in Table 6.1 and Figure 6.1. Section classifications of these sections are determined according to the 'non-slender' requirement given in EN 1993-1-1. For those spliced columns, the heat input energy during welding are also provided in Table 6.1.

Table 6.1 Test program of stocky column test

Material	Specimen Label	Heat input of butt weld	Cross section	Plate thickness	Length	Section classification
		(kJ/mm)	(mm×mm)	(mm)	(mm)	
Q620 TM	H1	-	250×250	28	750	Class 1
	H2	-	320×320	28	960	Class 2
	H3	-	350×350	28	1050	Class 3
	H3-25	2.5	350×350	28	1050	Class 3
	H3-35	3.5	350×350	28	1050	Class 3
	H3-45	4.5	350×350	28	1050	Class 3

Section H1   **Section H2**

Sections H3, H3-25, H3-35 and H3-45
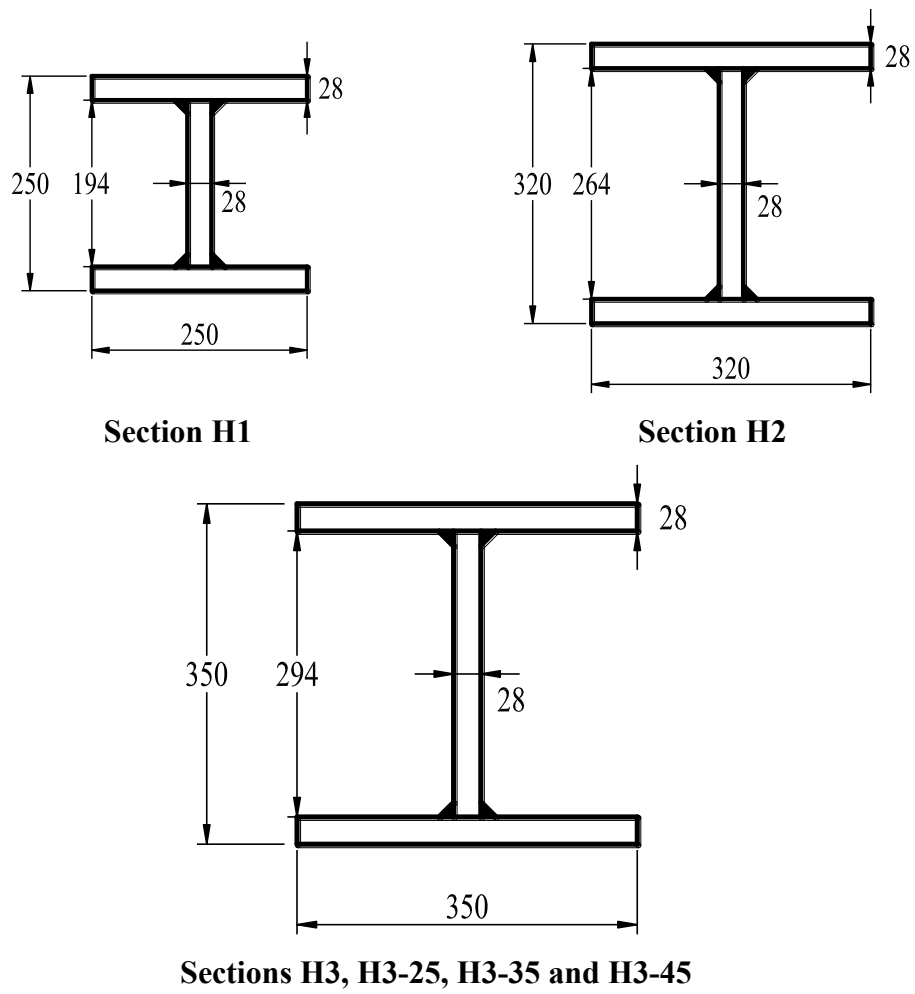
Figure 6.1 Nominal cross-sectional dimensions of Q620 TM H-sections

6.2.1 Fabrication of welded H-section columns

The size of the fillet weld was determined using Equation 6.1 given in AWS Welding Handbook (2001). After several trial runs for selection of welding parameters, a weld size of 18 mm was adopted.

$$\begin{cases} r \leq 1.2 * t_{min} \\ r \geq 1.5 * \sqrt{t_{max}} \end{cases} \tag{6.1}$$

where r is the weld size.

t_{min} is the thickness of the thinner plate in a junction, t_{min}=28mm in this case.

t_{max} is the thickness of the thicker plate in a junction, t_{max}=28mm in this case.

Figure 6.2 shows the welding setup for a welded H-section. Both the flanges and the web of the H-section were first temporarily spot welded and fixed with run-on plates. The sections was rotated 45° for the SAW process. Preheat with electric heating panels was carried out before welding. In order to minimize any welding-induced distortion, the welding sequence of a total of four grooves was designed as shown in Figure 6.2 (b), and a small lifting machine was used to rotate the section after finishing each groove. The welding parameters of typical weld pass were recorded and tabulated in Table 7.2.
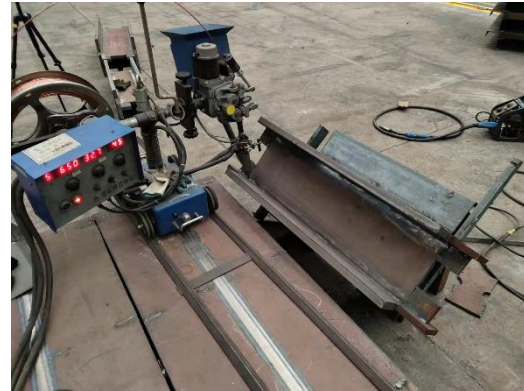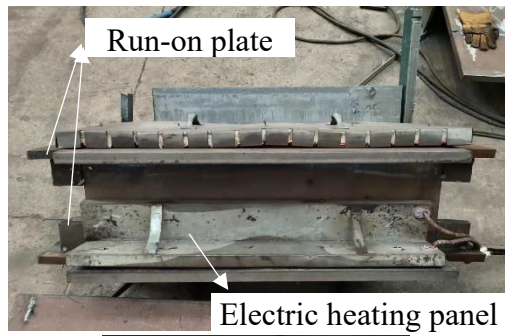
Temperature measurement after preheating ➡️ SAW

a) Welding process
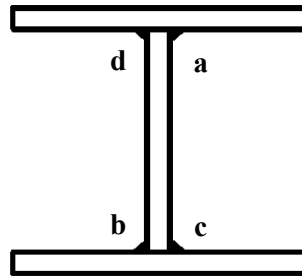
b) Welding sequence of four welds

Figure 6.2 Welding setup for welding of a H-section

Table 6.2 Typical welding parameters

Weld pass	Weld method	Voltage (V)	Current (A)	Weld speed (mm/s)	Heat input energy (kJ/mm)
1	SAW	32	650	7.5	2.63
2				5.7	3.47

6.2.2 Fabrication of spliced welded H-section columns

Spliced welding of the H-sections was designed as shown in Figure 6.3, i.e. two H-sections were assembled and welded with the process shown in 6.2.1 (stage 1), and then, these two H-sections were splice welded to form a H-section (stage 2). The joint details of both the web and the flanges are shown in Figure 6.4. Both ends of the H-section were properly welded onto 30 mm thick S355 steel plates to ensure consistent deformations of the sections under compression.
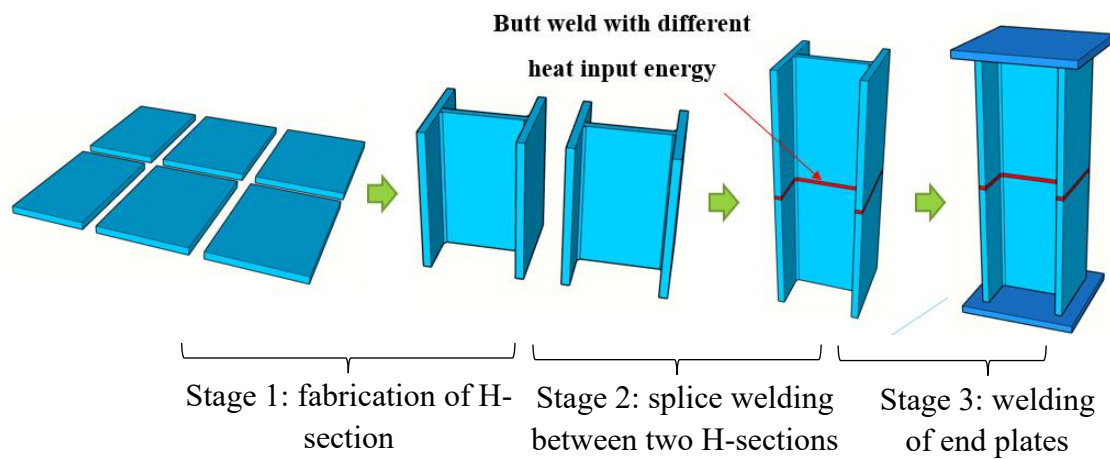
Figure 6.3 Fabrication sequence of typical spliced column

a) Web plates   b) Flange plates
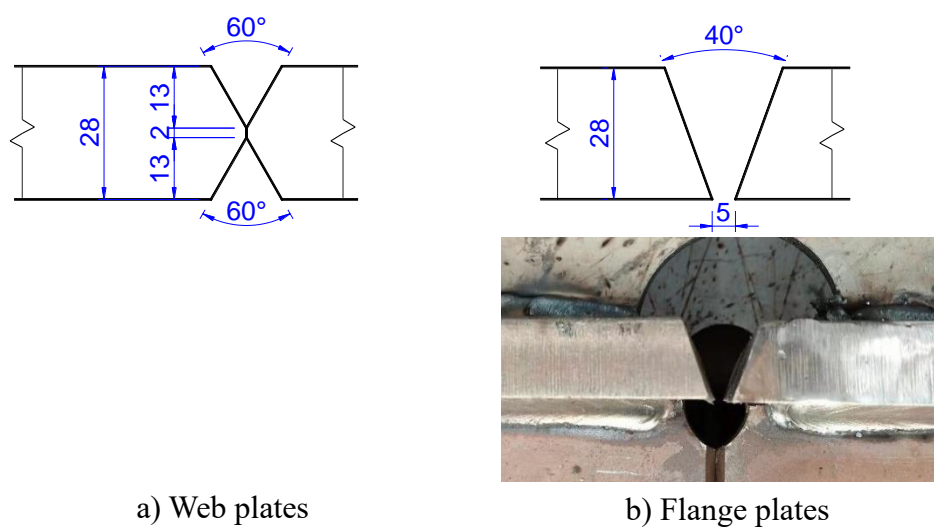
Figure 6.4 Joint details of web and flange plates

The web plates were first welded with the GMAW process, as shown in Figure 6.5. After welding one side of the groove, carbon arc gouging was then conducted at the back of the weld before welding the other side. The recorded welding parameters were listed in Table 6.3, and they were adopted in splice welding of all these H-sections.

Set-up → Pre-heating → GMAW at one side

GMAW at the other side and post heat ← Carbon arc gouging at the back
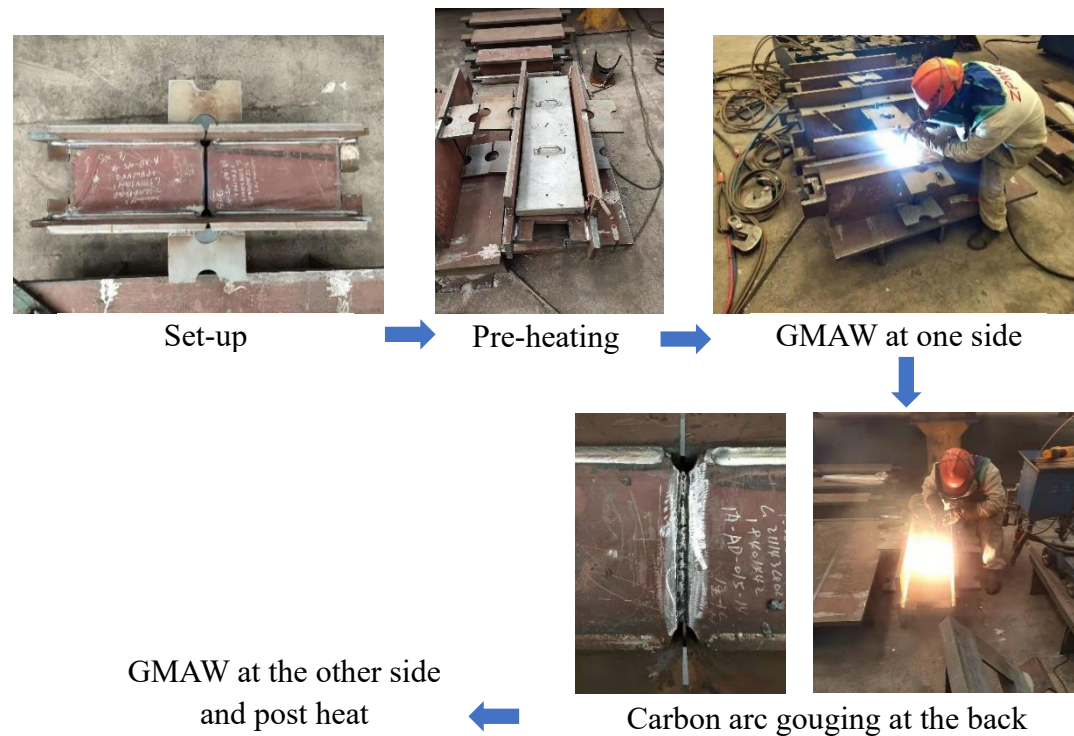
Figure 6.5 Typical spliced welding of a H-section – web plates

Table 6.3 Welding parameters of GMAW for web plates

Side	Number of passes	Weld method	Voltage (V)	Current (A)	Weld speed (mm/s)	Heat input energy (kJ/mm)
Front	3	GMAW	33.0~33.6	257~263	3.8~2.6	1.90~2.83
Back	6					

For the flanges, the GMAW process was also used for the first two passes with ceramic backing, and then the SAW process was used for the rest in order to achieve a high heat input energy. The welding process is shown in Figure 6.6. In this way, an access hole was needed, and it was filled with GMAW after the SAW process.

All the welding parameters are shown in Table 6.4. It should be noted that as limited by the capacity of the GMAW process, the first two passes of all the flanges plates followed these welding parameters while the rest of the welding process were welded by SAW with increased heat input energy as specified.

a) GMAW for root pass

b) Removal of temporary attachment

c) SAW
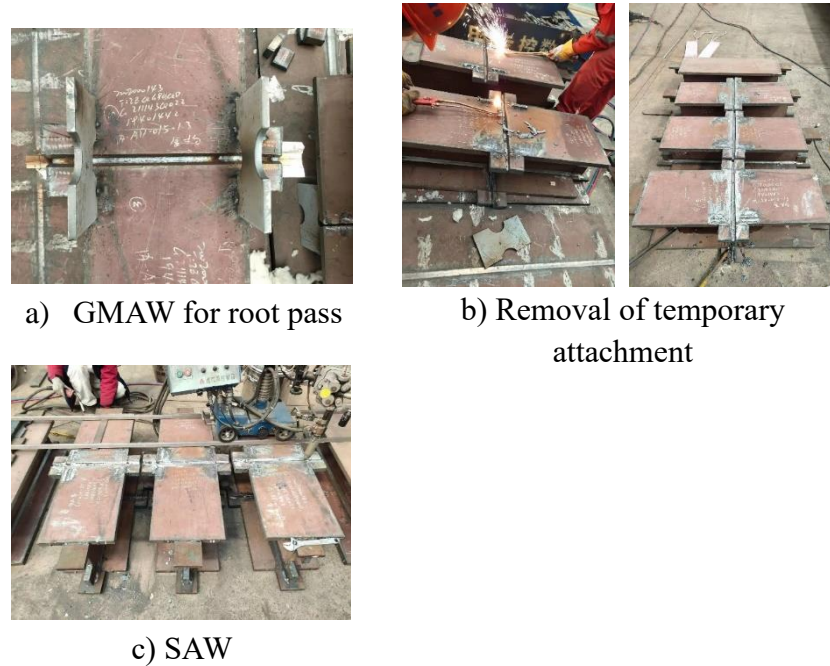
Figure 6.6 Typical splice welding for a H-column – flange plates

Table 6.4 Welding parameters during welding of the flange plates

Specimen	Passes	Number of passes	Weld method	Voltage (V)	Current (A)	Weld speed (mm/s)	Heat input energy (kJ/mm)
H3-25	Root	2	GMAW	36.2-36.8	252-260	2.3-3.1	2.56-3.45
	Other	8	SAW	31.8-32.3	617-623	7.53	2.51
H3-35	Root	2	GMAW	36.2-36.8	252-260	2.3-3.1	2.56-3.45
	Other	7	SAW	31.8-32.3	617-623	5.38	3.50
H3-45	Root	2	GMAW	36.2-36.8	252-260	2.3-3.1	2.56-3.45
	Other	6	SAW	31.8-32.3	617-623	4.19	4.50

6.3 Compression tests

6.3.1 Test setup and instrumentation

All six columns were tested with a large compression testing system with a loading capacity of 25,000 kN. Typical test setup of the stocky columns under compression is shown in Figure 6.7. A total of four LVDTs were installed to record axial shortenings of the test specimens. The probes of these LVDTs were positioned to touch the top end plates while their seats were placed on the bottom end plates. In this way, the relative shortenings between the two end plates were readily measured.

| a)   Test set-up | b)   Arrangement of LVDTs |
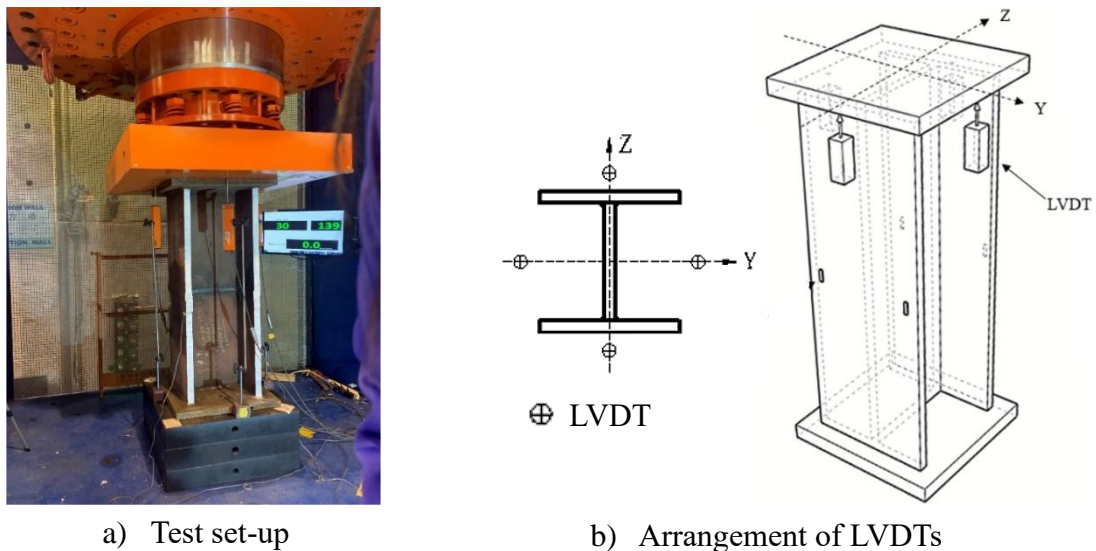
Figure 6.7 Setup and instrumentation of compression tests

During each test, the following loading scheme was adopted:

➢ To apply a compression force up to 30% of the predicted section resistance, $N_{c,Rd}$, and then, unload back to zero with a rate of 0.5mm/min;

➢ To apply a compression force up to 0.8 $N_{c,Rd}$ with a loading rate of 0.3mm/min;

➢ To continue the loading through displacement control with a rate of 0.5 mm/min;

➢ To terminate testing when the applied load was reduced by 0.5% of its maximum value.

225

It should be noted that all these columns were unloaded at about 99.5 % of their respective maximum loading in order to avoid significant deformations and rotations of the loading attachments. In all tests, unintended eccentricities of load application were successfully eliminated with careful alignment of the test specimens.

6.3.2　Test results

All six H-columns were tested successfully. In general, all these H-columns failed in local buckling, and the maximum deformation points of these columns were typically located in the mid-height, or in the 1/3 of the total height to the upper or the lower ends of the H-columns. Typical deformed shapes of these columns after tests are shown in Figure 6.8. Symmetrical local buckling appeared in the flanges of these columns, while complementary local buckling was also found in their webs.

Section H1	**Section H2**	**Section H3**
Section H3-25	**Section H3-35**	**Section H3-45**
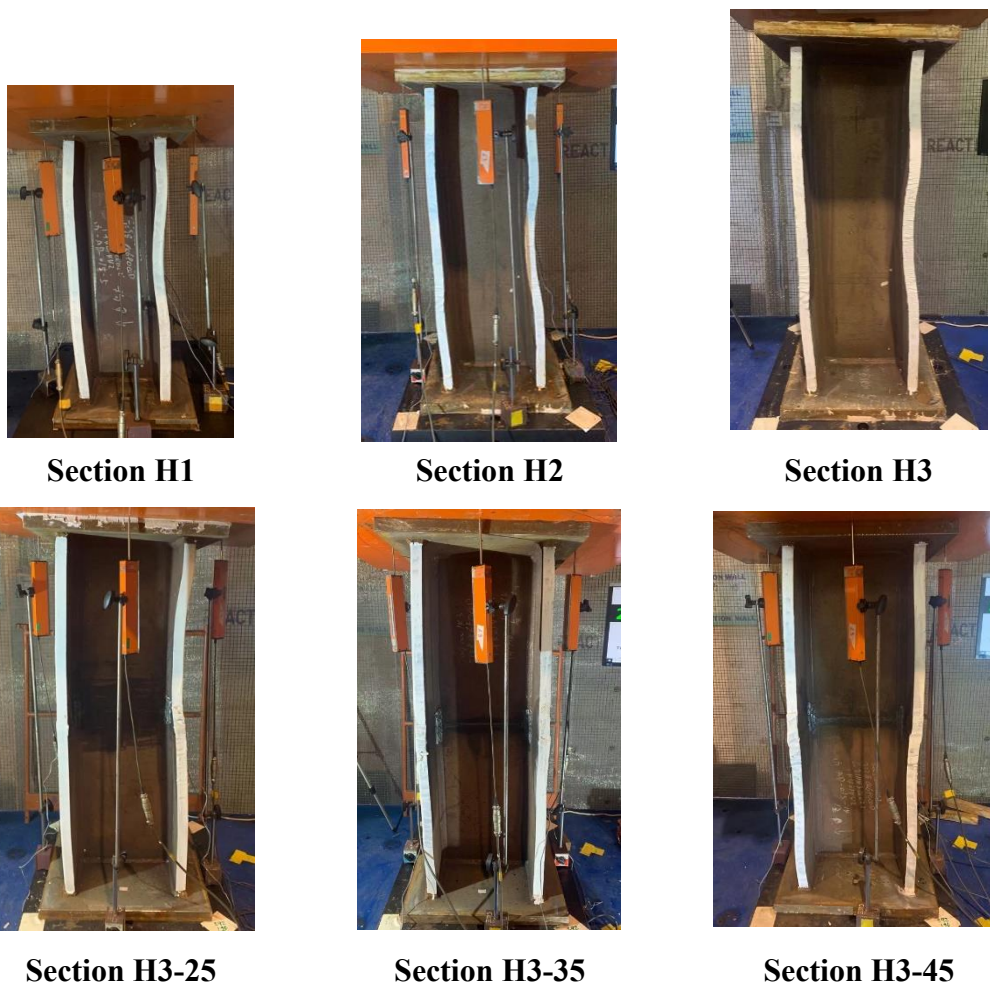
Figure 6.8 Deformed shapes of H-columns after test

Figure 6.9 plots the measured applied load-axial shortening curves of Sections H1, H2 and H3. The axial shortening of each column was taken as the average value of four LVDTs. It should be noted that all the curves extend well above the respective design section resistances of the sections, the current design rules given in EN 1993-1-1 are able to predict the section resistances of these Q620 H-columns conservatively.
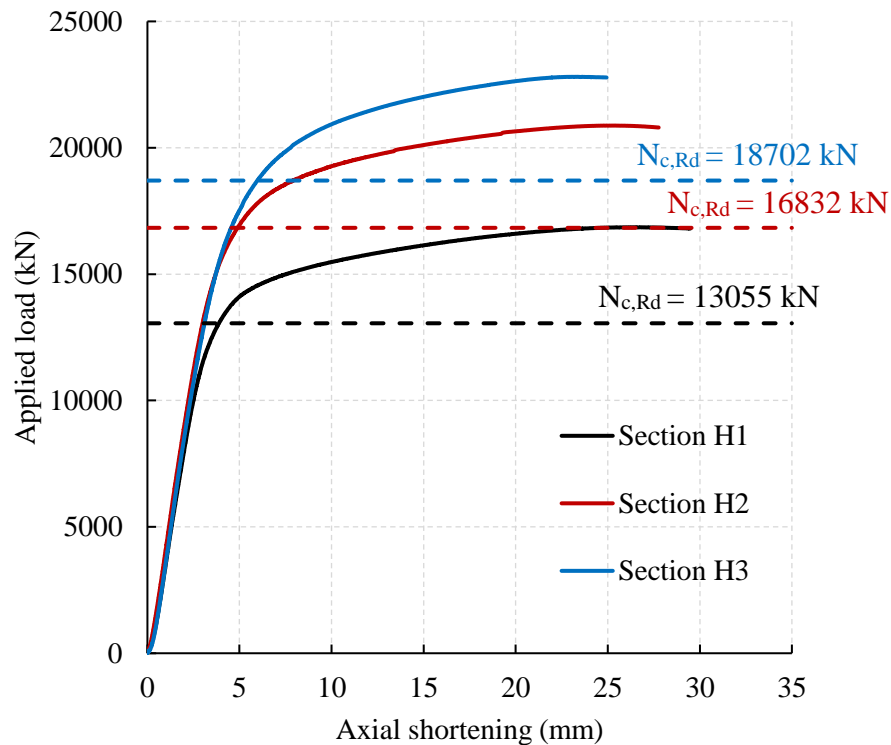
Figure 6.9 Applied load-axial shortening curves of Q620 H-columns

Figure 6.10 plots the applied load-axial shortening curves of the spliced H-sections, namely, Sections H3-25, H3-35 and H3-45, together with that of Section H3. It is evident that the cross-section resistances of all these H-columns are significantly larger than their respective design values. It is important to note that full section resistances are readily mobilized even in these spliced columns. Hence, the current design rules given in EN 1993-1-1 are considered to be able to predict the cross section resistances of these spliced stocky columns of Q620 welded sections.
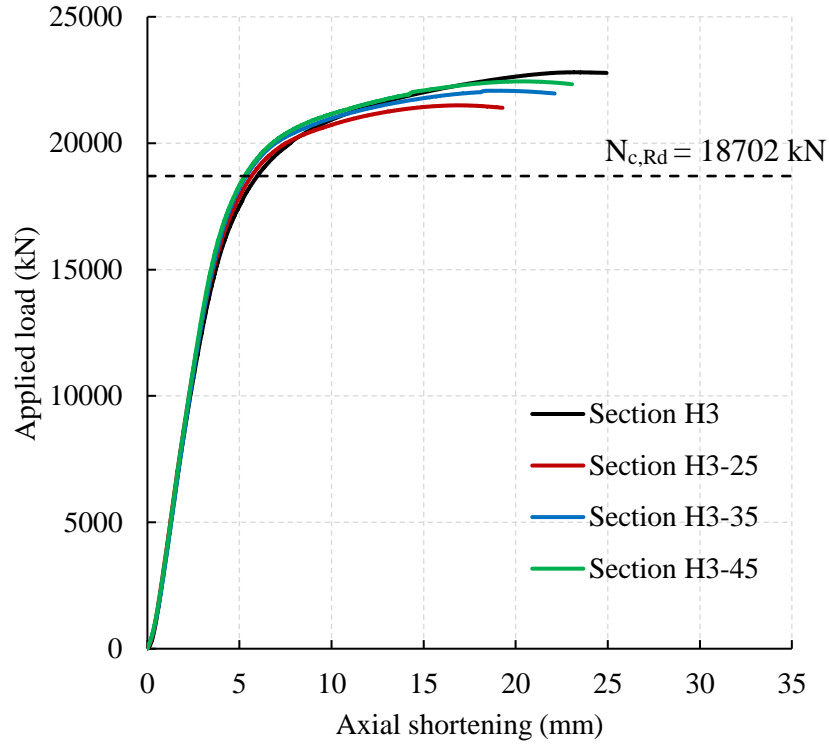
Figure 6.10 Applied load-axial shortening curves of spliced H-columns

Table 6.5 presents a comparison of the measured resistances, $N_{c,Rt}$, and the design resistances, $N_{c,Rd}$, of these six H-columns. It is found that:

1) By comparing the ratios of the measured cross section resistances $N_{c,Rt}$ divided by the design value $N_{c,Rd}$, a strength enhancement is found to range from 22% to 29%.

By comparing these ratios of the measured cross section resistance between H3, H3-25, H3-35 and H3-45, such strength enhancement decreases in these spliced H-sections columns, and with an increase in heat input energy of butt welding at mid-height, this ratio increases.

228

Table 6.5 Cross-sectional resistances of Q620 H-columns under compression

Specimens	Heat input energy (kJ/mm)	Section classification	Design resistance $N_{c,Rd}$ (kN)	Measured resistance $N_{c,Rt}$ (kN)	$N_{c,Rt}/N_{c,Rd}$
H1	-	Class 1	12562	16854	1.34
H2	-	Class 2	16196	20878	1.29
H3	-	Class 3	17995	22806	1.27
H3-25	2.5		17878	21500	1.20
H3-35	3.5		17842	22075	1.24
H3-45	4.5		18052	22446	1.24

Note: The cross-sectional resistance, $N_{c,Rd}$ is predicted with measured dimensions and yield strength as follows:

$$N_{c,Rd} = f_y \cdot (2bt_f + dt_w) \qquad \text{Equation 6.1}$$

Where f_y——measured yield strengths of the steel plate.

b——measured width of the flange.

d——measured overall depth of the web.

t_f——measured thickness of the flange.

t_w——measured thickness of the web.

6.4 Numerical modelling of welded H-section

Considering that the effects of welding onto residual stresses and mechanical property changes exist at the same time in a welded section, an integrated numerical modelling approach was proposed. The flow chart of the proposed approach is presented in Figure 6.11. A heat transfer analysis is carried out to attain the temperature history caused by welding, then the temperature history is input into a mechanical model to calculate the residual stresses. The changes of mechanical properties in HAZ are determined with the Critical Sub-Zone method illustrated in Chapter 6. Then, the residual stresses and the simplified sub-zones in HAZ are input to define the initial state for subsequent structural analysis.

In this section, Columns H3, H3-25 and H3-45 were selected to demonstrate adequacy of the proposed approach.
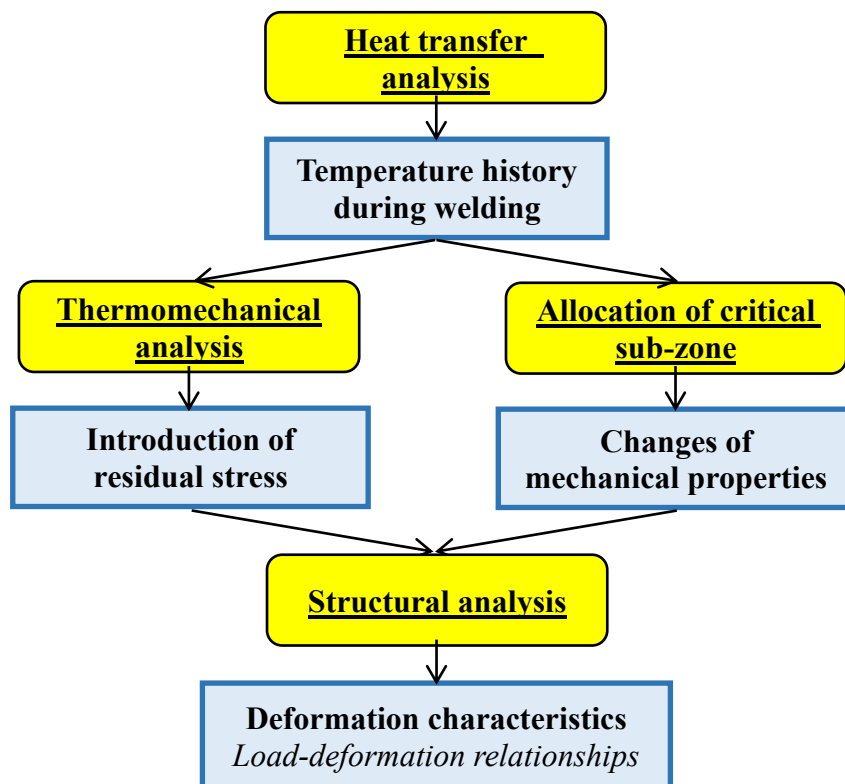
Figure 6.11 Flow chart of integrated welding model

6.4.1 Modelling process

The finite element meshes of Models H3, H3-25 and H3-45 are shown in Figure 6.12. The general element sizes in these three models is the same, except those elements at the mid-height of Models H3-25 and H3-45. A graded meshing strategy was adopted in these regions, that is, the elements adjacent to the weldment were designed to have smaller sizes. It should be noted that these models were built according to their nominal dimensions for easy comparison.

a) Model H3

Graded mesh at the flange plate

Graded mesh at the web plate

b) Models H3-25 & H3-45

■ Base plate   ■ Weld metal
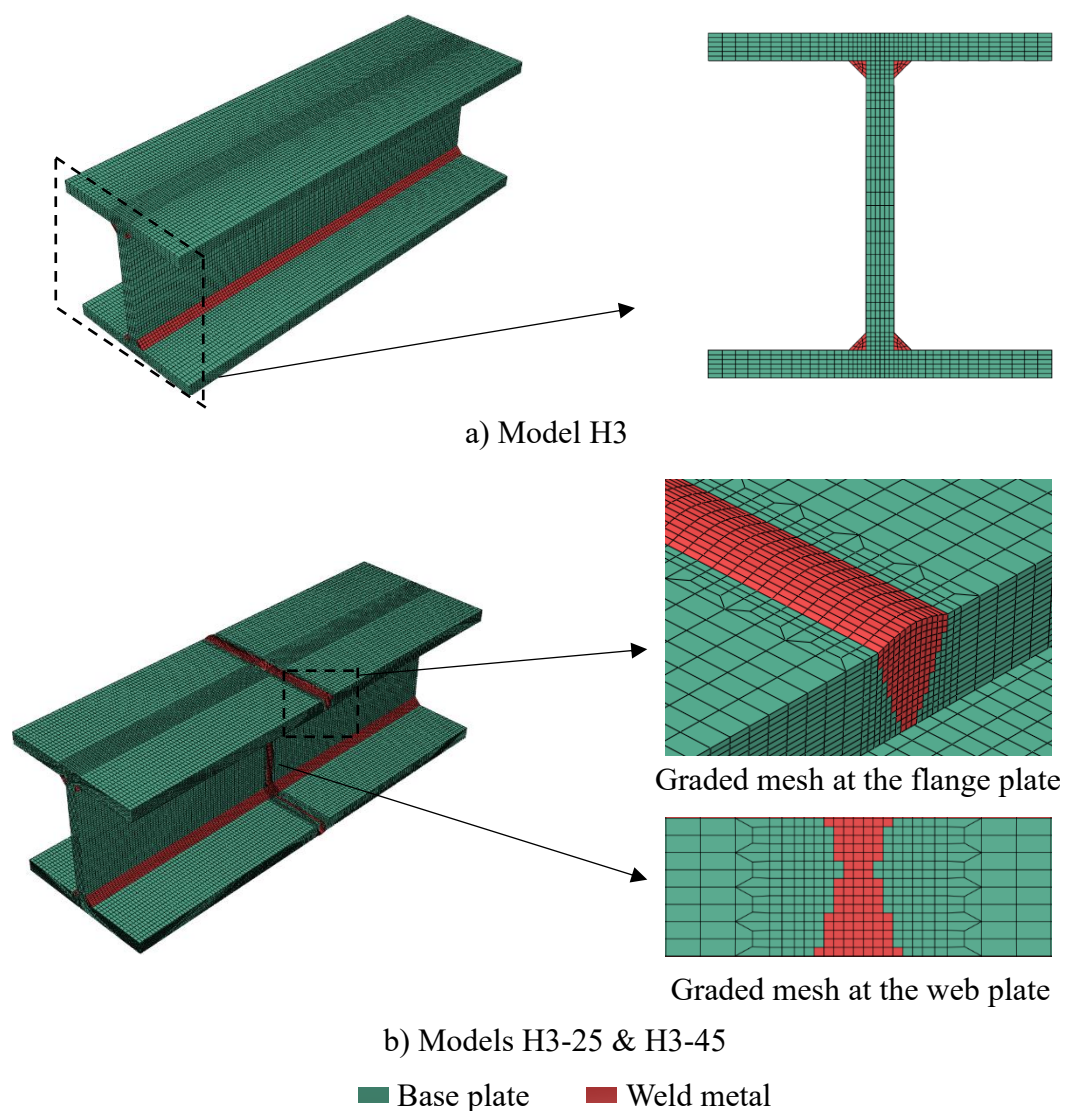
Figure 6.12 Overview of finite element models

It should be noted that Models H3-25 and H3-45 have the same welding sequence, and the same joint designs in both the flanges and the web, and welding parameters the during welding of their webs. While those parameters for welding of the flanges were different. As shown in Figure 6.13, these two models have the same arrangement of weld passes in the web plates, and the elements in the flanges plates are classified into different sets to simulate various weld passes.
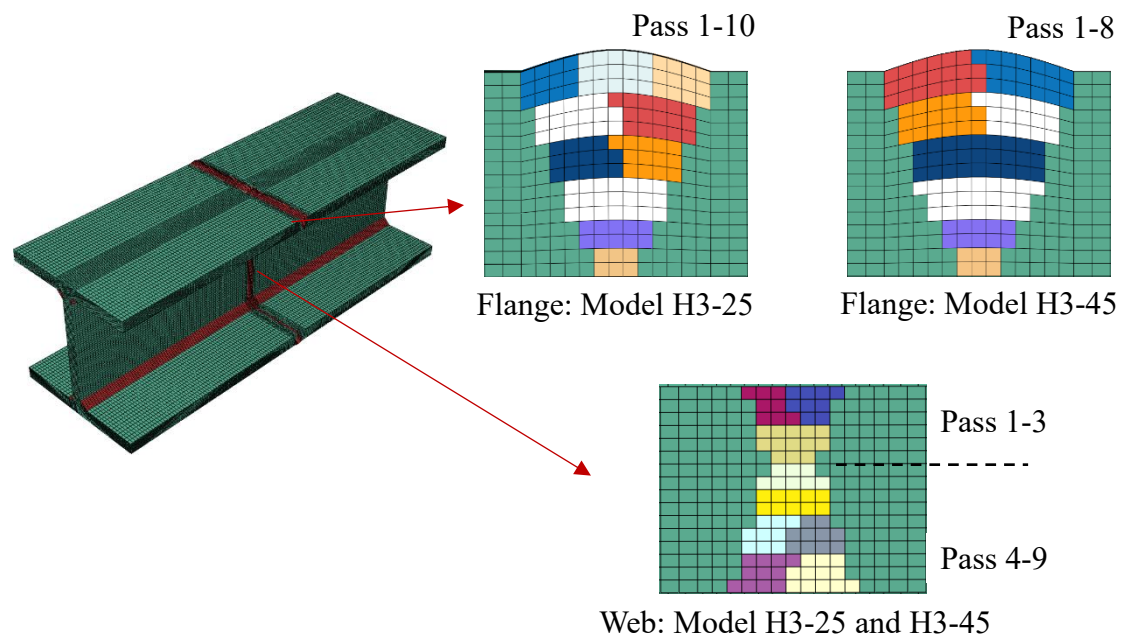
Figure 6.13 Weld passes in webs and flanges of Models H3-25 and H3-45

6.4.2 Welding sequence

➢ Model H3

As shown in Figure 6.14, Model H3 follows the welding sequence in the fabrication process of Column H3 shown in Section 6.2.1
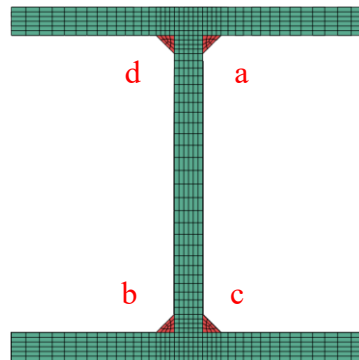
Figure 6.14 Welding sequence in Model H3

➢ Models H3-25 and H3-45

The welding sequence of these two spliced H-columns follows the fabrication process presented in Section 6.2.2. As shown in Figure 6.15, the fillet welding is carried out first onto two H-sections (Step 1), and then, the webs and the flanges of these two H-sections are welded together (Steps 2 and 3). Finally, the access holes are welded (Step 4). It should be noted that the welding sequence of fillet welds (Step 1) of these two H-sections in the spliced H-section is the same as in Model H3 shown in Figure 6.14.

<div align="center">
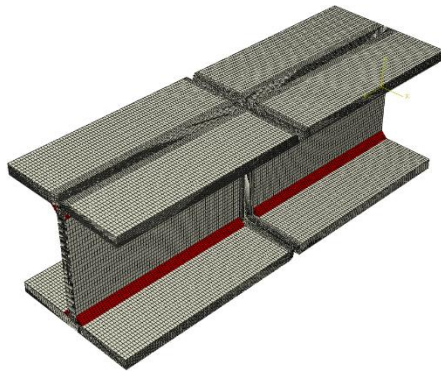
Step 1: Fillet welding   Step 2: Butt welding of the web plate
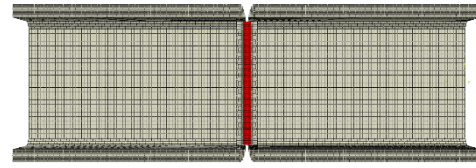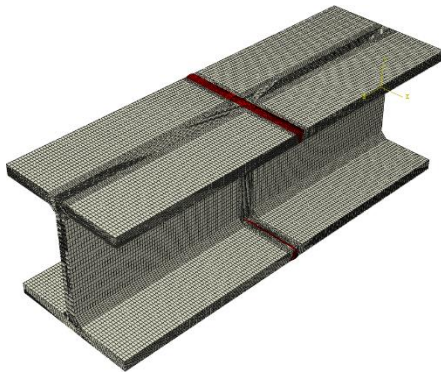
Step 3: Butt welding of the flange plates   Step 4: Fillet welding of access hole
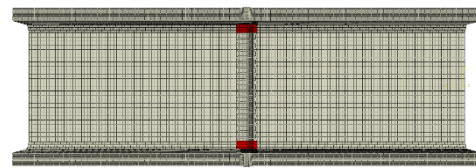
■ Weldment in this step

Figure 6.15 Welding sequence in Models H3-25 and H3-35

</div>

6.4.3 Welding parameters and techniques

The mechanical properties of the Q620 TM steel and the weld metal at room temperature are presented in Section 5.5.3. The thermal material properties, and the reduction factors to Young's modulus, yield strength and tensile strength of this Q620 TM steel are set to be the same as those of the S690 QT steel in Sections 4.4.4 and 4.4.5, respectively.

A heat source in the form of a double ellipsoidal heat source model was adopted in the heat transfer analysis to obtain the temperature history during welding. Then, the sequentially coupled thermomechanical analyses were adopted to obtain the residual stresses caused by welding.

6.4.4   Effect of welding on residual stress

Figure 6.16 shows the typical transient temperature field during welding, and the predicted longitudinal residual stress caused by welding of each model of Sections H3, H3-25 and H3-45.

a) Model H3

b) Model H3-25

c) Model H3-45
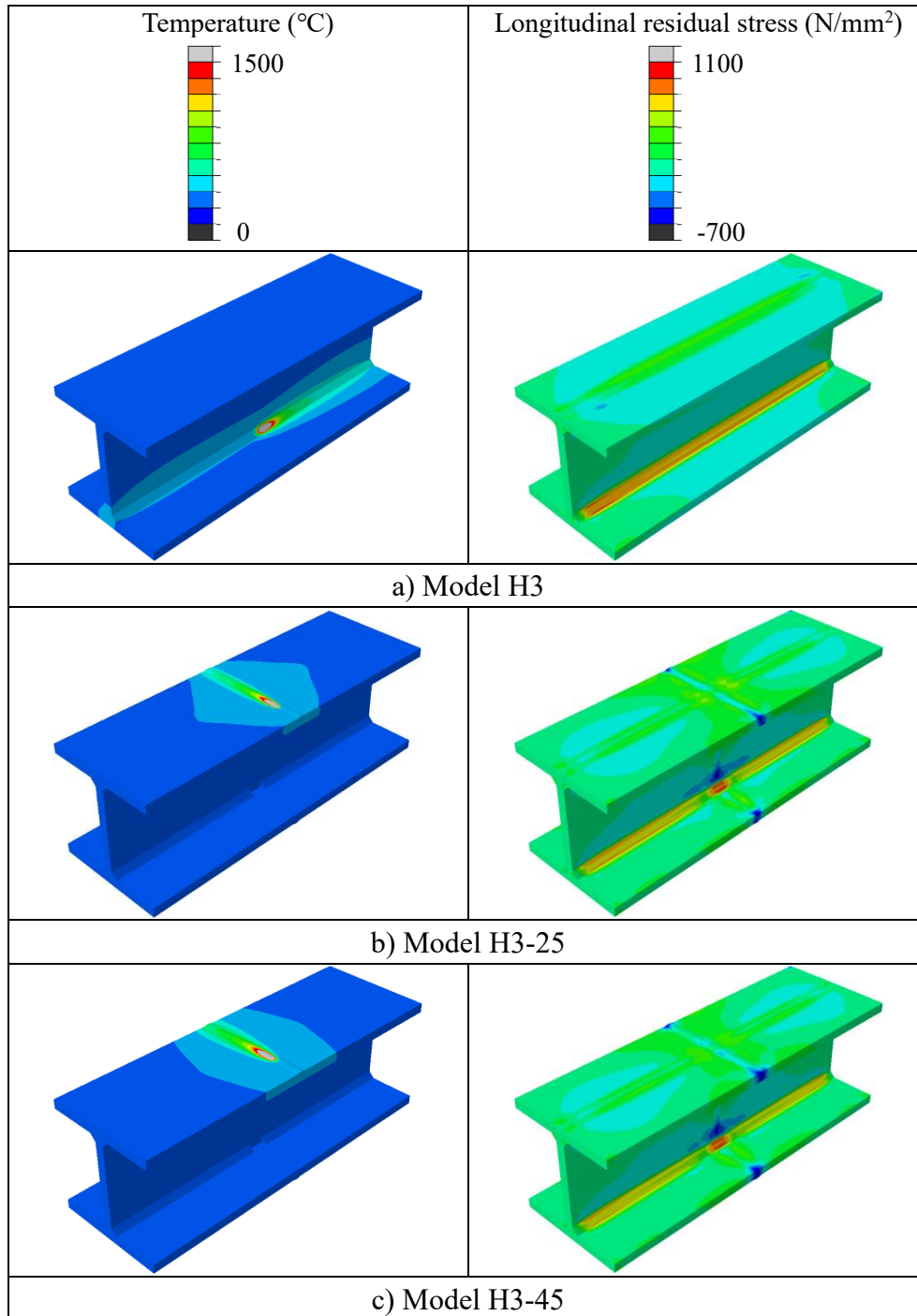
Figure 6.16 Predicted temperature field and longitudinal residual stresses

6.4.5 Effect of welding on mechanical properties changes

Based on the predicted temperature field, the cooling time $t_{8/5}$ of each weld joint is readily obtained. Then, with the Critical Sub-Zone method presented in Section 5.5.3, the widths of the critical sub-zones of these welded joints are derived, and they are summarized in Table 6.6.

Table 6.6 Critical sub-zones in various locations of columns

Model	Weld joint	Heat input energy (kJ/mm)	Cooling time $t_{8/5}$ (s)	Width of critical sub-zone (mm)
H3	Fillet weld	3.0	23.2	3.3
H3-25	Fillet weld	3.0	23.2	3.3
	Web	2.5	17.4	2.6
	Flange	2.5	17.4	2.6
H3-45	Fillet weld	3.0	23.2	3.3
	Web	2.5	17.4	2.6
	Flange	4.5	35	4.0

In this section, two series of models were established as follows:

➢ Case 1: Without the changes of mechanical properties in HAZs in the columns under compression

➢ Case 2: With the changes in mechanical properties

The coordinates of nodes of elements adjacent to the weld metal regions were changed in order to achieve the width of critical sub-zones listed in Table 6.6. Figure 6.17 shows the locations and dimensions of critical sub-zones in Models H3-case 2, H3-25-case 2 and H3-45-case 2.

Model H3-case 2

Base plate   Weld metal   23.7-700

a) Model H3-case 2

3.3 mm

2.6 mm

4.0 mm

Flange: Model H3-25-case 2   Model H3-25-case 2

2.6 mm

Web:
Models H3-25-case 2 and H3-45-case 2

3.3 mm

Fillet weld:
Models H3-25-case 2 and H3-45-case 2

Base plate   Weld metal   23.2-700   17.4-700   35-700

b) Models H3-25-case 2 and H3-45-case 2
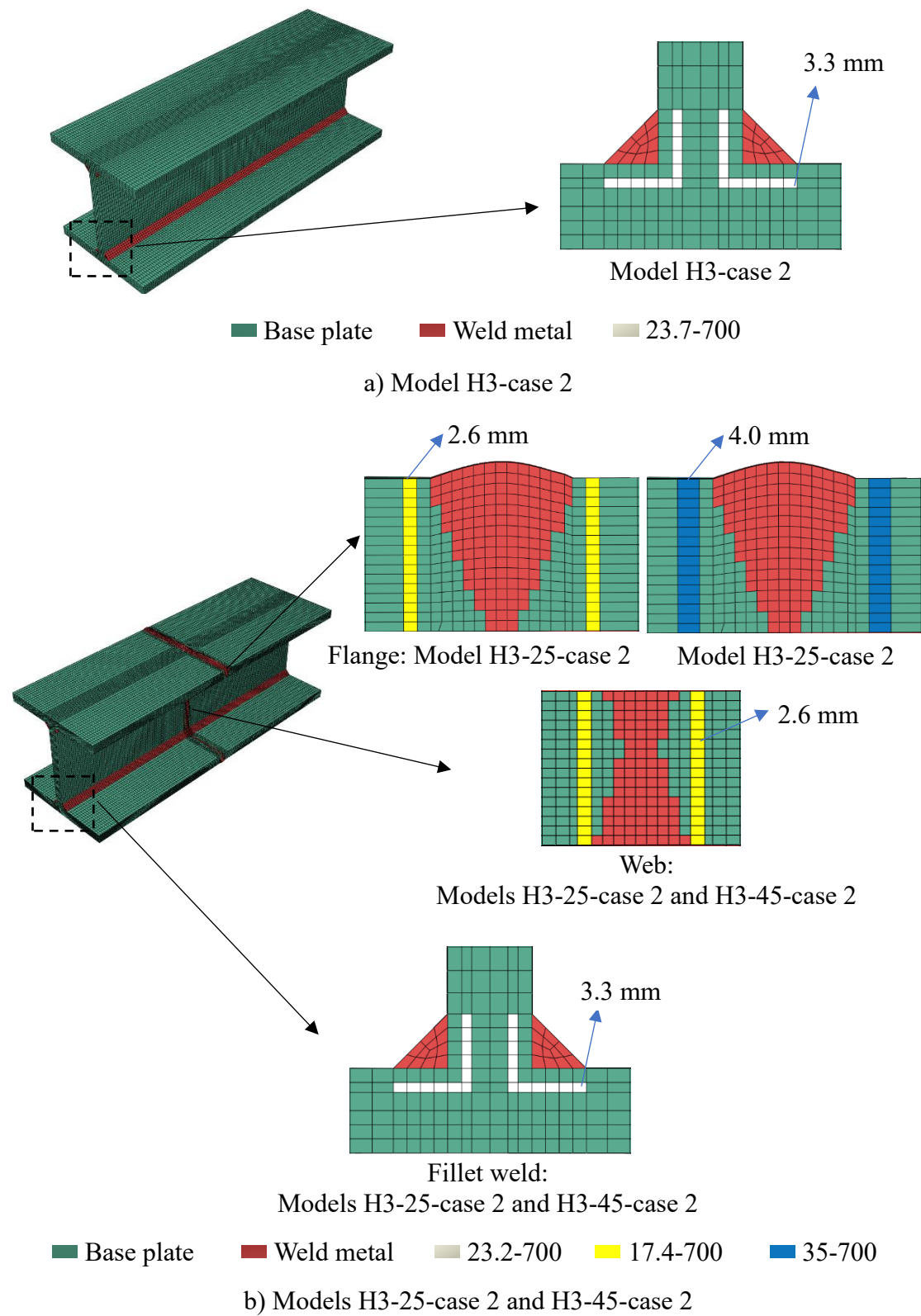
Figure 6.17 Allocation of critical sub-zones in welded H-sections

6.4.6 Boundary conditions in compression

In those models, the end plates were not included directly while their effects were provided with a proper setting of boundary conditions. Considering in each model that the end plate limits relative deformations of the connected end of the column, the bottom end of the column was fully restrained. While a reference point was defined at the centre of the top end and, all the six degrees of freedom of the surface of the top end were coupled with this point. Hence, axial shortening was imposed on this reference point.
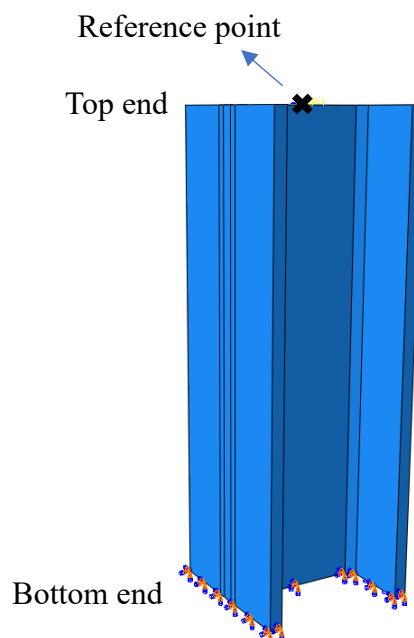
Figure 6.18 Typical boundary conditions of a H-column

6.4.7 Initial out-of-straightness

In general, both the assembly and the welding processes introduce initial geometrical imperfection in these welded sections. However, it is difficult to quantify the magnitudes of these geometrical imperfection taken place in the assembly process, and the accuracy of distortion predicted with the existing welding simulation technique still needs further investigation. To solve this, the eigenmode with the lowest eigenvalue is

238

adopted to both the initial geometrical imperfection according to common practice. The maximum initial geometric imperfection was taken to be 1/500 of the plate width of the welded H-sections.

6.4.8   Results of simulations

Figure 6.19 shows the measured and the predicted deformed shapes of these columns. It should be noted that the models plotted in Figure 6.19 have the same axial shortening values as those of test specimens in each group. It is obvious that the models give symmetric deformed shapes while different deformed shapes in the test specimens are observed.

H3	Model H3-C 1	Model H3-C 2
H3-25	Model H3-25-C 1	Model H3-25-C 2
H3-45	Model H3-45-C 1	Model H3-45-C 2
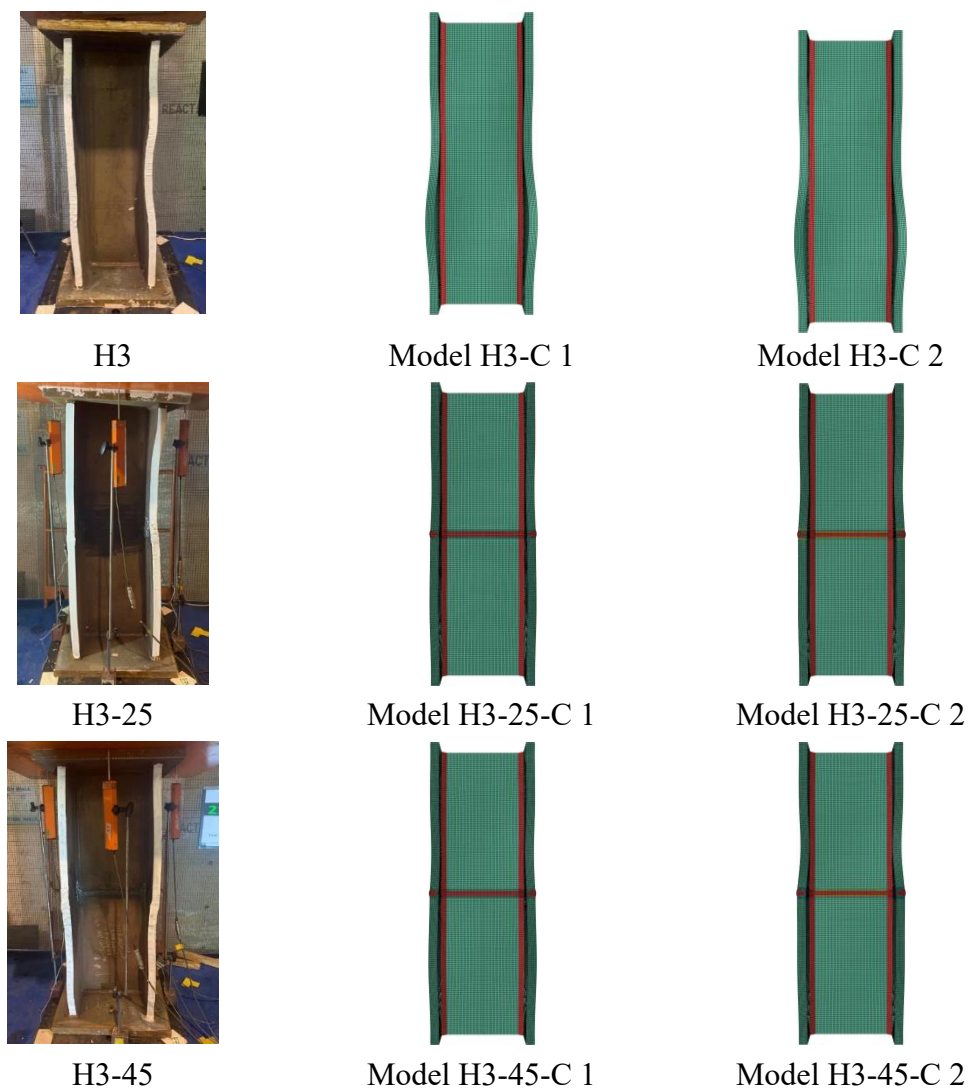
Figure 6.19 Deformed shapes of measured and predicted results

239

In order to allow for effective comparison with the numerical models, the measured applied load in the tests are normalized with respective to their respective cross-sectional areas, as shown in Figure 6.20. It is shown that both Models Case 1 and 2 meet measured results well in the elastic stage and the hardening stage in each group. However, the applied load given by Case 2 at the hardening stage is smaller than that given by Case 1 in each group. It is considered that the critical sub-zones in Case 2 lead to the reduction of applied load as that is the only difference between these two models.

As shown in Table 6.7:

1) By comparing the compression resistance between Case 1 and 2 in each group, a reduction of 1%, 1.9% and 1.9% of compression resistances predicted by Case 2 than those of Case 1 was found in Models H3, H3-25 and H3-45, respectively.

   It is considered that the critical sub-zones in Case 2 lead to such a reduction. As there are more critical sub-zones in these spliced H-sections, greater reductions of Models H3-25 and H3-45 were found than that of Model H3.

2) By comparing the resistance predicted by Case 1 in each group, Model H3-25 and H3-45 give the same prediction results, while the resistance predicted by Model H3 is 272kN smaller than the other two models. While in Case 2, such a difference becomes smaller and is found to be 63kN, and that's only 0.3% of the predicted resistance. Based on this, the presence of butt welds with different heat input energy at mid-height of these sections has negligible effects on the compression resistance of these Q620 welded sections.

3) However, the differences of normalized measured resistances between Columns H3 to H3-24 and H3-45 are found to be 4.9% and 4.5%, respectively, which are much larger than the predicted ones shown above. This may be explained by the fact that the spliced H-sections were welded with two H-sections and such a step will lead to a much larger geometry imperfection compared with the reference H-sections.

240
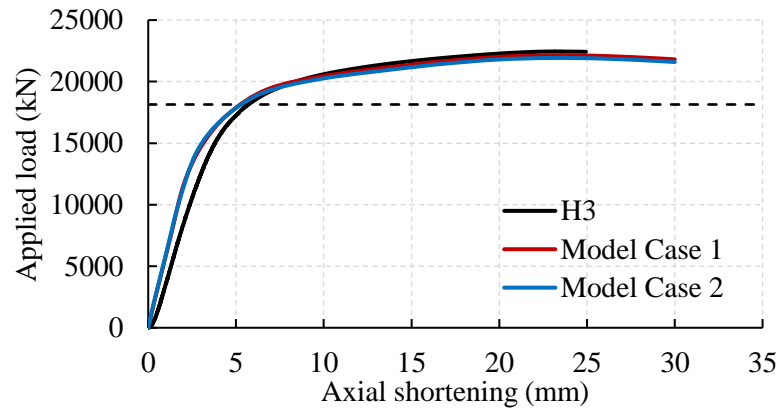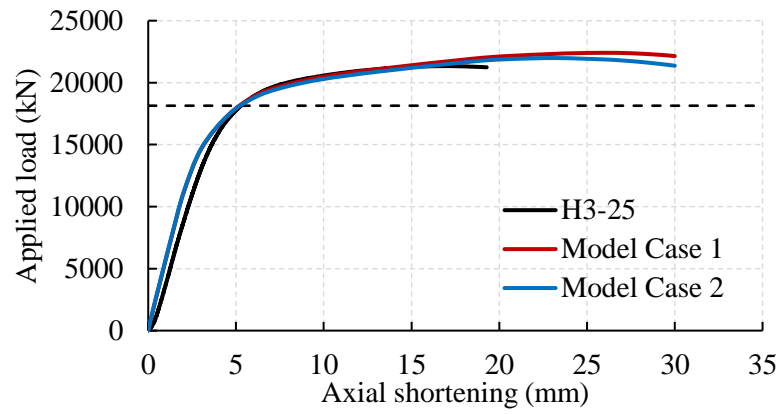
a) Model H3

b) Model H3-25
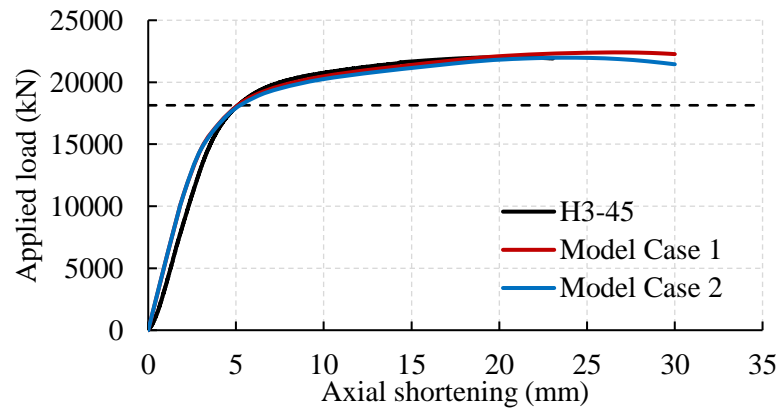
c) Model H3-45

Figure 6.20 Applied load-axial shortening curves of measured and predicted results

Table 6.7 Measured and predicted compression resistances

Section	Compression resistances			Resistance ratios	
	Normalized test results (kN)	Case 1 (kN)	Case 2 (kN)	Case 1	Case 2
H3	22 450	22 135	21 919	1.01	1.02
H3-25	21 340	22 409	21 986	0.95	0.97
H3-45	21 437	22 407	21 982	0.96	0.98

Note: the resistance ratio is calculated by the compression resistance of normalized test result over that of the predicted one.

6.5 Conclusions

➢ **Compression tests on welded H-sections and spliced H-sections**

Three spliced Q620 welded H-sections with different heat input energy adopted in the welding processes together with three reference columns were tested. Full section resistances of all the stocky columns are readily mobilized despite the presence of butt welded joints at mid-height. Hence, the current design rules given in EN 1993-1-1 are able to predict the section resistance of these high strength Q620 stocky columns.

➢ **Simulation of compression with the integrated model**

An integrated model which considered the residual stress and changes in mechanical properties was proposed. 1 reference and 2 spliced columns were simulated and the effect of heat input energy on the structural performance of this stocky column was investigated with this mode. It is found that:

1) The existence of critical sub-zones leads to a 1% to 2% of reduction of compression resistance.

2) Although there are different levels of reduction of mechanical properties in HAZs of butt weld joints, the difference in compression resistance between the reference column and the spliced columns is neglectable. Consequently, the structural adequacy of the Q620 steel welded joints with different heat input energy is provided scientifically to confirm its applications in construction.

3) However, there is still a difference in the measured resistance between the reference column and the spliced columns. This may be explained as different levels of geometry imperfections caused in the assembly process.

Chapter 7. Conclusions and future plan

7.1 Introduction

In this study, a systematic experimental and numerical investigation into the structural effects of welding onto high strength QT and TM steel thick welded sections was conducted, including the mechanical properties of welded sections, the residual stresses of welded sections and the structural performance of welded members. Moreover, a critical sub-zone method was proposed to provide a numerical solution to model any reduction in the mechanical properties of the HAZ in finite element models. This chapter summarizes key findings of Chapters 3 to 6, and a plan for future work is also recommended.

7.2 Research methodology and key findings

With a comprehensive investigation, the following 4 tasks were completed successfully as follows:

7.2.1   Mechanical properties of high strength QT and TM thick welded sections

A total of 56 standard tensile tests were conducted onto both QT and TM welded sections under monotonic loadings, and key findings are summarized as follows:

1)   For these 50 and 70 mm thick S690 QT steel:

It is found that with an increase in plate thickness, a reduction in the strength of the steel in the mid-thickness occurs. For coupons extracted from the mid-thickness of the 70mm steel plates, reductions in the yield and the tensile strengths were found to be 7.1% and 6.6%, respectively, when compared with those results of the top and the bottom layers. However, there is no significant difference in the mechanical properties

of those coupons extracted from different locations within the thickness of the 50 mm thick steel plates.

2) For these 50 and 70 mm thick S690 QT welded section:

   a) The heat input energy in this study are 2.4, 3.5 and 5.0 kJ/mm, and reduction factors for the tensile strengths of the 50 mm thick welded sections were found to be 0.96, 0.95 and 0.97, respectively. For those 70 mm thick welded sections, the reduction factors were 1.00, 0.99 and 1.00.

   b) There are only small reductions in the tensile strengths of all these welded sections when compared with those of the base plates. All the welded sections can satisfy the strength requirements stipulated in EN ISO 15614-1 even the heat input energy at 5.0 kJ/mm is adopted which is considered to be the maximum value in practice.

   c) The mechanical properties of these 50 and 70 mm thick welded sections in this study are demonstrated not to vary significantly. Hence, the effects of welding onto the mechanical properties of these thick S690 welded sections are insignificant.

3) For these 28 and 44 mm thick Q620 TM welded sections:

   a) The heat input energy are 2.4, 3.5 and 5.0 kJ/mm, and the reduction factors for the tensile strengths of the 28 mm thick welded sections were found to be 0.97, 0.95 and 0.95, respectively. For these 44 mm thick welded sections, the reduction factors were 0.98, 0.97 and 0.96.

   b) There are only small reductions in the tensile strengths of all these welded sections when compared with those of the base plates. All the welded sections can satisfy the strength requirements stipulated in GB 50661 even the heat input energy at 4.5 kJ/mm is adopted.

Consequently, it is considered that application of these heat input energy in welding these S690 QT and Q620 TM thick sections using conventional welding methods is highly acceptable.

7.2.2 Residual stress distribution in thick welded sections

A hole-drilling method was adopted to measure the surface residual stresses of thick high strength steel welded sections. While a local material removal method was involved, i.e. parts of the top and the bottom layers of the welded section was removed with the milling process and the hole-drilling method was applied on the newly formed surfaces to obtain the corresponding residual stresses. As these residual stresses do not represent the original stress state before material removal. Finite element models were established to obtain the residual stresses within the thick welded sections.

It should be noted that the welding parameters and the surface temperature history during welding were measured and heat transfer models were established carefully calibrated with these data. Then, with the sequentially couple thermomechanical analyses, the residual stresses were obtained. Both the measured and the predicted residual stresses on the top and the bottom surfaces, and the measured and the predicted residual stresses after local material removal were found to agree with each other well. Hence, the predicted residual stresses before material removal were predicted with sufficient accuracy.

It should also be noted that:

1) The predicted residual stresses at different layers within the 50 mm thick welded section were found to have similar levels, and the differences of these residual stresses between those welded sections with 2.4 and 5.0 kJ/mm is negligible.

2) Existing standard, i.e. BS 7910 is able to predict the residual stress of these 50 mm

thick welded sections quite well.

7.2.3　Critical sub-zone method

In order to simulate the effects of welding onto the mechanical properties of high strength steel welded sections, a Critical Sub-Zone methodin which a critical sub-zone within the heat affected zones of these welded sections are modelled with specific dimension and reduced mechanical properties.is proposed to define the dimension and mechanical properties of the most critical sub-zone.

It should be noted that:

1) The mechanical properties of each sub-zone within the HAZ of both the S690 QT and the Q620 TM welded sections were investigated. A total of 48 heat-treated coupons were tested and each of them was heat treated with a specific combination of $t_{8/5}$ and T_{max}. By comparing the tensile strengths of these heat-treated coupons, the most critical T_{max}, i.e. the coupons with the smallest tensile strengths in each group, were obtained. It is found that the range of T_{max} with reduction factors smaller than 1.0 for the TM steel is larger than that for the QT steel, and the reduction factors for the tensile strengths of the TM steel at critical temperature are larger than these of the QT steel.

2) The geometry of these critical sub-zones were readily determined from the cross sectional distributions of temperature predicted by heat transfer analysis.

3) The following simplifications are also adopted:
   a) Only the most critical sub-zone in the HAZ is considered in the models.
   b) The $t_{8/5}$ is simplified to be constant for a given welded section with one heat input energy for each weld pass.
   c) The boundaries of the critical sub-zone are simplified to be straight lines.

247

7.2.4 Effect of welding onto H-section stocky columns

A total of 3 reference and 3 spliced stocky columns of Q620 welded H-sections with different heat input energy were tested under compression. It was found that full section resistances were readily mobilized in all these 6 columns, despite the presence of butt-welded splices at the mid-height. Nevertheless, when compared with the reference columns, small reductions in their compression resistance were found in these spliced columns.

In order to assess the effects of welding onto the compression resistances of these stocky columns, an advanced finite element model with the proposed Critical Sub-Zone method was established. Both the residual stresses and the reduced mechanical properties in the critical sub-zone within the HAZ were incorporated. A reference welded H-section, namely Section H3, and two spliced H-sections, namely Sections H3-25 and H3-45, were selected for modelling.

It should be noted that:

1) The compression resistances of models with reduced mechanical properties in their critical sub-zones are 1% to 2% smaller than those of the models without. Hence, the softened HAZ in those stocky columns will lead to only a small reduction in the compression resistance.

2) The difference between the compression resistances of Model H3 to those of Models H3-25 and H3-45 is within 0.3%. Hence, the current design rules are equally applicable to predict the section resistances of these spliced H-sections.

However, the difference between the normalized compression resistance of Column H3 to Columns H3-25 and H3-45 is found to be about 4.9%. The differences between the experimental and numerical investigation may be explained as different levels of initial geometry imperfections in these columns.

7.3 Recommendations for future work

In this study, the residual stresses and the changes in mechanical properties within HAZ were simulated successfully. However, there is another welding effect on a welded structure, i.e. welding induced distortion, which usually leads to misalignment, and directional mismatch etc. There are several methods to prevent or minimize these welding distortions, however, not all these methods are suitable for high strength steel. For example, provision of strongback is one of the most frequently used technique for distortion control in butt welding of plates. Usually, several clips or dog plates are welded at the back of the weld grooves of both plates, as shown in Figure 8.1. However, removal of these strongback leads to the risk of cracks on the surfaces of high strength steels.
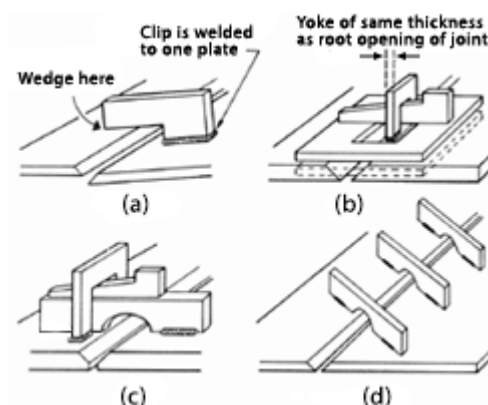
Figure 7.1 Strongback used in butt welding process (Lincoln electric)

Heat straightening or flame straightening is another frequently used method for distortion correction after welding. The welded sections are heated up, and then cooled down in air. As the steel is able to contract more than expand, and hence, any distortions can therefore be straightened out. However, it is important to control the temperature as reductions in the mechanical properties occur when the temperature goes above 800°C in these QT steel and 700°C in these TM steel.

In general, it is necessary to establish models for predictions of welding induced

249

distortion before the actual fabrication process to make a proper design. It should be noted that in many existing welding models, those elements which represent the weld metal are deactivated before welding, and then they are reactivated at once altogether, while in the actual welding process, the weld metal is deposited sequentially. Such a difference in the welding simulation to formation of distortion, as shown in Figure 7.2, should be investigated.

| a) Reactivate in one step | b) Reactivate continuously |
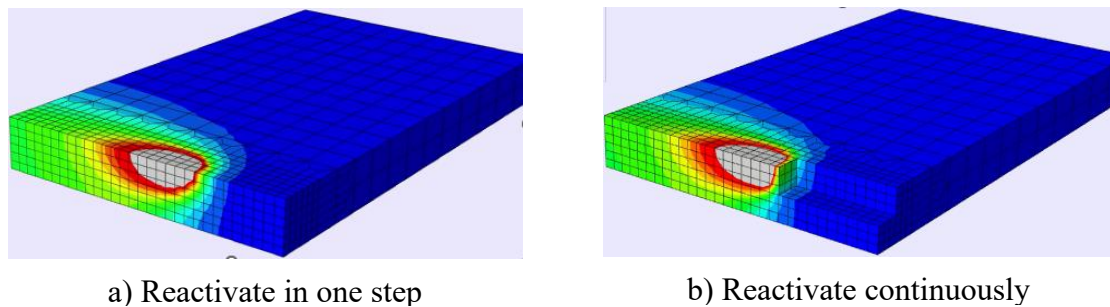
Figure 7.2 Reactivate of elements of weld metal

To solve this issue, a welding test is designed to provide data for calibration of this new welding model as follow. A stress annealing process should be conducted on all the steel plates before welding to remove any initial residual stresses. Then, the temperature history, the distortion history, and the residual stresses of the welded sections will be measured. Two heat input energy, i.e. 1.0 and 2.0 kJ/mm, are employed to cover a wide range of practical welding.

As shown in Figure 7.3, a 50 mm length with a heat input energy of 1.0 kJ/mm is provided to each end of the weld groove. Then, the edge of one steel plates is fixed onto the welding table, and there is no other external constraint onto these steel plates.
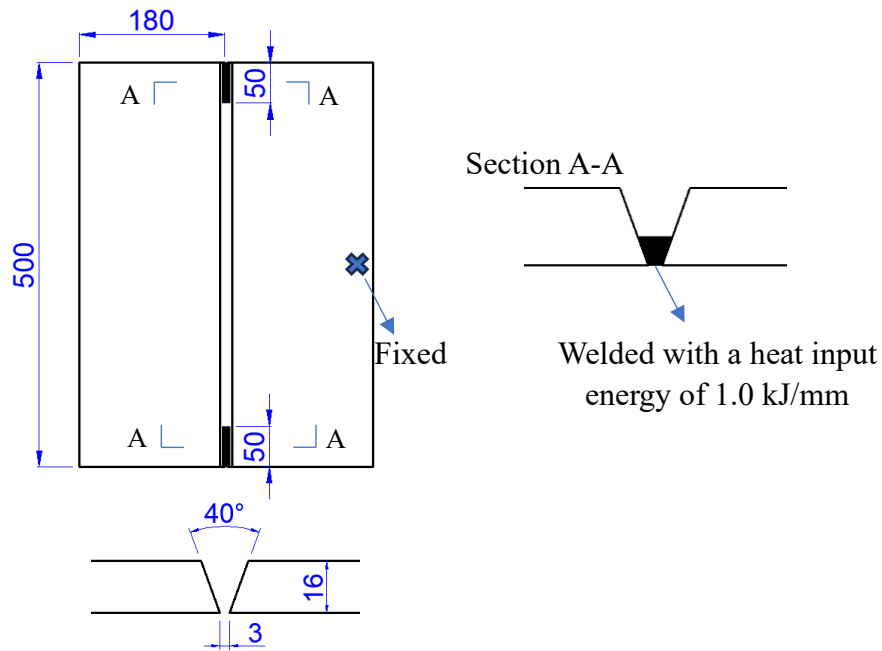
Figure 7.3 Initial test setup before welding

In addition, 3 LVDTs are provided near the edge of the unrestrained plate to measure the displacements and 3 pairs of thermocouples are provided adjacent to the groove edge with a distance of 10 mm, as shown in Figure 7.4.
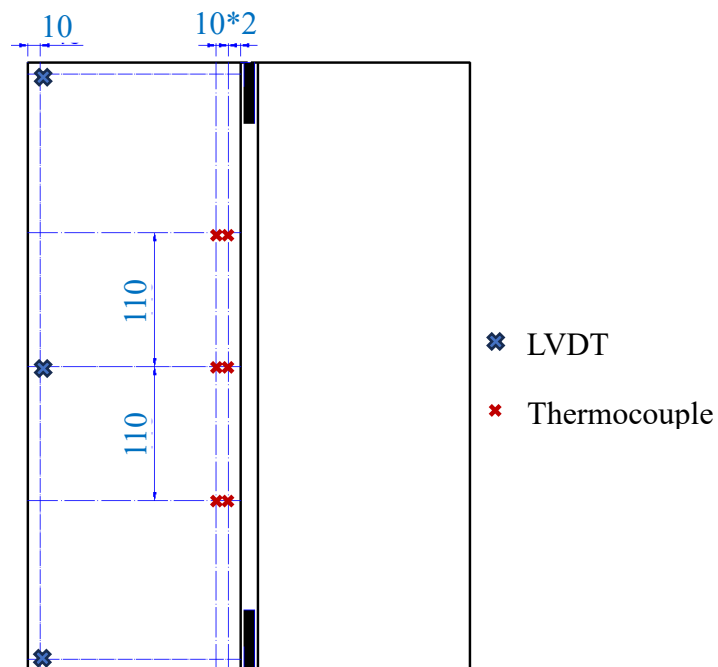
Figure 7.4 Test setup for distortion measurement during welding

To achieve a continuous filling of the weld metal in the finite element model, it is recommended to employ Python code in the modelling process to reactivate the elements of the weld metal together with the movement of the heat source, as shown in Figure 7.2.

Reference

Liu, X., & Chung, K. F. (2018). Experimental and numerical investigation into temperature histories and residual stress distributions of high strength steel S690 welded H-sections. Engineering Structures, 165, 396-411.

ISO 15614-1:2017; Specification and Qualification of Welding Procedures for Metallic Materials-Welding Procedure Test—Part 1: Arc and Gas Welding of Steels and Arc Welding of Nickel and Nickel Alloys. ISO: Geneva, Switzerland, 2017.

Willms, R. (2009). High strength steel for steel constructions. Nordic Steel.

CEN. (2019c). Hot rolled products of structural steels - Part 6: Technical delivery conditions for flat products of high yield strength structural steels in the quenched and tempered condition. BS EN 10025-6:2019, European Committee for Standardization (CEN), Brussels, Belgium.

CEN. (2019b). Hot rolled products of structural steels - Part 4: Technical delivery conditions for thermomechanical rolled weldable fine grain structural steels. BS EN 10025-4:2019, European Committee for Standardization (CEN), Brussels, Belgium.

GB/T 1591-2018. High strength low alloy structural steels. China Standardization Publishing House Press, China, 2018.

Eleni Gogou (2012). Use of High Strength Steel Grades for Economical Bridge Design. Masters Thesis Report 2012 April. Delft University of Technology.

Ban Huiyong (2012). Research on the Overall Buckling Behavior and Design Method of High Strength Steel Columns under Axial Compression. Doctoral Thesis Report

2012 May. Tsinghua University.

Langenberg P (2008). Relation between design safety and Y/T ratio in application of welded high strength structural steels. Beijing: China Steel Construction Society, 2008: 28-46.

CEN. (2005). BS EN 1993-1-2, Eurocode 3: Design of Steel Structures, Part 1-2: General rules — Structural fire design. European Committee for Standardization.

Chen, J., Young, B., & Uy, B. (2006). Behavior of High Strength Structural Steel at Elevated Temperatures. Journal of Structural Engineering (New York, N.Y.), 132(12), 1948–1954.

Qiang, X., Bijlaard, F., & Kolstein, H. (2012). Dependence of mechanical properties of high strength steel S690 on elevated temperatures. Construction & Building Materials, 30(1), 73–79.

Wang, W., Wang, K., Kodur, V., & Wang, B. (2018). Mechanical properties of high-strength Q690 steel at elevated temperature. Journal of Materials in Civil Engineering, 30(5).

Winful, D. A., Cashell, K. A., Afshan, S., Barnes, A. M., & Pargeter, R. J. (2017). Elevated temperature material behaviour of high-strength steel. Proceedings of the Institution of Civil Engineers. Structures and Buildings, 170(11), 777–787.

Xiong, M.-X., & Liew, J. Y. R. (2020). Experimental study to differentiate mechanical behaviours of TMCP and QT high strength steel at elevated temperatures. Construction & Building Materials, 242, 118105.

254

TWI, 2019. What is welding? – Definition, processes and types of welds. The Welding Institute https://www.twi-global.com/

Håkansson, K. (2002). Weld metal properties for extra high strength steels. Doctoral Thesis Report 2002-August. Division of Welding, Department of Production Engineering, The Royal Institute of Technology (KTH).ISSN 1650-1888.

Funderburk, R. (1997). Fundamentals of preheat. Welding Innovation, 14(2).

CEN. (2001). BS EN 1011-2, Welding - Recommendations for welding of metallic materials - Part 2: Arc welding of ferritic steels. European Committee for Standardization.

ANSI. (2004). AWS D1.1:2004, Structural Welding Code - Steel. American National Standards Institute.

Funderburk, R. S. (1998). Post Weld Heat Treatment. Welding Innovation, 15(2).

Easterling, K. (1992). Introduction to the physical metallurgy of welding. Elsevier.

Ramirez, J. E., Mishael, S., & Shockley, R. (2005). Properties and sulfide stress cracking resistance of coarse-grained heat-affected zones in V-microalloyed X60 steel pipe. Welding journal, 113, 123.

Tong, L., Niu, L., Ren, Z., & Zhao, X. L. (2021). Experimental investigation on fatigue behavior of butt-welded high-strength steel plates. Thin-Walled Structures, 165, 107956.

Liu, X., Chung, K. F., Ho, H. C., Xiao, M., Hou, Z. X., & Nethercot, D. A. (2018).

Mechanical behavior of high strength S690-QT steel welded sections with various heat input energy. Engineering Structures, 175, 245-256.

Chen, C., Chiew, S. P., Zhao, M. S., Lee, C. K., & Fung, T. C. (2020). Influence of cooling rate on tensile behaviour of S690Q high strength steel butt joint. Journal of Constructional Steel Research, 173, 106258.

Wang, Y.-B., Li, G.-Q., & Chen, S.-W. (2012). Residual stresses in welded flame-cut high strength steel H-sections. Journal of Constructional Steel Research, 79, 159–165.

Thiébaud, R., & Lebet, J.-P. (n.d.). Experimental study of residual stresses in thick steel plates.

Jokiaho, T., Laitinen, A., Santa-Aho, S., Isakov, M., Peura, P., Saarinen, T., ... & Vippola, M. (2017). Characterization of flame cut heavy steel: Modeling of temperature history and residual stress formation. Metallurgical and Materials Transactions B, 48(6), 2891-2901.

Alpsten, G. A., & Tall, L. (1970). Residual stresses in heavy welded shapes (pp. 93-105). American Welding Society.
ECCS. (1976). Manual on Stability of Steel Structures (Second Edition): European Convention for Constructional Steelwork Publication.

Masubuchi, K. (1996). Prediction and control of residual stresses and distortion in welded structures. Transactions of JWRI, 25(2), 53-67.

TWI, 2020. What is residual stress? The Welding Institute https://www.twi-global.com/

Tebedge, N., Alpsten, G., & Tall, L. J. E. M. (1973). Residual-stress measurement by

the sectioning method. Experimental Mechanics, 13(2), 88-96.

ASTM (2013). Standard test method for determining residual stresses by Hole-Drilling Strain-Gage Method (E837-13), 2013, ASTM International: West Conshohocken, US.

GB/T 31310–2014 (2014) Metallic Material: Determination of Residual Stress: Hole Drilling Strain-Gauge Method. China National Standard Press of China, Beijing

Fitzpatrick, M. E., Fry, A. T., Holdway, P., Kandil, F. A., Shackleton, J. & Suominen, L. (2005). Determination of residual stresses by X-ray diffraction.

Pintschovius, L., Jung, V., Macherauch, E., & Vöhringer, O. (1983). Residual stress measurements by means of neutron diffraction. Materials Science and Engineering, 61(1), 43-50.

Rosenthal D. (1947) Mathematical theory of heat distribution during welding and cutting. The Welding Journal.1947, 20(5): 220-234.

Rykalin, N. N. (1960). Calculation of heat processes in welding.

Teixeira, P. R. D. F., Araújo, D. B. D., & Cunda, L. A. B. D. (2014). Study of the gaussian distribution heat source model applied to numerical thermal simulations of TIG welding processes.

Balasubramanian, K. R., Shanmugam, N. S., Buvanashekaran, G., & Sankaranarayanasamy, K. (2008). Numerical and experimental investigation of laser beam welding of AISI 304 stainless steel sheet. Advances in Production Engineering & Management, 3(2), 93-105.

257

Deng, D., & Murakawa, H. (2008). Prediction of welding distortion and residual stress in a thin plate butt-welded joint. Computational Materials Science, 43(2), 353-365.

Sonti, N. & Amateau, M. F. (1989). Finite-element modeling of heat flow in deep penetration laser welds in aluminum alloys. Numerical heat transfer, 16(3), 351-370.

Bonifaz, E. A. (2000). Finite element analysis of heat flow in single-pass arc welds. WELDING JOURNAL-NEW YORK-, 79(5), 121-s.

Khurshid, M., Barsoum, Z., & Barsoum, I. (2015). Load Carrying Capacities of Butt Welded Joints in High Strength Steels. Journal of Engineering Materials and Technology, 137(4).

Chen, C., Chiew, S.-P., Zhao, M.-S., Lee, C.-K., & Fung, T.-C. (2019). Welding effect on tensile strength of grade S690Q steel butt joint. *Journal of Constructional Steel Research*, *153*, 153–168.

EN ISO 6892-1:2019, (2019). Metallic Materials – Tensile Testing Part 1: Method of Test at Ambient Temperature Brussels, Belgium, CEN

GB 50661, (2011). Code for welding of steel structures Beijing, China, China Architecture & Building Press.